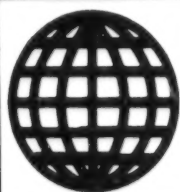


JPRS-JST-92-025
2 OCTOBER 1992



**FOREIGN
BROADCAST
INFORMATION
SERVICE**

JPRS Report

Science & Technology

Japan

FUNCTIONALLY GRADIENT MATERIALS SYMPOSIUM

SCIENCE & TECHNOLOGY
JAPAN

FUNCTIONALLY GRADIENT MATERIALS SYMPOSIUM

926C0014 Tokyo FGM '91 in Japanese 8-9 Oct 91

[Selected articles from the proceedings of the 4th Functionally Gradient Materials Symposium (FGM '91) held 8-9 Oct 91 in Kawasaki City, sponsored by the Functionally Gradient Materials Forum]

CONTENTS

Thermal Fatigue of FGM at High Temperature Differences [Masaki Sasaki, Akinaga Kumakawa, et al.].....	1
High-Temperature Supersonic Gas Flow Heating Test [Yoshio Wakamatsu, Toshihito Saito, et al.].....	8
Fundamental Design, Multiobjective Optimization for FGM [Tohru Hirano, Tomohiko Yamada, et al.].....	15
FEM Program for Analysis of Transient Thermal Stress [Junichi Teraki, Tohru Hirano].....	28
Steady State Thermal Stress in FGM Plates [Yoshihiro Obata, Naotaka Noda, et al.].....	36
Fundamental Studies of TiAl-Based FGMs [Yuji Matsuzaki, Masashi Kawamura, et al.].....	45
Fabrication Process for Actively Cooled FGM Plate [Chikara Fujiwara, Satoshi Nagata, et al.].....	60
Bonding of FGM to Actively Cooled Panel [Yukio Yamaoka, Kazuyoshi Ninomiya, et al.].....	70
Second Phase of Development Plan for FGM Project [Masayuki Niino].....	76

Microstructure, Fracture Mechanism of LPPS FGM [Hideki Hamatani, Nobuyuki Shimoda, et al.].....	86
Thermal Evaluation Test of LPPS FGM [Nobuyuki Shimoda, Hideki Hamatani, et al.].....	95
Gradient Coatings Formed by Plasma Twin Torch Spraying [Shigeru Kitahara, Takeshi Fukushima, et al.].....	98
Plasma Sprayed Intermetallic Matrix Composite Coatings [Masahiro Fukumoto].....	101
Effect of Microstructure on Properties of Sintered FGMs [Shunsuke Yamakawa, Akira Kawasaki, et al.]... ,	111
Joining of Metal, Alloy to Magnesia Using FGM [Koji Atarashiya].....	116
Study of Cooling Structure to FGM [Shinya Akama, Shin-ichi Ohama].....	119
Temperature Response, Thermophysical Properties of FGMs [Nobuyuki Araki, Atsushi Makino, et al.].....	124
Evaluating Thermal Barrier Property by Burner Heating Test [Atsushi Hibino, Akira Kawasaki, et al.].....	133
Evaluation of 8YSZ/NiCrAlY FGM in Arc-Heated Flow [Yasuo Watanabe, Takashi Matsuzaki, et al.].....	137
Evaluation of FGM for Simulated High-Temperature Rotors [Masanobu Taki, Yoshiaki Fujusawa, et al.].....	143
Evaluation of Cylindrical High-Pressure Thrust [Akinaga Kumakawa, Hiroshi Sakamoto, et al.].....	149
Structure, Function of FGM Database Network [Takayasu Sudo, Katsuto Kisara, et al.].....	160

Thermal Fatigue of FGM at High Temperature Differences

926C0014A Tokyo FGM '91 in Japanese 8-9 Oct 91 pp 185-191

[Article by Masaki Sasaki, Akinaga Kumakawa, Mamoru Takahashi, Masayuki Niino, and Masahiro Sato, National Aerospace Laboratory, Science and Technology Agency; Kazunobu Aoyama, Satoshi Nagata, and Shinichiro Kiyoto, Mitsubishi Heavy Industries, Ltd.; Yoshinari Miyamoto, Osaka University; Nobuhiro Sata, Government Industrial Research Institute, Tohoku; Tohru Saito, Nippon Steel Corporation; Hideyuki Arikawa, Hitachi, Ltd., and Yukinori Kude, Nippon Oil Co.]

[Text] Abstract: The thermal fatigue properties of some kinds of functionally gradient material (FGM) specimens, TiB_2/Cu , PSZ (partially stabilized ZrO_2)/Cu, PSZ/Ni-Cr, SiC/C/C, and TiC/Ni-FGM, were characterized by means of effective thermal conductivity, K_{eff} , under high heat flux conditions in the temperature different field.

It was observed that the thermal fatigue properties of TiB_2/Cu and PSZ/C were superior because the deterioration of normalized K_{eff} was small by 30 or more thermal cycles. In SiC/C/C, the value of K_{eff} of FGM decreased less than that of non-FGM (NGFM) as the number of thermal cycles increased. It was inferred that FGM prevented the peeling of surface SiC coating layer.

In TiC/Ni-FGM, four FGM specimens which had different compositional distributions were tested. It was experimentally confirmed that there was an optimum compositional distribution against thermal fatigue.

1. Introduction

Functionally gradient materials (FGMs) are promising heat-resistant materials for use in the projected space plane. However, when the material is subjected to repeated heat cycles, it is believed that thermal fatigue develops in the material as a result of the development of macroscopic heat stress caused by large temperature differences within the FGM and of microscopic heat stress caused by the difference of thermal expansion coefficients between the ceramic and metallic materials used in the FGM. We have conducted thermal fatigue tests of a number of FGM samples created using different synthesizing methods.

We have obtained basic evaluation data concerning thermal fatigue characteristics by subjecting these samples to heat cycles with large temperature differences. In the following, we will discuss the characteristic degradation and damage caused to these samples by the heat cycle tests, and will investigate the development mechanism of thermal fatigue damage.

2. Samples and Test Method

2.1 Samples

Our tests used five kinds of samples: a TiB_2/Cu -system sample synthesized by the Government Industrial Research Institute, Tohoku, using the self-heat generation reaction method; a TiC/Ni -system material produced by Osaka University; a PSZ/Cu -system sample produced by Hitachi, Ltd., using the dynamic mixing method, physical vapor deposition (PVD); a $\text{PSZ}/\text{Ni-Cr}$ -system sample synthesized by Nippon Steel Corp. using the simultaneous heteropowder grain thermal spraying method; and a $\text{SiC}/\text{C}/\text{C}$ -system sample created by Nippon Oil Co. using the chemical vapor phase infiltration (CVI) method. Each of the specimens had a diameter of 30 mm. Table 1 provides further details about these samples.

Table 1. Test Samples Used in This Study

Sample number	Material system		Synthesis method	Producers	FGM layer compositional distribution	Shape (mm)	FGM layer thickness (mm)	Substrate material, other information	
	Ceramic	Metal							
GT-48	TiB ₂	Cu	Self-heat generation reaction	GIRI, Tohoku	8 layers	φ30	8.57	Cu	
GT-51					13 layers		8.1		
NS-47	PSZ	Cu	Dynamic mixing	Hitachi, Ltd.	Linear distribution	φ30	0.015	Cu	
NS-50							0.017		
NS-55	PSZ	Ni-Cr	Simultaneous heteropowder grain thermal spraying	Nippon Steel Corp.	Optimum distribution	φ30	1.2	SUS	
JS-57	SiC	C/C (3D)	Chemical gas phase infiltration	Nippon Oil Co.	FGM	Steel-shaped φ30/40 coated by 8.1 mm SiC layer on surface	0.02	3D-C/C L:5mm	
JS-58					Single layer NFGM		~0.03		
JS-59							—		
OH-61	TiC	Ni	Self heat generation	Osaka University	Nonlinear FGM	φ30	7	3-mm thick Cu brazed onto Ni layer	
OH-62					≈0.5				
OH-63					≈0.3				
OH-64					≈1.0				
					≈0.7				

2.2 Testing Setup

Figure 1 shows the large temperature difference FGM testing system that we used in our research. In this system, a large temperature difference is produced by heating one face of an FGM sample with a 30-kW xenon arc lamp by focusing the light from the lamp on the face and by cooling the other face of

the sample with liquid nitrogen. Heat cycles are produced by opening and shutting the light beam shutter.

2.3 Testing Method

Prior to subjecting a sample to the heat cycle test, a carbon film was sprayed onto the surface of the samples involved to maintain the radiation rate on the surface of the sample at a constant level. The sample pieces of TiB_2/Cu , TiC/Ni , and PSZ/Cu were fixed on the holder of the testing system by soldering or brazing. The step-shaped testpiece of $SiC/C/C$ was fixed on the holder under a weight. In this instance, a

graphite sheet was inserted between the testpiece and the holder to lower the heat resistance. The $PSZ/Ni-Cr$ sample consisted of a testpiece and an accompanying structure that served as the holder.

During a heat cycle test, temperature distributions on the surface of the sample and within the holder area under the steady state were measured every 10 cycles. The surface temperature was measured with a radiation thermometer, while the heat flux level and the temperature on the other face of the sample were obtained from the values indicated by a thermocouple buried inside the holder. The effective thermal conductivity K_{eff} is calculated from the surface temperature and the back face temperature using the equation

$$K_{eff} = q \cdot t / (T_{ws} - T_{wb}) \quad (1)$$

where q denotes the heat flux level, T_{ws} is the areal mean value of the sample surface temperature, T_{wb} represents the back face temperature, and t denotes sample thickness. In order to study changes in the effective thermal conductivity in each of these samples, we also studied their thermal fatigue characteristics based on effective television ratios $\overline{K_{eff}} = K_{eff}/K_{eff0}$ which were rendered dimensionless by dividing the effective thermal conductivities at each heat cycle (K_{eff}) by the thermal conductivities prior to applying heat cycle (K_{eff0}).

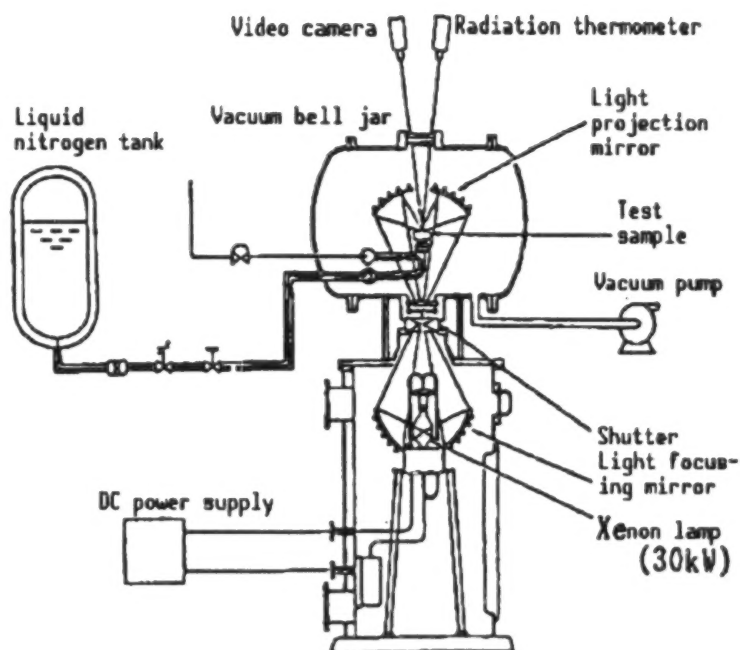


Figure 1. Large Temperature Difference FGM Testing System

3. Results

Table 2 gives the results of testing these samples. Figures 2-5 and 7 show the relationships between the numbers of heat cycles and effective thermal conductivities $\overline{K_{eff}}$ in these samples. These figures show that thermal fatigue in these samples begins to appear around the 25th heat cycle. Table 2 gives the $\overline{K_{eff}}$ values of these samples at the 25th heat cycle.

Table 2. Test Results

Sample number	Material system		Heat flux (MW/m ²)	Maximum surface temperature (K)	Average surface temperature (K)	Temperature difference (K)	Number of heat cycles	Decline of $\overline{K_{eff}}$ at 25th cycle (%)
	Ceramic	Metal						
GT-48	TiB ₂	Cu	2.8	1000	890	290	40	0
GT-51			2.6	860	700	290	40	5
NS-47	PSZ	Cu	2.8	800	590	180	25	8
NS-50			2.8	860	530	100	40	0
NS-55	PSZ	Ni-Cr	2.8	1400	1000	350	45	37
JS-57	SiC	C/C (3D)	0.45	2000	1600	310	29	33
JS-58			1.1	1900	1350	440	23	(42)
JS-59			0.62	1900	1450	240	18	(57)
OH-61	TiC	Ni	2.1	1300	1000	610	30	24
OH-62			1.9	1300	930	580	9	—
OH-63			1.7	1400	940	590	20	(49)
OH-64			1.9	1400	1030	650	23	(15)

* Figures within parentheses are estimated values.

Figure 2 compares the results for an eight-layer TiB₂/Cu FGM sample and its 13-layer counterpart. It can be seen that $\overline{K_{eff}}$ in the former begins to deteriorate sharply at around the 30th heat cycle. We believe this deterioration is caused by an abnormal high-temperature condition in the sample that occurred because of the peeling of the TiB₂ layer from the Cu layer in the sample. The 13-layer sample, which has a smoother material compositional distribution pattern, displays no significant deterioration of its $\overline{K_{eff}}$ value.

Figure 3 shows the results of a PSZ/Cu FGM sample. We believe that the nearly constant $\overline{K_{eff}}$ values reflect the small temperature difference because of the comparative thinness of the sample.

Figure 4 shows the test results for a PSZ/Ni-Cr FGM sample. In this sample, $\overline{K_{eff}}$ continues to decrease at a comparatively steep rate up to the 25th heat cycle, and after this, the change in $\overline{K_{eff}}$ values levels off.

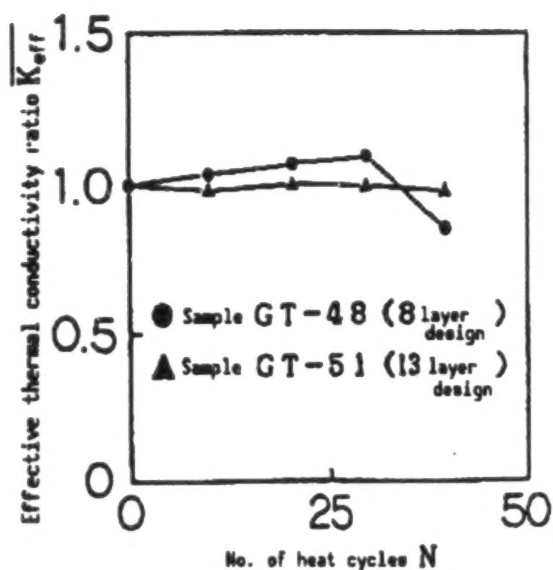


Figure 2. Results of Large Temperature Difference Test (TiB_2/Cu FGM, Government Industrial Research Institute, Tohoku)

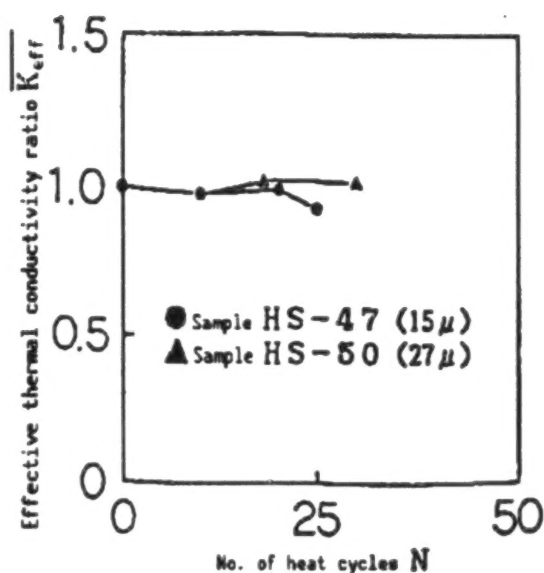


Figure 3. Results of Large Temperature Difference Fatigue Test (PSZ/Cu FGM, Hitachi, Ltd.)

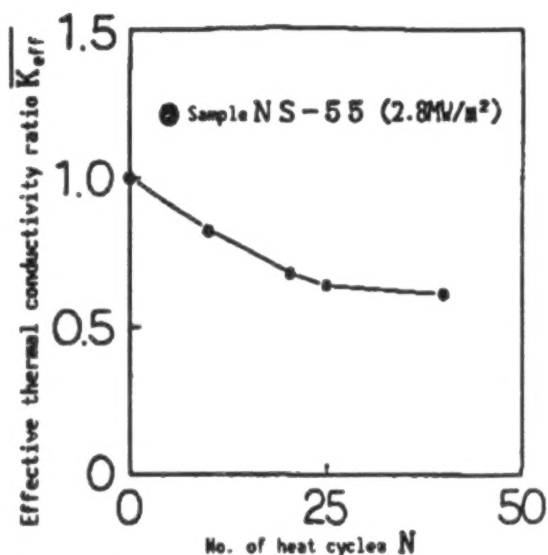


Figure 4. Results of Large Temperature Difference Fatigue Test ($PSZ/Ni-Cr$ FGM, Nippon Steel Corp.)

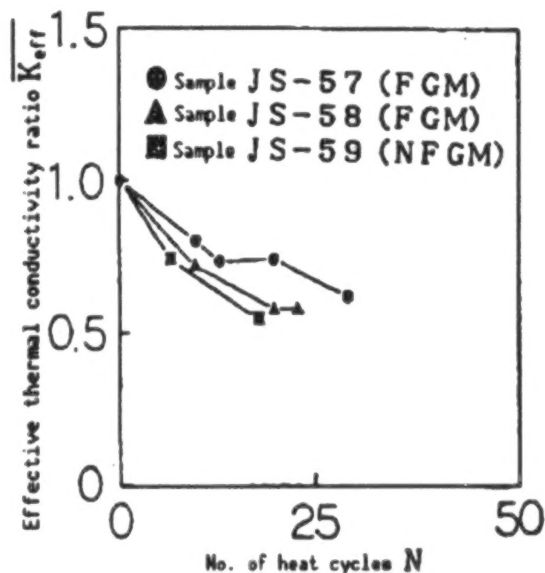
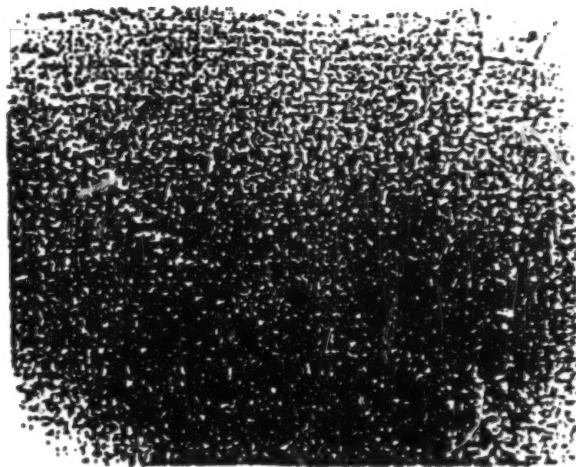


Figure 5. Results of Large Temperature Difference Fatigue Test ($SiC/C/C$, Nippon Oil Co.)

Figure 5 shows the results for the $SiC/C/C$ -system samples. The JS-58 FGM sample displays a larger characteristic deterioration than the FGM JS-57 sample because the former was subjected to a larger thermal load condition. JS-57, meanwhile, exhibits a smaller deterioration in K_{eff} than the NFGM sample JS-59, although they were subjected to almost the same thermal load. Figure 6



(a) Sample JS-57 (FGM)



(b) Sample JS-58 (FGM)



(c) Sample JS-59 (NFGM)

Figure 6. Observation Results of Surface Conditions of SiC/C/C-System FGM

shows the surface conditions of these three samples after undergoing the heat cycle test. The cracks in the turtle-back pattern are seen on the SiC-coated surface of the FGM and NFGM samples. In the NFGM sample, peeling of a coated SiC layer is observed. From these results, it is believed that an FGM layer is effective in preventing heat fatigue damage to the coated layer.

Figure 7 provides a comparison among TiC/Ni-system FGM samples having different material chemical properties. The compositional distribution is represented by following compositional distribution function

$$C = (X/t)^n \quad (2)$$

where X denotes the distance of a composition-controlled layer from the TiC side, t is the thickness of the composition-controlled layer, n is an index, and C represents the mol density of Ni. These four samples have n values of 0.3, 0.5, 0.7, and 1.0, respectively. In the 0.3 n sample, testing was

suspended at the ninth heat cycle when peeling was observed on the surface. In the 0.5 n sample, turtle-back patterned cracks running in the vertical direction were found on the surface after the test was finished. In the 0.7 n sample, the conditions in the test sample no longer returned to a normal state after the 23d heat cycle, and the surface temperature began to increase gradually after the cycle. This is believed to have been caused by the progress of peeling within the FGM sample. Surface cracks also were observed in the 1.0 n sample. The value of K_{eff} began to show distinct differences in these samples after the 10th heat cycle. These results lead us to conclude that the optimum compositional distribution for the best antithermal characteristics of an FGM is between 0.5-0.7 n value.

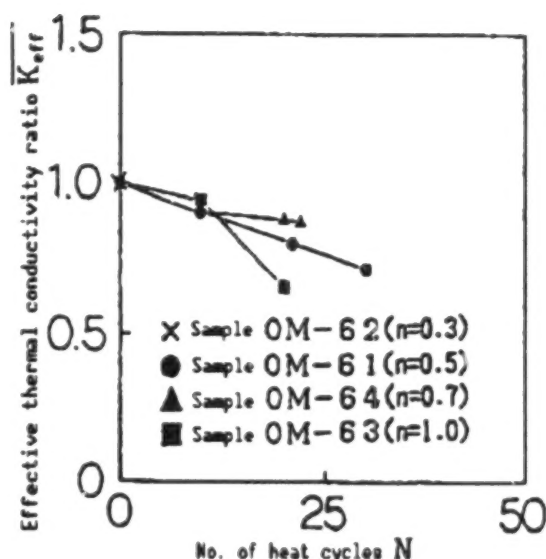


Figure 7. Results of Large Temperature Difference Fatigue Test (TiC/Ni FGM, Osaka University)

From the test results of these five different types of samples, it may be said that in these FGMs, when the effective thermal conductivity deteriorates substantially, cracks and peeling develop more easily. It must be said, however, that evaluation of conductivity alone is not sufficient to assess the thermal fatigue characteristics of FGMs, because of differences in material composition, heat flux level, maximum surface temperature, and temperature drop among them.

4. Conclusion

Basic evaluation data, including data on the change of K_{eff} values, in these different types of FGM samples were accumulated to study the thermal fatigue characteristics of these materials. The data were acquired by subjecting sample materials to heat cycle tests to evaluate the effects of material compositional distribution and the number of controlled FGM layers involved on their characteristics. In SiC/C/C-system materials, it has been discovered that the presence of an FGM layer is effective in restraining the peeling of coated surface layers in these samples caused by thermal fatigue. In TiC/Ni-system FGM samples, it has been found that the optimum compositional distribution for the best thermal fatigue characteristics exists in an n level between 0.5-0.7. As for this distribution condition, we will continue study by comparing the test-obtained values with the corresponding values calculated in the material design stage.

High-Temperature Supersonic Gas Flow Heating Test

926C0014B Tokyo FGM '91 17 Japanese 8-9 Oct 91 pp 193-198

[Article by Yoshio Wakamatsu, Toshihito Saito, Noboru Sakuranaka, Shuichi Ueda, Tatsuo Kumagai, Kazuo Kusaka, Masahiro Takahashi, Katsuto Kisara, Takayuki Sudo, and Masayuki Niino, National Aerospace Laboratory-KRC; Masataka Yamamoto, NASDA; and Satoshi Nagata, Mitsubishi Heavy Industries]

[Text] Abstract: An experimental test program is in progress to evaluate the structural safety degrees for functionally gradient materials (FGMs) under the condition of high temperature and supersonic air flow. This condition is almost the same with that of the nose-cone and intake section of the scramjet engine for the space plane. A preliminary test was conducted to obtain additional data for examining possible merits of the experimental test. In this test of a $\text{NTO}/\text{N}_2\text{H}_4$ propellant system, it was found that the heat-flux for the nickel test sample was on the order of 3 MW/m^2 at a section inclined by 30 degrees to the chamber axis. We are preparing to operate the hot gas generation system using the gas condition of $\text{H}_2/\text{O}_2/\text{N}_2$, in order to evaluate the FGM in November 1991.

1. Purpose

Functionally gradient material (FGM) research is under way to develop materials for use in the projected space plane's fuselage and engines. Our research is aimed at evaluating larger size FGM samples under conditions close to those that would be encountered in actual use.

The tests in our research involve the evaluation of heat and pressure characteristics of FGM samples within a hot, high-speed air flow environment: 3,000 K for total temperature, 3 MPa for total pressure, and Mach 3.0 for air flow speed. The air itself contains about 21 percent oxygen, the same oxygen level as in the atmosphere. These conditions are created by burning a content-adjusted mixture of hydrogen, oxygen, and nitrogen to realize a near-actual-utilization environment

2. Significance of Near-Actual Environment Test and Test Method

We have defined the significance of using FGM in the space plane, and the importance of conducting tests to develop the FGM for this application, for reasons that will be discussed below. We have also studied test methods.

2.1 Significance of Applying FGM to Space Plane and Its Engines

The heat flux q caused by the convection of heat that is generated on an object traveling through the atmosphere at a high speed is expressed by

$$\dot{q} = h_g(T_r - T_w) \quad (1)$$

where h_g denotes heat transfer coefficient, T_r the recovery temperature, and T_w the wall temperature. T_r is defined as

$$T_r = T_\infty \left(1 + r \frac{\gamma - 1}{2} M_\infty^2\right) \quad (2)$$

(Recovery temperature: the gas temperature on the adiabatic wall surface)

where T_∞ denotes the static gas temperature, and T_0 is the total temperature of the gas. The relationship between T_∞ and T_0 can be defined as

$$T_0 = T_\infty \left(1 + \frac{\gamma - 1}{2} M_\infty^2\right) \quad (3)$$

In these equations, r represents the recovery coefficient. Also, there is a relationship between r and the Prandtl number, which is as follows:

$$r = \text{Pr}^{1/2} \quad (4)$$

(Laminar flow: about 0.8 in air)

$$r = \text{Pr}^{1/3} \quad (5)$$

(Turbulent flow: about 0.9 in air)

When a space plane in flight encounters a dynamic pressure ($\rho_\infty u_\infty^2/2$) of 100 kPa without taking into account the dissociation effect of air, there is an interaction among the static temperature of the standard atmosphere at the altitude of the flying plane, its Mach speed, the total temperature around the plane, and the recovery temperature, as shown in Figure 1. However, in actuality, the dissociation of air occurs, and because of this the temperature rise is more restricted than is shown in Figure 1. But at high Mach speeds, the temperature rises to considerably high levels. When a heat-resistant FGM is used on the surface with a heat-insulating material beneath it, the temperature rise on the surface comes to a so-called radiation balanced temperature where the inputted heat level and the heat radiated from the surface balance. When the back surface of the FGM is cooled, the front surface temperature decreases, and this, in turn, causes an increase in the heat flux. When the surface material consists of a single layer, the temperature variation within the layer as a result of the passage of the heat flux through

it becomes steep, generating a higher heat stress within the layer. A common phenomenon that occurs in the boundary between a freedom-restrained metallic component and other material components when the metallic component is heated is that the compressive stress generated by its expansion causes a plastic deformation in the component when the stress is substantial. And when this thermally expanded component is cooled, a tensile stress is generated as a result of the component's contraction. When this expansion and contraction cycle is repeated, it causes cracks on the component because of thermal fatigue, which ultimately will cause the component to break.

One method for reducing this thermal fatigue is to ease these stresses within a metallic component by obstructing the invasion of heat flux. This can be accomplished by coating the component surface with heat-insulating materials, such as ceramics. This ceramic layer eases the deterioration of the strength of a metallic material beneath it by preventing the temperature of the metallic material from rising to dangerously high levels. However, the difference in thermal expansion rates between the ceramic coating and the metallic layer beneath causes the coated layer to peel.

A similar problem occurs with an antioxidation coated layer applied to carbon/carbon materials, which are promising heat-resistant materials. This requires an effort to reduce the difference in boundary stress by improving the functionally gradient material between these two layers of different materials to make it possible to use such multilayered FGMs in the space plane's fuselage and engines.

2.2 Significance of Conducting Practical Utilization Environment Test

The gas heat transmission coefficient h_g along the surface of a material changes depending on the shape of the space plane's fuselage and engines, the flight conditions, and the material wall temperature. The recovery temperature

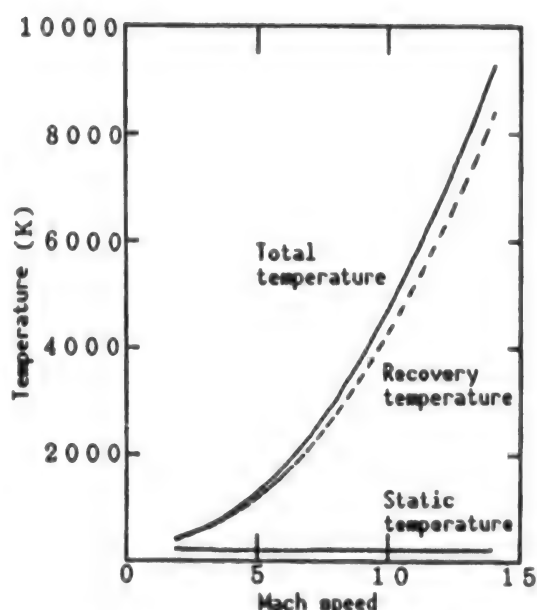


Figure 1. Relationship Among Mach Speed, Static Temperature, and Total Temperature at a Dynamic Pressure of 100 kPa (Dissociation of air is not taken into account.)

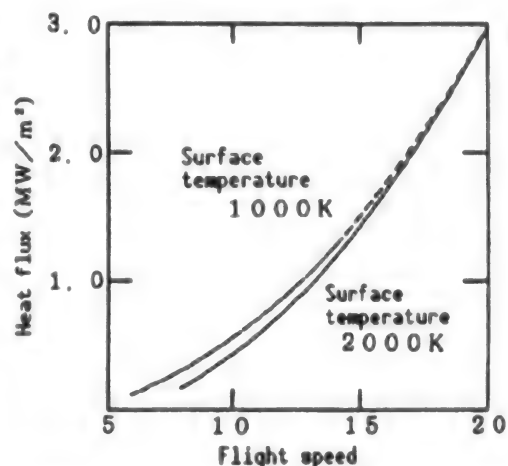


Figure 2. Change in Heat Flux Level When Flight Conditions Change Under a Dynamic Pressure of 100 kPa (Dissociation of air is not taken into account.)

T_r , meanwhile, changes depending on flight conditions and the location on the fuselage or the engines.

As an example, Figure 2 shows the relationship between heat flux and flight speed in a space plane flying under conditions where the dynamic pressure is 100 kPa. The heat flux vs. flight speed curves were plotted for a plane having a nose cone section with a curvature radius of 0.5 m, and by maintaining the nose cone surface temperature at 1,000 K or 2,000 K, respectively, by changing the cooling level. Calculations were made by assuming that vertical shock waves are present in front of the nose cone and by using Cohen's formula.

In practical space plane utilization, FGMs will undergo various types of thermal stress. This makes it necessary to conduct evaluation tests of FGMs by changing the heating conditions, such as gas temperature and moving gas speed, and the cooling conditions, such as the flow rate of a coolant, to ensure the structural safety of the FGM.

Space plane engines burn hydrogen as fuel, and there is a possibility that unburned, high-temperature hydrogen and the water vapor resulting from fuel combustion could damage the structural materials used in the engines. This also makes it necessary to conduct material evaluation tests under various environmental gas compositions to ensure structural safety.

2.3 Practical Utilization Environment Test Method

Based on the considerations discussed above, it is clear that FGM evaluation tests must be conducted within a high-temperature air environment or within a hydrogen gas current moving at high speed while changing the hydrogen content. Securing a large volume of heated air calls for the introduction of a costly heating furnace and high-pressure air storage tanks. As an alternative to constructing these costly facilities, our method makes it possible to produce high-temperature air containing residual oxygen at 21 percent mol density, the oxygen mol density equivalent to that of the atmosphere, by burning a ratio-adjusted mixture of nitrogen, oxygen, and hydrogen to produce a hot nitrogen/water vapor gas containing the residual oxygen. In this method, it is also possible to produce a combustion gas composed of nitrogen, water vapor, and hydrogen by adjusting their mixing ratios.

3. Preliminary Test

We conducted a preliminary test by subjecting an FGM panel equipped with a cooling mechanism to the supersonic stream of a high-temperature gas generated by an N_2H_2 (or MMH)/NTO burner to determine whether it is possible to conduct heat tests of FGM samples properly within the supersonic current of a hot gas or not, to find out what amount of heat flux such samples receive, and to determine the optimum conditions for installing samples to conduct heat tests.

3.1 Experiment Method

We conducted a heat flux distribution test by heating a 200-mm x 50-mm nickel panel equipped with nine-channel cooling pipes (Figure 3) within a supersonic, high-temperature gas produced by a rocket combustion facility. The nickel panel was cooled by circulating water through the pipes. The inputted heat (heat flux) level in the test panel was calculated using data on the flow volume of water through each cooling pipe and the rise in temperature of this cooling water. The test conditions are given in Table 1. The use of a fuel that is different from the one used in the full-fledged test makes the oxidation condition and heat transfer coefficient in the preliminary test display different results from those obtained when using the simulated hot air current containing 21 percent residual oxygen.

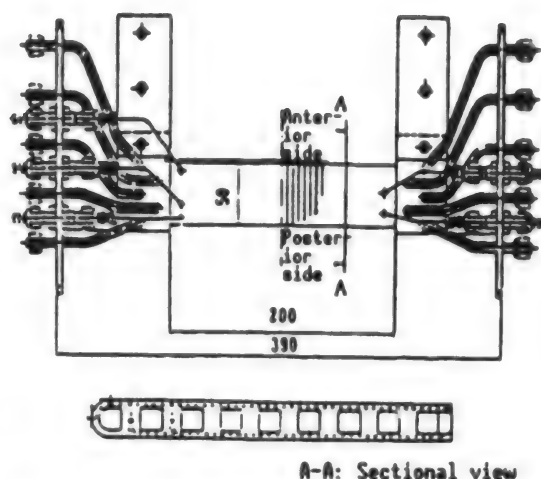


Figure 3. Nickel Test Panel Equipped With Built-In Water Cooling Pipes

Table 1. Gas Conditions for a Preliminary Test

Nozzle shape	Circular shape
Nozzle dimension	100φ
Nozzle aperture ratio	7.07
Propulsion agent	NTO/N ₂ H ₄
Combustion pressure (MPa)	0.9
Mixing ratio	0.95
Theoretical combustion temperature (K)	2946
Mach speed	3.08
Static pressure (MPa)	0.02
Density (kg/m ³)	2.5 x 10 ⁻²
Specific heat ratio	1.269

3.2 Test Results

In order to study the optimum installation position of the sample FGM panel for the preliminary test, we attempted to calculate heat flux levels on the panel by changing the panel surface angle vis-a-vis the hot gas flow. We did this by placing the front rim of the panel near the lower front end of the hot air thruster, and used this rim as a pivot to change the angle (Figure 4). As the effective heat transfer area—a parameter necessary to calculate the heat flux level—we used the area covered by the hot air current thrust, assuming that the gas expands uniformly across the panel surface.

Considering that little is known about gas flow behavior along the sample's front rim, there is a possibility that the data shown in Figure 4 contain a significant error. However, we found that in the lower portion of the sample panel (the area beyond the fourth cooling water channel), the heat flux level is uniform across the lower portion, and that it increases when the α angle (see the figure) increases. At an α value of 30 degrees, the heat flux level stood at about 3 MW/m². At this angle, scorching occurred on the sample surface, but this was not sufficient to cause the material to break.

3.3 Discussion

Our preliminary test has made it possible to confirm the following points:

- (1) When the α angle increases, the flow direction distribution of the heat flux becomes more uniform, and the strength of the heat flux increases.
- (2) Little is known about the behavior of the gas flow in the lower front rim section of the test panel, and this makes it difficult to estimate the strength of the heat flux in the area along the rim. Consequently, an FGM test must be conducted by placing the sample at the lower point of a horizontal hot air blast, where a comparatively uniform heat flux level is obtained.
- (3) Under the test conditions described in Table 1, a heat flux strength of about 3 MW/m² was obtained at an α angle of 30 degrees.

4. Improvement of High-Temperature Supersonic Gas Flow Evaluation System and Test Schedule

Using the data obtained from the preliminary test, we have created a high-temperature supersonic gas flow test system (Figure 5).

4.1 Simulated High-Temperature Supersonic Gas Generator

The simulated high-temperature supersonic gas generator is designed to produce a hot gas flow having a combustion temperature of 3,000 K, a combustion pressure of 3 MPa, a flow speed of Mach 3.0, and an oxygen density of 20 percent. This is achieved by burning an appropriate mixture of oxygen, hydrogen, and nitrogen. The gas generator is currently being improved to make it capable of generating a hot supersonic gas within 30 seconds, the length of time that is required to make test sample temperature high enough to be ready to commence testing.

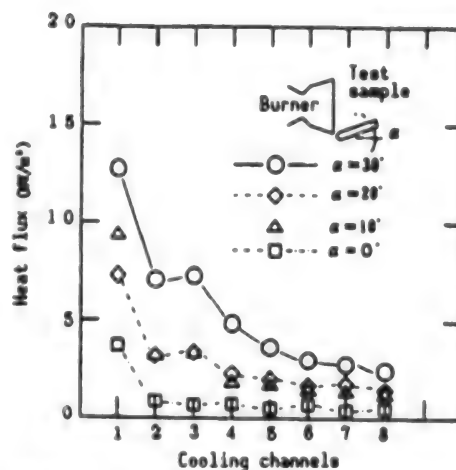


Figure 4. Heat Flux Distribution

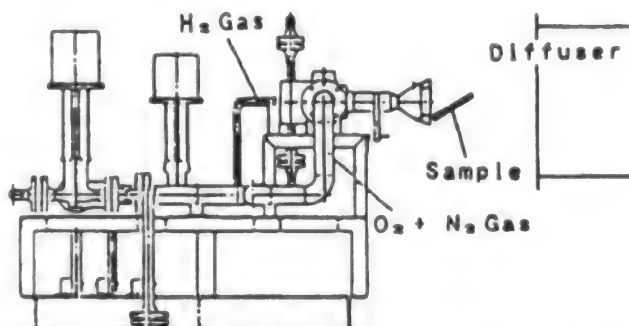


Figure 5. High-Temperature Supersonic Gas Flow Test System

In June 1991, we conducted a combustion test of the gas generator. We started at a combustion pressure ranging from 1.0-1.5 MPa, and a total temperature ranging from 2,000-2,500 K. The test showed that the generator produces combustion vibrations at around 500 Hz, and at higher frequencies ranging between 5-7 kHz. We believe that these low frequency vibrations are caused by an insufficient pressure difference at the burner thruster. The high-frequency vibration probably represents a primary tangential-model acoustic vibration. This conclusion derives from the results of frequency analysis. Based on these findings, we are taking steps to boost the flow volume of the combustion gas to restrain the low frequency vibration, and to reduce the high-frequency vibration by introducing an acoustic cavity.

4.2 Dummy Test Sample and Sample Holder

We created a sample holder to hold a 100 mm x 100 mm FGM sample equipped with a cooling system. We also created a conventional material dummy test sample for heat test confirmation.

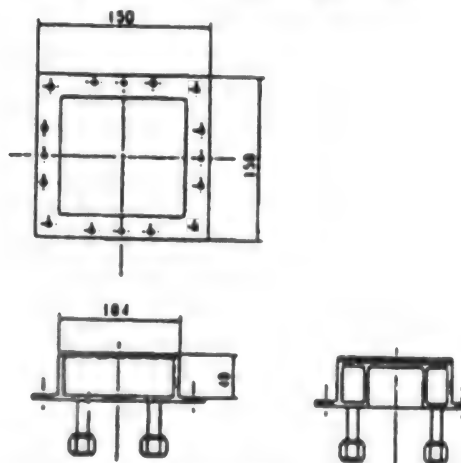


Figure 6. Dummy Test Sample

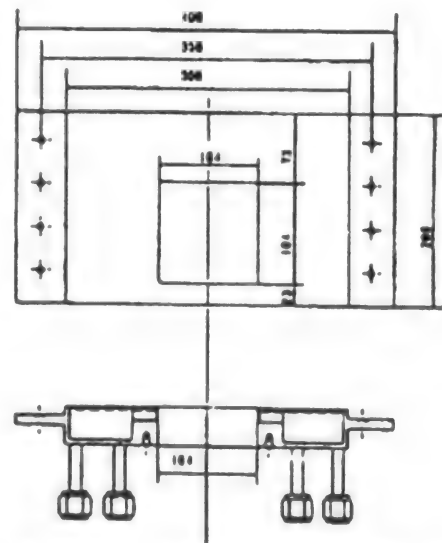


Figure 7. Test Sample Holder

The upper surfaces of the dummy and the test sample are covered by a copper layer, while the lower surfaces are covered by an SUS layer. These layers are soldered to the material bodies (Figures 6 and 7). The dummy and the holder are fixed in front of the supersonic high-temperature gas thruster at an α angle of 30 degrees, using the preliminary test data as a reference.

4.3 FGM Test Sample

For use in the upcoming evaluation test, which will be conducted in November [1991], FGM test samples and the holder are being developed by establishments specializing in material structural controlling technology. The shape of these samples is almost identical with the dummy.

References

1. "Dendo Kogaku Shiryo [paper on heat transfer engineering]," revised 4th edition, Japan Machinery Association, 1986. p 85.

Fundamental Design, Multiobjective Optimization for FGM

926C0014C Tokyo FGM '91 in Japanese 8-9 Oct 91 pp 199-208

[Article by Tohru Hirano, Tomohiko Yamada, and Junichi Teraki, CAE Center, Daikin Industries, Ltd.]

[Test] **Abstract:** In this paper, the fundamental design procedure for FGM is presented. At first, distribution functions are introduced, and estimation methods for the effective material properties of the intermediate compositions are explained. Then, thermal stress calculation methods for different processes and geometrical configurations are described. Finally, the multiobjective optimization problem is defined for the design process of FGM and solved by several methods including application of Fuzzy Set Theory.

1. Introduction

We have conducted research to establish a theory for the optimum design of functionally gradient materials (FGMs), and to develop a design support system based on this theory. Already we have developed a semianalytical method to analyze steady state as well as non-steady state thermal conductivity and thermal stress in a one-dimensional FGM plane or in a cylindrical FGM model. We also have developed an axial-symmetric finite element method program to analyze a two-dimensional plane. In addition, we have developed an expert system for FGM design support (Figure 1). This system combines an analytical structure for seeking an optimized quantity through mathematical programming, and a repeated process of these analyses and an inference structure to control the global search-optimization process involving the use of symbolic parameters for describing the

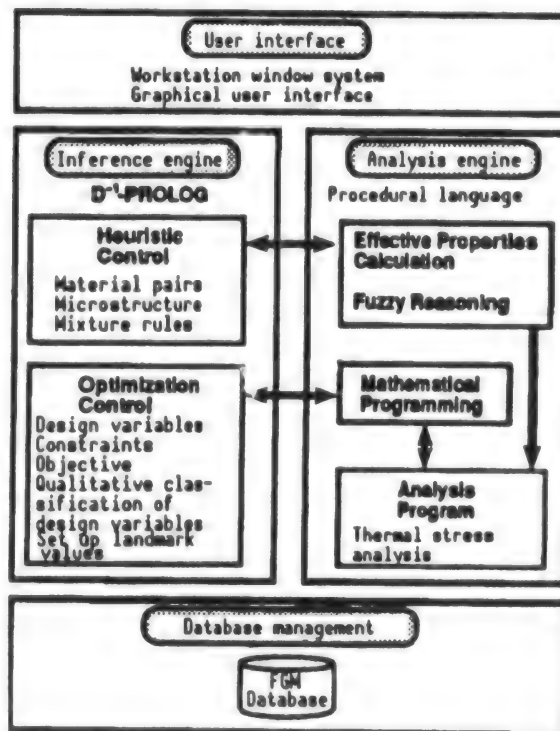


Figure 1. Expert System for FGM Design Support

microstructure model used in inferring material properties. Using this system and these analytical methods, we have produced a basic design of FGMs by combining various materials.

Our ongoing effort to create larger FGM test samples is experiencing a number of problems, including several associated with cooling mechanism-related junction residual stress, three-dimensional material structure, and nonsteady state thermal load conditions. In this article, we will describe our attitude toward the effort to achieve basic design of FGMs, and will discuss the relationship of this effort with three-dimensional material design efforts. We also will discuss the multipurpose optimization method involving the use of fuzzy reasoning for an overall evaluation of the stress produced in material bonding, heat testing, and production of FGM products.

2. Basic Design of FGM

The design of an FGM must be conducted by taking into account the conditions it will encounter in practical application. This involves an effort to select an optimum material combination to ease heat stress, an optimum intermaterial compositional distribution that is suitable for production conditions, and optimum microstructures for the materials involved. Figure 2 shows the inverse design procedure employed in our design effort. The inverse design procedure works like this. First, required shape and heat boundary conditions are set in developing an FGM structure, and the selection of suitable materials and a production method is made using the database. Second, the selection of an optimum compositional distribution function is made to control and to represent the required gradient material composition, and the profiles of the FGM are determined by setting the parameters. Third, the selection of an inferred model of material properties is made based on the required microstructure of the FGM. This is achieved by obtaining data on the properties of the basic compositional materials involved from a material property database. At the same time, the shape parameters of the mathematical model of the microstructure are determined. Using property values obtained from an arbitrary material composition created by these processes, the analyses of temperature distribution and thermal stress distribution are conducted. Fourth, an effort is made to derive a compositional distribution profile, and an optimum material combination, to minimize the specific stress (stress/material strength) by adjusting gradient distribution parameters and material combination.

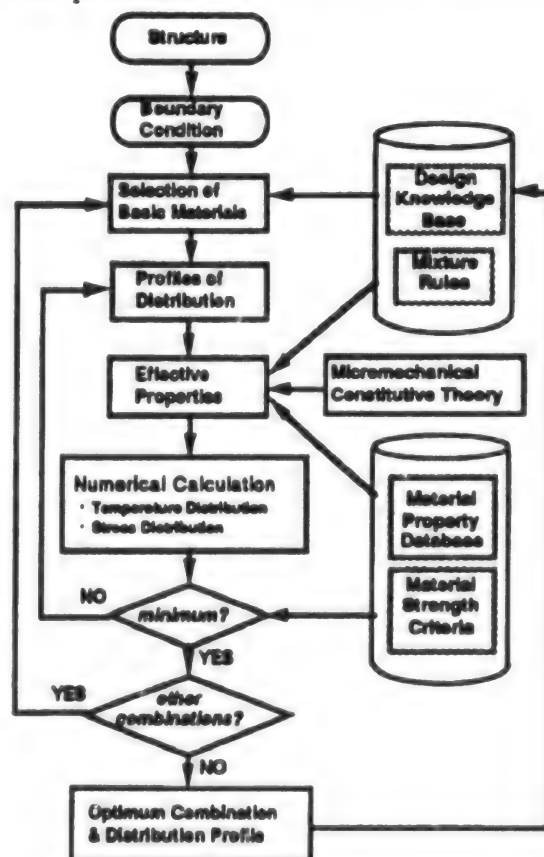


Figure 2. Inverse Design Procedure To Design an FGM

Considering that these requirements involve repeated calculations to attain a global optimization in basic design, a three-dimensional analysis by the finite element method is not practical because of its limitations in terms of analysis time. In addition, a method for controlling three-dimensional compositional distribution has yet to be established. Under these circumstances, in the basic design state, it is important to make an effort to attain a one-dimensional optimum compositional distribution in designing the basic shape of an FGM before two-dimensional optimization becomes possible. At the same time, in the detailed design stage, an effort must be made to analyze the nonlinear effects for material shapes that are in practical use, to evaluate thermal fatigue strength, and to optimize localized compositional distribution using the compositional distribution data obtained in the basic design stage.

3. Gradient Compositional Distribution Function

Supposing that there is a three-element FGM composed of an A element (ceramic), a B element (metal), and a porous structure, and supposing their volume fractions to be V_A , V_B , and V_P , respectively, the following equation is formulated from the distribution function shown in Figure 3:

$$V_A + V_B + V_P = 1 \quad (1)$$

Here, dimensionless parameters as described below are introduced to make calculation easier.

$$V_B' = V_B / (V_A + V_B) \quad (2)$$

The gradient compositional distribution function in the FGM is defined by the following equation, which introduces the element of dimensionless distance ξ for V_B' :

$$V_B' = f(\xi) = \begin{cases} f_0 & : 0 \leq \xi \leq \xi_0 \\ (f_1 - f_0) \left[\frac{\xi - \xi_0}{\xi_1 - \xi_0} \right]^n & : \xi_0 \leq \xi \leq \xi_1 \\ f_1 & : \xi_1 \leq \xi \leq 1 \end{cases} \quad (3)$$

The profile of the compositional distribution function that can be expressed by the above equation can be applied over a wide range by varying the distribution function parameters (f_0 , f_1 , ξ_0 , ξ_1 , n). Parameters ξ_0 and ξ_1 represent the thickness of nongradient material layers, both on the surface and within an FGM; parameters f_0 and f_1 are the compositional rates in these layers; and exponent n denotes the parameter for continuously controlling gradient compositional profiles. In the case of a planar material, dimensionless distance ξ is expressed by the distance in the thickness direction (z coordinate), while in the case of a cylindrical material, it is expressed by the distance in the radius direction (r coordinate).

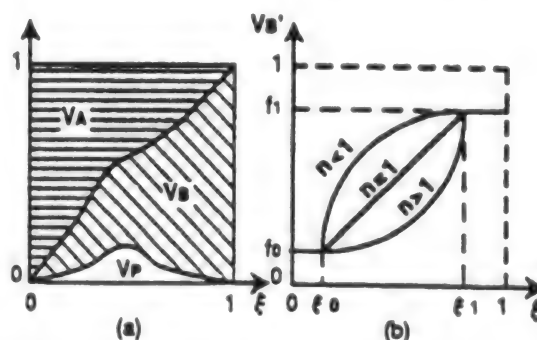


Figure 3. Gradient Compositional Distribution Function

When the pore distribution is dealt with independently, the volume fraction distributions for the material elements A and B are expressed by the following equations

$$V_A = (1 - V_p) \cdot (1 - V_B'), \quad V_B = (1 - (V_p)) \cdot V_B' \quad (4)$$

In the above equations, when $V_p = 0$ the value of V_B becomes equal to that of V_B' , corresponding to the notation for a two-element material.

4. Database for FGM Property Inference

In order to obtain a temperature distribution pattern or a thermal stress distribution pattern within an FGM, the availability of property values in an arbitrary mixing ratio of material components in multilayer FGMs is essential. It is known that material property change depends not only on compositional variation, but also on the production process employed. Consequently, in order to obtain material properties through experiments, it is necessary to create many NFGM samples having different compositional ratios by keeping the material combination and production process the same. To obtain data concerning the effects of temperature on these properties, it will be necessary to conduct many more experiments and measurements.

Meanwhile, not much is known about the properties of ceramic-metal combination materials having different compositional ratios. Under these circumstances, if the inference of material properties for an intermediate composition ratio using the known property values of basic FGMs becomes possible, the efficiency of FGM design and development will be improved significantly. In the following, we will discuss experience-based composite material rules, and the microdynamic approach using mathematical microstructure models. The method for describing the reversal between the matrix phase and the dispersed phase due to a compositional change, a phenomenon peculiar to FGMs, will also be introduced.

4.1 Experience-Based Composite Material Rules

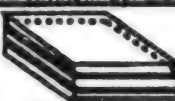




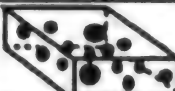

In the field of material science, research on composite material rules involving the property values of various kinds of multiphase materials has been conducted by Kerner and other researchers for many years. In this section, we will discuss the relationship between composite material rules and corresponding microstructures in order to use this relationship as the knowledge database for inferring material properties (Table 1).

Commonly, these rules are expressed by the following equation:

$$P(\xi) = V_A(\xi) \cdot P_A + V_B(\xi) \cdot P_B + V_A(\xi) \cdot V_B(\xi) \cdot Q_{AB} \quad (5)$$

where P denotes macroproperty values (Young's modulus, Poisson ratio, thermal conductivity, thermal expansion coefficient), P_A and P_B are the basic properties of each material involved, and Q_{AB} is the function of V_A , V_B , P_A , P_B , and V_p . In addition, Q_{AB} changes substantially depending on differences among microstructures.

Table 1. Knowledge Database To Help Generate Proper Composite Material Rules Based on a Material's Microstructure

Microstructure in the Hypothetical Layer (white:Matrix, black:Filler)	Thermal Conductivity λ	Coefficient of Thermal Expansion α	Elastic Moduli E, K, G	Material Strength σ, γ
 Laminar	Reuss Rule	Modulus based Rule	Voigt Rule	Voigt Rule
 Fibrous (1)	Reuss Rule	Modulus based Rule	Voigt Rule	Voigt Rule
 Fibrous (2)	Voigt Rule	Voigt Rule	Reuss Rule	(Reuss Rule)
 Thin Layer	Voigt Rule	Voigt Rule	Reuss Rule	(Reuss Rule)
 Flake-like	Eshelby's Theory	Eshelby's Theory	Eshelby's Theory	?
 Spherical Particulate	Kerner's Equation	Kerner's or Turner's Equation	Kerner's Equation	?
 Skeletal	Tuchinski's Method	Tuchinski's Method	Tuchinski's Method	(Tuchinski's Method)
Micro-Pores	Maxwell's Equation	—	Mackenzie's Equation	Haynes or Ryskewitsch's Equation

What is important to note here is that the strength of multiphase materials changes substantially depending on the state of the microstructure, and on the compositional ratio of the materials involved. However, a microdynamic model for inferring the strength of a multiphase material from its microstructure has yet to be established. And currently, few data are available about experience-based composite material rules that could be used to infer the strength of typical microstructures. Pores are regarded as a third element for controlling the characteristics of FGMs. However, no mathematical model has been established to infer the degradation of material strength due to the presence of pores. This makes it necessary to use the composite material rules listed in Table 1.

4.2 Microdynamic Approach

Eshelby tried to analyze the stress distribution within an uninterrupted uniform parent phase material when an elliptical phase (an inclusion) was introduced into the material to create an interrupted phase. However, in practically used materials there exist many uniformity-disturbing inclusions, and Wakashima, et al., expanded Eshelby's equivalent inclusion theory by

introducing the idea of an average stress field. This expanded theory also is used to calculate the thermal elastic constant. In calculating macroproperty values of an FGM at an arbitrary compositional ratio, this microdynamic approach is used when no microstructures corresponding to known experience-based composite material rules are found.

In this expanded theory, the presence of a dispersed phase within the parent phase is transformed into an elliptical body model in which many of the dispersed elliptical phases are oriented in a single direction (Figure 4). In this situation, the condition of the microstructure is dictated by the aspect ratio $L (= c/a)$, and by the orientation angle (θ/ϕ) . By changing the aspect ratio, it becomes possible to deal with various dispersed phase types, including fibrous, spherical, and flake-like types by the same theory. Using this theory, a macroproperty value, such as compliance-tensor M is calculated using the following equation:

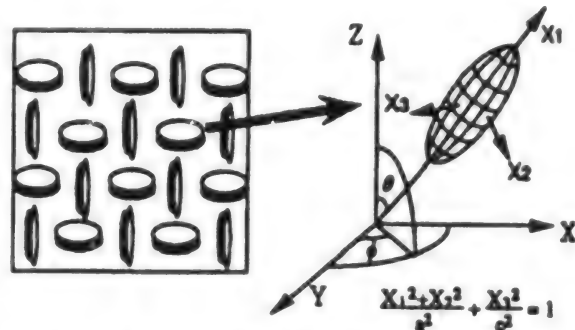


Figure 4. Elliptical Body Model in the Microdynamic Approach

$$\bar{M} - M_0 = \sum_r V_r \cdot (M_r - M_0) \cdot B_r \quad (6)$$

Here, \bar{M} denotes macro compliance, M_0 is the compliance of the parent phase involved, M_r represents the compliance of the dispersed phase, and \sum_r is the aggregate of the dispersed phases. B_r is a constant called the phase stress concentration factor tensor, and it is calculated as a function of the above-mentioned elliptical phase parameters, and as the function of the elastic constant of the parent phase and the dispersed phase.

The use of this theory makes it possible to deal with pores as a dispersed phase having a zero elastic constant. In addition, the use of the microdynamic approach makes it possible to calculate macroelastic and plastic deformations, thus taking into account nonelastic effects in the parent phase. This theory and this approach make it possible to implement material design based on nonlinear analysis by incorporating them into the design support system shown in Figure 1.

4.3 Application of Fuzzy Theory to Material Property Inference

In common composite materials having a fixed material composition, the parent phase can be separated from the dispersed phase clearly. However, in an FGM in which material composition varies from zero percent to 100 percent, the separation is not easy, particularly in intermediate compositions. When conducting calculations using composite material rules or the microdynamic approach, different results are obtained depending on the condition of the microstructure involved when the relationship between the parent phase and the dispersed phase is reversed. In a ceramic microstructure in which the ceramic volume fraction is decreasing, it is very difficult to identify the point where the ceramic content changes from the initial parent phase to the

dispersed phase. To deal with this ambiguous phenomenon, we have developed a method that makes use of the membership function in fuzzy theory.

In our research, we regarded the reversal of the relationship between the parent phase and the dispersed phase as a change in a microstructure. For example, let's consider a case in which the microstructure in a two-phase material, composed of materials A and B, changes over a range ($i = 1 \sim I$). By using the fuzzy membership function μ_i , let's define a probable macroproperty value, for example, a compliance tensor. A compliance tensor can be defined by the following equation:

$$\bar{H} = \sum_i \mu_i(V_g') \bar{H}_i / \sum_i \mu_i(V_g') \quad (7)$$

where \bar{H}_i represents the macroproperty value that was calculated about the i th microstructure using equation (6). Membership function can be defined as a single constituting phase's affiliation degree (grade) to the i th microstructure at a value of dimensionless parameter V_g' of the compositional distribution (Figure 5). As shown in Figure 5, the membership function is dictated by the changing position of a microstructure P_j and the width of the changing area d_j ($j = 1 \sim I - 1$).

As an example of using this function-based technique, we evaluated the combination between ZrO_2 and Ni as an FGM that was produced using the plasma spray method. With this material combination, the macroproperty values in the intermediate compositions that had been calculated prior to the evaluation by anticipating the presence of a spherical dispersed phase within it. With this material system, the following three different microstructures are believed to exist:

- (i) a structure in which Ni is scattered uniformly as a spherical dispersed phase within a ZrO_2 parent phase;
- (ii) a structure in which ZrO_2 is scattered uniformly as a spherical dispersed phase within an Ni parent phase;
- (iii) a microstructure transformation from type i into type ii at p_1 position and with d_1 width.

The macroproperty values calculated using Kerner's composite material rules for a spherical dispersed phase displayed almost a straight line relationship vis-a-vis the changes of Ni's volume fraction, except for changes in thermal conductivity, and in this regard there was little difference between type i and type ii. This is because the Q_{AB} value in equation (5) is very small. At the same time, with regard to thermal conductivity, a substantial difference was observed between type i and type ii, as shown in Figure 6(b). Type iii is a condition that is close to practical situation. The identification of a membership function for type iii from the actually measured values indicated a p_1 value of 0.7 and a d_1 value of 0.2, as shown in Figure 6(a). Figure 6(b) shows the inferred value curves that were obtained using a membership function. The use of the higher-order S function as a membership function makes the macroproperty values in the intermediate compositional range display comparatively gradual changes.

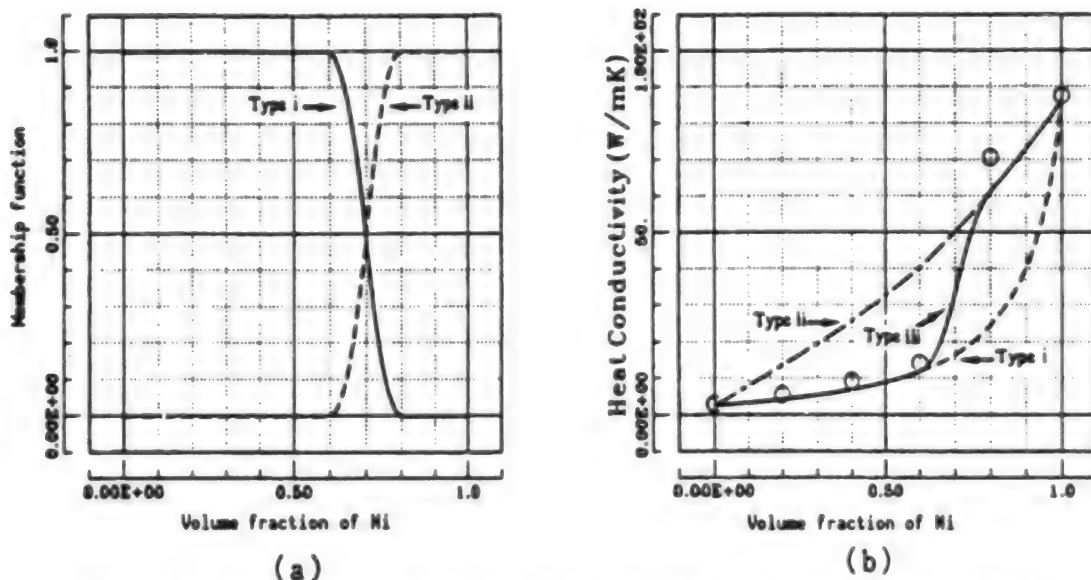


Figure 6. Membership Function for ZrO_2/Ni FGM and Macrothermal Conductivity Value Curves

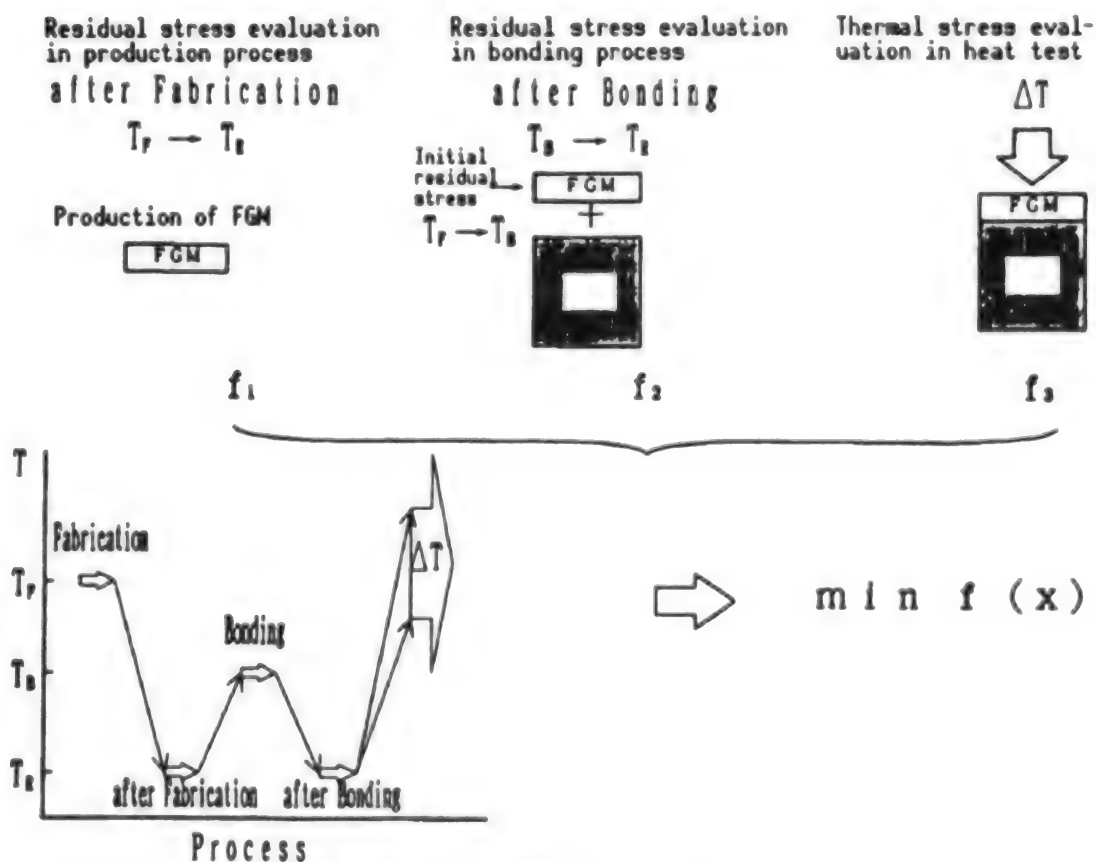


Figure 7. FGM Design Steps

The controlling parameters of the fuzzy membership function discussed above were introduced based on our experience, and in this sense they are subjective values. Consequently, it is necessary to generate more objective values for increasingly varied material combinations and production methods by accumulating microstructure data for these combinations through experiments.

5. Residual Stress Evaluation in Test Stage and Production Process

In testing and producing larger-dimension FGM samples, the heated layer boundary condition and the structurally-restraining condition required differ among production-related processes, such as the bonding of an FGM to the cooling structure, heat test process under simulated practical utilization condition, and FGM production process (Figure 7). A problem in this test and production process is that the stress generated in one process immediately affects the ensuing process adversely. This makes it very important to estimate residual stress at each process as accurately as possible. The residual stress in the production process is calculated from the temperature difference between a production temperature (commonly the melting temperature of a metallic material) and room temperature by assuming that production temperature decreases down to room temperature in a quasi-static manner. In the bonding process, calculations are made using the temperature difference between the bonding temperature and room temperature. Using a linear analysis, the actual next-process stress distribution can be determined by overlaying the stress distribution pattern of each preceding process. In any of these processes, a nonstationary analysis must be conducted when quick cooling is involved.

6. Expansion of Optimum Design Technique

The effort to design FGMs has been promoted as a way to minimize thermal stress within these materials when they are subjected to large temperature differences by employing mathematical programming and knowledge engineering techniques. These FGMs must be free from damage caused by any of the above high-temperature processes, and this calls for ensuring a comprehensive design optimization in all the processes involved. This in turn requires minimizing the vector objective function by combining the objective functions that are set for each process. This must be tackled as a multiobjective problem by expanding individual process efforts.

6.1 Introduction of Multiobjective Optimization Technique

Multiobjective optimization calls for obtaining an n th dimensional variable vector x^* that minimizes the p th dimensional vector objective function.

$$f(x) \rightarrow \min; \quad \text{subject to } x \in X \quad (8)$$

In designing an FGM that involves the above three processes, the following size objective functions have to be set:

f_1 : Residual stress in the production process (maximum tensile specific stress)

f_2 : Residual stress in the production process (maximum compressive specific stress <absolute value>)

f_3 : Residual stress in the bonding process (maximum tensile specific stress)

f_4 : Residual stress in the bonding process maximum compressive specific stress <absolute value>)

f_5 : Residual stress in the heating process (maximum tensile specific stress)

f_6 : Thermal stress in the heating process maximum compressive specific stress <absolute value>)

6.2 Scalar Technique

A popular technique for dealing with the multiobjective optimization problem involves a conversion (expressed in scalar quantity) of the problem into an equivalent nonlinear programming problem. A number of scalar methods have been proposed to date. In our research, we studied the application of the total load minimization method, and the largest element minimization method.

(i) Total load minimization method (weight coefficient method)

This method employs a weighted linear sum as the vector objective function to be minimized, as represented by the following equation:

$$w^T \cdot f(x) = \sum_{i=1}^p w_i f_i(x) \rightarrow \min \quad (9)$$

where $w = (w_1, \dots, w_p)^T$ denotes a weight coefficient vector that satisfies $w \geq 0$, $\sum w_i = 1$. This method is valid only with a convex problem (a problem in which the objective functions involved are all convex functions).

(ii) Largest element minimization method

In this method, the vector function to be minimized can be expressed in scalar quantity using the following formula

$$\max_{1 \leq i \leq p} \{w_i f_i(x)\} \rightarrow \min \quad (10)$$

In contrast to the total load minimization method, this method does not assume a convex element. In a practical sense, this method is aimed at "correcting the most unwanted factors as much as possible."

(iii) Section of unique solution

The above two methods are unfit for obtaining a unique solution, because the weight coefficient w_i takes an arbitrary value. The only method that makes it possible to obtain a unique solution is to set an ideal point as the goal for

decisionmaking and to minimize the distance from the goal. The solution that is obtained using this method can be called a compromise solution. In our research, a unique solution was calculated by supposing that w_i in the cases (i) and (ii) is equal to $1/p$ for the sake of simplicity in calculation.

6.3 Multiobjective Decisionmaking Based on Fuzzy Theory

In addition to the scalar method, we used a method based on the fuzzy theory membership function to compensate for the ambiguities involved in human decisionmaking. First, to evaluate physical parameter P_i , the membership function shown in Figure 8(b) is defined as

$$\mu_i = s_i(P_i) \quad (11)$$

By assuming the objective function ($f_i(x)$) dictated by design variable x shown in Figure 8(a) as physical parameter P_i , the relationship between design variables and the membership function is expressed as

$$\mu_i(x) = s_i(f_i(x)) \quad (12)$$

In the instance shown in Figure 8(c), the design value for the center of gravity is determined by seeking the product set of the membership function (μ_i) developed using Equation (12). The disadvantage of this method is that the definition of the membership function is based largely on experience-derived data. However, this method makes it possible to trade off the ambiguity among multiobjective functions.

$$x^* = \text{center of gravity} \bigcap_{i=1}^p \mu_i \quad (13)$$

The above membership function can be defined by the following equation:

$$s(X) = \begin{cases} 1 & 0 \leq x \leq a \\ (x-b)/(a-b) & a \leq x \leq b \\ 0 & x \leq 0, b \leq x \end{cases} \quad (14)$$

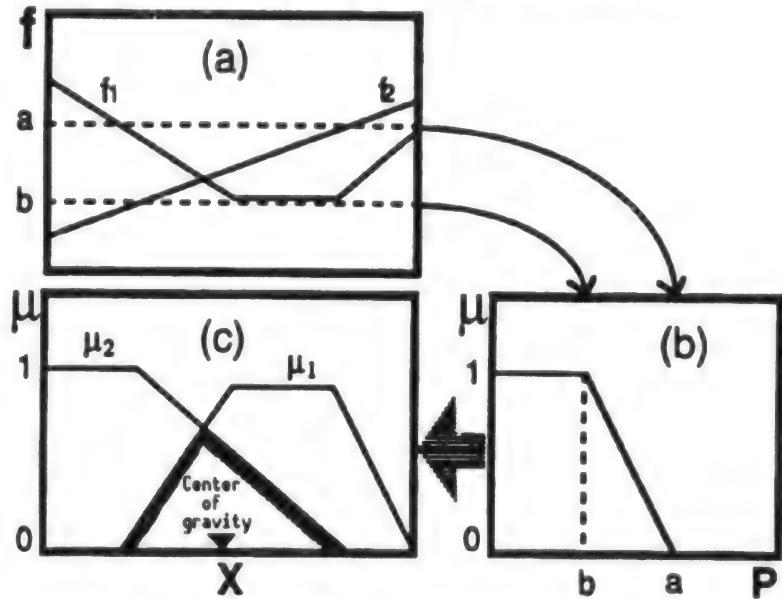


Figure 8. Multiobjective Decisionmaking Process Through Fuzzy Inference

6.4 Example of Application of Multiobjective Optimization Technique

In this section we will present an example of applying the above methods in designing a ZrO_2 -8 wt % Y_2O_3 (YSZ)/Ni-20%Cr (NiCr)-system FGM that was synthesized by Shimoda, et al., using the reduced-pressure plasma thermal spraying method.

The YSZ/NiCr layer is coated directly to a SUS304 cooling structure. Consequently, the design requires the establishment of an objective function for minimizing residual stress after thermal spraying, and another objective function for minimizing thermal stress when a heat test is being conducted. The compositional distribution parameter n represents the design variable. The tolerated range for the design variable was derived from the relationship between the thickness of the FGM and the compositional distribution parameter required to meet the design goal.

The following four objective function values were obtained from thermal stress analyses. The results of these analyses are shown in Figure 9(a) in which the x axis represents maximum specific stress values, and the y axis is the compositional distribution parameter.

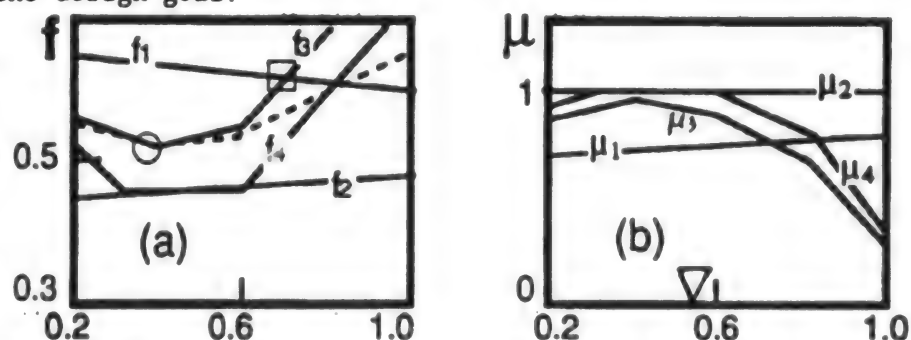


Figure 9. Design Variables and Objective Functions in Designing a YSZ/NiCr-System FGM

f_1 : Residual stress in the production process (maximum tensile specific stress)

f_2 : Residual stress in the production process maximum compressive specific stress <absolute value>

f_3 : Residual stress in the heat test process (maximum tensile specific stress)

f_4 : Residual stress in the heat test process maximum compressive specific stress <absolute value>

First, the processes for obtaining the scalar solution will be introduced. In Figure 9(a) the minimum point of the maximum element (maximum specific stress) was found to be at $x = 0.68$ (\square mark point). The dotted curve, meanwhile, represents a load sum $1/p \sum f_i(x)$, and its minimum point was located at $x = 0.4$ (\circ mark point). Next, the solution by fuzzy theory will be sought. In membership function equation (14) we assumed that $a = 0.5$ and $b = 1.0$. This means that if the specific stress is higher than 1, there is a possibility of damage occurring ($\mu = 0$). Figure 9(b) is a plot of the membership function obtained using equation (12). By seeking the product set within the design

Table 2. Results of Using Multiobjective Optimization Method

Multiobjective optimization method	n	t (mm)	Maximum specific stress	Load sum
Maximum element minimization method	0.68	1.23	0.62	0.53
Load sum minimization method	0.4	1.48	0.64	0.52
Membership function, gravity center method (a=0.5, b=1)	0.57	1.3	0.62	0.53

variable x , the center of gravity was obtained at $x = 0.57$ (∇ mark point). Table 2 summarizes these results.

From the viewpoint of "improving the items that are likely to encounter the most rigorous situations," the maximum element minimizing method is believed to be an acceptable design strategy. In Figure 9(a), f_3 and f_4 have clear minimum value points. However, in f_1 and f_2 , far smaller variation ranges in their values make it difficult to obtain the optimum solutions. Consequently, an alternative is to adopt near-the-minimum points in the f_3 and f_4 curves as optimum solutions. In this case, the load sum minimization method is the most acceptable design strategy. The solution for the gravity center method based on the fuzzy membership function falls between these two solution methods. This means that the use of fuzzy theory makes it possible to realize a trade off (weak Pareto solution) between the two different design strategies.

7. Summary

In this article, we have discussed the basic design procedure for FGMs using the macroproperty influence method, and have described the distribution function as a method of representing gradient composition distribution in these materials. We also discussed the residual stress produced during the production and bonding processes, a problem we encountered in creating FGM test samples. In this connection, we introduced the comprehensive multi-objective optimization method, which encompass all processes up to heat testing. These methods are useful in reducing the weight of the space plane. Continued efforts must be made to accumulate more experimental data, and to coordinate the experience-derived knowledge base for microstructures and synthesis methods to improve both design techniques for FGMs and the accuracy of material analysis.

Our research was conducted as part of "the research to establish fundamental technologies to develop parent phases with less thermal stress," and was funded by the Science and Technology Agency's 1990 science and technology promotion program budget.

FEM Program for Analysis of Transient Thermal Stress

926C0014D Tokyo FGM '91 in Japanese 8-9 Oct 91 pp 209-214

[Article by Junichi Teraki and Tohru Hirano, CAE Center, Daikin Industries, Ltd.]

[Text] **Abstract:** In this paper, we present the results of an analysis of thermal stress in circular plates of functionally gradient material (FGM). We develop a two-dimensional FEM program to analyze the transient heat conduction and the thermal stress in FGMs. By means of this program, we simulate the thermal stress of zirconia (PSZ)/steel (SUS) FGM in a high-temperature gradient environment, and reveal the transient effect and local heating effect.

1. Introduction

In designing a functionally gradient material (FGM), it is essential to conduct thermal stress analysis under practical utilization conditions. Currently, a number of stress analysis and material design methods are available. In recent years, thermal stress analysis has involved not only one-dimensional analysis, but also the finite element method (FEM)-based two- or three-dimensional analysis—sometimes under a nonsteady state. However, it seems that there has not been enough discussion about nonsteady condition effects, and about changes in thermal stress due to two-dimensional effects caused by localized heating.

For this reason, we have developed a two-dimensional FEM program for nonsteady state thermal stress analysis of FGMs. Using this program, we have conducted analyses of the effects of large temperature difference. The testing was conducted using an FGM sample consisting of partially stabilized zirconia (PSZ), and stainless steel (SUS), and a ceramic coating material. The analysis was aimed at clarifying nonsteady state effects and two-dimensional effects in these samples by conducting analyses under localized heating or overall heating conditions.

2. Thermal Stress Analysis

The disk-shaped FGM (Figure 1) was assumed to have material properties that change in thickness direction only, and to have an axis symmetry temperature distribution. First, we calculated a nonsteady state temperature distribution in these samples through thermal conductivity analyses.

Then the thermal stress corresponding to this temperature distribution was calculated quasistatically using the finite element method.

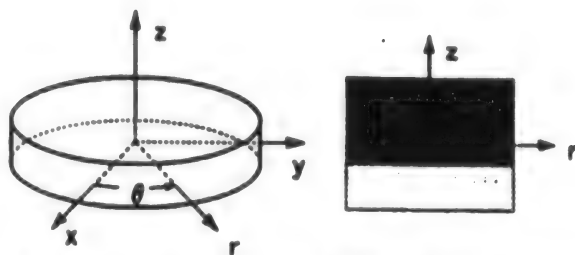


Figure 1. Disk-Shaped FGM Test Sample

The equation for representing a nonsteady state thermal conductivity analysis using the finite element method is given as

$$[C] (\dot{T}) + [R] (T) = \{Q\} \quad (1)$$

where $[C]$ denotes a thermal capacity matrix, $[R]$ is a thermal conductivity matrix, (T) is the temperature vector, $\{Q\}$ represents the heat flux vector, and $(\dot{\cdot})$ represents the differential of time. By assuming that c denotes the specific heat of the area V , ρ the density, $[\lambda]$ the thermal conductivity, q_n the heat flux perpendicular to the boundary S_1 , α_c the thermal conductivity on the boundary S_2 , and T_c the temperature of the outer fluid, each matrix can be given as

$$[C] = \sum_V \int_V c \rho [N]^T [N] dV \quad (2)$$

$$[R] = \sum_V \int_V (\nabla [N])^T [\lambda] (\nabla [N]) dV + \sum_{S_1} \int_{S_1} [N]^T [N] \alpha_c dS \quad (3)$$

$$\{Q\} = \sum_{S_1} \int_{S_1} [N]^T q_n dS + \sum_{S_2} \int_{S_2} [N]^T \alpha_c T_c dS \quad (4)$$

$[N]$ denotes a shape function, $\nabla [N]$ the function incline, and Σ the superimposition of elements. The involvement of a nonsteady problem made us choose the Crank-Nicolson method for time integration.

Similarly, the matrix representation of thermal stress using FEM obtains

$$[K] (U) = (F) \quad (5)$$

where $[K]$ denotes a rigidity matrix, (U) is the displacement vector, and (F) represents the node load vector. By assuming that the elasticity stiffness of the area V is $[D]$, the thermal distortion is (ϵ^t) , and the external force on the boundary S_3 is (p) , each of the matrixes can be given as

$$[K] = \sum_V \int_V [B]^T [D] [B] dV \quad (6)$$

$$[F] = \sum_{s=1}^n \int_{s_s} [N]^T \{p\} dS + \sum_v \int_v [B]^T [D] \{\epsilon^e\} dV \quad (7)$$

where $[B]$ is a matrix representing the relationship between displacement and distortion. This matrix can be obtained by differentiating a shape function.

As for the element, a four-node element was adopted. To take into account the change of material property values within an FGM sample, material property values were defined at each node, and a shape function was introduced for interpolation among the elements (Figure 2).

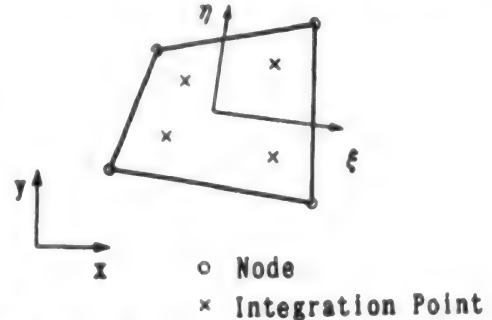


Figure 2. Four-Node Element

Based on this theory, we have developed a two-dimensional FEM program. This program is applicable not only to axis symmetrical problems, but also with flat plane problems.

3. Analysis Results and Discussion

Figure 3 shows a disk-shaped FGM sample like those used in our experiment, together with a large temperature difference analysis model. Measurement of the heat-resistant characteristics of the FGM sample was conducted by bonding the sample onto the testing system's Cu holder and by heating the sample with an arc lamp. The system is capable of creating a temperature difference of about 1,000 K by heating the upper surface with the lamp, and cooling the lower surface of the holder with liquid nitrogen. The model is for a sample 5 mm thick, and a Cu-holder 14 mm thick. When the sample is exposed to a step-mode heat flux, the Cu bottom is assumed to have a constant thermal conductivity. An analysis was conducted under a heat flux step width of 30 seconds, a coolant temperature of 90 K, a thermal conductivity between the coolant and the Cu holder of $1 \times 10^4 \text{ W/m}^2\text{K}$, and an initial temperature of 90 K. The PSZ/SUS FGM sample was supposed to have a compositional distribution in which the composition changes from PSZ to SUS linearly.

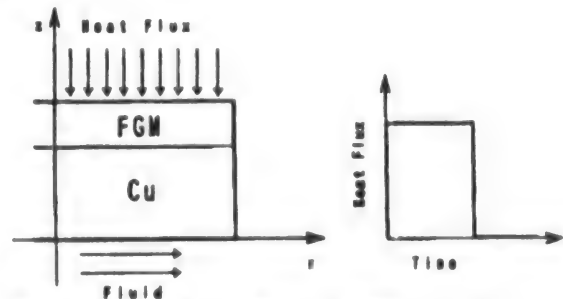


Figure 3. Disk-Shaped FGM Sample and a Model for Large Temperature Difference Analysis

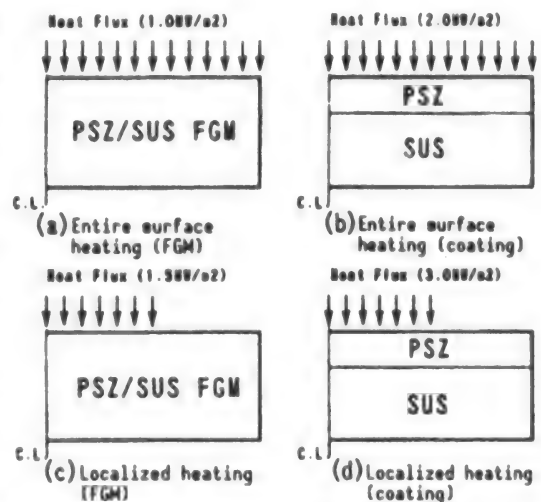


Figure 4. PSZ/SUS-System FGM Analysis Models

Figure 4 shows the four models of the samples used in the analysis. In the

analysis, we compared these FGM samples and ceramic-coated samples by heating their entire surface uniformly or locally. The ceramic-coated samples were composed of a 4.5 mm-thick SUS and an 0.5 mm-thick PSZ. In each sample, the heat flux was adjusted to produce a temperature difference of about 1,000 K.

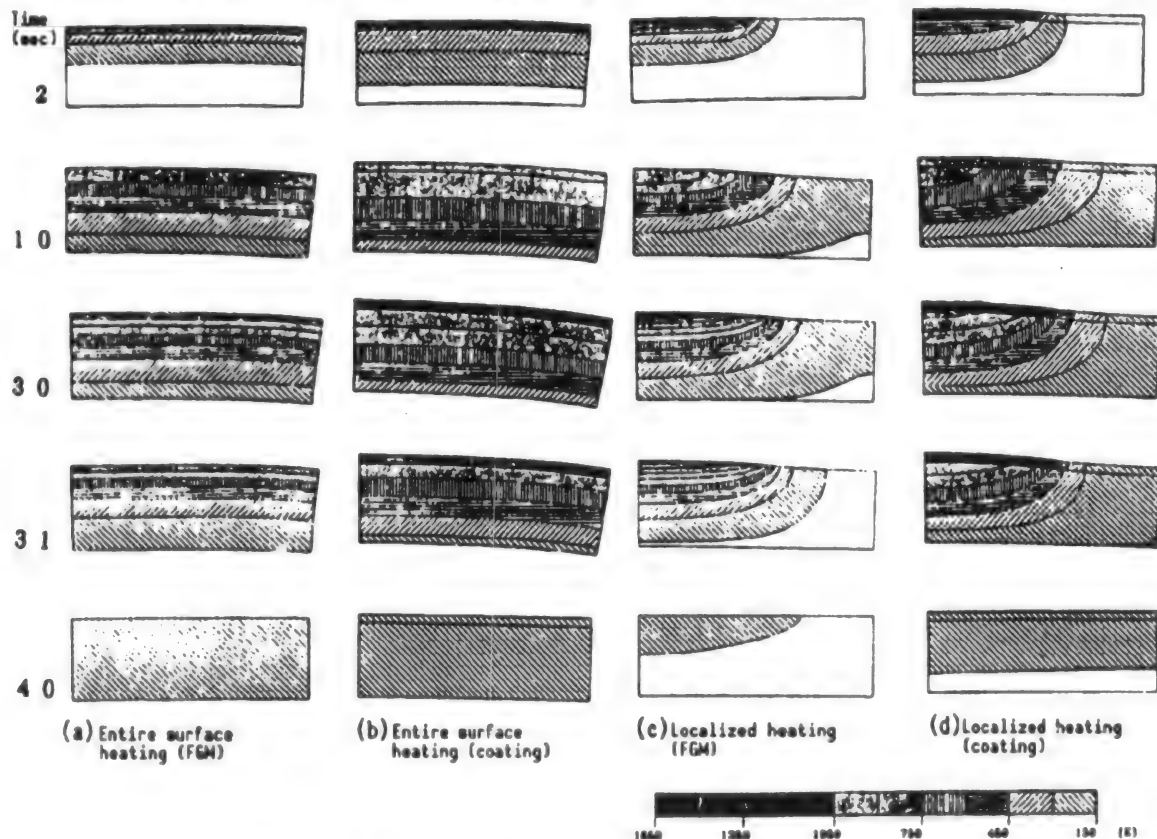


Figure 5. Temperature Distribution Patterns

Figure 5 shows the changes in the temperature distribution pattern over time in these samples. Heat was applied up to 30 seconds. In the figure the conditions at 31 seconds represent those immediately after heating was stopped. The figure shows that the temperature distribution in the FGM samples varies smoothly, both in the entirely heated as well as the locally heated samples. This is because the material property values in these samples change gradiently in the vertical (thickness) direction. However, in ceramic-coated NFGM samples, larger temperature differences appear in the ceramic-coated layer side than in the metallic material side. Immediately after the suspension of heating, these NFGM samples display smaller temperature differences inside the material than is the case for their FGM counterparts. This indicates that, in the former, the cooling process proceeds at a faster pace. In the figure, the heat deformations in these samples are magnified by a factor of 10 to make the deformation condition easier to see.

Figure 6 shows the changes in the radial stress distribution pattern over time. The conditions indicated in the figure are based on the assumption that there is no initial stress in these samples. Heating results in a compressive stress in the ceramic layer side, and a tensile stress in the metallic

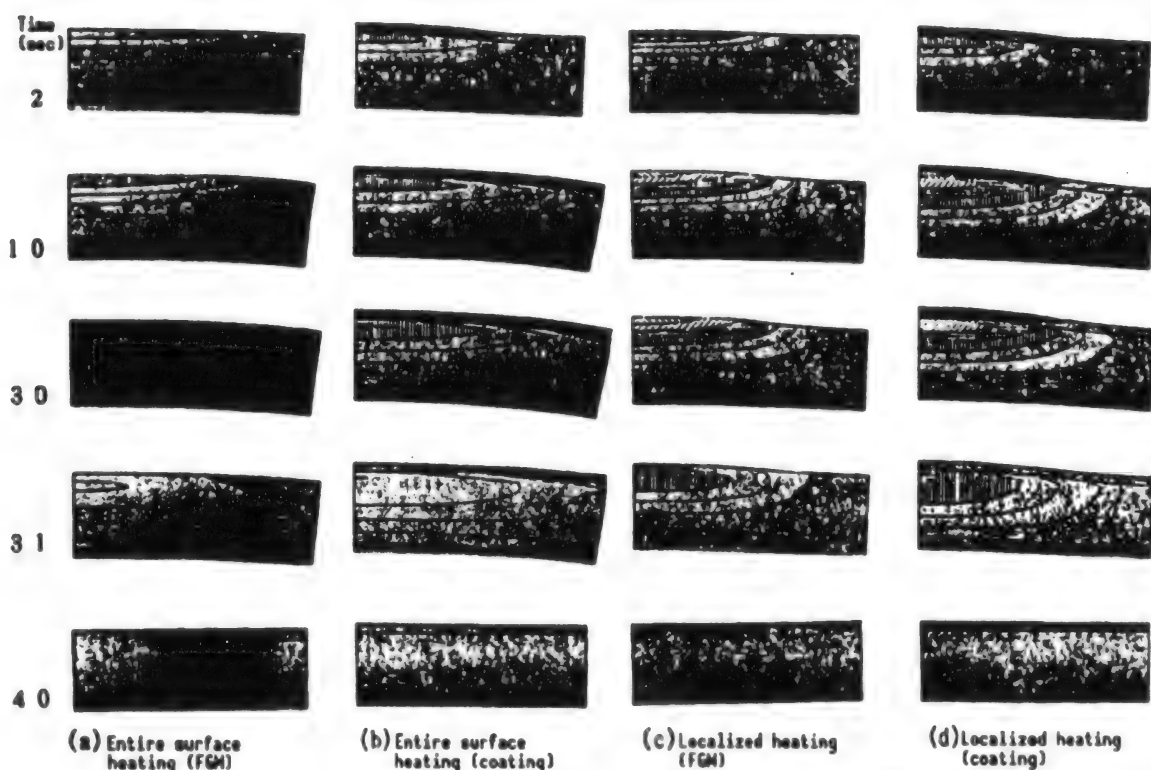


Figure 6. Radial Stress Distribution Patterns

material side. Similar to the case of temperature distribution, the stress distribution changes comparatively smoothly in the FGM samples, regardless of differences in the heating method. However, the ceramic-coated samples produce more complex stress distribution patterns within the ceramic layer. In the case of ceramic-coated samples when the entire surface was heated, it can be seen that a large tensile stress is produced in the boundary region between the ceramic layer and the metallic material layer near the surface of the sample. In the ceramic-coated samples, it can also be seen that a tensile stress has spread across the ceramic layer by the time heating is stopped. This stress could lead to the development of cracks in the ceramic surface in a circular pattern after heating is stopped. In contrast to these ceramic-coated samples, no similar surface effects nor nonsteady state effects are observed in the FGM samples.

Figure 7 shows the changes in the circumferential stress distribution pattern over time. Similar to the radial stress distribution, a compressive stress appears on the ceramic-coated surface, and a tensile stress appears in the metallic material side. Compared to the distribution pattern in FGM samples, the stress distribution pattern is that a tensile stress appears near the ceramic layer's top-most surface when localized heating is applied. When localized heating is applied, there is a possibility that radial cracks could appear near the surface of the ceramic layer. Similar to the situation for

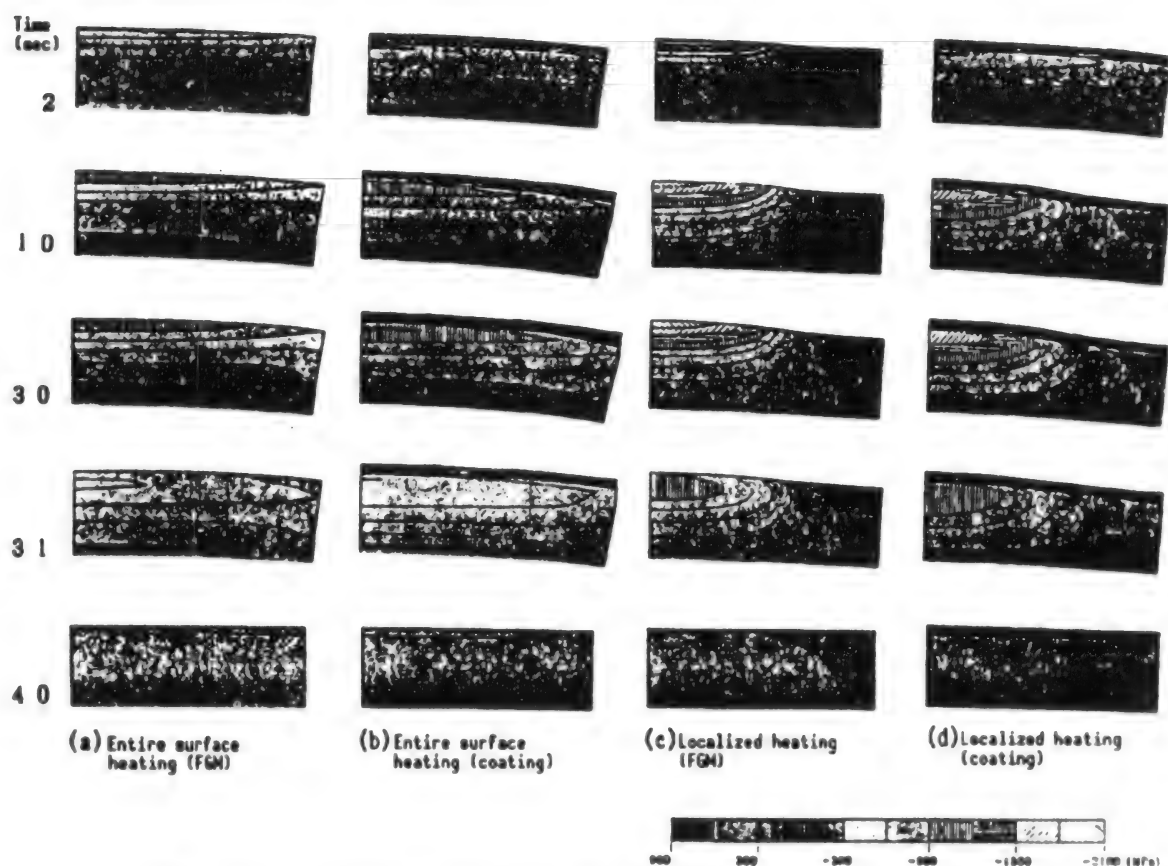


Figure 7. Circumferential Stress Distribution Patterns

radial stress distribution, it can be seen that a tensile stress has spread across the ceramic layer by the time heating is stopped. There is a possibility that this condition will cause radial cracks on the surface of the ceramic layer shortly after heating is stopped. In FGM samples, these nonsteady state effects are observable.

Figure 8 shows the changes in the axial stress distribution pattern over time. In this case, too, the stress in the surface of the ceramic layer is supposed to be zero. This, combined with the fact that the bottom of the metallic material is bonded to the Cu holder, causes a compressive stress to appear near the side faces of the ceramic-coated samples, and creates a tensile stress in the center face region. This tendency appears more conspicuously in the samples whose entire surface was heated. When the sample is not firmly bonded to the Cu holder, there is possibility of separation between the sample and the holder. The magnitude of the stress in this case is substantially smaller than that for both radial stress and circumferential stress. When the entire surface is heated, it can be seen that a tensile stress appears in the boundary between the ceramic layer and the metallic material near the sample's side face. It also has been determined that the stress peaks immediately after heating was stopped because of nonsteady state effects, and this creates the possibility that the ceramic layer could begin to peel. This type of stress does not appear in FGM samples or when localized heating was applied.

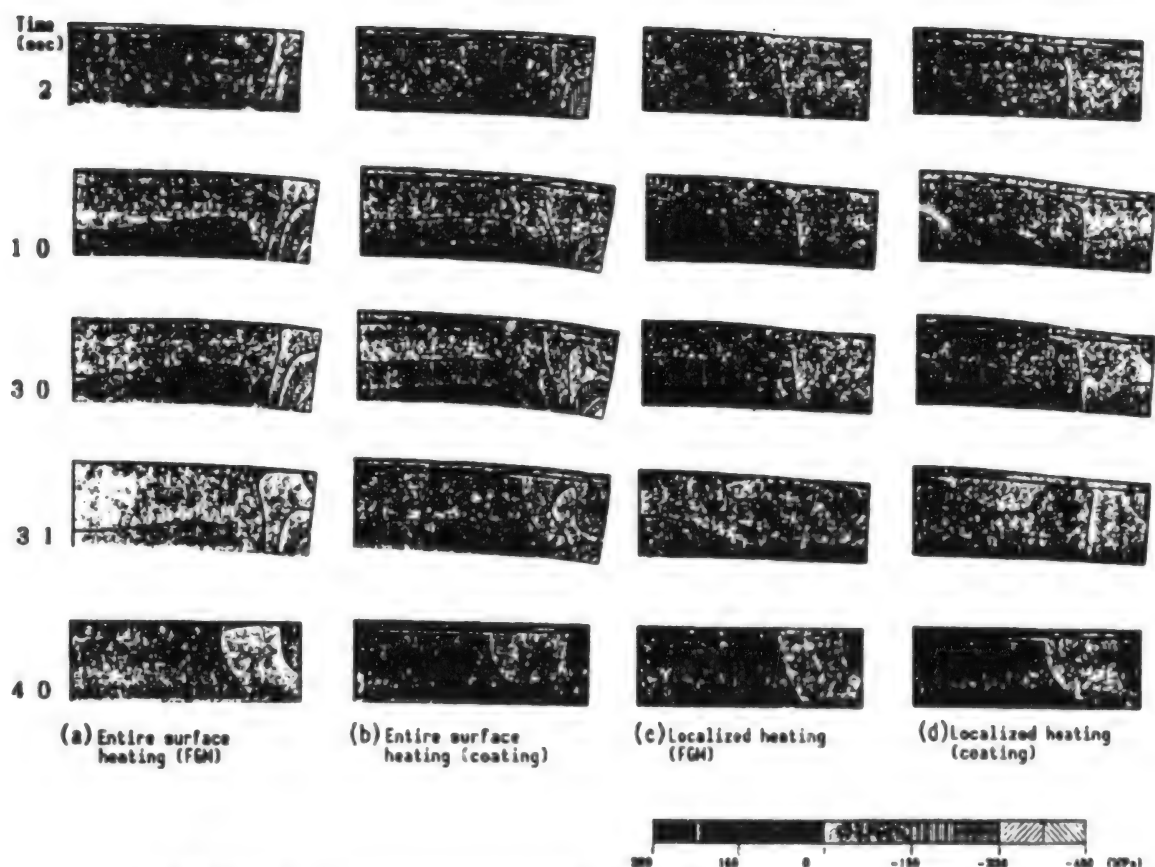


Figure 8. Axial-Direction Stress Distribution Patterns

Figure 9 shows the changes in the shearing stress distribution pattern over time. Just as in the case of axial-direction stress, shearing stress is substantially smaller than radial stress or circumferential stress. However, it can be seen that when the entire surface is heated, a large shearing stress appears in the boundary between the ceramic layer and the metallic material near the sample's side face. Because of nonsteady state effects, shearing stress peaked immediately after heating was stopped. This, combined with the axial-direction stress, has the possibility of causing the ceramic layer to peel away from the side face. Shearing stress does not appear in FGM samples or when localized heating was applied.

4. Conclusion

We have developed a two-dimensional FEM program for the analysis of nonsteady state thermal stress in FGMs. Using this program, we conducted large temperature difference stress tests by heating locally or the entire surface of two types of samples—disk-shaped PSZ/SUS FGM samples and ceramic-coated PSZ/SUS NFGM samples. The tests showed that nonsteady state effects and two-dimensional end face effects are more conspicuous in ceramic-coated samples than in FGM samples. This means that FGMs are effective in restraining these adverse effects.

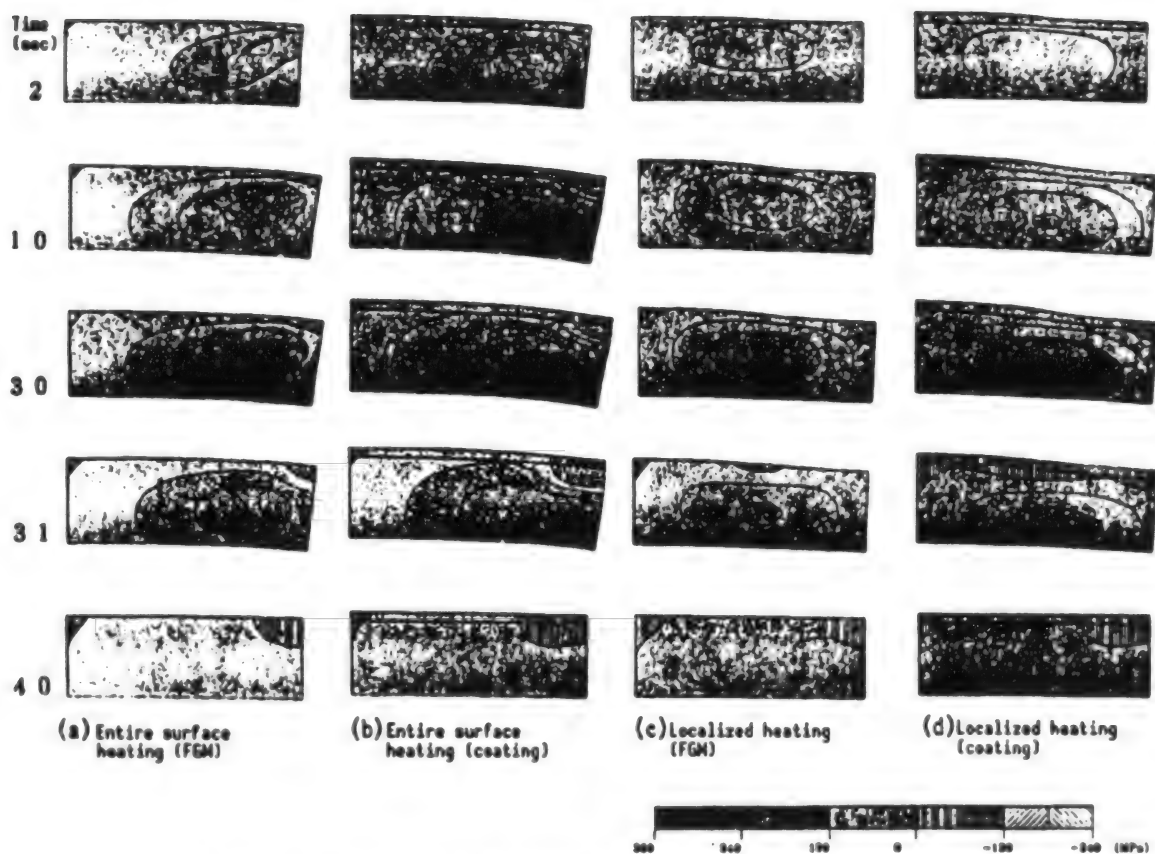


Figure 9. Shearing Stress Distribution Patterns

Our research was conducted as part of a government-subsidized program to develop the fundamental technologies for creating FGMs with a better heat stress alleviating capability. This research was funded by the Science and Technology Agency's 1990 budget for the science and technology promotion program.

Steady State Thermal Stress in FGM Plates

926C0014E Tokyo FGM '91 in Japanese 8-9 Oct 91 pp 215-222

[Article by Yoshihiro Obata, Government Industrial Research Institute, Nagoya; and Naotaka Noda and Tomoaki Tsuji, Shizuoka University]

[Text] Abstract: A functionally gradient material (FGM) which decreases thermal stresses has been developed for structural components and/or mechanical elements in fields such as nuclear, aircraft, and space engineering. Steady-state thermal stresses in a plate made of the FGM are discussed. The main theme of this subject is how to distribute the component of the material in the FGM to decrease thermal stress for different mechanical boundary conditions. In estimating the stress ratio, which means the safety factor, the compressive strength of the material was considered too. We discussed a general method to decrease thermal stress in laminated plates made of two and three layers. The plate of an optimal FGM was determined to increase the safety factor.

1. Introduction

Active efforts to develop heat-stress alleviating functionally gradient material (FGM) include research on developing new materials that are capable of withstanding superhigh speeds and superhigh-temperature conditions. Such materials could be utilized in the fields of aviation, space development, and nuclear engineering. The FGMs currently under development are composed of a ceramic for the high-temperature side, and metals for the low-temperature side. In these FGMs, easing the heat stress is achieved by gradiently changing the compositional distribution to improve its heat-shutting capability.

As for the research on thermal stress alleviation using an FGM, there are a number of reports, including one by Watanabe, et al., in which they conducted experiments using cylindrical molybdenum/zirconia-system FGM samples. We have conducted research on a method to alleviate thermal stress and to find the optimum material compositional distribution and pore rate within FGMs using pore-containing FGM plates, and two- or three-layer FGM plates having dynamically free end boundary conditions. In our current research, we have studied the effect of various dynamic environmental conditions on the optimum distribution pattern and pore rate to alleviate steady-state thermal stress by

using FGM plates having three dynamically different restraint conditions—free elongation and clamped bending, free elongation and free bending, and clamped elongation and clamped bending. These plates have a two- or three-layer structure or contained pores. By noting that the compressive strength of ceramics is greater than their tensile strength, we used the compressive strength of the materials involved in our research as compressive thermal stress in calculating the stress ratio.

2. Analysis

Here, we will study the steady state thermal stress in an FGM that has a thickness of h , a uniform temperature of T_0 , and contains no stress when the temperature on the lower surface is kept at T_a and on the upper surface at T_b (Figure 1). When thermal conductivity λ is a function of the position, temperature T is obtained by

$$T = T_b + (T_a - T_b) \left[1 - \frac{\int_0^x \{1/\lambda(x)\} dx}{\int_0^h \{1/\lambda(x)\} dx} \right] \quad (1)$$

If the distortion on the lower surface ($x = 0$) of a plate is ϵ_0 , and the radius of the curvature is ρ , then the thermal stress σ is obtained by

$$\sigma = \frac{E(x)}{1-\nu(x)} \left[\epsilon_0 + \frac{xh}{\rho} - \alpha(x) (T(x) - T_0) \right] \quad (2)$$

where E denotes the modulus of longitudinal elasticity, α is linear expansion coefficient, and ν is Poisson ratio. Each property value is the function of the position.

We studied four cases involving different dynamic boundary conditions:

- (a) Free end: $\int_0^h \sigma dx = 0$, $\int_0^h x \sigma dx = 0$
- (b) Free elongation and clamped bending: $\int_0^h \sigma dx = 0$, $\rho = \infty$
- (c) Clamped elongation and free bending: $\epsilon_0 = 0$, $\int_0^h x \sigma dx = 0$
- (d) Clamped elongation and clamped bending: $\epsilon_0 = 0$, $\rho = \infty$ (3)

The thermal stress in each of these cases can be calculated by obtaining the values of ϵ_0 and ρ for each of the conditions in equation (3), and by solving equation (2) using these values.

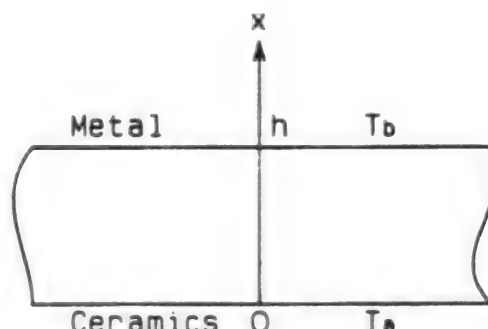


Figure 1. FGM Plate Used for Analysis

3. Calculation Results and Discussion

3.1 Property Values

As an FGM for thermal stress alleviation, we have studied a combination of ZrO_2 , a material that has superior heat-resistant adiabatic capability, and Ti-6Al-4V, which is lightweight and has a high level of strength. Table 1 lists the property values for these materials at room temperature. The table indicates that ZrO_2 has a compressive strength that is about 21 times greater than its tensile strength.

Table 1. Material Property Values

	λ W/(mK)	E GPa	α 1/K	ν	σ_{Bt} MPa	σ_{Bc} MPa
ZrO_2	2.09	151.0	10.0×10^{-6}	1/3	146	3136
Ti-6Al-4V	7.50	116.7	9.5	1/3	921	921

λ : thermal conductivity

E: modulus of longitudinal elasticity

α : linear expansion coefficient

ν : Poisson ratio

σ_{Bt} : tensile strength

σ_{Bc} : compressive strength

3.2 Evaluation

The tensile stress ratio f_t , the compress stress ratio for tensile stress f_c , and the compressive strength generated within an FGM plate can be defined by the following equations

$$\begin{aligned}
 f_t &= (\sigma_{Bt}(x)/\sigma(x)) & (\sigma(x) > 0) \\
 f_c &= (\sigma_{Bc}(x)/\sigma(x)) & (\sigma(x) < 0) \\
 f &= \text{Min}(f_t, f_c)
 \end{aligned} \tag{4}$$

where f takes the smaller of the f_t and f_c values. Supposing that a material break takes place when the tensile and compressive stresses within an FGM surpass the tensile strength σ_{Bt} and compressive strength σ_{Bc} . Thus, when $f_t < 1$ and $f_c < 1$, the stress ratios f_t , f_c , and f are considered to represent safety rates.

3.3 Two-Layer Plate

In this section, we will examine the steady state thermal stress in a two-layer plate consisting of a lower ZrO_2 plate having a thickness of h_1 , and an upper Ti-6Al-4V with a thickness of h_2 . The initial temperature T_0 , and the boundary temperatures T_a and T_b are set as follows:

$$T_0 = 300 \text{ K} \quad T_a = 1,800 \text{ K} \quad T_b = 900 \text{ K} \tag{5}$$

Figure 2 shows the thermal stresses σ that appear in the boundary between the two different material plates when the dynamic boundary conditions and the plate thickness are changed.

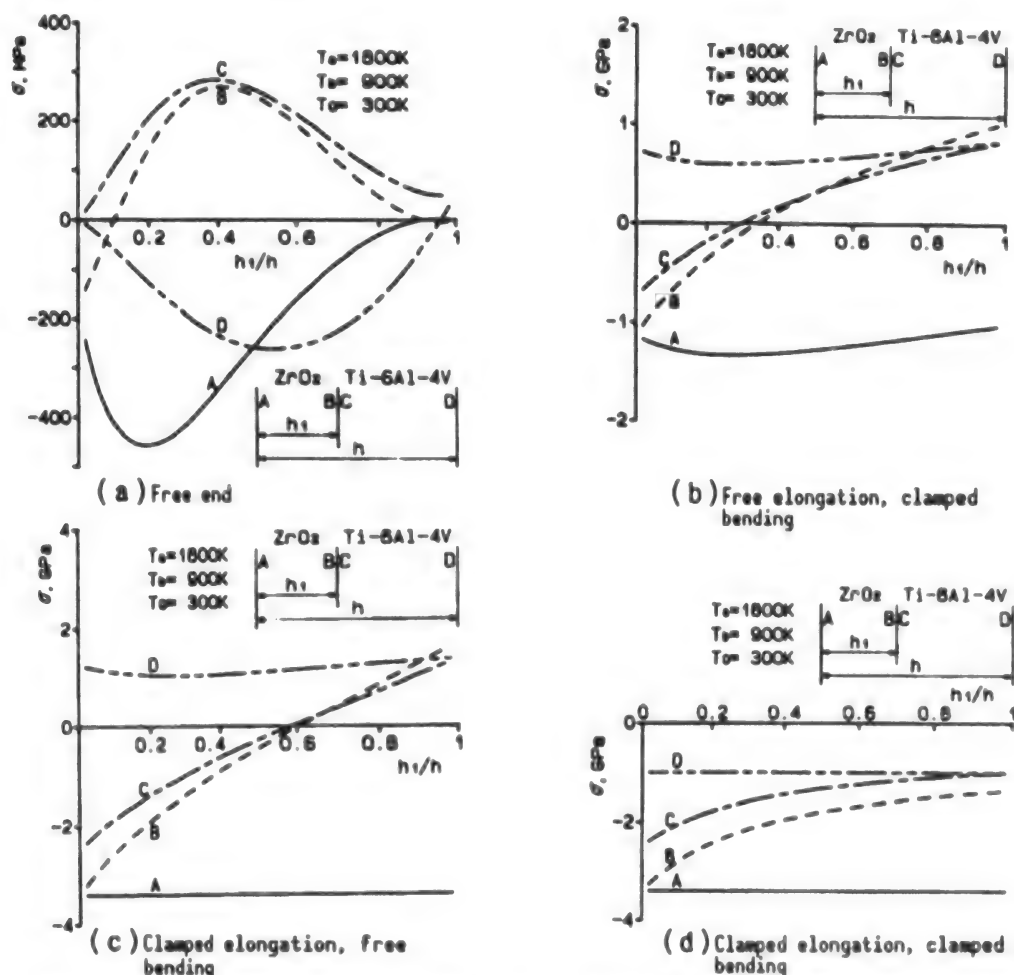


Figure 2. Relationship Between ZrO_2 Plate Thickness on Thermal Stress in a Two-Layer Plate

In the case of (a), the boundary stress changes greatly depending on the thickness of the ZrO_2 layer, and the maximum thermal stress can be lowered by adjusting the thickness to an optimum value. Under the clamped conditions, the boundary thermal stress also changes depending on the thickness of the ZrO_2 layer, but little change is observed in the thermal stress that appears on the plate surface. This indicates that the maximum value of the thermal stress cannot be reduced substantially by adjusting the thickness of the ZrO_2 layer only.

Figure 3 shows the stress ratios f under each of the dynamic boundary conditions.

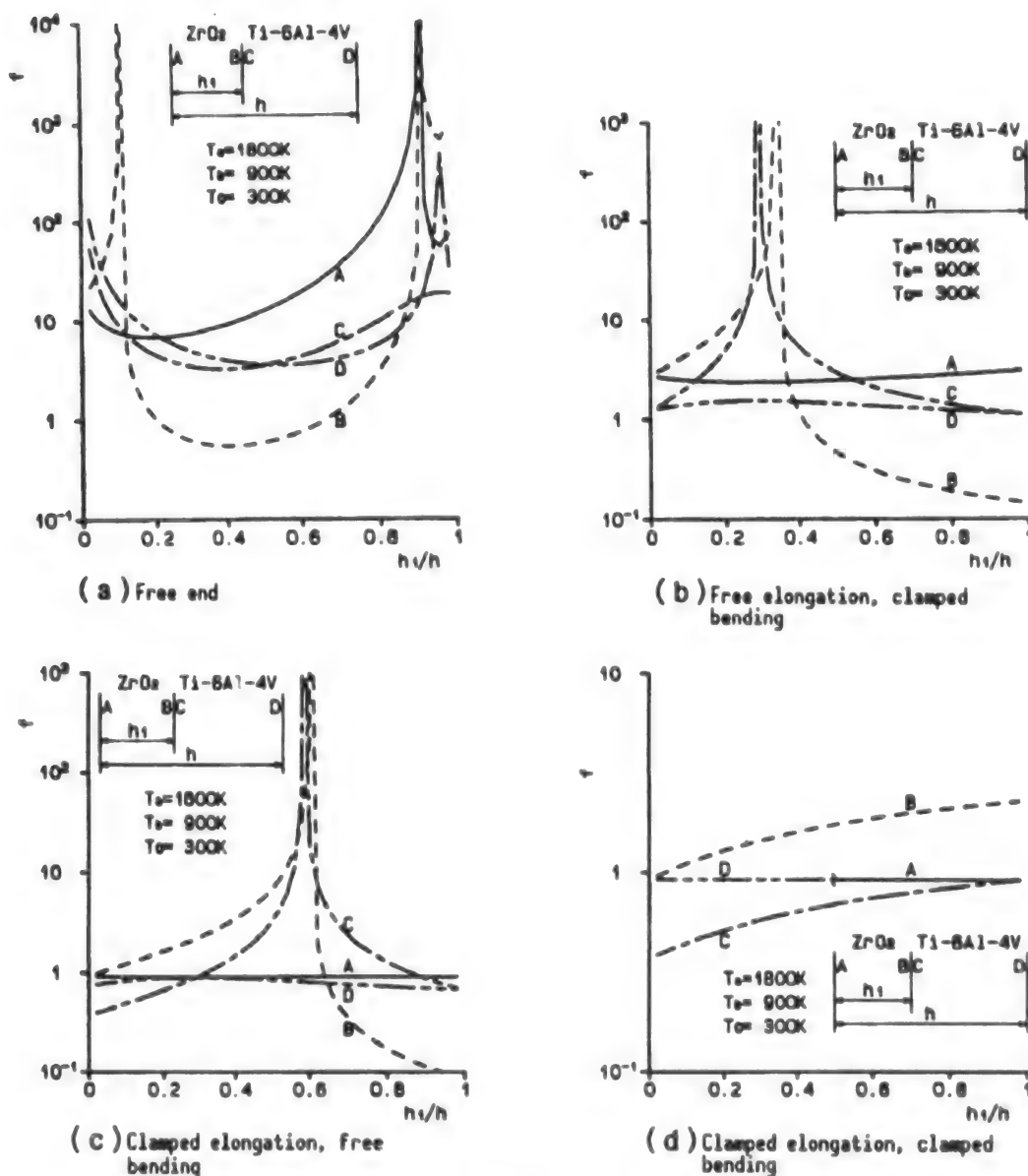


Figure 3. Thickness of ZrO_2 Layer and Stress Ratio in a Two-Layer Plate

In Figure 2, stress ratio f is high at the maximum stress point A because the compressive strength within the ZrO_2 layer is high, while at the B point a tensile stress is present within the layer, and there is a possibility that a break could occur because f becomes smaller than 1. In Figure 3, the peak points represent the points where stress becomes zero. By modifying the thicknesses of the ZrO_2 layer at these points, it is possible to obtain high f values on a localized basis. Figure 4 shows the range of ZrO_2 layer thicknesses in which f is larger than 1—the range in which material damage does not occur because of thermal stress. Figure 4 indicates that the two-layer plate is free of total thermal stress damage when $x = 1$.

In the case of the free and dynamic boundary, there are two optimum ZrO_2 layer thicknesses—one for the thin side and one for the thick side, respectively—in which no damage occurs in the two-layer plate. In the case of (b), there is only one optimum thin thickness. In the case of the clamped elongation, free bending, h_1/h peak is present at an h_1/h ratio of around 0.3 (Figure 4), and this differs from the peak point near $h_1/h = 0.6$ in Figure 3(c). This means that a localized increase in the stress ratio does not necessarily lead to an improvement of strength over the entire area of a plate. In the case of the clamped elongation and clamped bending, only compressive stress is generated within the plate (Figure 2(d)), and this causes the n-break region to increase in proportion to an increase in the thickness of the ZrO_2 layer. However, in the last two boundary conditions, there is no ZrO_2 layer thickness in which $x = 1$, and thus no total plate damage occurs.

3.4 Three-Layer Plate

In this section, we will examine steady state thermal stress in a three-layer plate composed of a Ti-6Al-4V layer, a layer of an arbitrary material, and a ZrO_2 layer, arranged from top to bottom.

Figure 5 shows the no-damage plate thickness range when the thickness h_2 of the middle layer was changed while keeping the thickness of the top and bottom layers at an equal h_1 . The summed averages of the top and bottom layer property values were used as the property values for the middle layer.

In a three-layer plate, too, there is no optimum middle layer thickness that can avoid a total break of a plate under the dynamic boundary conditions of (c) or (d). In the case of the latter condition, the presence of the middle layer sacrifices the compressive strength of the ZrO_2 layer, and the maximum value of x is smaller than that for its two-layer counterpart.

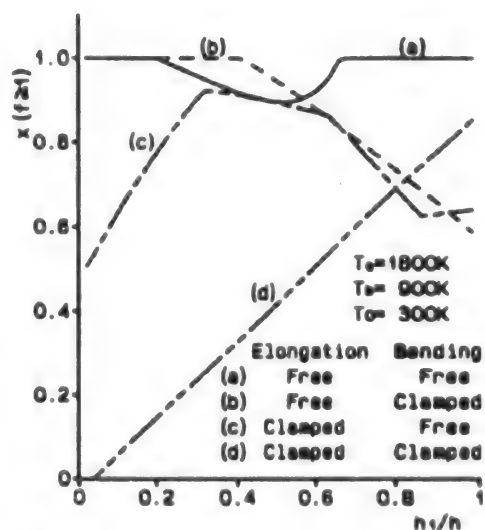


Figure 4. Thickness of the ZrO_2 Layer and Break-Free Thickness of the Two-Layer Plate

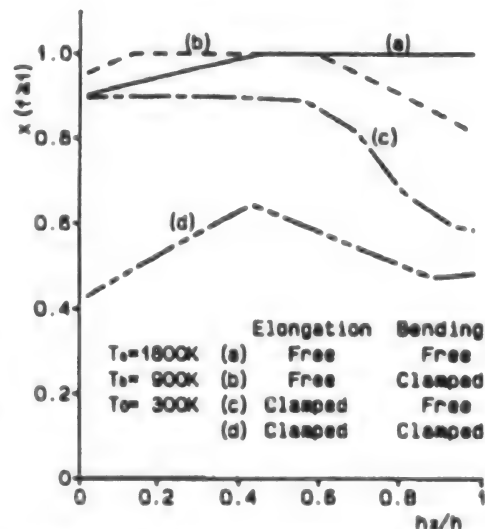


Figure 5. Relationship Between the Thickness of the Middle Layer and the No-Damage Thickness of a Three-Layer Plate

3.5 FGM Plate

In this section, we will study the performance of a $ZrO_2/Ti-6Al-4V$ FGM plate containing pores within the plate. To determine the property values for the materials involved, we adopted the following equations from among a number of equations that have been proposed for calculating property values in a mixed composition material.

$$\begin{aligned}\lambda &= [(1-P^{1/3})/\lambda_0 + P^{1/3}/((1-P^{2/3}) \lambda_0 + P^{2/3} \lambda_a)]^{-1} \\ E &= E_0(1-P)/[1+P(5+8 \nu_0) (37-8 \nu_0)/(8(1+\nu_0)(23+8 \nu_0))] \\ \alpha &= \alpha_0, \quad \nu = \nu_0, \quad \sigma_{Bt} = \sigma_{Bt0} (1-P), \quad \sigma_{Bc} = \sigma_{Bc0} (1-P)\end{aligned}\quad (6)$$

In the above equations, P denotes the pore rate, and λ_a is the thermal conductivity of air. Also,

$$\begin{aligned}\lambda_0 &= \lambda_c + 3\lambda_c (\lambda_m - \lambda_c)V_m / (3\lambda_c + (\lambda_m - \lambda_c)(1-V_m)) \\ E_0 &= E_c (E_c + (E_m - E_c)V_m^{2/3}) / (E_c + (E_m - E_c)(V_m^{2/3} - V_m)) \\ \alpha_0 &= (\alpha_m K_m V_m + \alpha_c K_c (1-V_m)) / (K_m V_m + K_c (1-V_m)) \\ \nu_0 &= \nu_m V_m + \nu_c (1-V_m) \\ \sigma_{Bt0} &= \sigma_{Btm} V_m + \sigma_{Btc} (1-V_m) \\ \sigma_{Bc0} &= \sigma_{Bcm} V_m + \sigma_{Bcc} (1-V_m) \\ K_m &= E_m / (2(1-\nu_m)), \quad K_c = E_c / (2(1-\nu_c))\end{aligned}\quad (7)$$

where c denotes ceramics, m is metal, and V_m represents the volume rate of the metal involved.

Here, we will consider the cases in which V_m and P are expressed by the following equations:

$$V_m = x^m \quad (8)$$

$$P = Ax (1 - x), \quad 4 > A \geq 0 \quad (9)$$

Figure 6 shows the no-break thickness range for an FGM plate when the values of parameters m and A were changed.

In the case of the boundary condition depicted in (a), any combination of parameters m and A makes it possible to create an FGM plate that will be free from total break. In the case of (b), A 's influence is small. However, when m exceeds 3, the break range increases sharply. In the case of (c), no-break thickness decreases irrespective of m 's value. When A 's value increases, no-break thickness increases. However, there are no optimum combinations for pore rate or volume rate that can prevent the total break of an FGM plate.

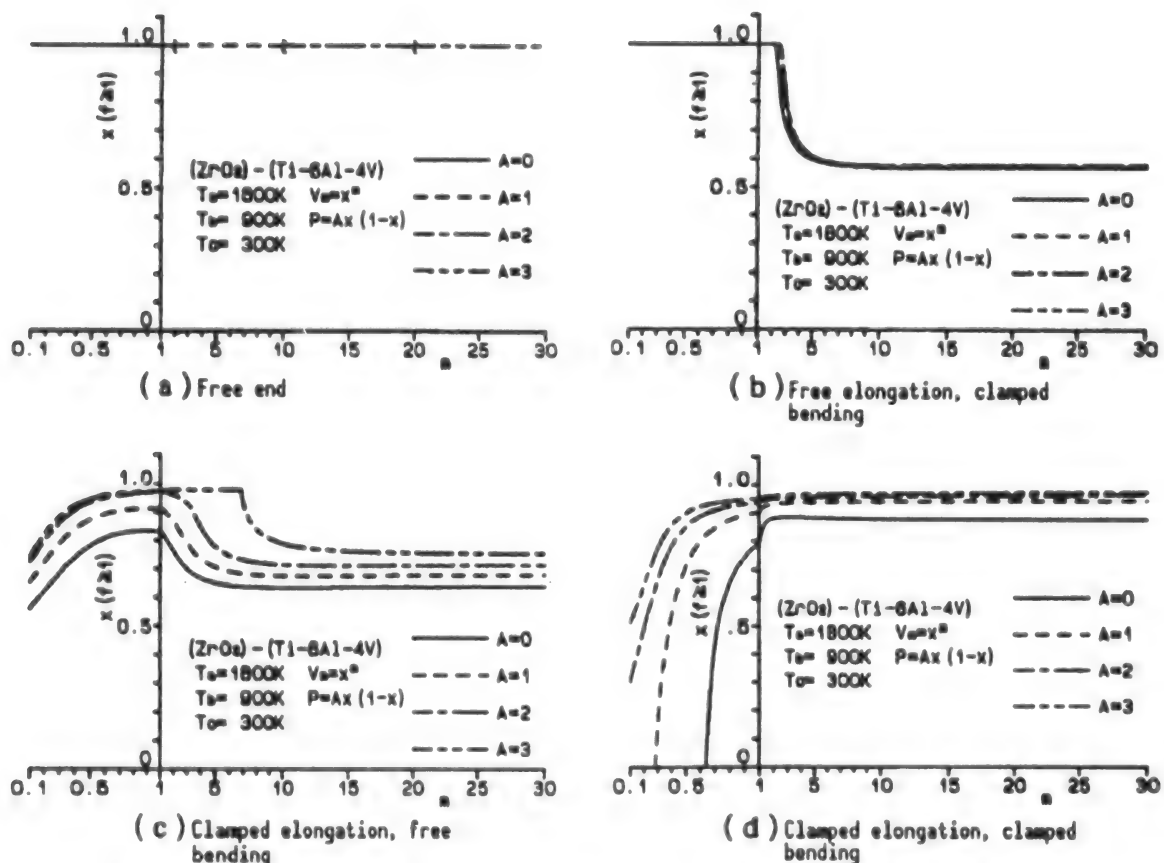


Figure 6. Effect of Pore Rate and Volume Rate on the No-Break Thickness Range of an FGM Plate

When both the elongation and bending are clamped, the no-break thickness decreases when m 's value decreases. Depending on A 's value, a total break of an FGM plate could occur. The effect of A is the same in the case of (c), and there is no optimum combination of pore rate and volume rate that can prevent a total break. Consequently, in the cases of (c) and (d), it is necessary to change the temperature condition to avoid a total break.

When the boundary condition is either (a) or (b), the concept of an inverse problem of steady state thermal stress can be used to seek the values of m and A for both the volume rate V_m and pore rate P to maximize the stress ratio f within the no-break range of an FGM plate. The solution to this problem can be obtained under the following conditions:

Objective function: Maximize the minimum stress ratio f when $f \geq 1$.

Limiting conditions: $4 > A \geq 0$, $30 \geq m \geq 0.1$

Controlling parameters: m , A

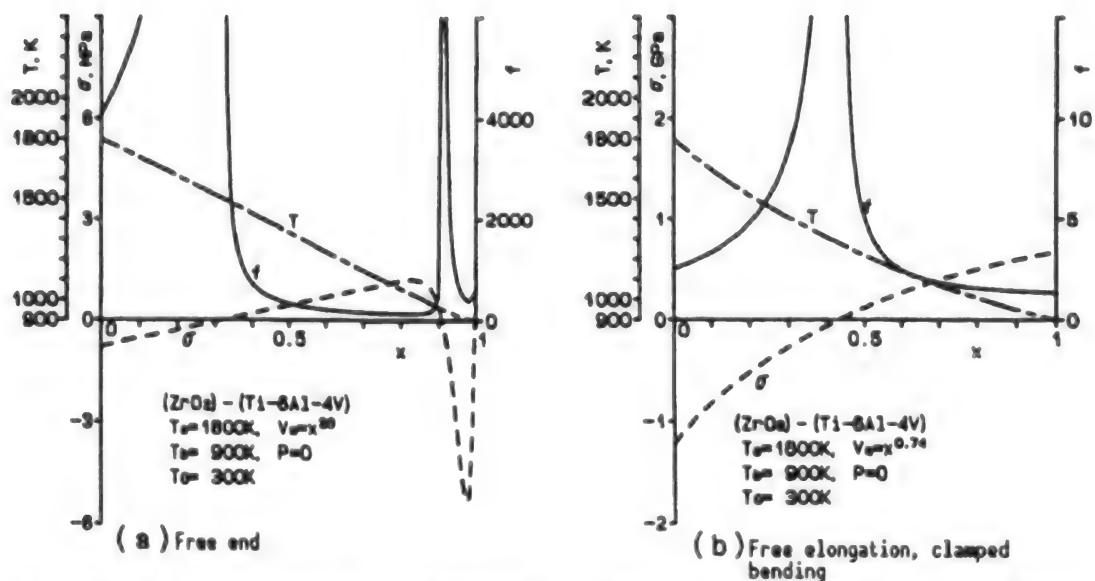


Figure 7. Distribution Temperature, Thermal Stress, and Stress Ratio in a Parameter-Optimized FGM Plate

The optimum values for boundary condition (a) are $m = 30$, and $A = 0$, and for boundary condition (b) $m = 0.74$ and $A = 0$. Figure 7 shows the temperature, thermal stress, and stress ratio distributions under these parameters conditions.

4. Conclusion

By analyzing the steady state thermal stress in a $\text{ZrO}_2/\text{Ti-6Al-4V}$ FGM plate, we obtained the following results:

- (1) When the dynamic boundary condition changes, the optimum FGM composition also changes. This means that in designing an FGM, anticipated restraining conditions in which the material will be used must be taken into account.
- (2) Ceramics have a very high compressive strength. We believe it is practical to use their compressive strength for compressive stress to define stress ratios in ceramics.
- (3) It is impossible to create an FGM plate free of total break under dynamic boundary conditions (c) or (d), and when $T_a = 1,800\text{ K}$ and $T_b = 900\text{ K}$. This suggests that there is a total break-free temperature range for a $\text{ZrO}_2/\text{Ti-6Al-4V}$ FGM plate under each of those dynamic boundary conditions.

Fundamental Studies of TiAl-Based FGMs

926C0014F Tokyo FGM '91 in Japanese 8-9 Oct 91 pp 223-234

[Article by Yuji Matsuzaki, Masashi Kawamura, Junzo Fujioka, Shun-ichi Minakata, Hiroyasu Nishikawa, and Takao Yoshikawa, Akashi Technical Institute, Kawasaki Heavy Industries, Ltd.; and Yoshinari Miyamoto, Industrial and Scientific Institute of Research, Osaka University]

[Text] Abstract: Because of their low density and outstanding high-temperature strength, TiAl intermetallic compounds are expected to be applicable to hypersonic transport (HST) aircraft. The aim of this study is to develop TiAl-based functionally gradient materials (FGMs) with superior heat insulation and thermal stress relieving functions, in order to apply them to those components of an HST aircraft that would be subject to extremely large heat loads.

First, the properties required of heat-insulating FGMs were collated, and then, possible material systems that might satisfy the requirements were studied. As a result, it is concluded that the most promising material system would be a multiphase FGM of Al_2O_3 -SiC-TiC-TiAl which has lower density, excellent thermal insulation property, thermodynamic stability, and oxidation resistance. Furthermore, the heat transfer properties and thermal stress properties of the multiphase FGMs were examined analytically, and a possible compositional distribution of the FGM was proposed.

1. Introduction

To construct the next-generation supersonic transport (HST) aircraft's fuselage, engines, and nuclear fusion reactors, the development of a material structure that is capable of withstanding very rigorous operational conditions, particularly superhigh temperatures, is essential. In an HST plane that will be equipped with a regenerative cooling structure, ensuring structural stability in a superhigh-temperature environment is very important. Also, limiting the volume of liquid hydrogen required as a coolant for the HST structures is equally important in reducing the weight of the plane.

In order to solve these problems, an effort must be made to reduce the thermal load on these structural materials by introducing the concept of thermal barrier coating (TBC). This concept already has been applied to gas turbine

engines that have been used in practical applications. However, greater difficulties are expected in applying the concept to the HST plane because of the enormous magnitude of the thermal load involved. In practical operation, the HST plane's fuselage will be exposed to a supersonic, superhigh-temperature gas current, whose temperature may well reach 3,000 K. In the HST, the heat-relieving structural material layer must have a steep temperature gradient to ensure that the structural members of the plane operate within safe operational conditions with a limited cooling capability. In these applications, the thermal stress generated within these structural materials when they are exposed to various high temperature conditions is expected to be far beyond what a single layer of ceramic coating or conventional TBC technology can handle safely. Heat barrier FGMs (HBFGMs) have been developed to deal with these problems. An HBFGM is required to have excellent heat barrier (heat resistance) characteristics on the heated side, and good dynamic structural characteristics on the cooled side. HBFGM is defined as a macroscopic/microscopic material in which the compositional distribution of different elements having different functions shifts from one material to another continuously to prevent the concentration of stress (for example, residual stress generated in the process of FGM component manufacturing or thermal stress caused by actual temperature gradient use) in a localized place. In our research, we sought to clarify the characteristics that HBFGMs must have to meet the above requirements. To this end, we studied a number of material combinations to find those combinations that would satisfy these requirements. In addition, we studied analytically the heat insulating and thermal stress relieving characteristics of these material combinations.

2. Characteristics Required in HBFGMs

2.1 Heat Insulating Capability (Thermal-resistant characteristics)

In the development of the projected space plane, it is important to reduce the volume of liquid hydrogen used for structural cooling as much as possible to attain an economic balance (balance between required coolant volume vs. required fuel volume). This problem can be solved by reducing heat input level by developing heat insulating materials. In the following, we will discuss how the heat insulating function is realized in HBFGMs.

Heat transfer in a ceramic/metal laminar structure is expressed as

$$q_g = \alpha_g (T_g - T_{co}) \dots \dots \text{High temperature side heat transfer equation (1)}$$

$$q_c = \lambda_c (T_{co} - T_{mo}) / t_c \dots \text{Ceramic layer heat transfer equation 1 (2)}$$

$$q_m = \lambda_m (T_{mo} - T_{mi}) / t_m \dots \text{Metal layer heat transfer equation 2 (3)}$$

$$q_f = \alpha_f (T_{mi} - T_f) \dots \dots \text{Low temperature side heat transfer equation (4)}$$

where,

q : denotes heat flux (W/m^2),

α : is a heat transfer coefficient (W/m^2K),

T : represents temperature (K),

λ : is thermal conductivity (W/mK),
 t : denotes the material layer thickness (m),
 g : is the hot-side current (gas),
 f : is the cooled-side fluid,
 c : denotes a ceramic layer (ceramics),
 m : is a metallic layer (metals),
 o : represents the high-temperature side (outer), and
 i : is the low-temperature side (inner).

Here, the effect of heat radiation is ignored.

The gas-side heat transfer coefficient (α_g), gas temperature (T_g), and the cooling-side fluid temperature (T_f) are all constants that are set as environmental conditions. Thermal conductivity, denoted by λ_c and λ_m , is a property value inherent to the materials involved. The thickness of the metallic layer (t_m) is a constant that is determined by taking system design-related factors into account to satisfy required structural characteristics. However, in practical application, the maximum utilization temperature of a material (in this instance T_{co} and T_{mo}) must be defined as the restraining conditions in calculating thermal transfer problems. (In many cases of practical application, T_{mo} works as the restraining condition.)

In a steady state condition in which the heat exchange between the hot gas and the cooling agent is implemented via a material layer, heat flux q in equations (1) through (4) assumes a constant value because there is a heat energy balance. From this, the following equation can be derived:

$$q_g = q_c = q_m = q_f \quad (5)$$

Removing the temperature variables (T_{co} , T_{mo} , T_{mi}) from the material surface as well as from inside it, and then solving equations (1) through (5) to calculate heat flux q obtains

$$q = k' (T_g - T_f) \quad (6)$$

Here,

$$\frac{1}{k'} = \frac{1}{\alpha_g} + \frac{t_c}{\lambda_c} + \frac{t_m}{\lambda_m} + \frac{1}{\alpha_f} \quad (7)$$

where k' denotes an overall heat transfer coefficient, and it has the same dimension as that of heat transfer coefficient α .

From equations (1) through (7), it can be found that to reduce the required volume of cooling agent—or to reduce the heat transfer rate on the cooling side—the selection of a material combination and the structural design must be conducted in a way that keeps ceramic surface temperature (T_{co}) at a high level (and consequently higher T_{mo} and T_{mi}) to reduce the heat flux (q) in the inner part of the material. In addition, the critical heat transfer rate on the cooling side (corresponding to the minimum cooling capability needed to

confine T_{no} within the maximum operating temperature) can be reduced further by reducing the overall heat transfer coefficients (λ_c/t_c and λ_m/t_m) in the ceramic and metallic layers.

Meanwhile, from equation (2) which is applicable to a composite material laminar plate made up of n layers and consequently serving as FGM layers, the following equations can be derived:

$$\begin{aligned} q_{FGM} &= \lambda_1 (T_{1o} - T_{1i})/t_1 \\ &= \lambda_2 (T_{2o} - T_{2i})/t_2 \\ &\vdots \\ &= \lambda_k (T_{ko} - T_{ki})/t_k \\ &\vdots \\ &= \lambda_n (T_{no} - T_{ni})/t_n \end{aligned} \quad (8)$$

Consequently,

$$q_{FGM} = \lambda_e \cdot \Delta T / \Delta \quad (9)$$

And then,

$$\Delta = \sum t_k = t_{FGM} \quad (10)$$

$$\lambda_e = \Delta / \sum (t_k / \lambda_k) \quad (11)$$

(where λ_e is effective transfer rate)

$$\begin{aligned} \Delta T &= \sum \Delta T_k = \sum (T_{ko} - T_{ki}) \\ &= \Delta T_{FGM} = T_s - T_{no} \end{aligned} \quad (12)$$

(where T_s is surface temperature of FGM)

Consequently, equation (9) can also be expressed as

$$q_{FGM} = \lambda_e (T_s - T_{no}) / t_{FGM} \quad (13)$$

This corresponds to the description of heat transfer within a ceramic layer in equation (2), and consequently the following equation for steady state heat exchange can be obtained:

$$q = k (T_g - T_f) \quad (14)$$

$$\frac{1}{k} = \frac{1}{\alpha_g} + \frac{t_{FGM}}{\lambda_e} + \frac{t_m}{\lambda_m} + \frac{1}{\alpha_f} \quad (15)$$

Effective thermal conductivity λ_e changes depending on temperature and the compositional distribution pattern in an FGM layer. Thus it is important to accumulate reliable data about the value by conducting numerical analyses, and large temperature difference environment tests, using the thermal property values of uniform quality materials (non-FGMs: NFGMs) having different

material compositions. The overall heat transfer coefficients (λ_e/t_{FGM} and λ_m/t_m) in an FGM layer, and in a metallic layer in equation (15), affect the required volume of cooling agent under steady state heating conditions. These coefficients also serve as important parameters in dealing with thermal stress problems in FGMs, and because of this they must be handled carefully.

From the above discussion, the characteristics required for HBFGMs can be summed up as follows:

- (1) Must have low thermal conductivity to keep the temperature on the material surface and within it high.
- (2) Must have high heat-resistant capability to withstand high temperatures on the surface and within the material.

2.2 Anticorrosion Characteristics (Oxidation, oxygen permeation, hot corrosion)

High-temperature oxidation is a major problem facing the use of high-temperature structural ceramics in aviation and space applications. Considering that the space plane navigates through the atmosphere, the plane's structural material must have good oxidation-resistant characteristics. Figure 1 shows the oxidation characteristics of several nonoxide materials (SiC, MoSi₂, HfC, HfB₂) that are reported to have comparatively good anti-oxidation characteristics. SiC and MoSi₂ display excellent antioxidation characteristics. HfB₂ shows a gain in mass because of oxidation in a very short time after being exposed to an oxidizing atmosphere. In contrast, HfC becomes completely oxidized in a very short time after exposure. These results indicate that as far as oxidation resistance is concerned, oxide ceramics and silicon-system nonoxide ceramics (SiC, Si₃N₄, MoSi₂ and composite materials made of these ceramics) are suitable for use on the high-temperature side of FGMs.

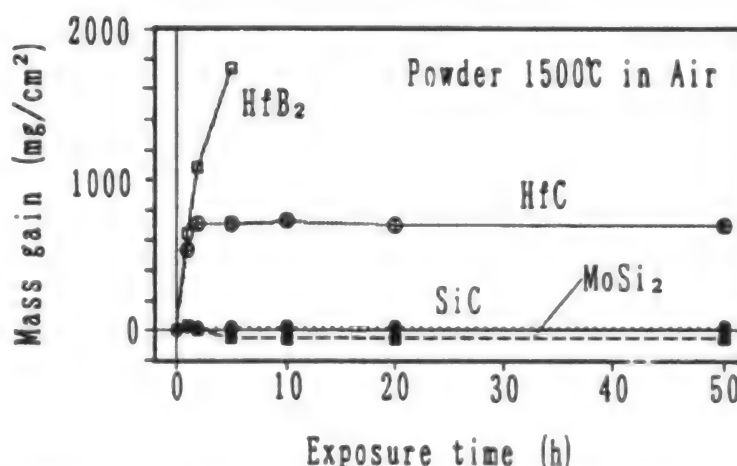


Figure 1. Typical Antioxidation Characteristics of Several Types of Nonoxide Materials

Stabilized zirconia (including partially stabilized zirconia), is a principal TBC material. It is an excellent solid electrolyte, and has an oxide permeability based on ion conduction. Because of this, MCrAlY, a material that has good antioxidation capability, is used for TBC bonding. Despite this, oxidation reactions still occur on the material boundary that is exposed to an oxidizing environment through a TBC layer. Oxidation causes the volume of the material being oxidized to change, and this leads to peeling of the ceramic

coating layer. In FGMs in which a metallic phase starts at a depth very close to the high-temperature surface, the selection of materials for the high-temperature and low-temperature sides must be made very carefully by taking into account the oxidation behaviors of these materials.

In addition to these problems, hot environment corrosion, which occurs in the middle-temperature area of an FGM, poses an equally serious problem. Yttria-stabilized zirconia is a commonly used TBC material. However, it has been reported that the stabilizing agent, yttrium oxide, is vulnerable to corrosion by sulphur, sodium, and vanadium, and that this causes the coated layer to peel and drop from the FGM surface. This is a major problem in the development of TBC technology. Considering the possibility that similar problems may occur in the reusable space plane, selection of the materials for the HBFGMs to be used in the plane's fuselage and engines must be made carefully.

2.3 Thermodynamic Stability

It is important for composite materials, including FGMs, that the composite material elements involved be thermodynamically stable in the material boundary region to avoid a compositional change from occurring during use. For example, a (MoSi₂-SiC)/TiAl-system FGM, which is produced by the gas pressure sintering method involving SHS reactions, has a thermodynamically imbalanced phase. However, if this FGM is to be used under HBFGM utilization conditions, it is difficult to maintain the imbalanced phase condition up to super-high-temperatures. Figures 2 and 3 show the results of studying the thermodynamic stability of Hf-system ceramics, one of the most thermodynamically stable ceramics, and TiAl. This study is based on thermodynamic calculations or experiments. According to our calculations, we would expect that these Hf-system ceramics, when combined with TiAl, would be thermally stable at temperatures from room temperature up to 2,000 K. To confirm this estimate, NFGMs each containing TiAl at a ratio of 50 percent by volume were created by the glass capsule hot isostatic pressing (HIP) method, and the materials thus created were analyzed by X-ray diffraction. The analysis showed that HfC-50 vol% TiAl contained small amounts of TiC and HfAl, and that HfB₂-50 vol% TiAl contained TiB₂ and HfAl. For HfO₂-50 vol% TiAl, the analysis detected no reaction products. These results suggest that when combined with TiAl, oxide materials form more stable composite materials than nonoxide materials.

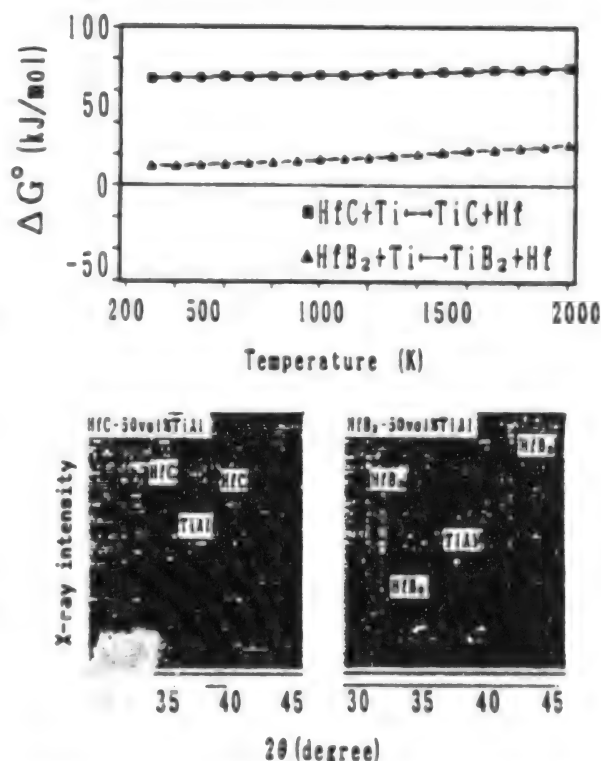


Figure 2. Thermodynamic Stability of Hf-System Nonoxide Materials

And judging from the fact that the volume of reaction products increases in proportion to the absolute value of the variation of product free energy, ΔG^0 , we would expect that the thermal stability of composite materials can be inferred to a certain degree from thermodynamic calculations.

2.4 High-Temperature Strength (Ductility-brittleness transition temperature)

The usefulness of HBFGMs is measured by the temperature to which they can be used reliably. In these HBFGMs, one must take into account the possibility that, even in the ceramic coating, nonelastic deformations may occur on the heat side surface when exposed to a high-temperature environment. There is a high possibility of thermal fatigue damage occurring because of nonelastic deformations on the ceramic layer, or in the composite phase between the ceramic layer and the metallic layer, when the material is subjected to repeated heating-cooling cycles.

To deal with this problem, it is important to study the criteria for FGM design carefully, or, in other words, to balance the heat insulation characteristics with the thermal stress relief characteristics in order to keep the FGMs ceramic-side surface temperature below the ductility-brittleness transition temperature to avoid thermal stress damage. Thus it is important to use ceramic materials whose ductility-brittleness transition temperature is as high as possible and that also have an appropriate thermal expansion coefficient on the high-temperature side of FGMs.

Figure 4 shows the relationship between temperature and antifracture strength for low thermal conductivity oxide ceramics, and for composite ceramics created using these ceramics. All of these ceramic samples were created by sintering at temperatures ranging from 1,200–1,350°C in an Ar

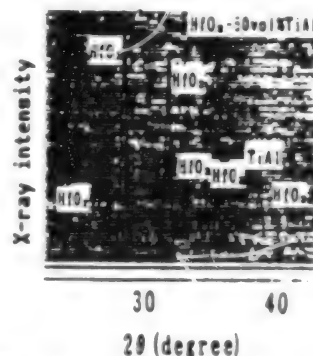
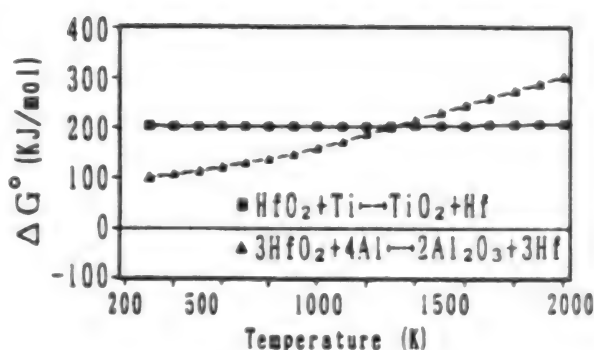


Figure 3. Thermodynamic Stability of Hf-System Oxide Materials

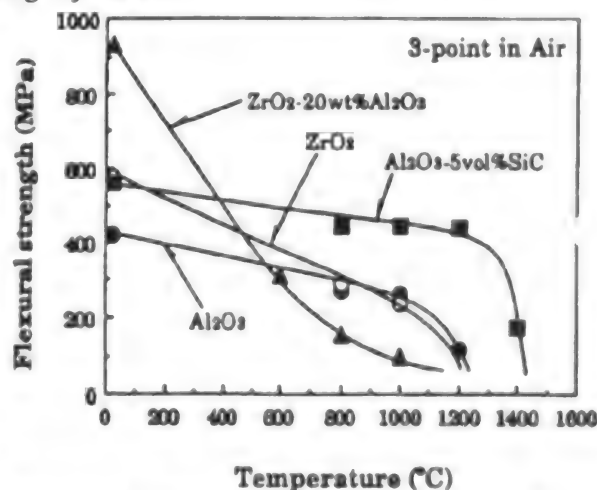


Figure 4. High-Temperature Strength Characteristics of Oxide System Ceramics

environment at pressures ranging from 1,300-1,400 normal atmospheres using the glass capsule HIP method. In general, ZrO_2 (3 mol% Y_2O_3 partially stabilized ZrO_2) ceramics display a substantial deterioration of strength as the temperature increases, despite their comparatively high strength at room temperature. This is because the toughness-improving effects are weakened as the result of a stress induction transformation in the room temperature stabilizing composition when the temperature increase nears the stabilized temperature range of the tetragonal system, a phase that ZrO_2 enters at high temperatures. The comparatively low ductility-brittleness transition temperature is due to the ion bonding characteristics of ZrO_2 ceramics. In contrast, Al_2O_3 ceramics display higher ductility-brittleness transition temperatures than their ZrO_2 -system counterparts, thanks to their strong covalent bonding capability, although they have lower strength at room temperature than ZrO_2 ceramics. The introduction of 5 vol% SiC improves high-temperature strength and produces a higher ductility-brittleness transition temperature. It is believed that this improved toughness is the result of restrained crystal growth, the pinning of dynamic dislocation, and crack deflection.

These ceramic samples were not necessarily sintered under optimum sintering conditions, and their flexural strength is no match for the "champion data" that have been reported to date. The reason it is difficult to optimize ceramic sintering conditions when sintering FGMs is because it is necessary to ensure a balance with the low-temperature side metallic materials, such as Ni-system superalloys or Ti-system alloys. This constitutes a major limiting factor in creating FGMs using currently available powder sintering technology.

3. Material Selection

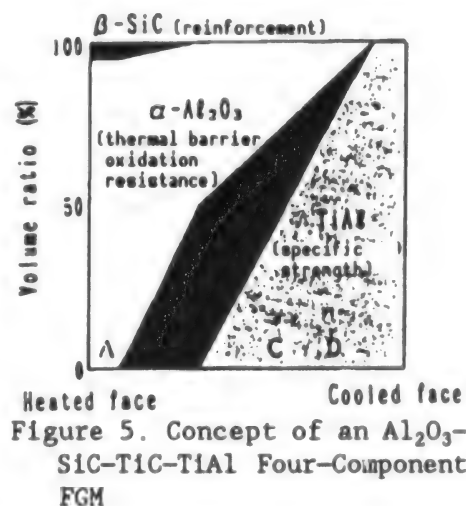
We selected our material combinations for practical utilization by taking into account the various requirements discussed above. As a cooling side (low-temperature side) material, we selected a Ti-Al system intermetallic compound, a material that is attracting international attention for its good high-temperature specific strength (strength/specific gravity), which makes it suitable for use as a high-temperature structural material. In the United States, long fiber-reinforced $\text{Ti}_3\text{Al}/\text{SiC}^f$ (FRIM: fiber-reinforced intermetallics) and grain dispersion-reinforced $\text{TiAl}/\text{TiB}_2^p$ (XD) are regarded as the materials on which the success of the National Aerospace Plane Project hinges. In particular, TiAl has a targeted utilization temperature of 1,250 K, about 130 K higher than Hastelloy X. The use of this material could contribute to raising the surface temperature of FGMs, and, in turn, to lowering the heat transfer rate to the cooling side of these materials. One reason that prompted us to select TiAl was our company's many achievements in research on TiAl component utilization. Table 1 lists the characteristics required for heat-side (high-temperature side) application materials. ZrO_2 and HfO_2 have excellent heat isolation and antioxidation capabilities. However, commonly used stabilized zirconia and stabilized hafnia were dropped from the list of FGMs topmost surface material candidates because of their comparatively high oxygen permeability. MoSi_2 was excluded from the list because of its poor dynamic thermal stability when it is used together with TiAl. Hf-system nonoxide materials were omitted because of their low antioxidation capability,

Table 1. Candidate Materials for Use in the High-Temperature Side of FGMs

	Stabi- lized ZrO ₂	Al ₂ O ₃	Stabi- lized HfO ₂	TiC	HfC	HfB ₂	MoSi ₂	SiC
Thermal protectivity	++	++	++	—	—	—	+	+
Oxidation resistance	++	++	++	—	—	—	++	++
Oxygen permea- tion resistance	—	++	—	+	+	++	++	++
Thermodynamic stability	+-	+	+-	++	+-	+-	—	—
Ambient tempera- ture strength	++	+	+	+	+	+	+	+
Elevated tempera- ture strength	—	+	—	+	+	+	+	++

++: Excellent; +: Acceptable; +-: Under examination
 -: Poor —: Unacceptable

high specific gravity, and the very high cost of their materials. TiC, too, has poor anti-oxidation characteristics. In contrast to these materials, Al₂O₃ has good chemical, thermal, and dynamic characteristics that make it suitable for use as the FGMs topmost surface material. In particular, its dynamic characteristics should be improved by the introduction of a reinforcing material (such as SiC grains or whiskers). When introducing these reinforcing materials, it is important to ensure thermal stability between the TiAl and these materials. Figure 5 shows the concept of a heat-isolating FGM material composition that is regarded as the best attainable using currently available technology. As the hot side topmost surface of the FGM, Al₂O₃ is used because of its heat-insulation, antioxidation, antierosion and resistance to hot environment corrosion capabilities. SiC is used to improve the FGM's dynamic strength characteristics. The TiC layer, as an intermediate layer, is used to prevent mutual reactions between the SiC and TiAl, and it also relieves nonelastic deformations of the FGM in hot conditions. Chemically stable TiC may be used effectively with active silicon-system ceramics or intermetallic compounds to form high-temperature side materials. Photo 1 shows the macrostructure and microstructures of this four-layer FGM.



The use of multi-component materials in an FGM makes it possible for these components to assume different functions, but increasing the material component makes material design more complex. However, this means that there is greater freedom for macroproperty control. For example, in this four-layer FGM, freedom in controlling the thermal and mechanical properties of the topmost surface material ($\text{Al}_2\text{O}_3\text{-SiC}$) is provided by changing the amount of SiC introduced, and changing the amount of TiC and its distribution pattern equally increases freedom in controlling the macroproperties of the entire FGM. The development of this multicomponent FGM will lead to the realization of FGM design using the reverse problem analysis design method, the utmost goal in FGM design efforts. This method calls for obtaining an ideal property distribution to achieve a targeted function by calculation, and to determine the materials to be used, the shape, compositional distribution and microstructure.

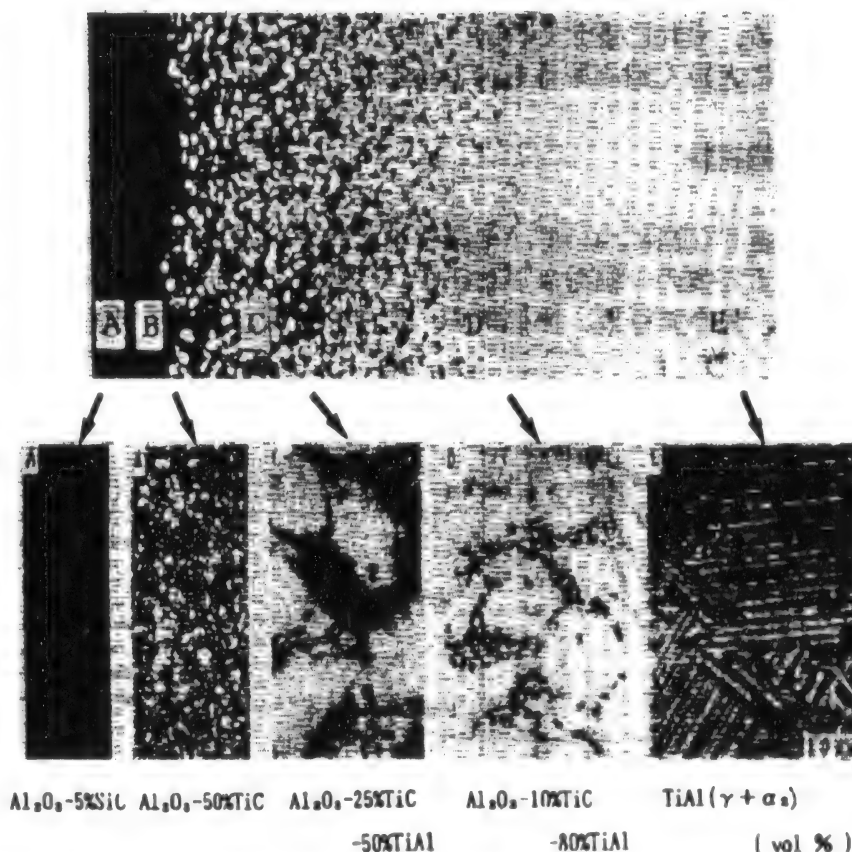


Photo 1. Macrostructure and Microstructures of an $\text{Al}_2\text{O}_3\text{-SiC-TiC-TiAl}$ Four-Component FGM

4. Multicomponent FGMs

In this section, we will discuss the results of numerical analyses of the macroproperties (heat insulation characteristics, thermal stress alleviation characteristics) a number of four-component FGMs. First, nine-composite material NFGMs were created for use in analyses of their density, flexure strength, elastic coefficient, thermal expansion coefficient, thermal diffusivity, and the effect of temperature on specific gravity for temperatures between room temperature and $1,400^\circ\text{C}$. Using these data, we analyzed the thermal conductivity and elastic thermal stress of those FGMs having different material compositional distribution patterns (Figure 6), while taking material nonlinearity into account. To simplify analytical calculations, a multicomponent (four component) FGM will be handled as a macroscopic two-component FGM,

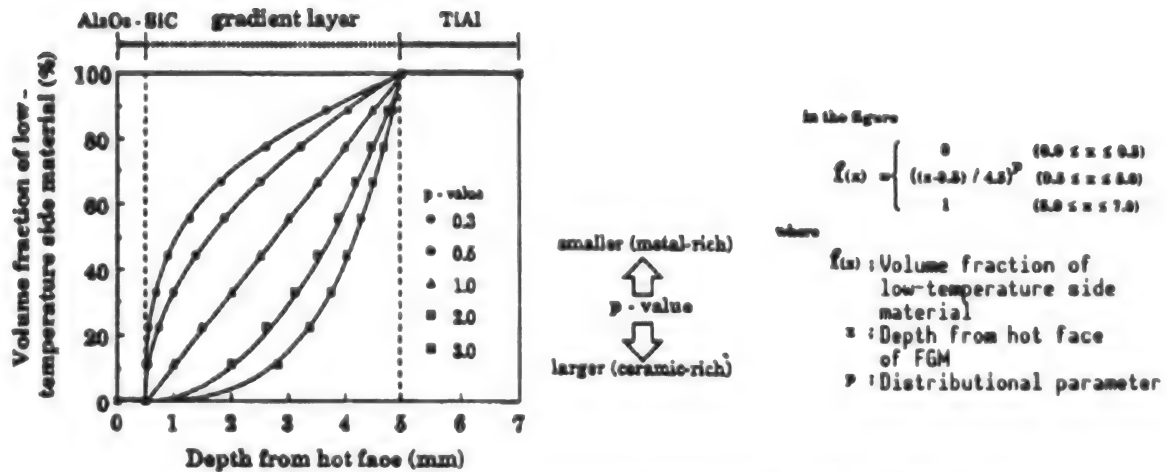


Figure 6. Compositional Distributions of FGMs Used for Heat-Related Characteristics Analysis

and will be expressed by the compositional distribution function used for common two-component FGMs in the following discussion.

By assuming that a two-component FGM has a metallic volume rate of V_B , and that V_B at the starting point of the TiAl component in this four-component FGM is $V_{B/t}$, the volume rates for each material component in the FGM can be expressed as:

$$V_{Al_2O_3} = \begin{cases} 0.95 - 0.9V_B & (0 \leq V_B \leq V_{B/t}) \\ 1 - V_B & (V_{B/t} \leq V_B \leq 1) \end{cases} \quad (16)$$

$$V_{SiC} = \begin{cases} 0.05 - 0.1V_B & (0 \leq V_B \leq V_{B/t}) \\ 0 & (V_{B/t} \leq V_B \leq 1) \end{cases} \quad (17)$$

$$V_{TiC} = \begin{cases} V_B & (0 \leq V_B \leq V_{B/t}) \\ 1 - V_B & (V_{B/t} \leq V_B \leq 1) \end{cases} \quad (18)$$

$$V_{TiAl} = \begin{cases} 0 & (0 \leq V_B \leq V_{B/t}) \\ 2V_B - 1 & (V_{B/t} \leq V_B \leq 1) \end{cases} \quad (19)$$

By expressing nondimensional distance as ξ , V_B can be given as follows, which is similar to the case of using a compositional distribution function in dealing with common two-component FGMs.

$$V_B = \begin{cases} 0 & (0 \leq \xi \leq \xi_1) \\ \left(\frac{\xi - \xi_1}{\xi_2 - \xi_1} \right)^p & (\xi_1 \leq \xi \leq \xi_2) \\ 1 & (\xi_2 \leq \xi \leq 1) \end{cases} \quad (20)$$

One feature of multicomponent FGMs is that the value of $F_{B,t}$ in the above compositional function (in this case $V_{B,t} = 0.5$) can be handled as a parameter.

Our analytical calculations were conducted by using a $30 \times 7^t \text{ mm}\phi$ FGM by regarding it as an axial symmetrical body of rotation. The analysis involved giving a thermal load of $q = 2.25 \text{ MW/m}^2$ to the surface of the high-temperature surface of the FGM, and keeping heat transfer in the cooled side constant by maintaining the temperature at 900°C by forced cooling. As for stress boundary conditions, no clamping was applied during fabrication. For bonding, a uniaxial load was applied after the temperature was raised to a desired level to facilitate diffusion bonding, and the FGM samples were then cooled by clamping dislocation in the bonded plane's axial direction. Axial dislocation, too, was clamped under a steady state thermal load condition.

Figure 7 shows the effect of material surface temperature and effective thermal conductivity on compositional distribution based on data obtained from a thermal conductivity analysis. The analysis was conducted by maintaining the heat flux on the FGM sample surface at a constant level to make analysis conditions the same as the heating conditions adopted in the high temperature difference (radiation heating) test, which was aimed at measuring effective thermal conductivity. The figure clearly shows that as the p value increases, effective thermal conductivity decreases, raising the temperature on the sample surface. The effective thermal conductivity stood at about 20 W/mK at $p = 0.5$, and at 12 W/mK at $p = 2.0$ —displaying a comparatively good heat insulating capability.

The results of the thermal stress analyses are shown in Figures 8 through 10. These figures give the maximum values for specific stress (maximum principal stress/fracture strength) within these five FGM samples (upper and lower surfaces included), and on the sample surfaces, under normal temperature difference conditions. These samples have different compositional distribution, as shown in Figure 6. These specific stress values were obtained through elasticity analysis (nonelastic deformations are not taken into account), and the break-resistant strength is used to measure fracture strength. This means that the

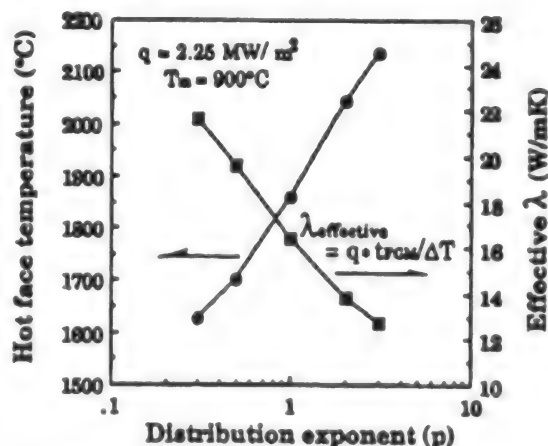


Figure 7. Effect of Compositional Distribution and Surface Temperature on Effective Thermal Conductivity in FGMs

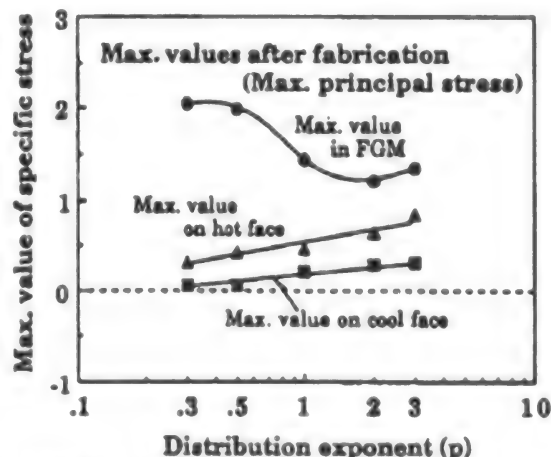


Figure 8. Relationship Between Maximum Stress and Material Compositional Distribution (Postfabrication residual stress)

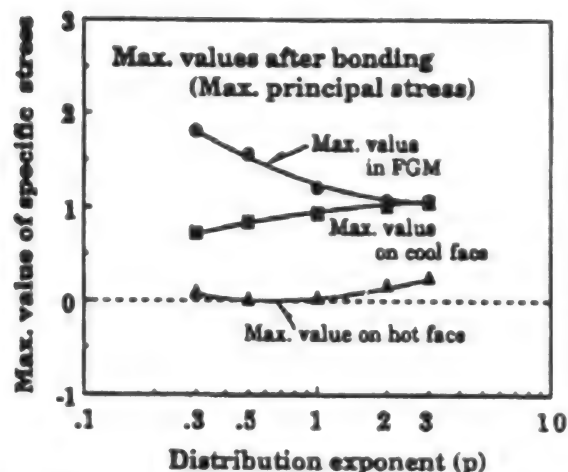


Figure 9. Relationship Between Maximum Specific Stress and Material Compositional Distribution (Postbonding residual stress)

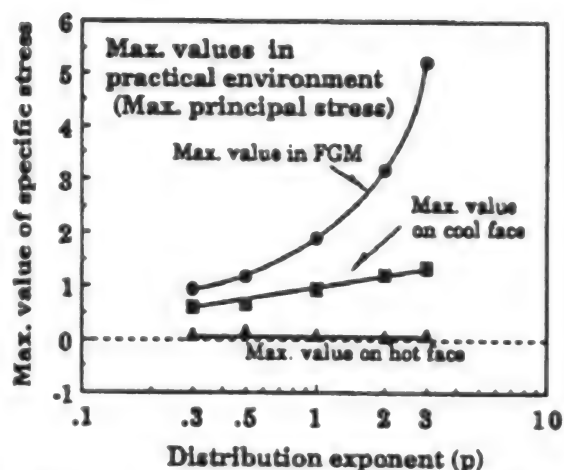


Figure 10. Relationship Between Maximum Specific Stress and Material Compositional Distribution (Thermal stress in steady state temperature difference environment)

specific stress value of 1.0 does not necessarily represent the critical condition of thermal stress fracture.

The post-fabrication residual stress analysis in these samples showed that the generation point for maximum specific stress is located in the outer rim areas of the ceramic layer at a depth slightly beneath the topmost surface of the layer, and extending toward the metallic layers. This is true for all the different compositional distribution FGMs. As for residual stress on the upper and lower surfaces of an FGM, specific stress is higher in the ceramic layer side than the other side, and the stress level increases in proportion to the compositional distribution index (in proportion to an increase in the ceramic content). Both on the surface and inside an FGM, the maximum specific stress generally is dominated by radial stress and circumferential stress; other stress elements (axial-direction stress, shearing stress) are far smaller than radial and circumferential stresses. Figure 8 shows that the compositional distribution index value suitable for fabricating an FGM having small maximum specific stress and high reliability is 2.0. The results of an experiment using the FGM samples that were fabricated by the gas pressure sintering method indicated, however, that a highly reliable FGM could be obtained at p values lower than 0.5. At values higher than 1.0, conspicuous damage caused by thermal stress was observed. Such damage originated in the topmost surface of the ceramic layer in all samples involved. The results of these experiments correspond to the results of analysis of the effects of material surface stress. In a previous report, we demonstrated that in $(\text{MoSi}_2\text{-SiC})/\text{TiAl}$ -system FGMs, it is possible to determine the residual stress generated within them after the fabrication by analyzing radial stress on the topmost surface of the high-temperature side. It has yet to be determined whether this analytical method is applicable to FGMs composed of varied material systems and material structures. We believe, however, that it could be used effectively as a means of inferring a tendency for use in material design.

We also analyzed the maximum specific stress levels within an FGM and on its surface to study post-bonding residual thermal stress on the cooled structure, and to examine the thermal stress generated under a steady state temperature difference environment. In all the different heat environments involved in our experiment, maximum specific stress was measured mostly within FGMs. Between the two surfaces of an FGM, a larger stress was measured in the low temperature side of the material, which is the side that comes into contact with the cooled structure. In the ceramic-rich layer ($p = 2.0-3.0$) in particular, the post-bonding residual stress increases to a level matching the maximum specific stress measured within the entire FGM sample. As described above, the results of this stress analysis do not take into account the effect of nonelastic deformations, and because of this it is believed that these stress values are higher than the actual values, particularly in the low temperature side. However, stress analysis using Meese's [phonetic] equivalent stress, a method popularly used with metallic materials, obtained results similar to the above results. The large stress on the surface of the low-temperature side is believed to be caused by the external clamping effect on the bonded boundary.

Figure 11 shows the relationship between maximum specific stress and compositional distribution under various heat conditions. The analysis, the results of which are shown in the figure, involves measuring the maximum specific stresses on both the hot and cooled surfaces. We are not sure to what extent this analytical method is applicable. If these analysis results are reliable, it can be said that the thermal stress alleviation capability of an FGM increases when the compositional distribution index declines—or when the metallic content increases. However, in this case the effective thermal conductivity of the material increases, and it becomes necessary to take into account the degeneration of the FGM's heat insulating capability. In a material in which the compositional distribution index is lower than 1.0, such as FGMs with a high metallic content, the utilization of suitable bonding technology is most important when it is bonded onto a cooled structure for the reasons discussed above.

5. Conclusion

An FGM has many parameters that must be controlled properly. For those FGMs to be used in aviation and space applications, in particular, it is very difficult to attain material optimization because of the many conflicting requirements. Under these circumstances, it is important to accumulate reliable data. And this, in turn, makes it necessary to promote the efficient

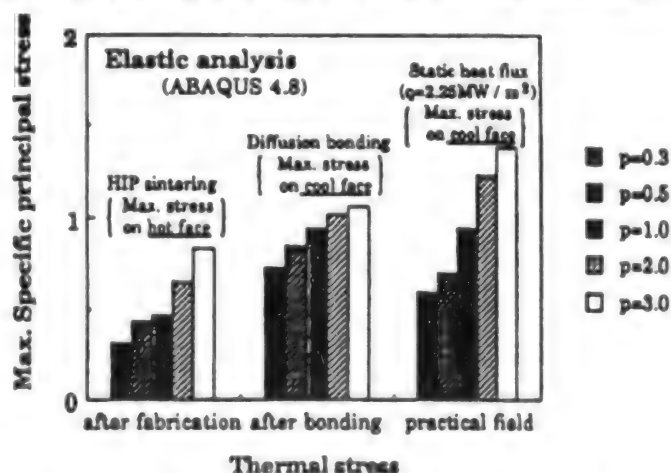


Figure 11. Relationship Between Values for Maximum Specific Stress and Compositional Distribution in Various Thermal Environments

creation of test samples using inferred data obtained by analytical calculations and the confirmation tests of these samples.

The next goal of our current research is the selection of suitable materials based on the results of material characteristic evaluation tests, and the confirmation of the effectiveness of our analytical methods. As the first step in these efforts, we will evaluate the effective thermal conductivity and heat stress alleviation characteristics in a radiation-heated, high-temperature difference environment. These evaluations will be conducted in the near future at the National Aerospace Laboratory. We intend to establish a characteristic inferring method with a higher degree of reliability by having the results of these evaluations reflected in the analytical method discussed above. As the second step, an evaluation of the heat insulation characteristics of these selected materials in a heat transfer environment, and an evaluation of thermal stress alleviation characteristics within a high-temperature gas flow environment also are scheduled to be conducted at the laboratory in the current fiscal year [FY 1991]. In order to obtain meaningful data in these evaluations, it is important to conduct a thermal transfer evaluation by taking the thermal transfer rate into account. It also is important to clarify the relationship between an FGM's overall heat transfer coefficient (λ_e/t_{FGM}) and the cooled-side heat transfer rate. To demonstrate that the heat insulation problem and the thermal stress problem are related to each other, it will be necessary to identify the relationship between the cooled-side thermal transfer rate and thermal stress. This can be accomplished by using the overall heat transfer coefficient, the thickness of the FGM, and compositional distribution as parameters.

Our current research has been conducted as part of the comprehensive research sponsored by the Science and Technology Agency which is aimed at improving the fundamental technology to develop FGMs for thermal stress alleviation applications.

Fabrication Process for Actively Cooled FGM Plate

926C0014G Tokyo FGM '91 in Japanese 8-9 Oct 91 pp 235-243

[Article by Chikara Fujiwara, Satoshi Nagata, and Shinichiro Kiyotoh, Nagoya Aerospace System Works, Mitsubishi Heavy Industries, Ltd.; Akinaga Kumakawa and Masayuki Niino, Kakuda Research Center, National Aerospace Laboratory; and Manabu Tamura and Tamako Hyakubu, Steel Research Center, NKK Corp.]

[Text] Abstract: A fundamental study on brazing of a functionally gradient material (FGM) fabricated by the thin sheet lamination method to metal plate was carried out to develop the fabrication process of an actively cooled panel with an FGM. The FGM is designed to reduce thermal stress in service where the top surface is heated heavily and the bottom surface is cooled with coolant resulting in a large temperature difference between both surfaces. The FGM is constituted of zirconia and nickel, and the composition is varied gradiently from the top surface to the bottom surface. Thus, a layer in the FGM is different in coefficient of thermal expansion from any other layer. Consequently, the FGM changes inherently in shape as its temperature varies uniformly, such as in the case of brazing. Therefore, an investigation was begun to evaluate the flatness difference of the FGM plate at room temperature and at brazing temperature. Then, brazing parameters were optimized to establish the fabrication process for an actively cooled panel with FGM.

1. Introduction

There have been active efforts to develop functionally gradient material (FGM) fabrication technologies, and thus the importance of developing evaluation technologies for FGMs has been mounting. Among those evaluation methods developed to date, a method that involves heating the top surface of an FGM by a powerful arc lamp and cooling the bottom surface to produce a large temperature difference in the material's thickness direction is attracting attention as the most promising method to simulate actual utilization conditions. This method requires an FGM sample to have an active cooling structure, and this in turn calls for bonding the FGM sample to a metallic plate. However, little progress has been made in the bonding technology. Our current research is aimed at identifying problems encountered in FGM fabrication processes (particularly the brazing process), and at studying measures to deal with these problems to fabricate an FGM cooling plane by the thin-film lamination method.

2. Cooling Structure in FGM Cooling Plate

Two ideas are being studied as possible cooling structures in an FGM cooling plate (Figure 1). Idea A calls for bonding an FGM plane directly to a coolant duct structure with the plate serving as the lid of the ducts, while idea B involves bonding an FGM plate by a cooling structure plate. In our research, idea B was adopted largely because of our past experience in cooling structure plate development and fabrication. Figure 2 shows the outer appearance of the FGM cooling plate that has been developed based on idea B.

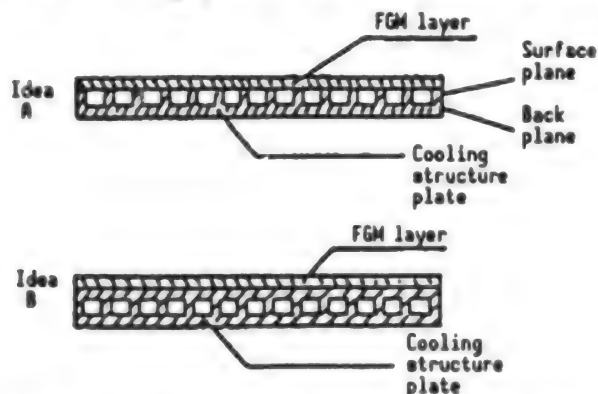


Figure 1. Sectional Views of Cooling Structures

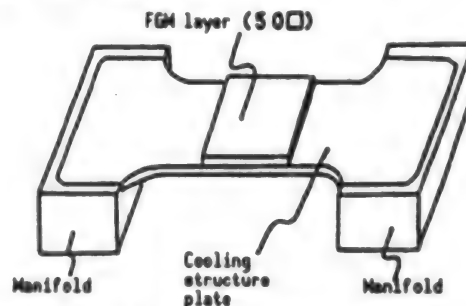


Figure 2. FGM Cooling Plate Fabricated by Thin Film Lamination Method

To bond an FGM plate to a metallic cooling structure plate, fused welding, diffusion bonding, or brazing can be used. In our experiment, we used brazing because of its ability to produce a bond between two planes with relative ease.

3. Basic Experiment for Brazing

The FGM used in our research was composed of six layers of ZrO_2 100%, ZrO_2 80%-Ni20%, ZrO_2 60%-Ni40%, ZrO_2 40%-Ni60%, ZrO_2 20%-Ni80%, and Ni100%. It was created by the thin film lamination method, which is based on the doctor blade method. The outermost layers of the ZrO_2 100% and Ni100% were formed by the plasma thermal spraying method and by the electroforming method, respectively. In this FGM, a ceramic material and a metallic material with different thermal expansion coefficients were composited microscopically and in an imbalanced composition, and the mixture ratio of the two elements changes in thickness direction. This makes the FGM warp because of differences in the thermal expansion rates of each of these layers when the entire surface of the material is heated for brazing. This creates the following problems when an FGM is brazed to a metallic cooling structure plate:

(1) It is difficult to attain an optimum brazing clearance over the entire brazing face.

(2) There is a possibility that cracks could develop within the brazed layer or within the FGM after brazing was completed because of the generation of a substantial level of thermal stress within them as a result of restrained free thermal deformations in the FGM when the material temperature drops.

To deal with these problems, we conducted a basic experiment that involved brazing two types of tiny FGM plates—one with an Ni100% layer and the other without the layer—to a metallic plate. The results of this experiment are as follows.

3.1 FGM With an Ni100% Layer

We conducted a brazing test using a five-layer FGM (Figure 3), including an Ni100% layer, and a 1.6-mm thick Inco 617 plate. The brazed face of the Ni100% plate underwent surface grinding, and the thickness ranged between 3.2 and 3.6 mm. The FGM sample measured 30 mm long x 8 mm wide, while the Inco plate it was 40 mm long x 16 mm wide x 1.6 mm high. Brazing was conducted using a BNi-2(Ni-7Cr-3Fe-3B-4.5Si) brazing filler sheet at 1,030°C for 10 minutes at a pressure below 5×10^{-4} Torr.

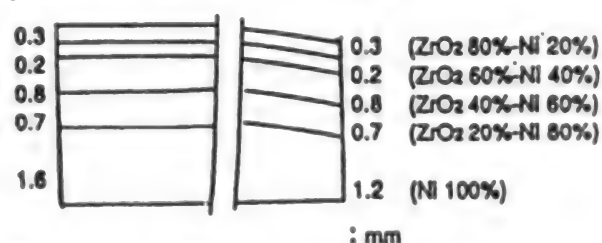


Figure 3. FGM Sample Including an Ni100% Layer for Use in Basic Brazing Experiments

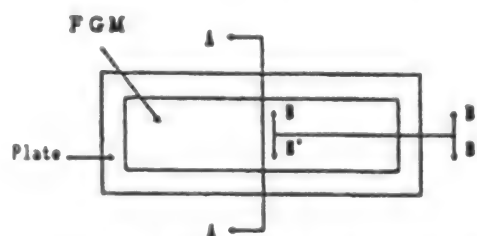


Figure 4. Sectional Observation Positions and Angles Adopted in Brazed FGM/Inco 617 Plate Combination

After brazing was completed, we studied the filler's wettability, brazing clearance, and other aspects through external and sectional observations. Figure 4 illustrates the positions and angles adopted for sectional observation. The typical macroscopic and microscopic sectional structures of the brazed sections are shown in Figure 5. The results of these observations are as follows:

(a) Good brazing results were obtained. There was evidence of good filler flow, and the satisfactory formation of a fillet.

(b) The brazing caused a concave cavity in the Inco 617 that warped toward the FGM side. The degree of concavity measured 0.15 mm over 30 mm of distance. The brazed side of the FGM's Ni100% layer remained flat. The thickness of the filler was measured at 0.06 mm in the middle of the brazed length of 30 mm and at 0.20 mm in the rim areas with a difference between them of 0.14 mm. The value of this difference almost coincides with that of the concave cavity, which was 0.15 mm. These results indicate that the flat surface of the FGM warped toward the flat Inco 617 plate when the brazing temperature increased, and that the warp returned to its normal flat state during the cooling process by pulling the brazed metallic plate toward the FGM side.

(c) After brazing was completed, we found that many voids like the one shown in Figure 5 had been formed within the Ni100% layer (electroformed layer). And when the FGM was subjected to a brazing heat cycle within a vacuum furnace, blister-like formations were produced on the Ni100% layer surface (Figure 6).

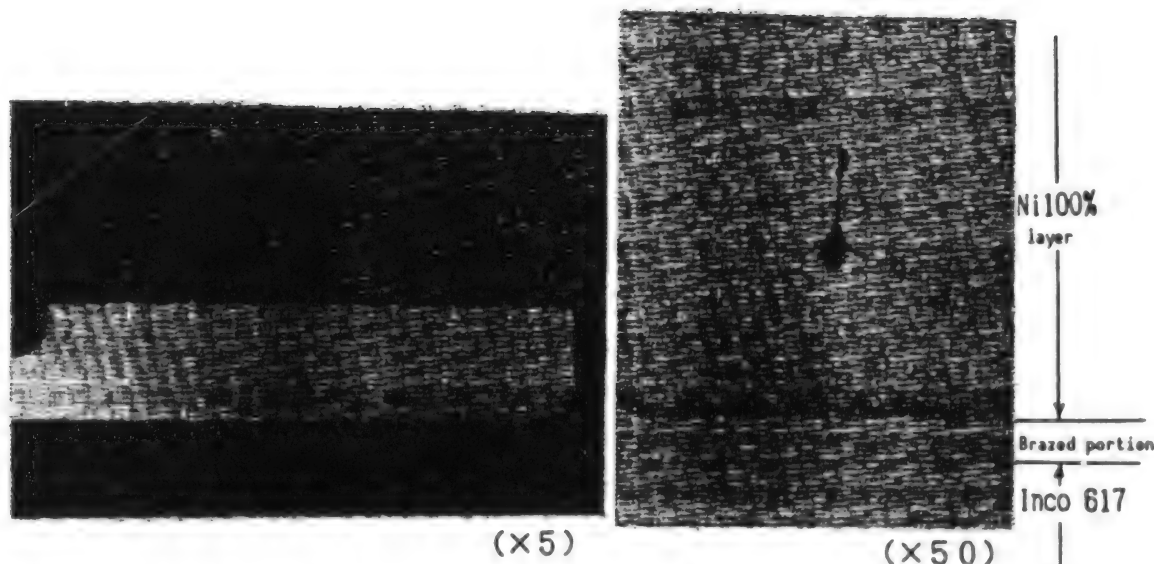


Figure 5. Sectional Structures of a Brazed Ni100% Layer FGM/Inco 617 Plate Combination

These results indicate that Ni electroforming conditions have yet to be optimized. They also reflect the difficulty involved in creating an Ni electroforming layer that is not affected by brazing heat.

These results indicate that in order to attain an optimum clearance level in brazing an FGM sample to a metallic plate, the shape of the FGM sample must be adjusted to make sure that it has flat brazing surface at the brazing temperature. In addition, it is important to optimize the electroforming conditions to create an Ni100% layer that is little affected by brazing heat, or to develop other methods to create such an Ni100% layer.

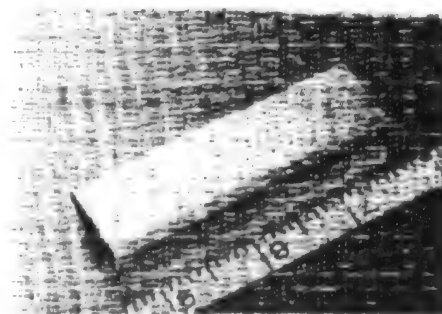


Figure 6. Outer Appearance of an Ni100%, Five-Layer FGM Sample That Has Undergone a Brazing Heat Cycle

3.2 FGM Having No Ni100% Layer

We also conducted an experiment in which a four-layer FGM having no Ni100% layer was brazed to a 1.6 mm thick Inco 617 plate (Figure 7). The FGM was created by hot pressing at 1,200°C and cooling the pressed sample to room temperature after removing the stress from inside the sample. This made it possible to create a sample having a uniform thickness.



Figure 7. Four-Layer Structure of No-Ni100%-Layer FGM Sample for Use in Brazing Experiments

At room temperature the sample plane had a concave warp in the high Ni content side (brazing face side). The sample measured 40 mm long x 10 mm wide x 2.35 mm high, while the Inco 617 plate was 64 mm long x 20 mm wide x 1.6 mm high. A BNi-5(Ni-19Cr-10Si) sheet was used as the brazing filler, and brazing was conducted at 1,160°C for 5 minutes at a pressure less than 5×10^{-4} Torr. The outer appearance and the sectional structures are shown in Figures 8 and 9. The results of the experiment are as follows.

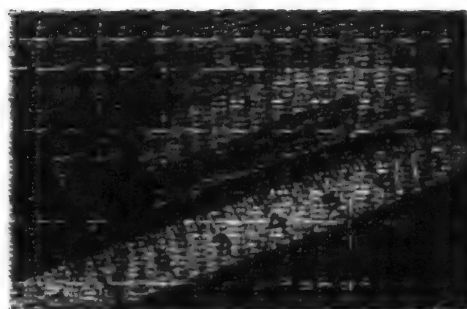


Figure 8. Outer Appearance of Brazed No-Ni100%-Layer FGM/Inco 617 Plate Combination

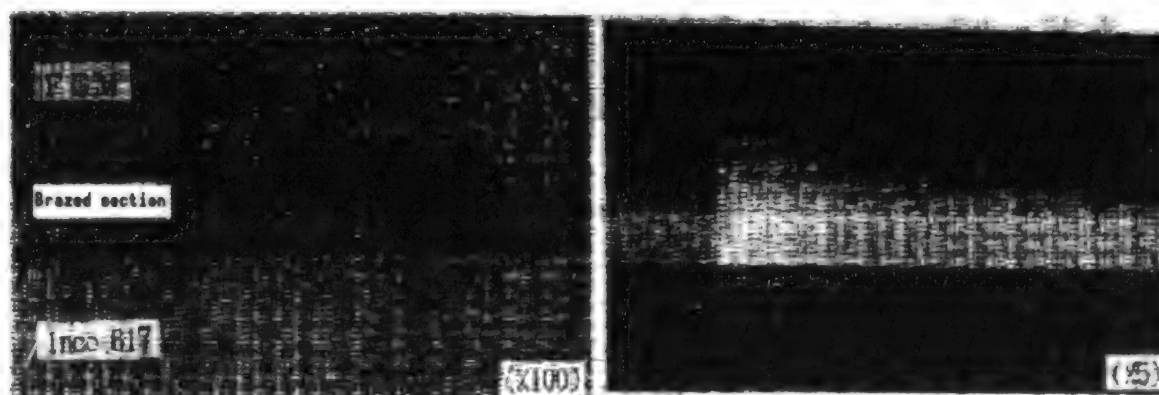


Figure 9. Sectional Structures of a Brazed No-Ni100%-Layer FGM/Inco 617 Combination

(a) The brazing face of the FGM (ZrO_2 40%-Ni60%) displayed comparatively poor wettability against the brazing filler, and the formation of a fillet was inadequate. However, comparatively good bonding was achieved, and no major defects were found in the brazed section.

(b) A warp was observed in the brazed FGM-Inco 617 combination with the degree of warp amounting to 0.7 mm over the Inco 617's length of 64 mm (Figure 10). In terms of FGM's length of 40 mm, this warp amounts to 0.3 mm, almost corresponding to the degree of warp in the FGM before it was brazed and the brazing filler's clearance

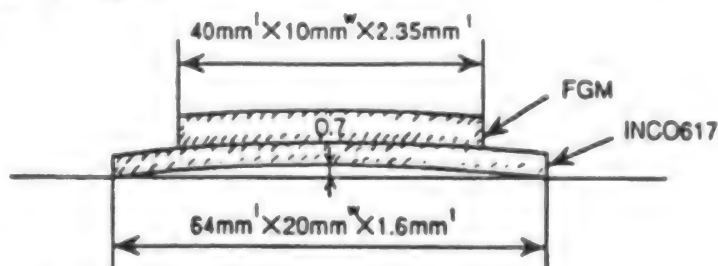


Figure 10. Sectional View of the Structure of the Brazed Section of a No-Ni100% Layer FGM/Inco 617 Plate Combination

was almost uniform. These observations lead us to conclude that the surface of the FGM became nearly flat when heated to brazing temperature, and then returned to its original shape when the brazed FGM-Inco 617 plate combination was cooled, thereby causing a concave deformation in the Inco 617 plate.

(c) No structural defects, including cracks, were found in the brazed section or in the FGM, indicating that the brazed combination withstood the thermal stress generated during the cooling process.

From these observations, we determined that good brazing results can be obtained without an Ni100% layer. As a method to create an Ni100% layer, we studied the possibility of using an Ni sheet in place of the electroforming method, as discussed in section 3.1, by brazing the no-Ni100% layer FGM to an Ni sheet. This was done by inserting an 0.2 mm high Ni sheet between the FGM and the Inco plate, and by brazing under the same conditions adopted for brazing the Ni100% layer FGM. A sectional view of the brazed section is shown in Figure 11. Compared to the case (Figure 9) where there was no such insertion, structural defects resulting from brazing are less conspicuous, and an improvement is noticed in fillet formation, contributing to better brazing results. Based on these results, it can be said that for the formation of an Ni100% layer, good results can be obtained by brazing a no-Ni100% layer FGM to the cooling structure via an Ni sheet. Based on these findings, an experimental, actual-sized FGM panel was fabricated by inserting an Ni sheet.

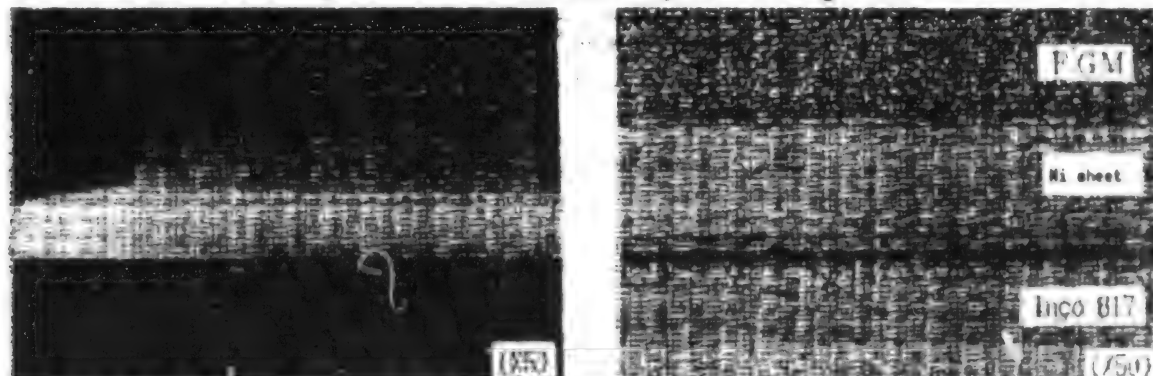


Figure 11. Sectional Structural View of the Brazed Section of a No-Ni100% Layer FGM/Ni Sheet/Inco 617 Plate Combination

4. Testing of Experimental FGM Cooling Panel

4.1 Brazing Test of Actual-Sized FGM

The size of an actual FGM plate that is to be used for brazing to an FGM cooling panel measures 44 mm x 44 mm. This is larger than the FGM plates used in the basic brazing test. It was feared that this larger size would cause structural defects like cracks in the brazed section, because of the larger and more complicated nature of the thermal stress between the FGM plate and the cooling structure panel. So we conducted another brazing test involving the brazing of an actual-sized FGM plate to a SUS 304 plane measuring 100 mm long x 50 mm wide x 3.1 mm high prior to fabricating an experimental FGM cooling panel.

The brazing was conducted using BNi-2 as a brazing filler at 1,030°C for 10 minutes and at a pressure less than 5×10^{-4} Torr. Figure 12 is a sectional view of the brazed section. In the center of the brazed stripe a eutectic phase as the solidification phase is observed on the stripe, and many pore-like

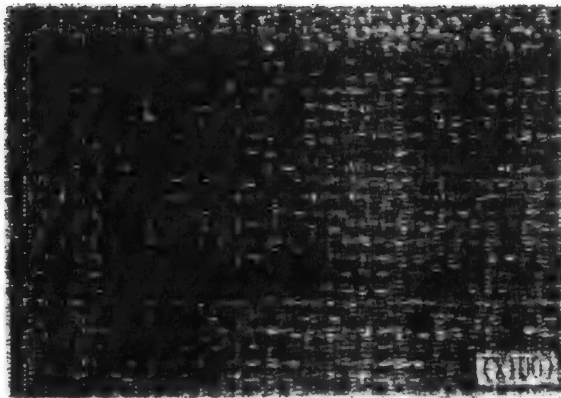


Figure 12. Sectional Microscopic Structural View in the Brazed Section of an Actual-Size FGM/SUS 304 Plate Combination

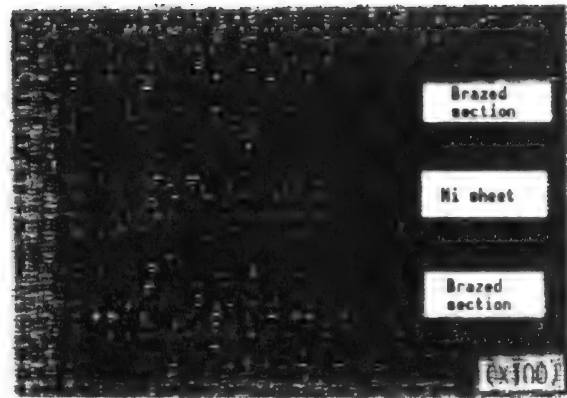


Figure 13. Microscopic Sectional Structural View of Liquid Phase Diffusion Brazed Section in an Actual-Sized FGM/SUS 304 Panel Combination

structural defects can be found within the eutectic phase. These defects are believed to be the result of the generation of thermal stress in the brazed section when the temperature begins to fall after the completion of brazing, and when the eutectic phase is still in a liquid state. This stress causes cracks—and these develop into pore-like defects—in the low strength liquid phase eutectic portion.

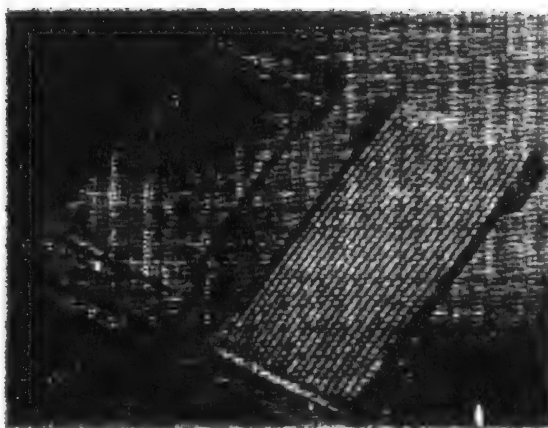
To prevent this defect, we tried liquid phase diffusion brazing in which the faces of the brazed material are kept at brazing temperature for a long time so that elements such as B and Si, which lower the melting point within the brazing filler material, will diffuse into the parent materials, thus promoting isothermal solidification to remove the liquid phase completely. Except for the fact that the diffusion time was extended to five hours, all other brazing conditions were the same as the conditions described above. Figure 13 shows the sectional structural view of the liquid phase diffusion bonded section. Neither the eutectic phase nor the pore-like defects visible in Figure 12 are present.

These results indicate that brazing an FGM plate to an FGM cooling panel can be conducted effectively by the liquid phase diffusion method, which involves the isothermal solidification of the liquid phase material.

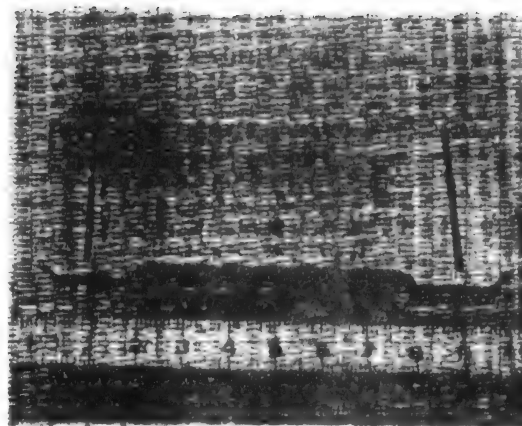
4.2 Experimental Fabrication of FGM Cooling Structural Panel

Based on the data obtained through the experiments described above, we fabricated an FGM cooling panel using the following procedure:

(1) A cooling structure panel was fabricated by brazing a grooved top surface panel (Figure 14(a)) to a bottom panel containing coolant pipes. Microbrazing No. 150 (Ni-15Cr-3.5B) was used as a brazing filler. Brazing conditions were 1,075°C for five hours at a pressure lower than 5×10^{-5} Torr (first brazing stage).



(a) Prior to brazing (top surface panel and bottom surface panel)



(b) After brazing

Figure 14. FGM Cooling Panel

(2) A SUS 304 cooling structure panel, SUS 304 manifolds, an Ni sheet, and an FGM plate were then brazed using BNi-2 as a brazing filler. Brazing conditions were 1,030°C for five hours at a pressure lower than 5×10^{-5} Torr (second brazing stage) (Figure 15). The Ni plate had a thickness of 2.0 mm, a value that had been predetermined by calculation. The FGM used in this experiment had been created experimentally, and the material compositional distribution—which is shown in Figure 16—was adopted arbitrarily without calculation.

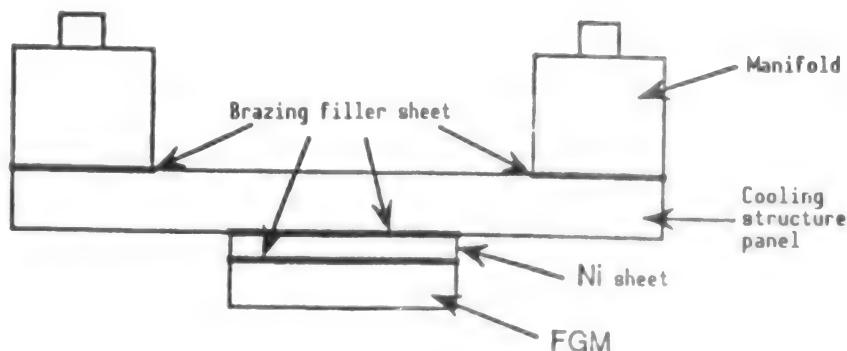


Figure 15. Two-Stage Brazing in Fabrication of an FGM Cooling Panel

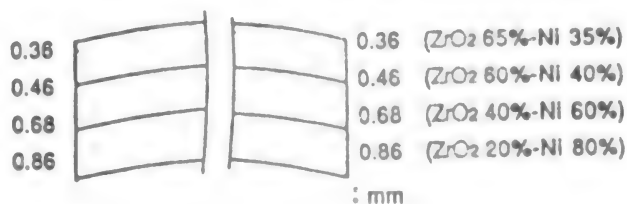


Figure 16. FGM Sample for Brazing to an Experimentally Fabricated FGM Cooling Panel

The outer appearance of the FGM/-cooling panel combination is shown in Figure 17, and a sectional view of the brazed section is given in Figure 18. No cracks or other structural defects caused by the thermal stress generated during the post-brazing cooling process can be seen in the FGM plate and the brazed section. As for the quality of brazing, in part of the brazed section between an FGM and an Ni sheet there is a eutectic phase where the brazing clearance is larger, and some pore-like structural defects can be observed within the phase. The other brazed sections are free from the eutectic phase and from pore-like defects.

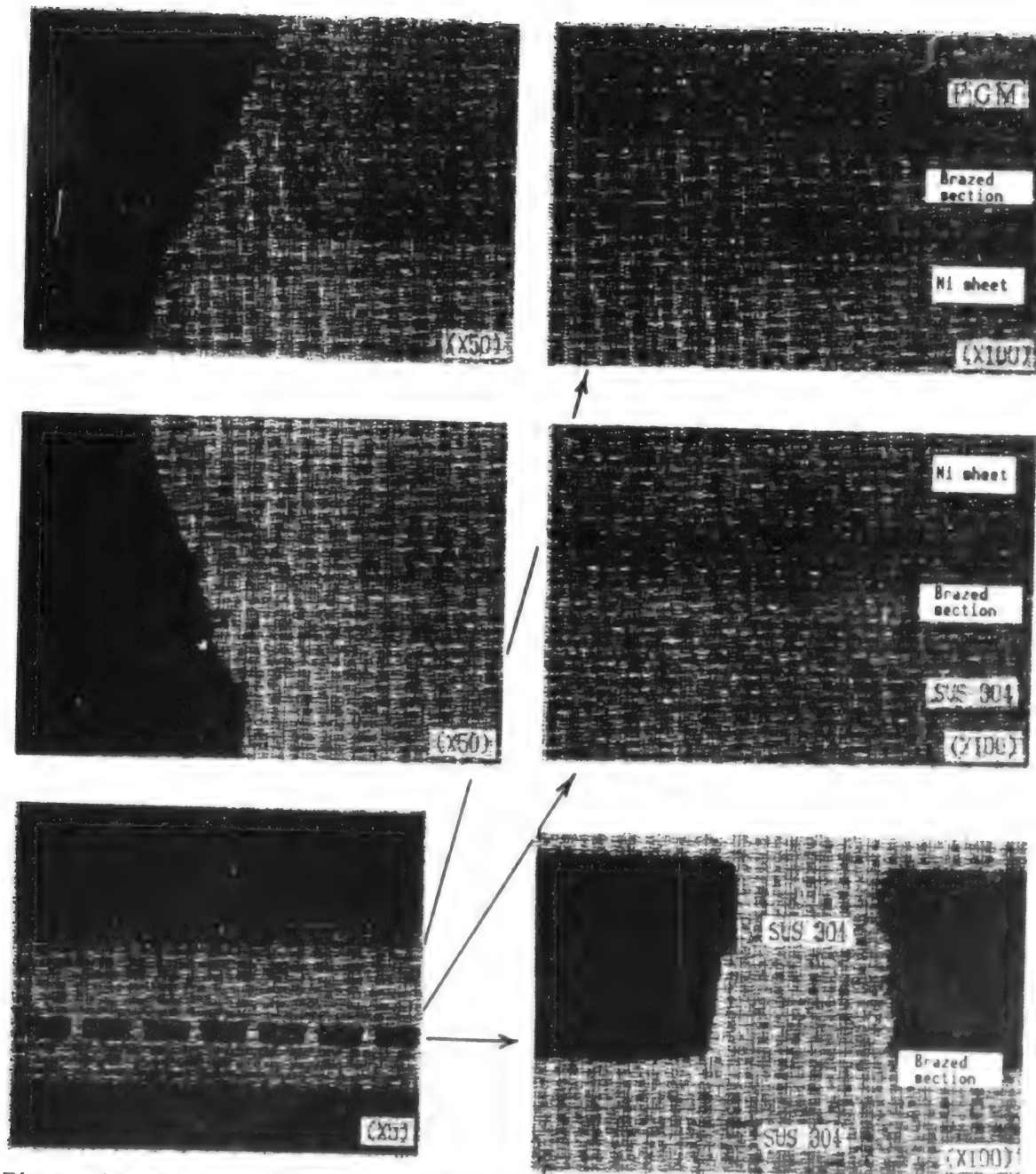


Figure 18. Sectional Structural Views of the Brazed Sections of an Experimentally Fabricated FGM Cooling Panel

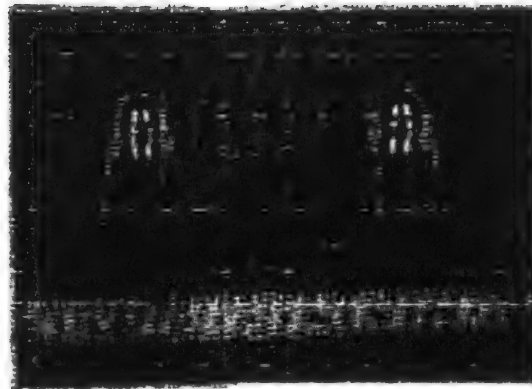
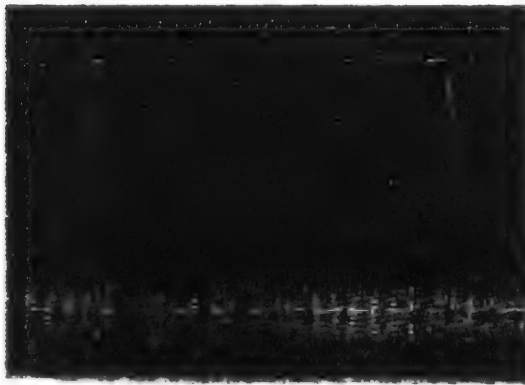


Figure 17. External Appearance of an Experimentally Fabricated FGM Cooling Panel

These results lead us to conclude that a basic fabrication process for an FGM cooling panel based on the thin film lamination method has been established, although more study is necessary for some aspects, such as the length of the diffusion process.

5. Conclusion

We conducted brazing experiments aimed at establishing an FGM cooling panel fabrication technology using the thin film lamination method. The experiments demonstrated that:

(1) In order to ensure a brazing clearance in brazing an FGM plate to a metallic plate, the FGM plate must be formed into a shape that will produce a flat surface when it is heated to brazing temperature.

(2) In brazing an FGM plate to a metallic plate via an Ni brazing filler, pore-like defects tend to appear within the eutectic phase formed between the plates. An effective way to prevent such defects from forming is to use liquid diffusion brazing for isothermal solidification of the filler at brazing temperature. We will continue our research to create FGM samples that are suitable for use in high-temperature difference tests based on the results of our design calculations.

Bonding of FGM to Actively Cooled Panel

926C0014H Tokyo FGM '91 in Japanese 8-9 Oct 91 pp 245-251

[Article by Yukio Yamaoka, Kazuyoshi Ninomiya, Katsuaki Kosaka, and Seiji Ishimoto, Aerospace Division, Nissan Motor Co.; and Masayuki Niino and Akinaga Kumakawa, Kakuda Research Center, National Aerospace Laboratory]

[Text] **Abstract:** In real condition tests, a functionally gradient material (FGM) must be actively cooled to generate a high-temperature gradient in its depth direction. To assure proper cooling between tests, bonding of the FGM and an actively cooled panel is very important. So thermal/structural analyses and fundamental experiments for C-SiC FGM on a C/C composite brazed with an actively cooled panel were performed. Two- and/or three-dimensional transient thermal/structural analyses were performed in the conditions of brazing and high-enthalpy gas exposure test. And optimization of brazing parameters were also investigated for the fabrication of an actively cooled panel with FGM.

1. Introduction

Current efforts to develop functionally gradient materials (FGMs) are aimed at using these materials in the projected space plane. The testing of these FGMs under simulated actual utilization conditions also is planned. These simulated tests are aimed at realizing an FGM surface temperature of 2,000 K and a temperature difference within an FGM sample of 1,000 K. This can be accomplished by heating the high-temperature side with a high-temperature, high-velocity gas, and by cooling the low-temperature side with a coolant. In this report, we will discuss the results of bonding an FGM plate to an FGM cooling panel, and will present thermal as well as structural analyses of the bonding.

2. Sample

We have studied a method for effectively bonding an FGM to a material cooling panel by subjecting the bonded FGM and cooling panel sample to a high-temperature gas flow using the test setup shown in Figure 2.1. The carbon/carbon (C/C) composite FGM cooling panel sample used in our experiment consisted of layers of C/SiC-system material. We used oxygen-free copper as the material for the cooling panel because of its high thermal conductivity.

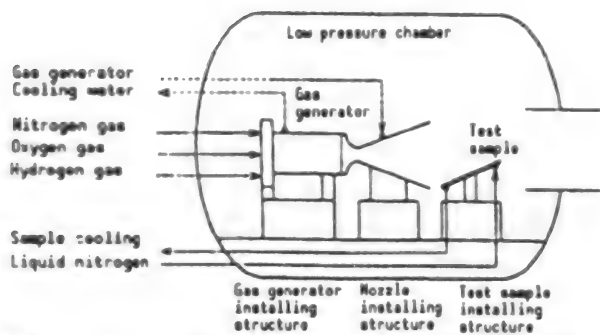


Figure 2.1 High-Temperature Gas Flow Testing and Evaluation System

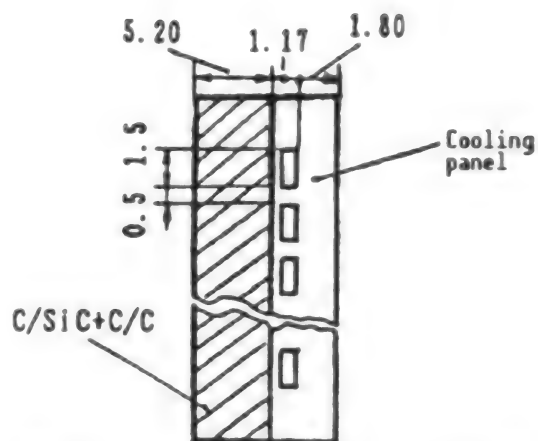


Figure 2.2 Cross-Sectional Diagram of an FGM Plate Bonded to a Cooling Panel

Figure 2.2 is a cross sectional diagram depicting the FGM bonded to the cooling panel. In conducting bonding, it is important that an FGM sample and the cooling panel be bonded firmly with no peeling and flaking, and to prevent damage due to insufficient cooling. It also is important to make the results of comparisons between test data and analytical data, as well as the results of evaluations, meaningful and reliable.

3. Analysis

We compared and studied the thermal stress at the bonded section under bonding or evaluation test conditions. The results are described below.

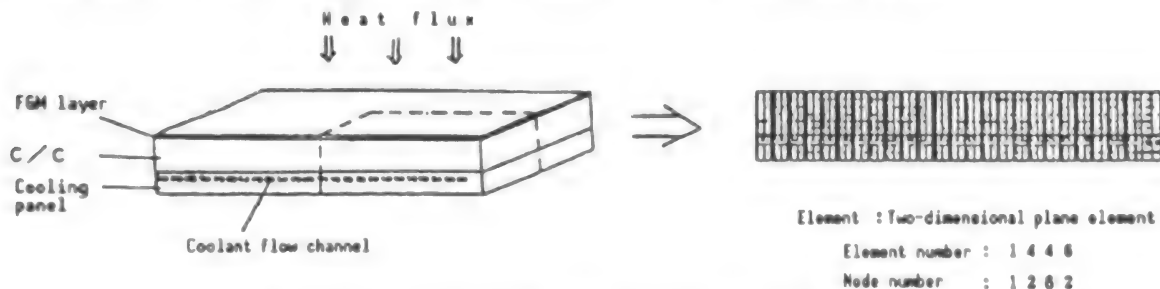


Figure 3.1 Cooling Capacity Analysis Model

3.1 Analysis Method and Analysis Conditions

We conducted our analysis using the general-purpose finite element code ABAQUS. A simplified cooling capability analysis model, shown in Figure 3.1, was employed because details of the actual shape and configuration of the FGM cooling panel sample to be used in a realistic utilization condition test had yet to be determined. In this model, the value for the heat flux received from the FGM surface was determined to be about 3 MW/m^2 based on the results of a simulation. The heat flux changes when the surface temperature changes. However, the value remains close to 3 MW/m^2 in a steady state. Thus we applied a thermal stress of 3 MW/m^2 to the surface in this analysis.

As for the thermal conductivity of the cooling panel side, a value of $43 \text{ kW/m}^2\cdot\text{K}$ was adopted as a condition when the panel is cooled by water at 20°C that flows at a rate of 9 m per second. Heat was applied for a period of 30 seconds, and after heating was stopped water cooling continued.

The FGM plate was brazed to the cooling panel at a brazing temperature of 1,000 K, and we measured the thermal stress generated by this high brazing temperature.

The stress in the bonded section is generated by differences in the linear thermal expansion coefficients at bonding temperature in each of the material layers involved, by differences in temperature distribution, and by differences in linear thermal expansion coefficients when the experiment is being conducted.

3.2 Material Properties

With regard to compositional distribution in the FGM's gradient layers, we studied the distribution of gradient distribution parameter $N = 1.9$ at $(\text{SiC weight}/\text{Si} + \text{C weight}) = (X/t)^N$ in which t denotes the thickness of the gradient layers and X is the distance from the surface (Figure 3.2). For the relevant calculations, step-like distribution data were used, and material property values at each of the FGM's layers were obtained by linear mixture rules.

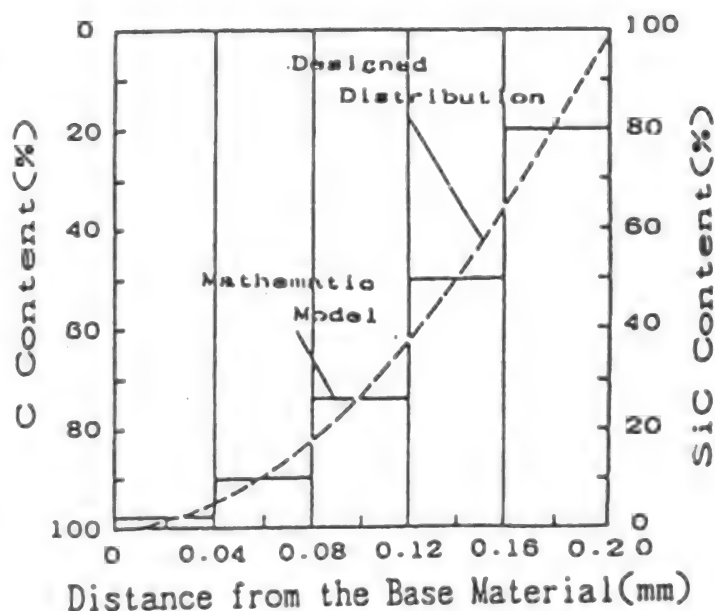


Figure 3.2 Gradient Pattern in FGM Layers

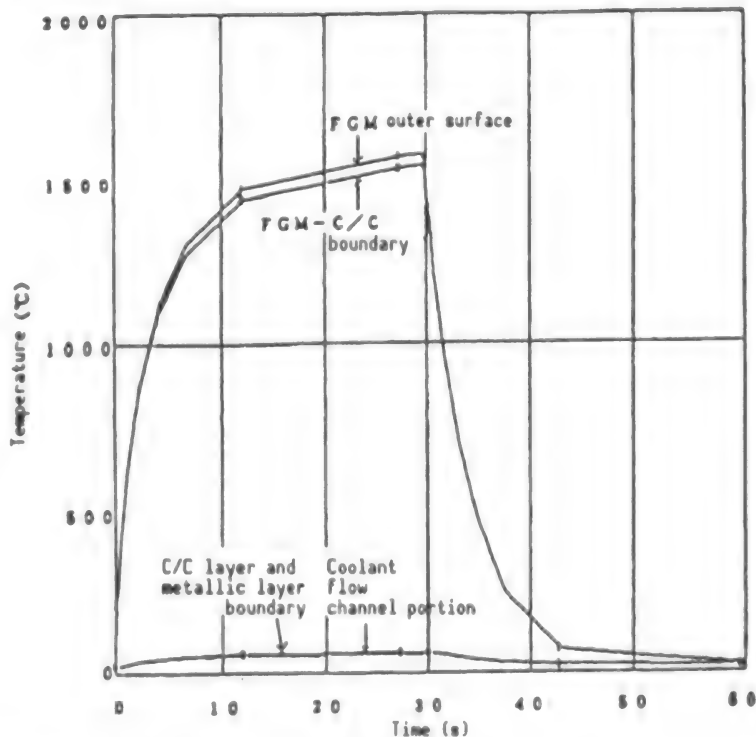


Figure 3.3 Temperature Hysteresis at Different Depths of the Test Sample

3.3 Analysis Results and Discussion

Figure 3.3 shows the temperature hysteresis at different depths of the evaluation test sample. The figure shows that a maximum surface temperature of 1,850 K was measured on the FGM surface, and a maximum temperature of 335 K was measured at the carbon/carbon (C/C) and oxygen-free copper boundary. the maximum stress generated in the bonded section under these temperature conditions was reached at 85 MPa in the end portions of the bonded faces (Figure 3.4).

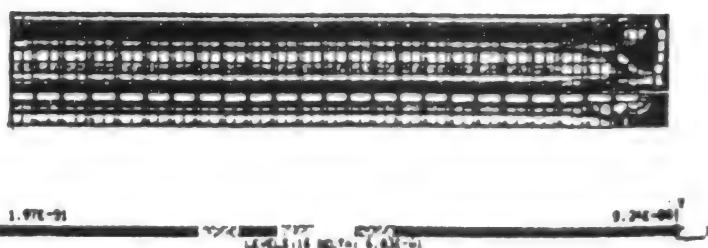


Figure 3.4 Stress Distribution Pattern Produced by a Test

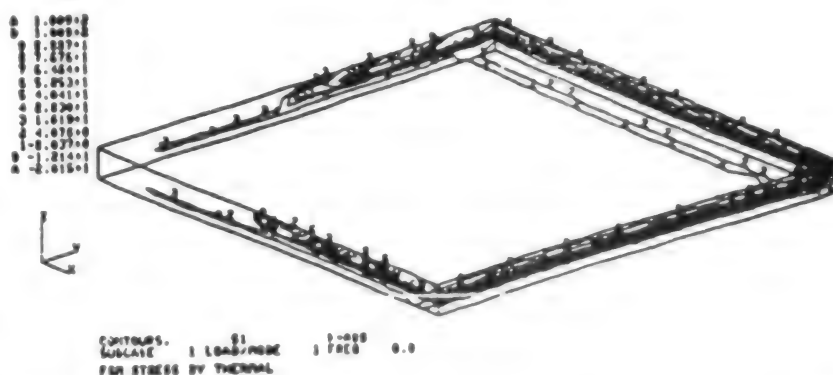


Figure 3.5 Stress Distribution Pattern Resulting From Brazing

The stress generated in the bonded faces when an FGM is brazed to a cooling panel increases to 980 MPa (Figure 3.5). These results show that the stress generated during brazing is about 10 times higher than the temperature encountered during the evaluation test because of the high bonded face temperature involved. This indicates that taking measures to prevent the boundary face from peeling during brazing is sufficient to counter overall stress-induced peeling problems in an FGM bonded to a cooling panel.

4. Bonding Test

4.1 Basic Test

The wettability and bonding capability of a silver solder and a soft solder have been studied by bonding a C/C plate to an oxygen-free copper panel.

The soft solder displayed poor wettability vis-a-vis the C/C material. As shown in Figures 4.1 and 4.2, the silver solder produced a good bonding result vis-a-vis the C/C material when brazing was conducted at 900°C for 60 minutes at 2×10^{-4} Torr.

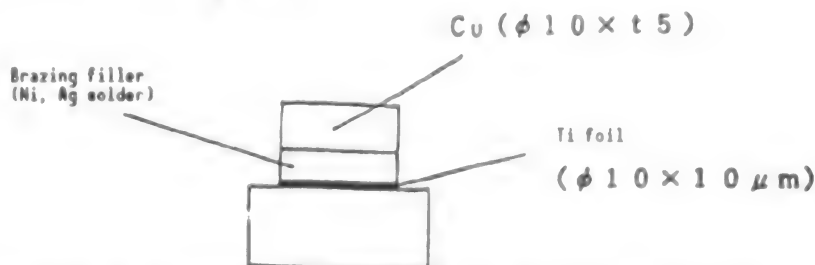
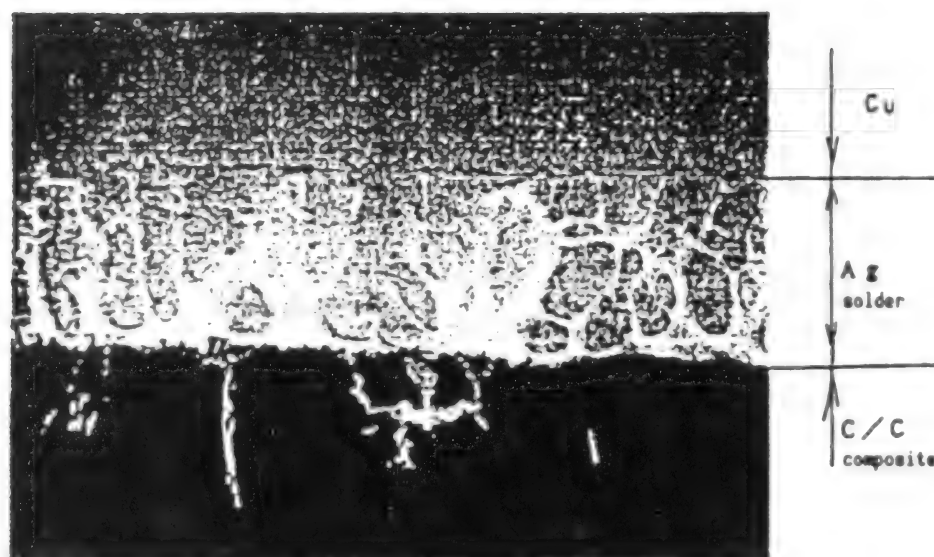


Figure 4.1 Sample Material Layer Arrangement for Testing Bonding Conditions



Bonded boundary conditions

$\times 100$

Figure 4.2 Boundary Conditions in a Silver Solder-Bonded Test Sample

4.2 Brazing Test Using Panel Large Enough for Practical Applications

We conducted a brazing test using a 100 mm^2 Cu plate and a C/C plate of the same size (Figure 4.3). These plates are large enough for practical applications. Initially, the test was conducted with no deformation restraint applied to the test sample.

This caused substantial warping and peeling of the plates along all sides of the sample. A basic experiment conducted to find a suitable brazing filler after this test showed that silver solder containing Ti is capable of obtaining a good bond between the C/C and Cu plates. Based on this finding, another brazing test was conducted by changing the cooling pattern and the brazing filler, and by improving the restraining method of the sample using the experimental setup shown in Figure 4.4. The results showed that by making a plastic deformation in the oxygen-free copper plate, it is possible to maintain overall flatness in the FGM plate, and this prevents peeling from occurring in the bonded boundary faces (Figure 4.5).

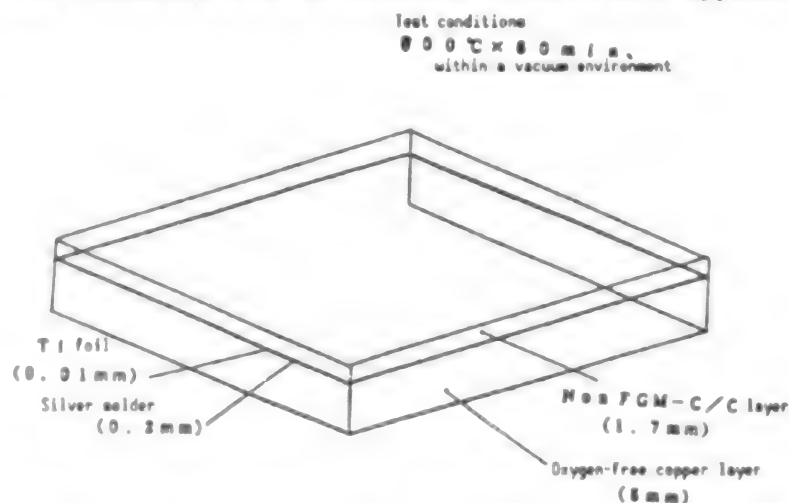


Figure 4.3 Material Layer Arrangement for Bonding Two 100 mm^2 Material Layers

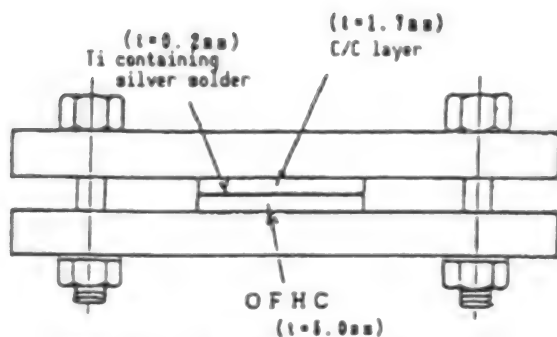


Figure 4.4 Setup for Brazing

5. Conclusion

In this article we have described the results of a basic analysis we conducted of a technique for bonding an FGM plate to a cooling panel, and presented the results of our bonding tests. Our efforts have contributed to establishing a method for brazing a C/C-system FGM plate to an oxygen-free copper cooling panel. We will continue our efforts to establish a method that will guarantee good bonding results by conducting more bonding tests together with nondestructive inspection of bonding conditions. Our efforts also will include a comparison and evaluation of test results by conducting analyses that take plastic deformation into account.

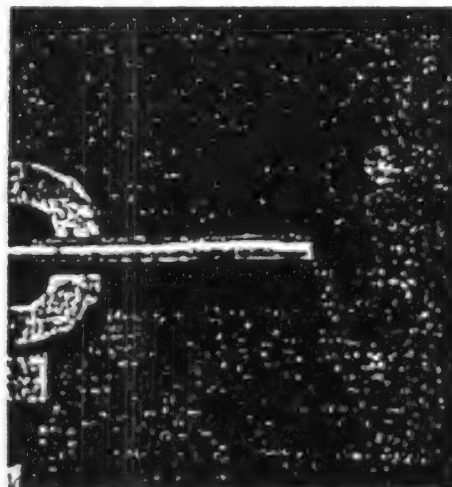


Figure 4.5 Test Sample After Brazing Was Completed

Second Phase of Development Plan for FGM Project

926C0014I Tokyo FGM '91 in Japanese 8-9 Oct 91 pp 253-259

[Article by Masayuki Niino, Rocket Altitude Performance Section, Kakuda Research Center, National Aerospace Laboratory]

[Text] Abstract: With a view to establishing the technology fundamental to creating FGMs for easing thermal stress in an environment with a maximum surface temperature of 2,000 K and a gap in temperature of 1,000 K, the project has succeeded in creating small sample pieces, 1-10 mm thick and 30 mm in diameter. This was a major success during its first phase, FY 1987-1989. The second phase, FY 1990-1991, has seen as its primary goal the production of 300 mm square shells.

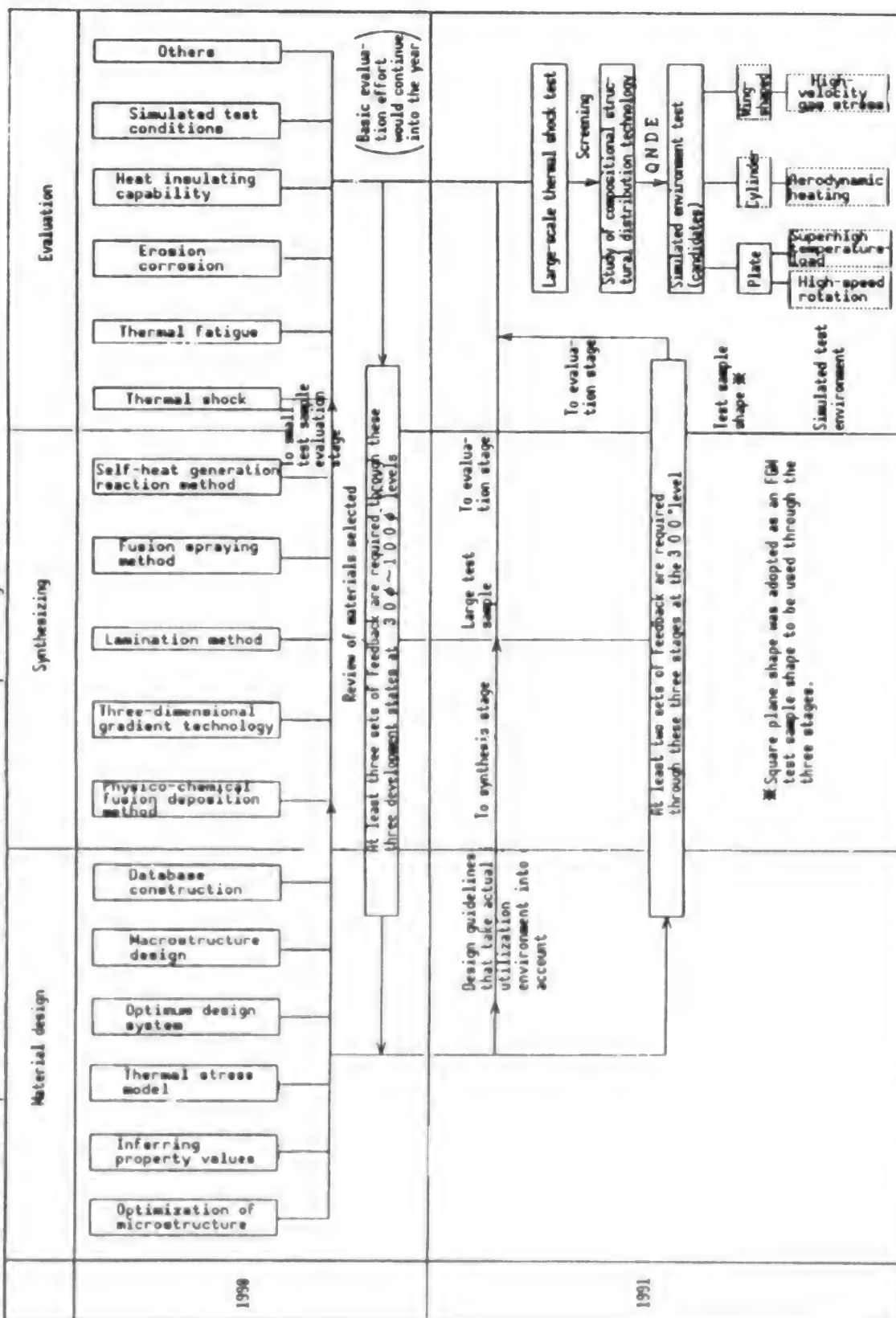
The latest achievements are given below.

1. Introduction

In 1987, basic research to develop functionally gradient materials (FGMs) that would relieve thermal stress was launched with subsidies provided by the Science and Technology Agency. This research encompasses FGM design, structural control of the material, and evaluating the newly developed material's characteristics. The goal of this research program is to establish the technology for creating an FGM that can be used at a maximum temperature on its high-temperature surface of 2,000 K, and a maximum temperature difference between the high-temperature surface and the low-temperature side of 1,000 K. The first phase of the five-year program ended in 1989, and the second phase will end in 1991.

The design team has completed its work to develop FGMs using the data obtained from uniformly mixed materials and empirical rules. The structural control team has succeeded in fabricating an FGM test sample 30 mm in diameter by combining various kinds of materials that were developed by the design group. Meanwhile, the evaluation team has gathered the property data for this test sample by conducting characteristic evaluation tests. The data obtained by these three teams are stored in the FGM database at the National Aerospace Laboratory. Currently, research in these three fields of FGM development is being conducted by sharing this database information.

Table 1. Flow of Development Efforts in the Second-Phase FGM Development Program



2. Outline of Second Research Phase

Emphasis in the second research phase is placed on establishing a material design technology for creating complex-shaped FGMs using the results of the first research phase, establishing structural controlling technology based on the design guidelines, and expanding the database so that it will better serve the efforts in these three research fields. The necessity of introducing FGMs into the fuselage and engines of the reusable shuttle plane and other supersonic planes has provided an impetus to promoting efforts in this government-subsidized research program. The final goal of the second research phase is to conduct large-scale actual utilization environment tests. To carry out these tests, active efforts will be made to develop thermal as well as structural analysis technologies for very high-temperature, high-velocity gas flow environments; to fabricate large FGM test samples; and to establish actual utilization environment test methods.

Table 1 shows the flow of these development efforts during the years of the second phase. The material design effort will focus on collecting the property values of various kinds of FGMs, centering on grain system FGMs, to establish an FGM design theory, and will improve elasticity-plasticity analysis techniques. To help the fabrication of large FGMs in the synthesizing effort that will follow work on de-

signs, efforts will be made to refine the three-dimensional finite element analysis method. As for the development of large FGM test samples, a number of basic shapes have been adopted to promote the use of FGMs in the space plane's fuselage and engines (Figures 1 and 2). These shapes include a semispherical shape that is required to create FGMs for use in the plane's nose cone section, a hollow cylinder to make FGMs for application in the front edges of the wings and engines, and a square plate to manufacture FGMs for use in other sections.

To fabricate these large FGM test samples, it is necessary to develop a fabrication technology that combines the physico-chemical fusion deposition method, lamination method, fusion spraying method, and the self-heat generation reaction method. In addition, the development of three-dimensional gradient technology is necessary to produce complex-shaped FGM products for use in practical applications. The synthesizing efforts will involve the promotion of the development of lighter materials and new material combinations that are more suitable for use in rigorous space development endeavors. These large-dimension samples will be used after being bonded to cooling panels for their evaluation in simulated actual utilization conditions, and

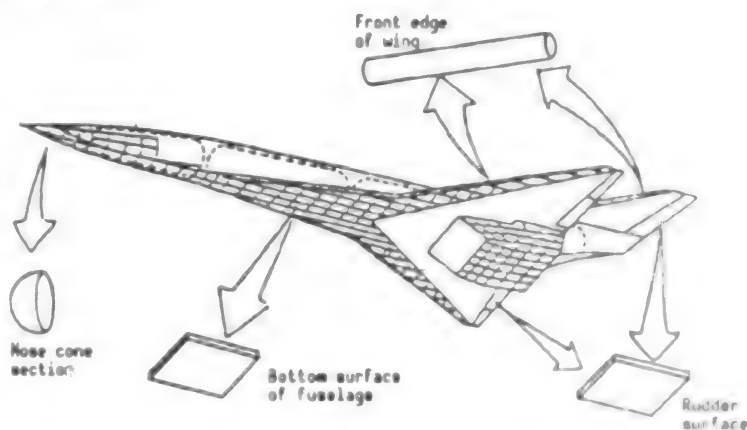


Figure 1. Shapes of FGMs To Be Developed for Space Plane Applications

this requires better sample processing technology. To deal with the problems involved in these efforts—including the design of a cooling structure, bonding FGMs, to conventional materials, and processing—it will be necessary to formulate a working group of researchers to discuss problems related to the design, synthesis, and evaluation efforts.

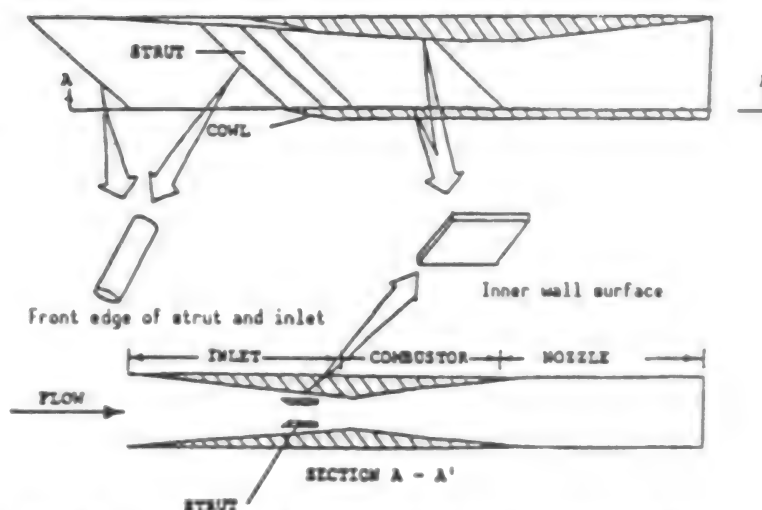


Figure 2. Shapes of FGMs To Be Developed for Scramjet Engine Applications

With regard to the evaluation, it is difficult to conduct many large-scale simulated actual utilization environment tests because of budgetary and development schedule constraints. To deal with these problems, these tests will be preceded by "screening tests" in which tests of selected elemental technologies needed for conducting the large-scale tests will be carried out using smaller 30¢ samples. The screening tests will include tests involving thermal shock, thermal fatigue, erosion, and corrosion. A quantitative nondestructive inspection technology is indispensable to maintain continuity between small-sample test data and large-sample test data. The inspection involves the use of X-ray, ultrasonic, and acoustic emission (AE) technologies. The simulated actual utilization environment test will involve many different tests depending on the FGM's utilization point in the space plane. However, limitations in the availability of test samples requires the use of a high-temperature gas stream that will make it possible to realize a universal heat test environment.

In the following, we will describe the work that is under way at a number of research institutes.

3. Research on FGM Design Technology

In the first research phase, efforts were made to determine a design concept for FGMs, and this led to the formulation of basic theories, the development of a thermal stress analysis program, and the development of a technology that makes it possible to infer the property values of a material from its microstructure. These programs and technologies made it possible to develop material design supporting systems, and the technology for structural control necessary to obtain an optimum material composition for efficient thermal stress alleviation.

During the second research phase, efforts will be made to develop an FGM design technology that will make it possible to deal with the problems involved in creating complex-shaped, three-dimensional FGMs, and the problems

associated with simulated actual utilization environment tests. To promote these efforts, it will be important to improve nonsteady state heat transfer analysis, and elastic as well as plastic thermal stress analysis, and to expand both the database and the knowledge base.

(1) Research on a Method of Inference Based on Elastic/Plastic Analysis Data Using a Microstructure Model (Tokyo Institute of Technology)

The Tokyo Institute of Technology is working to formulate a method for theoretically deriving the breakdown conditions in mixed ceramic-metallic materials, the flow rules, and the material properties using a microscopic theory based on an ellipsoidal grain scattered microstructure model. By translating these findings into a software program, the Institute aims at improving the database for the elastic and plastic thermal stress analysis of FGMs.

(2) Research on the Measurement and Analysis of Thermal Property Values (Shizuoka University)

Shizuoka University is seeking to improve its database quantitatively and qualitatively through research into the optimization of measurement techniques for measuring the thermal property values of mixed ceramic-metallic materials, and to improve data analysis methods. At the same time, the University is trying to establish a technique for the effective evaluation of FGM's heat transfer characteristics by conducting steady state/nonsteady state heat transfer analyses in a mixture ratio gradient multilayer material.

(3) Research on the Measurement and Analysis of High-Temperature Strength (Mechanical Engineering Laboratory, Agency of Industrial Science and Technology)

The Mechanical Engineering Laboratory is conducting research aimed at finding the most suitable technique for measuring the high-temperature strength of mixed ceramic/metallic materials, and at elaborating a data analysis method. The Lab also is seeking to improve its database quantitatively as well as qualitatively by collecting data about the high-temperature strength of various types of material mixtures, including dynamic fracture characteristic values.

(4) Research on Gradient-Structured Thermal Stress Model and Analysis Technique (National Aerospace Laboratory and Power Reactor and Nuclear Fuel Development Corp.)

The National Aerospace Laboratory and the Power Reactor and Nuclear Fuel Development Corp. are endeavoring to clarify the dynamic fracture characteristics of a two-dimensional gradient structure to promote the development of plate or shell-shaped structural components. In parallel to this effort, they are tackling the problems encountered in nonsteady state thermal transfer analysis, and elastic as well as plastic thermal stress analysis of a three-dimensional gradient structure to facilitate the development of complex-shaped FGM structural components.

(5) Research on Optimum Design Support System (Daikin Kogyo Co., Ltd.)

The Daikin Kogyo Co. is engaged in the development of FGM design routines based on nonsteady state thermal transfer, and elastic as well as plastic thermal stress analysis. The company also is engaged in research aimed at developing an optimum design system for FGMs based on its experience in knowledge engineering research that it promotes to build a knowledge database on the relationship among process parameters, microstructure, and material properties.

(6) Research on Structural Design Technology for Use in a Simulated Actual Utilization Environment (Nissan Motor Co., Ltd.)

The Nissan Motor Co. is in the process of formulating research guidelines for promoting the realization of an optimum FGM design through the study of various technical problems encountered in conducting thermal and dynamic structural analyses of structural materials placed within a high-temperature, high-velocity air current by assuming the conditions to which the scramjet engines of supersonic planes will be exposed.

(7) Research on Environmental Condition Design (Mitoh Kagaku Gijutsu Kyokai)

Mitoh Kagaku Gijutsu Kyokai has embarked on a course of research aimed at building a database of FGM design conditions by investigating aerodynamic heating conditions as well as chemical reaction conditions in the nose cone section, in the front edge of the wings, and in the rocket engines of the space plane.

(8) Building Database and Knowledge Base (National Aerospace Laboratory)

This database and knowledge base building effort involves the expansion and promotion of information exchange functions among the three FGM development arms—material design, structural control, and evaluation—using a database network encompassing these three research arms. This is in addition to the collection of various relevant data, and improvement of the data management system. Through these efforts, the building of a knowledge base on the relationship among process parameters, microstructure, and material properties is being promoted.

4. Research on FGM Structural Controlling Technology

In the first phase of the research, an FGM having a diameter of about 30 mm was created using the basic technology for controlling various material structures. The technology was developed to create heat-resistant FGMs using various ceramics and metallic materials, and based on the results of the material design efforts.

The second target phase is to establish a technology for controlling the structures of curved complex-shaped FGMs with a size of about 30 mm². This is being done to promote the use of these FGMs in practical applications.

(1) Research on Structural Controlling Technology by Physico-Chemical Deposition Method (Tohoku University, National Research Institute of Metals, and Sumitomo Electric Industries, Ltd.)

In the second phase, Tohoku University, National Research Institute of Metals, and Sumitomo Electric Industries are seeking to establish a structural controlling technology for use in improving the antioxidation quality of FGMs, and for bonding an FGM to an FGM cooling structure, a technology that is indispensable to promote FGM's practical utilization. This is to be done by combining the physical deposition and chemical deposition methods based on precision controlling technology.

(2) Research on Three-Dimensional FGM Fabrication Technology by Gas Phase Infiltration Method (Nippon Oil Co., Ltd.)

In the second phase, the Nippon Oil Co. is working to establish a technology for the structural control of C-SiC-system FGMs, which have a high antioxidation capability. This control is to be effected by having a gas phase infiltrate into a three-dimensional base material that was fabricated using C/C composite materials having high specific strength and high antiheat capability.

(3) Research on Three-Dimensional FGM Fabrication Technology by the Grain Blasting Method (Tohoku University and Ishikawajima-Harima Heavy Industries Co., Ltd.)

In the second phase, Tohoku University and Ishikawajima-Harima Heavy Industries are aimed at establishing a three-dimensional FGM technology using the jet shape control technology developed to create a three-dimensional gradient, and by controlling the blasting ratio of metallic and ceramic grains. In addition, thermal stability between different phases will be studied.

(4) Research on Structural Control by the Lamination Method (NKK)

In the second phase, NKK will try to establish a technology for controlling nonuniformity in film thickness, which occurs when creating a complex-shaped, large-dimensional thin film from metal and ceramic slurry.

(5) Research on Structural Control Technology by Fusion Spraying Method (National Research Institute of Metals)

In the second phase, the National Research Institute of Metals is endeavoring to establish a complex-shaped FGM fabrication technology using the basic technology developed to improve material density nonuniformity on the fusion-sprayed film formed on a complex-shaped FGM surface.

(6) Research on Structural Control Technology for Self-Heat Generation Reaction Method (Government Industrial Research Institute, Tohoku, Osaka University; and Kawasaki Heavy Industries, Ltd.)

In the second phase the Government Industrial Research Institute, Tohoku, Osaka University, and Kawasaki Heavy Industries are seeking to establish a complex-shaped FGM fabrication technology using the technology for temperature distribution control. This involves adjusting the heat generation level according to the curvature. Also, they are working to establish a basic technology for improving a material's antioxidation capability.

(7) Research on FGM Processing Technology (Mitsubishi Heavy Industries, Ltd., Nissan Motor Co., Ltd., Ishikawajima-Harima Heavy Industries, Ltd., Kawasaki Heavy Industries, Ltd., and 13 other research institutes)

Mitsubishi Heavy Industries, Nissan Motor Co., Ishikawajima-Harima Heavy Industries, Kawasaki Heavy Industries, and 13 other research institutes are seeking to establish a processing technology. Such a technology is indispensable in fabricating the experimental model of a large FGM cooling panel. This effort requires cooperation among the design, synthesizing, and evaluation divisions.

5. Research on the Characteristic Evaluation Technology for FGMs

In the first phase of the FGM development research, a technology for the quantitative representative of the thermal stress distribution in an FGM was developed. In addition, a technology to evaluate the heat insulation characteristics of an FGM was developed by conducting basic tests in a high-temperature environment. The relationship between the material's compositional gradient and FGM strength was clarified by conducting a series of tests on thermal fatigue, thermal shock, and superhigh-temperature creep and mechanical fracture.

In the second phase, these evaluation technologies will be used effectively, and continued efforts will be made to establish nondestructive FGM inspection technologies. Efforts also are being made to select material systems that are suitable for use in simulated actual utilization environment test. This involves conducting a series of tests on high-temperature oxidation, erosion, corrosion, and material fatigue under temperature-difference conditions. Simulated actual utilization environment tests will be conducted as part of a comprehensive evaluation of FGMs as structural components.

(1) Research on Erosion and Corrosion Characteristic Evaluation Technology (Tohoku University)

Tohoku University is developing technology for evaluating both the erosion and corrosion characteristics as well as the fracture characteristics of FGMs under various conditions—mainly in an oxidation environment. This is based on the basic technology that has been developed by conducting laser Doppler flow tests in the first phase of the current research.

(2) Research on FGM's Thermal Stability Evaluation Technology (National Research Institute of Metals)

The National Research Institute of Metals is conducting basic research on the high-temperature structural stability of a single metallic phase and a metallic-and-ceramic composite phase, and on changes in material characteristics over time.

(3) Research on Quantitative Nondestructive Inspection Technology (Ship Research Institute, Tohoku University, Hitachi Construction Machinery Co., Ltd.)

The Ship Research Institute, Tohoku University, and Hitachi Construction Machinery Co. are developing a nondestructive inspection method, and quantitative evaluation technologies that can be used with FGMs. The FGM that is being developed has a gradient structure that changes at a rate ranging from 1-10 mm. This means that any damage that occurs in the material developing will be on a microscopic scale. Efforts are being made to develop measures to deal with this damage.

(4) Research on Thermal Fatigue Evaluation Technology in a Temperature-Difference Environment (National Aerospace Laboratory, Mitsubishi Heavy Industries, Ltd.)

The National Aerospace Laboratory and Mitsubishi Heavy Industries are conducting the evaluation of thermal fatigue fracture characteristics, and the structural soundness of FGMs against thermal fatigue, using 30φ FGM samples and a high-temperature difference testing system that was developed in the first research phase. These evaluations involve conducting laser beam-heated thermal fatigue tests.

(5) Research on Characteristic Evaluation Technology by Conducting Large-Scale Thermal Shock Tests (Japan Atomic Energy Research Institute)

The Japan Atomic Energy Research Institute is conducting research aimed at clarifying crack development mechanisms in FGMs, and their fracture behavior, by irradiating a large FGM sample with an electron beam or a hydrogen ion beam as part of a beam heating system.

(6) Research on Technology for Conducting Extended, Small-Scale, Simulated Actual Utilization Environment Evaluations (National Aerospace Laboratory)

The National Aerospace Laboratory is conducting evaluation tests on extended utilization durability, which cannot be conducted in large FGM sample tests, under aerodynamically heated conditions and high-speed rotation heated conditions using small FGM testpieces.

**(7) Research on Large-Scale, Actual Utilization Environment Testing Conditions
(National Aerospace Laboratory, National Space Development Agency)**

The National Aerospace Laboratory and the National Space Development Agency are conducting a comprehensive evaluation of the heat insulating capability and the structural soundness of large FGMs by testing these material samples in a high-temperature, high-velocity air current, a condition which the space plane or other similar supersonic planes experience in practical operation.

6. Committee for Formulating Optimum FGM Design Guidelines

One of the functions of this committee is to take the necessary actions to deal with expanding FGM-related research activities, both in Japan and in other countries. The committee also is required to formulate guidelines for the efforts to create FGM test samples, to evaluate them, and to build databases ahead of other countries. The goal of this effort is to ensure smooth progress in these efforts after the current government-subsidized FGM project ends in 1991.

The formulation of a material design standard is indispensable for promoting the utilization of FGMs in various advanced technology fields, including applications in the space plane. And for this, it is important to foresee the necessary constitution of the design standard, and to strive to build the database needed for this formulation.

Through a preliminary study, the committee is selecting the items (metadata) needed to build the database, and is studying methods for processing these data in preparation for the formulation of the design standard structure/material). Standardization also is being promoted in creating FGM samples for use in collecting these data and in the evaluation of these samples. By taking the initiative in these standardization efforts, the committee is seeking to promote effective cooperation among research organizations in Japan as well as with foreign countries. The committee's activities would promote FGM research in material design, synthesis, and evaluation.

Microstructure, Fracture Mechanism of LPPS FGM

926C0014J Tokyo FGM '91 in Japanese 8-9 Oct 91 pp 265-271

[Article by Hideki Hamatani, Nobuyuki Shimoda, Yasutomo Ichiyama, Saburo Kitaguchi, and Tohru Saito, Joining Steel Research Laboratories, Nippon Steel Corp.]

[Text] **Abstract:** Studies on microstructures and fracture mechanism of FGMs consisting of YSZ and NiCr, prepared by LPPS, were carried out. MSP testing was performed to measure the fracture stress. Cyclic high-temperature difference field testing was used to investigate thermal fatigue properties. The microstructure of NiCr showed a columnar structure, and its growth was perpendicular to the interface. On the other hand, NiCr was surrounded by YSZ; its microstructure was found to show an equiaxed structure, initial particle size had a large effect on density, grain size, and fracture stress. The size for obtaining maximum fracture stress was not coincident with that for the maximum density of coatings. Through the results of high-temperature difference field tests, an optimum design to reduce thermal stress has been proposed.

1. Introduction

Functionally gradient materials (FGMs) designed to alleviate thermal stress are attracting attention as materials suitable for use in aviation and space development. Our company is seeking to establish a technology for the fabrication of Y_2O_3 stabilized ZrO_2 (YSZ)-NiCr-system FGMs using the low-pressure plasma fusion spraying method (LPPS). In this process, we employ a single four-port plasma gun that was developed by our company. The advantages of this method include greater tolerances for the materials used, and the comparative ease with which larger FGM plates can be fabricated. Thanks to these features, this method is the most promising method for the fabrication of FGM plates. To use this method in fabricating FGMs, a number of problems must be solved, including film quality control, the structure of fusion-sprayed mixed-component films, the relationship between structure and strength, attaining an optimum structure, and the properties of the material. In our current research, we have studied density control by changing the diameter of the starting material particles. We also have examined the relationship between the diameter and the structure, the strength of an FGM film, an optimum material structure to reduce thermal stress, and the fracture mechanism in the film.

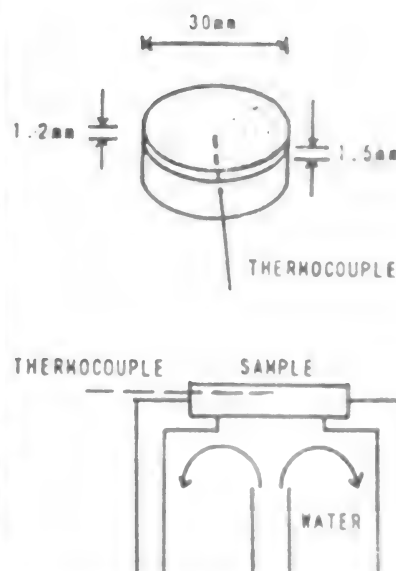
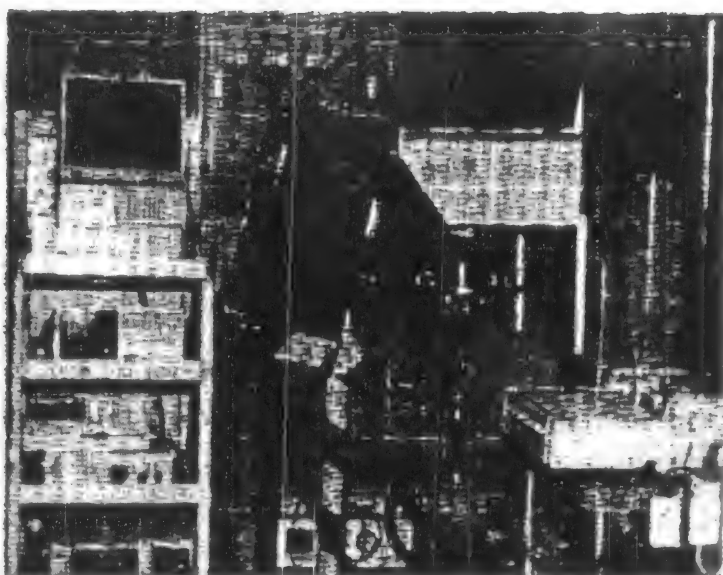


Figure 1. External Appearance of a Simplified Model of a Temperature Difference Thermal Shock Tester and the Sample Cooling Method Employed

2. Experiment Method

We produced FGM coating films using $\text{ZrO}_2\text{8wt}\% \text{Y}_2\text{O}_3$ (YSZ) powder, having a particle diameter of $27 \mu\text{m}$, and $\text{Ni20wt}\% \text{Cr}$ (Ni-Cr) powder having diameters of 29, 39, 57 or $81 \mu\text{m}$. These films were evaluated using scanning electron microscope (SEM), transmission electron microscope (TEM), EDX, X-ray diffraction (XRD), atomic force microscope (AFM), and Archimedes' methods for density measurement. Film strength

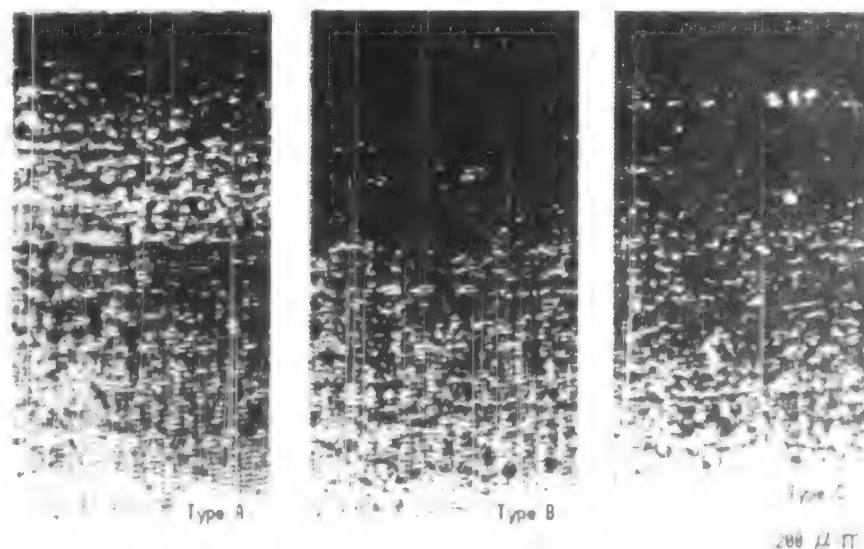


Figure 2. Sectional Views of FGM Samples Having Different Structural Change Hysteresis and the Results of EPMA Analysis

at room temperature was measured by the MSP method, and thermal stress alleviation capability was studied using a temperature difference thermal shock tester (Figure 1). The tester was developed from a similar piece of equipment made by the National Aerospace Laboratory in Kakuda. The thermal stress test involved measuring the compositional change hysteresis (Figure 3), film density, and film thickness in an effort to identify optimum structural conditions. The hysteresis can be divided into a YSZ-rich type (Type B) and NiCr-rich type (Type A), and an intermediate type (Type C).

3. Results

(1) Diameter of Starting Material Powder and Film Density

Figure 3 shows the relationship between the average particle diameters of pure NiCr starting material powder and the film density, as well as film thickness (sedimentation efficiency). The figure indicates that film density peaks when the diameter is a 57 μm . In the film consisting of YSZ and NiCr, as well, a peak was observed at a NiCr particle diameter of 57 μm .

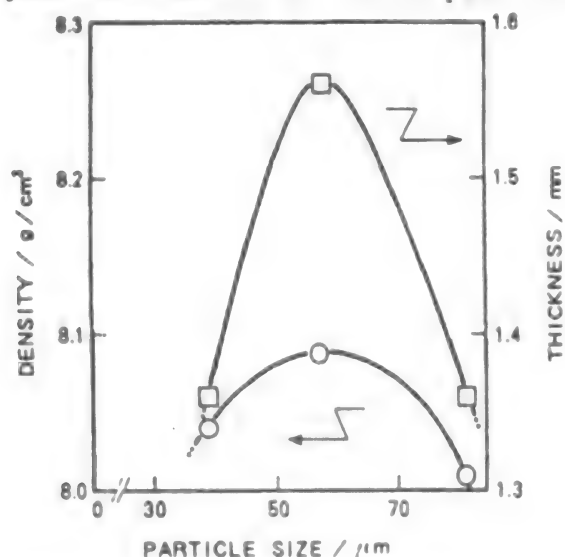


Figure 3. Relationship Between Average Particle Diameter of Starting Material Powder, Film Density, and Film Thickness

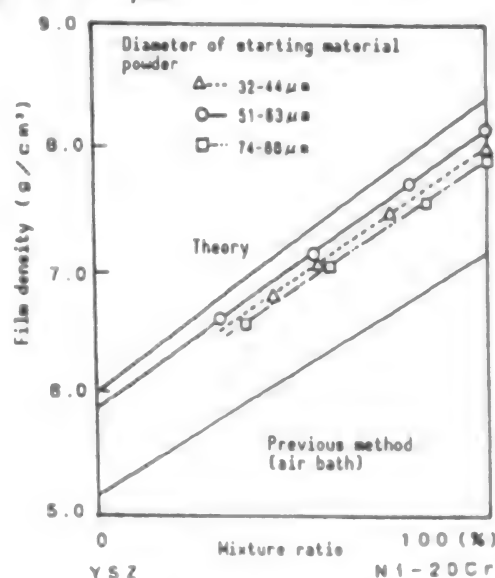


Figure 4. Relationship Between Film Density and YSZ-NiCr Mixing Ratio

Figure 4 shows the relationship between the YSZ-NiCr mixing ratio and film density when the particle diameter of the NiCr is varied. As in the case of an NiCr film, a peak is attained at a particle diameter of 57 μm , and it can be seen that the composite material rules dictate the relationship between mixture ratio and film density.

(2) Particle Diameter of Starting Material Powder and Film Strength

Figure 5 shows the relationship between the YSZ-NiCr mixing ratio and MSP strength when the particle diameter of the NiCr is varied. It can be seen that strength deteriorates in proportion to an increase in the YSZ ratio, and when the YSZ ratio is high, the film displayed a conspicuous deterioration in strength. For all of these different mixing ratios, strength increased in proportion to

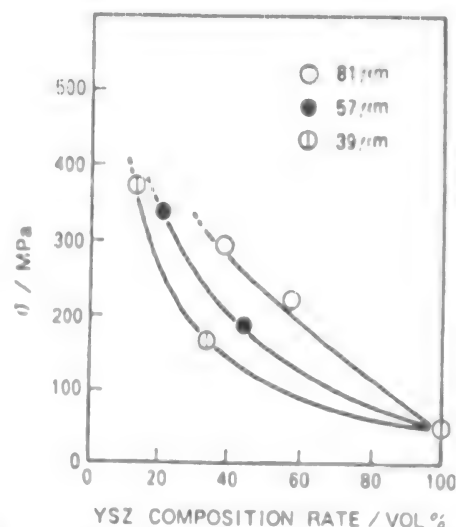


Figure 5. Relationship Between YSZ-NiCr Mixing Ratio and Film Strength

the particle diameter of the NiCr. This indicates that the conditions for improving strength do not necessarily coincide with the conditions for attaining maximum film density, as shown in Figure 3. EDX analysis of the fractured face found that YSZ density is conspicuously higher in the fractured face than in the non-fractured area around it. This indicates that in most cases a crack propagates selectively along the YSZ phase within a film, and that the NiCr phase works to deter the crack's progress. A larger NiCr particle diameter leads to the formation of a larger NiCr grain phase scattered across the film, and it is believed that this increases resistance to the crack's progress, thereby improving the strength of the film. The strength of the film also is affected by the scattering condition.

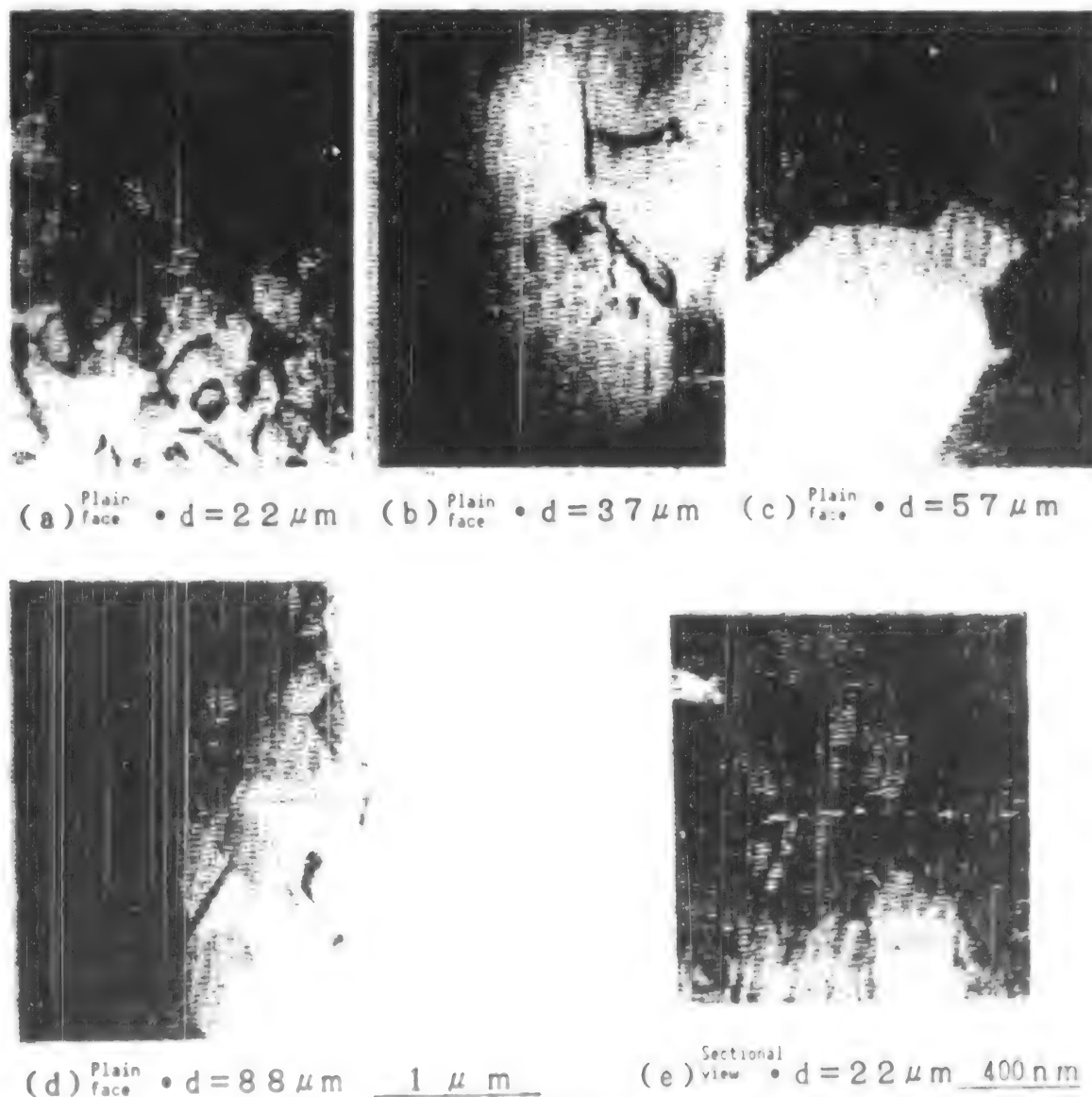


Figure 6. TEM Photos of NiCr Films

(3) Microstructure Within Film

Figure 6 shows several TEM photographs of NiCr films. In NiCr films, the microstructure consists of clusters of pillar-shaped crystals whose lengths

range from 100-1,000 nm. When the diameter of the starting material particle is 37 or 57 μm , crystals having comparatively larger diameters are formed. Figure 7 is a TEM photograph of a YSZ film. The YSZ film also has a pillar-shaped crystal structure. However, the diameter (20-100 nm) is about one-tenth that of NiCr films. In both NiCr and YSZ films, crystalline grains grow toward substrates having lower temperatures. XRD analysis found that the crystal structure within each of these fusion-sprayed films had an oriented growth.



Figure 7. TEM Photo of the Sectional Face of a YSZ Film



Figure 8. TEM Photo of the Sectional Face of a YSZ-NiCr Film

Figure 8 is a TEM observation of the sectional face of a YSZ-NiCr film. If the NiCr and YSZ, which have large melting temperature differences, are in contact with each other, the NiCr, which has the lower melting temperature, produces an equiaxed crystal. The YSZ, meanwhile, which has a higher melting temperature, has a crystalline grain structure that grows toward the lower temperature substrate and the NiCr with its lower melting temperature.

(4) Optimum Structure for Thermal Stress Alleviation

Figure 9 shows the surface conditions immediately after a coating film was applied to FGM samples while varying the FGMs compositional change hysteresis, the coating film density, and the thickness of the coating film. The results showed that cracks are likely to appear on the coating film surface that has a higher YSZ content, less thickness, and lower density.

Table 1 gives the results of an experiment that was conducted by varying the FGMs compositional change pattern and coating film density under a constant heat flow velocity. It can be seen that the development of cracks is deterred better when NiCr contents and film density are higher, as these contribute to a lower FGM surface temperature and a smaller temperature difference. A similar tendency was obtained in an experiment that was conducted by keeping the surface temperature constant.

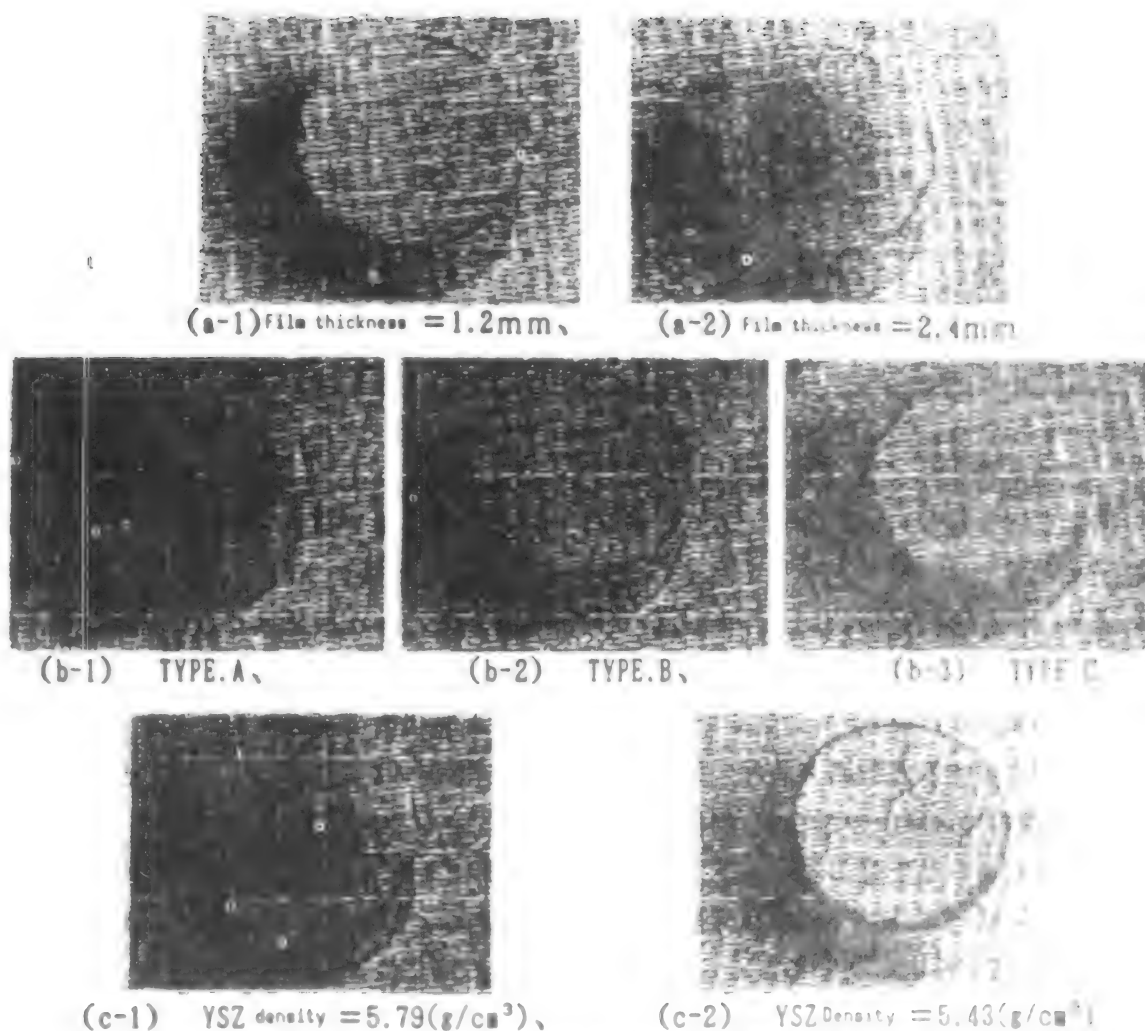


Figure 9 Structural Optimization in FGM-1-2B1-p-100

(5) Fracture Conditions

Figure 10 presents the SEM photos showing peeling. It can be seen from the photos that the peeling occurred on the topmost FGM layer, and that the peeling had expanded into the deeper layers along the YSZ grains. SEM and EDX analysis of the FGM sample revealed the presence of Zr, Y, O, Ni, and Cr in the peeled section. This indicates that the YSZ-NiCr grain boundary is the cause of the occurrence of peeling. The starting point of the vertical crack, which extends from the surface deep into the sample layers, had been located in the YSZ layer present within the YSZ layer. It is believed that the peeling occurred after a vertical crack has developed. XRD analysis conducted immediately after the fusion spraying found that the peeling caused a reaction between the FGM layer. This is because the NiCr layer becomes oxidized when it is exposed to the atmosphere through the opening in the peeling layer.

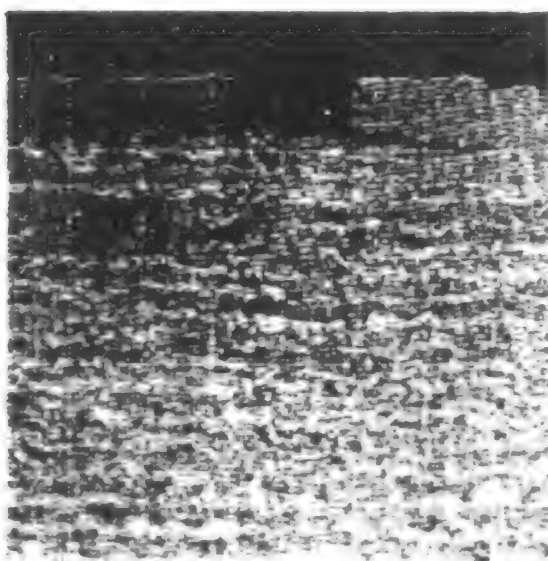
Table 1. Effect of Compositional and Density Change on Thermal Stress Alleviation

No	Dens-ity (YSZ)	Dens-ity (NiCr)	Gradi-ent TYPE	Surface temper-ature (°C)	Tempera-ture difference (°C)	Heat cycles completed before crack develops (number of cycles)
1	5.79	8.04	A	1,075	670	20-40
2	5.79	8.04	B	1,125	765	0-10
3	5.79	8.04	C	1,125	800	1-10
4	5.70	7.96	A	1,225	790	No cracks after 1 heat cycle
5	5.70	7.96	B	1,275	880	Cracking after 1 heat cycle
6	5.70	7.96	C	1,275	925	Peeling after 1 heat cycle
7	5.43	7.89	A	1,075	695	0-5
8	5.43	7.89	C	1,275	1,025	1
9	5.79	8.09	A	1,075	Impossible to measure	20-40
10	5.79	8.09	C	1,175	735	10-20
11	5.70	8.02	A	1,025	485	100-125
12	5.70	8.02	C	1,075	525	5-10

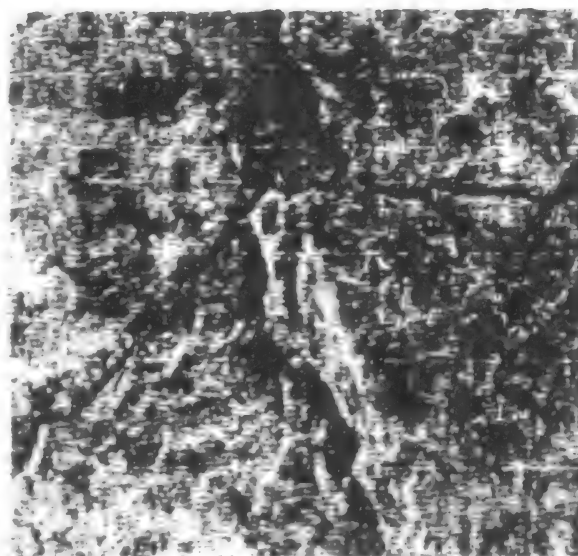
Diameter of starting material powder particle:

YSZ = 10-44 μm ; NiCr = 36-44 μm (1-8), 50-65 μm (9-12)

Surface observation revealed the presence of microscopic cracks that continued to expand independently from the cracks discussed above. Figure 11 shows two SEM photographs and corresponding EDX analysis of the peeled section, one immediately after the onset of peeling, and the second after 50 more heat cycles after peeling began. These results demonstrate that immediately after microscopic cracks appear, Ni and O precipitate on the cracked surface. As the number of heat cycles increases, the amount of Cr increases, and the NiCr grain boundary fracture becomes progressively more conspicuous. Based on these results, we believe that after the YSZ layer peels, fracture of the coating film occurs, even when the temperature is below NiCr's melting point.

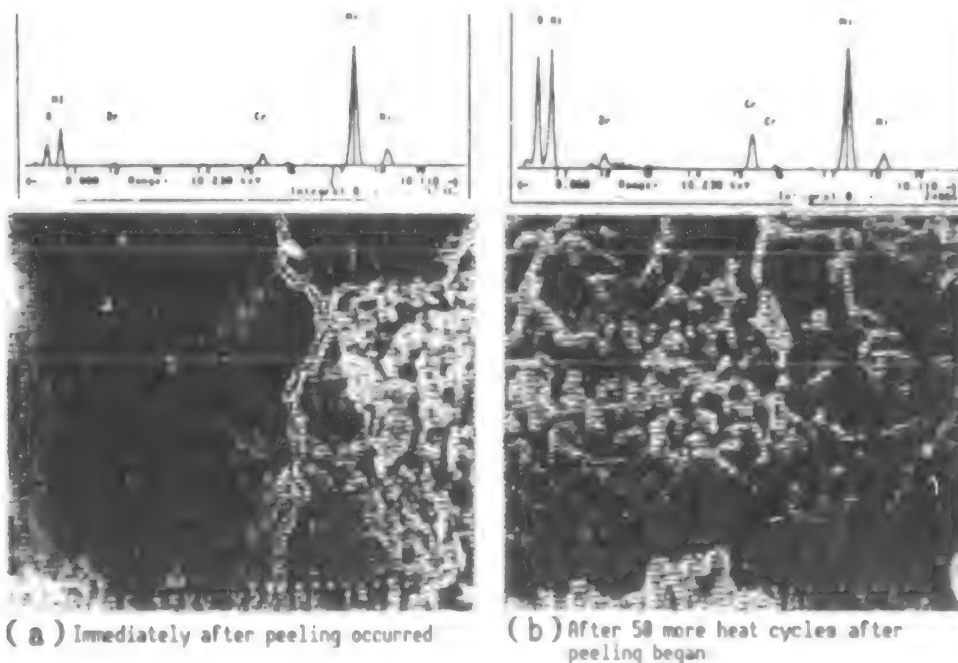


(a) Sectional SEM photo showing peeling
200 μ m



(b) Surface SEM photo showing peeling
25 μ m

Figure 10. Surface and Sectional Views of an FGM After Undergoing a Temperature Difference Thermal Shock Test Using the Simplified Tester



(a) Immediately after peeling occurred (b) After 50 more heat cycles after peeling began

Figure 11. Results of SEM Observation and EDS Analysis of Heat Cycle Change in Peeled Section

4. Conclusion

Our current research has enabled us to clarify a number of things, including differences in the crystal structures of FGMs and the top coating film; the possibility of independently controlling film density and film strength, which is difficult to implement in a single-layer film; the effectiveness of increasing the NiCr content to alleviate thermal stress; the importance of increasing film density; the effectiveness of decreasing the thickness of the coating film; and the importance of reducing the brittleness of the YSZ layer to restrain the development of cracks and FGM fracture.

5. Acknowledgement

Our current research has been conducted as part of the research effort to develop a basic technology for the fabrication of thermal stress alleviating FGMs funded by the Science and Technology Agency. We would like to express our gratitude to those who helped us in our work.

Thermal Evaluation Test of LPPS FGM

926C0014K Tokyo FGM '91 in Japanese 8-9 Oct 91 pp 273-275

[Article by Nobuyuki Shimoda, Hideki Hamatani, and Saburou Kitaguchi, Joining Steel Research Laboratories, Nippon Steel Corp.; and Ryuzo Watanabe, Akira Kawasaki, and Atsushi Hibino, Department of Materials Processing, Faculty of Engineering, Tohoku University]

[Text] Abstract: For a better understanding of the fracture process of functionally gradient materials (FGMs) in the temperature difference field, a burner heating test, using hydrogen and oxygen, was carried out. Plasma-sprayed FGM, consisting of zirconia and nickel alloy were prepared in this testing. Vertical cracks were observed in a ceramics (top) layer, and terminated mainly at metal layers in a metallic-ceramics mixing area. This is thought to suggest the advantage of FGM for it has vertical crack arrestability. Horizontal cracks, on the other hand, were found in a ceramics (top) layer and propagated between vertical cracks. In addition, some horizontal cracks which did not follow the vertical cracks have also been found through the observation.

1. Introduction

The high melting temperature and low thermal conductivity of zirconia-system ceramics make these ceramics suitable for use in heat-resistant protective films. Among these ceramics, yttria-stabilized zirconia, which is created by the plasma spray method, already is being used in the stationary as well as rotor blades of aircraft engines. However, heat insulators that will be used in the projected space plane, HOPE, will be required to withstand still higher temperatures and steeper temperature gradient utilization conditions. For example, the materials to be used in the burners of HOPE's reusable double-fluid storage-type engines (MMH, NTO), which will serve as the plane's OMS and RCS engines, are required to have a greater heat-resistant capability than that which is required for currently used heat insulation materials. Functionally gradient materials (FGMs) are being developed specifically for such applications. An FGM is a material whose design concept differs from those of conventional materials. Thus, it is very important to establish an evaluation method in developing FGM synthesis technology, and to determine the material's field of application. In addition, understanding the fracture mechanism in an

FGM is equally important in determining an optimum compositional variation profile.

In our current research, we have conducted fracture tests that involved heating zirconia fusion-warped films by a gas burner. Hydrogen gas was used as the combustion gas because it is comparatively easy to handle, compared to the double-fluid gas mentioned above.

2. Experiment Method

A schematic diagram of the hydrogen gas burner testing system that we used in our research is shown in Figure 1. The bottom surface of the 30 mm ϕ FGM sample was cooled by water. The sample's surface temperature was measured by a radiation thermometer, while the bottom temperature and the heat flux were measured by a thermocouple buried in the substrate. Heating lasted for two minutes after a steady state was reached. The experiment used $ZrO_2-8TY_2O_3$ as the zirconia, NiCrAlY as a bond coat, and Ni-20%Cr as the FGM's metallic component. After the experiment was over, the sample's surface condition was studied by an SEM and an optical microscope, and then fracture behavior was studied by cutting and grinding the sample.

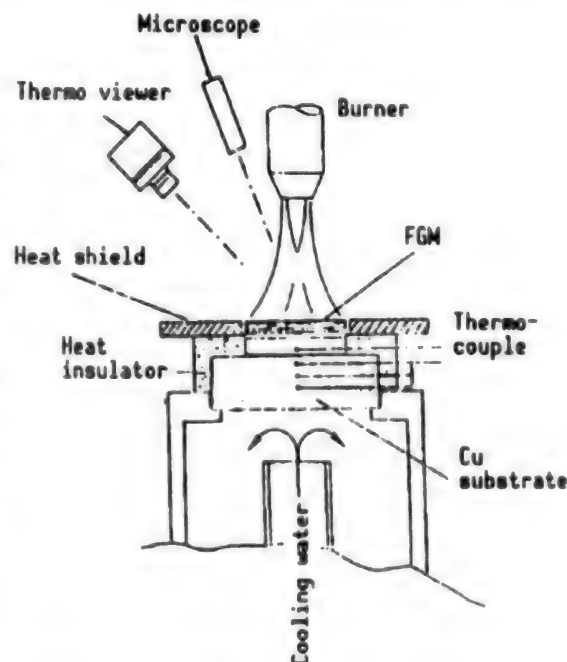


Figure 1. Diagram of Gas Burner-Heated Testing System

3. Experiment Results

Atmospheric Pressure Plasma Sprayed (APPS) Materials: Table 1 gives the testing conditions, and Photograph 1 shows the condition of the surface of a sample after a test. The measurement of the surface temperature was conducted by setting the emissivity ϵ of the radiation thermometer at 0.34. When temperature difference surpassed 400 K, a substantial material fracture was observed. The fracture presented the same appearance as one caused by laser irradiation. We studied changes in fracture conditions by changing the gas burner heat output.

Table 1. Test Results of APPS Materials

Test No.	Power/%	Ts/K	Tb/K	$\Delta T/K$	Q/MWm^{-2}
NSC-06	60	887.6	405.5	482.1	2.174
NSC-07	70	940.4	415.6	524.8	2.441
NSC-08	80	1014.4	430.8	583.6	2.948
NSC-09	50	791.4	391.2	400.2	2.117
NSC-10	40	729.9	372.5	357.4	1.519

Table 2. Test Results of LPPS Materials

Power	Ts (K)	Tb	ΔT	Q/MWm^{-2}
20	-U-	328.5K	—.-K	0.575
30	712 K	347.3	364.7	0.848
35	764 K	356.5	407.5	0.981
40	803 K	365.0	438.0	1.118
45	838 K	376.3	461.7	1.335
50	897 K	377.0	520.0	1.337
55	934 K	392.3	541.7	1.587
60	956 K	399.4	556.6	1.654
65	994 K	405.5	588.5	1.760
70	1017 K	411.8	605.2	1.862
80	1071 K	424.4	646.6	2.083

*Emissivity of radiation thermometer: 0.85

Low Pressure Plasma Sprayed (LPPS) Materials: Table 2 gives the testing conditions, and Photograph 2 shows a sectional view of an LPPS material after a test. The photo shows that vertical cracks within the ceramic layer disappear after they enter into the metallic mixed layers. This phenomenon could be used to restrain cracks within FGMs. In addition to vertical cracks, peeling (horizontal cracks) of the surface layer can be observed. In general, peeling cracks accompany vertical cracks, and in the photo it can be seen that most peeling cracks that developed accompany vertical cracks. However, there are some horizontal cracks whose development mechanism is not well understood. Such cracking is conspicuous within the ceramic layer.

4. Conclusion

We have discussed the results of a heat test of a plasma sprayed zirconia coating using a hydrogen gas burner as the heating test system. The coating can be used as a protective film to prevent heat stress fracture in FGMs. There is a high possibility that the peeling cracks have something to do with the thickness of the ceramic layer surface. We will continue our research to unravel the progressive crack mechanism, and to establish a technology to prevent an FGM layer from peeling.

5. Acknowledgement

Our current research was conducted as part of a Science and Technology Agency-subsidized program to develop the basic technology for thermal stress-alleviating FGMs.

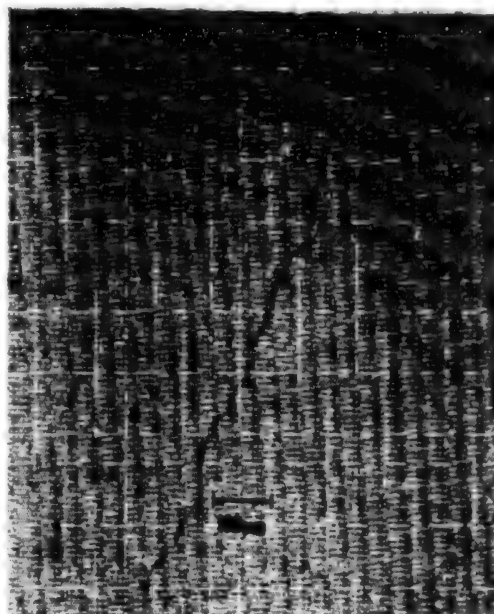


Photo 1. Surface Condition of an APPS Material After a Heat Test

Gradient Coatings Formed by Plasma Twin Torch Spraying

926C0014L Tokyo FGM '91 in Japanese 8-9 Oct 91 pp 277-279

[Article by Shigeru Kitahara, Takeshi Fukushima, and Seiji Kuroda, 4th Laboratory for Advanced Materials Processing Division, National Research Institute for Metals, Science and Technology Agency]

[Text] Abstract: For the purpose of property improvement of gradient coatings formed by the plasma twin torch spraying process, heat treatment was tried on the deposited coatings. Coatings were formed by deposition of Ni-Cr-Al-Y alloy (Ni base alloy) and Y_2O_3 (8%) stabilized ZrO_2 ceramics (YSZ) using the plasma twin torch spraying process, and heat treatment was carried out at conditions of 1,473 K, 144 h under a pressure of 1.33×10^{-2} Pa.

In the results of this experiment, it was recognized that heat treatment for Ni base alloy and YSZ coatings was effective in improving the denseness, uniformity, and cohesive strength of the coatings.

We have conducted research to fabricate a metallic-ceramic component functionally gradient material (FGM), and to improve its performance by increasing material density. This latter task was effected using the plasma twin torch spraying method. This is a method that we developed from the plasma spray method to fabricate thermal stress alleviating FGMs by controlling the structure of the material.

In our current research, we tried to fabricate an FGM in which the composition profile changes gradually from a metallic phase to a ceramic phase. This FGM was created using Ni-Cr-Al-Y alloy (Ni alloy), which has a grain diameter ranging from 10-44 μm , and Y_2O_3 (8%) stabilized ZrO_2 (YSZ) powder as the starting materials. The FGM was fabricated by spray-laminating these materials using twin plasma torches that were controlled independently. In the following, we will discuss the gradient structure of the spray-laminated film, and the results of a study that we conducted to identify the basic characteristics required for such a laminated structure. The results of our efforts to improve the characteristics of a gradient coating film by increasing its material density also will be introduced.

(1) Plasma Twin Torch Spraying Method

This method makes it possible to form a laminated composite material body on a base material by simultaneously spraying different kinds of materials at a given point on the base material from the nozzles of two plasma torches. These torches are set up so that the center axis of each nozzle meets at the spray-lamination point. The materials are sprayed under their optimum conditions.

In this plasma twin torch spraying method, little problematical mutual reaction was observed between the two plasma jet streams, and between the fused Ni-group alloy and YSZ particle currents. And it has been found that the composition of a composite laminated body can be changed freely thanks to the adoption of independent spraying torches for these two kinds of materials.

(2) Fabrication of Gradient Film

Based on the results of the above experiment, we tried to fabricate a gradient profile film composed of an Ni-Group alloy and YSZ. Prior to starting fabrication, the adhesion efficiency of the fusion material particles (sprayed material volume against adhesion volume), which is required for controlling the composition of the gradient film, was calculated. When each of the two torches was fixed at an angle of 30 degrees against the normal line of the base material plane, the adhesion rates of the Ni-group alloy and the YSZ were 70 and 43 percent, respectively, regardless of the volume of sprayed materials supplied to the torches.

Through experiments it has been found that a gradient film having an almost continuous compositional change profile from the Ni-group alloy to YSZ can be created easily by controlling the spraying volumes while making the necessary compensation for the above percentage figures.

(3) Characteristics of Fabricated Gradient Films

We have studied material density and material particle bonding strength as important basic characteristics of spray-lamination fabricated gradient films.

Density: The material density of the gradient films was evaluated by measuring the pore area rate on the sectional face of these laminated coating films. The results showed that the YSZ portion had a comparatively high pore rate of about 22 percent, while the Ni-group section had a very small pore rate. In the section that is made up of both of these materials, pore distribution changed almost in accordance with the changes in the compositional distribution pattern (* denotes points in Figure 1).

Bonding Strength: The gradient films had a lamination direction tensile strength ranging from 17-20 MPa within the YSZ layer. Fracture was confined within the YSZ layer. In contrast, within the Ni-group alloy layer the tensile strength ranged between 33-35 MPa, indicating a higher bonding strength than within the YSZ layer (* denotes points in Figure 2).

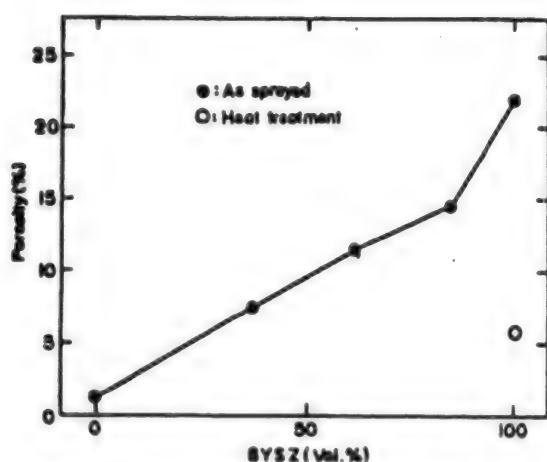


Figure 1. Porosity of Sprayed Coatings

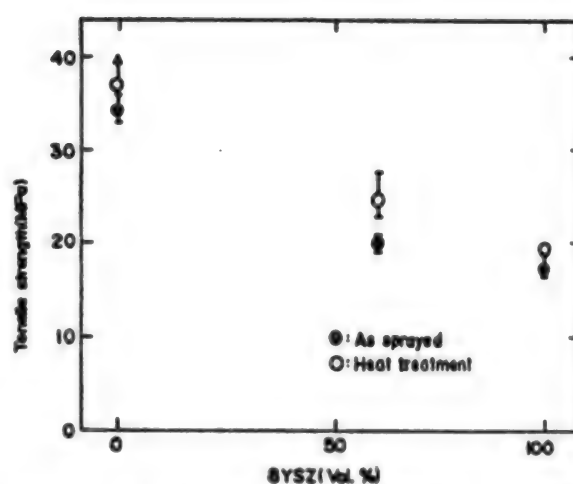


Figure 2. Tensile Strength of Sprayed Coatings

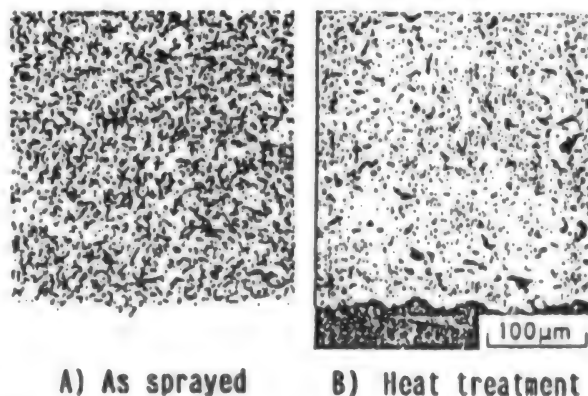
(4) Material Density in Fabricated Gradient Films

The YSZ lamination section of a gradient film that was created by the spray lamination method has a considerably large pore rate. As a means of improving material density, bonding strength, and the uniformity of the gradient film, we applied a heat treatment to the film after it was fabricated. As an example of this treatment, the YSZ lamination section of a gradient film was heated to 1,473 K for 144 hours at a pressure of 1.33×10^{-2} Pa (Table 1). This reduced the pore rate from a pretreatment value of 22 percent down to 5.7 percent, and the film's density as well as its uniformity also were improved (o mark in Figure 1; Figure 3). In addition, an improvement of bonding in the composite layers between YSZ and Ni-group alloy was achieved (o marks in Figure 2).

Table 1. Heat Treatment Conditions

Temperature (K)	Time (hours)	Atmosphere (Pa)
1,473	144	1.33×10^{-2}

Heat treating an FGM film formed by independent plasma spraying of an Ni-group alloy and YSZ has been found to be effective in improving film material density, as well as uniformity and the bonding strength, by optimizing the treatment conditions. It also has been found that the treatment provides a useful means to control pore distribution, which is necessary to improve the film's thermal stress alleviation and heat insulation capabilities.



A) As sprayed B) Heat treatment
Figure 3. Structures of YSZ Coatings

Plasma Sprayed Intermetallic Matrix Composite Coatings

926C0014M Tokyo FGM '91 in Japanese 8-9 Oct 91 pp 281-289

[Article by Masahiro Fukumoto, Department of Production Systems Engineering, Toyohashi University of Technology]

[Text] Abstract: Both Ti-Al and Mo-Si powders, which were highly mixed and bonded as raw metal materials by mechanical alloying, were introduced to rf plasma spraying. The dc plasma spraying was also conducted under the equivalent experimental conditions to compare with the rf plasma spraying results. To fabricate the intermetallic matrix composite coatings, Ti-Al-Si₃N₄ mechanical alloy (MA) precomposite powders were made and plasma sprayed. Whereas the complete Ti₃Al intermetallic coatings could not be obtained by dc plasma spraying, Ti₃Al intermetallic coating was fabricated by rf plasma spraying without after heat treatments. Intermetallic matrix composite coatings were also made in the similar spray processes of the Ti-Al/Si₃N₄ system. The phase obtained by spraying Mo-Si MA powder was fairly complicated. More detailed observation was required in this system.

1. Introduction

Ti-Al-system and Mo-Si-system intermetallic matrix composite coatings are drawing attention as promising materials for applications as superhigh-temperature environmental structural components by taking advantage of their high anticreep strength, high specific strength, and their excellent resistance to oxidation. To promote the utilization of these components in practical applications, it is important to step up basic research on improving ductility, and to develop suitable material processing methods. Applying a coating to these materials is an effective way to promote their utilization. Plasma spraying of coating materials is considered to be a very effective coating formation method because of its high heat capacity and fast coating formation speed.

In our current research, we have tried to form an intermetallic matrix composite coating having an intended material composition that does not require heat treatment after formation. The coating formation process involved rf plasma spraying of a mixture of Ti-Al-system and Mo-Si-system materials that was synthesized by the mechanical alloy (MA) method, a method used to create a material powder having an intermetallic reactivity. We also tried to

form an intermetallic matrix composite coating film by plasma spraying an MA composite powder containing scattered ceramic particles.

2. Sample Materials and Experiment Method

In our research, we took note of two kinds of intermetallic compounds: Ti_3Al , which has a high specific strength and excellent antioxidation capability, and $MoSi_2$, which has an excellent antioxidation capability, and features self-recoverability and high ductility at high temperatures. Table 1 gives the purity of a number of ceramic and metallic material powders used to produce MA powders, and the diameters of these starting material powders. An MA powder was created by putting these starting powders at the mixing ratios needed to produce an intended composite material into a revolving ball mill vial, and performing MA processing. A ceramic-scattered composite material powder was obtained by adding ceramic powder to the two metallic material powders, and processing them in the mill. To restrain the oxidation of these metallic powders, MA processing was conducted within an Ar atmosphere. The MA processing was started by putting these material powders into the vial together with methanol after repeated processes of increasing the vacuum level within the pot by a rotary pump, and after injecting Ar into the pot three times. Table 2 gives the optimum MA production conditions obtained through our experiment. The methanol content listed in the table is an initial charge value. The MA powder thus obtained was used to form a coating by rf plasma spraying. The formation of a coating using the same material by dc plasma spraying also was carried out to compare with the rf plasma-spray formed coating. Tables 3 and 4 give the plasma spraying conditions adopted in producing these coatings. All of the listed values for plasma gas flow rate, plasma output level, and the position for feeding powder into the plasma atmosphere are optimized for Ti powder. A blast-cleaned mild steel measuring $100 \times 100 \times 2$ mm was used as the substrate for rf plasma spraying, while #1000 emery-finished graphite ($\phi 100 \times 5$) was used for dc plasma spraying. To investigate element dispersion within the MA powder, we conducted pressureless sintering within an Ar atmosphere using an rf induction furnace prior to spraying under the conditions described in Table 5.

Table 1. Powder Materials Used

Ti	AMDRY	#918	<75 μm	99%
Al	METCO	#54NS	45<, <90 μm	99%
Mo	METCO	#63NS	30<, <75 μm	99%
Si	J.M.L.	#13594C	<90 μm	99.8%
Si_3N_4	CERAC	#S-1067	3<, <30 μm	98%

3.1 Establishment of MA Production Conditions and Pressureless Sintering

We conducted a study to determine an optimum powder grain size and mixing conditions for Ti-Al-system materials to use them for plasma spraying. The study, which involved changing the methanol content, showed that a methanol weight percentage of 2 wt% against material powders was the most appropriate

Table 2. Mechanical Alloying Conditions

Grinding vial	Stainless steel 3.65l
Ball pestle	Steel 12.7 mm diameter
Volume ratio of balls to vial	33%
Total weight of balls	5,000 g
Weight ratio of powder to ball	4%
Rotation speed of vial	75 rpm
Process control agent	Methanol (2 wt%)
Atmosphere	Ar (1.25 atm)

Table 3. RF Plasma Spraying Conditions

Plasma gas flow rate	28.5 l/min Ar
Sheath gas flow rate	81.0 l/min Ar+
	9.6 l/min H ₂
Carrier gas flow rate	5.0 l/min Ar
Plate power	30 kW
Powder feed rate	10, 20, 50 g/min
Spray distance from nozzle exit	25, 30 cm
Probe tip position from nozzle exit	70 mm
Atmosphere	250, 500 Torr Ar + H ₂
Substrate	Mild steel

Table 4. DC Plasma Spraying Conditions

Primary gas	35.4 l/min Ar
Secondary gas	7.1 l/min H ₂
Carrier gas	5.0 l/min
Powder feed rate	10.0 g/min
Plate power	30 kW
Chamber pressure	200, 250 Torr
Spray distance	16.0 cm
Substrate	Graphite

Table 5. Pressureless Consolidation and Sintering Conditions

	Ti-Al system	Mo-Si system
Furnace	RF furnace	RF furnace
Temperature	700, 900, 1,500°C	1,575°C
Holding period	3, 5 min	3 min
Sample weight	3 g	3 g
Sample	MA powder Mixed powder	MA powder
Atmosphere	Ar (1 atm)	Ar (1 atm)

level to obtain an optimum grain size at a powder recoverability ranging from 85-90 percent. In this research, grain size was measured by an X-ray grain distribution measurement system. Increasing the methanol weight percentage improved recoverability to about 95 percent, while a decrease below 2 wt% caused the powder to form into clumps and to adhere to the vial and balls, thereby reducing recoverability to 77 percent. We also conducted another experiment in which the duration of MA processing was 2, 5, 20, or 50 hours,

while the methanol weight percentage was fixed at 2 wt%. Figure 1 shows the sectional structure of the MA powder that was obtained after MA processing for 20 hours. Figure 2 shows the powder grain size distribution. In the cases of MA processing for two and five hours, many Ti powder clusters were found in the agglomerated powder, while the MA powder that was processed for more than 20 hours contained the lamellar structure of fine Ti and Al particles, a condition suitable for creating a ceramic particle-dispersed composite powder. Figure 2 indicates that in MA processing the mean diameter of the material powder alternately increases because of agglomerations and decreases because of crumbling of the agglomerated powder up to a processing time of 20 hours. It also can be seen that a mean diameter of about 25 μm , a diameter suitable for plasma spraying, can be obtained with 20 hours of MA processing. Based on these results, we created an MA powder for plasma spraying by setting the methanol weight percentage at 2 wt%, and MA processing time at 20 hours for Ti-Al-system materials. It was found that the change in the weight of the balls before the start of MA processing and after the processing was finished under above conditions was about ± 0.1 g. This indicates that the introduction of foreign metallic elements into the processed powder is negligible.

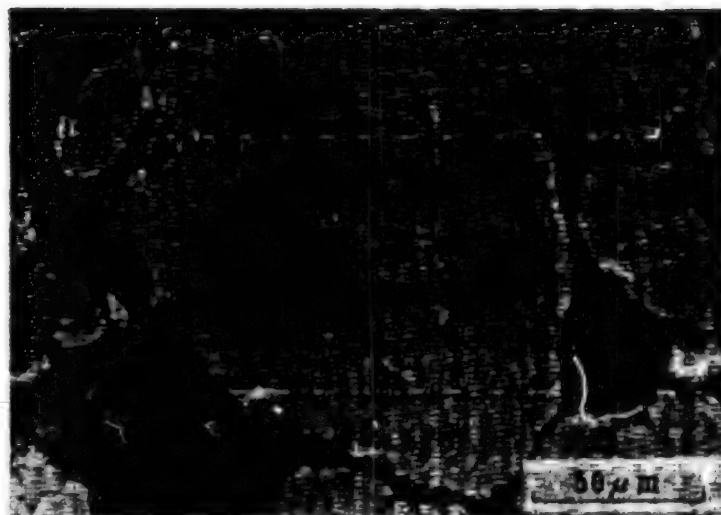


Figure 1. Cross Section of Ti-Al 20 Hours MA Powder

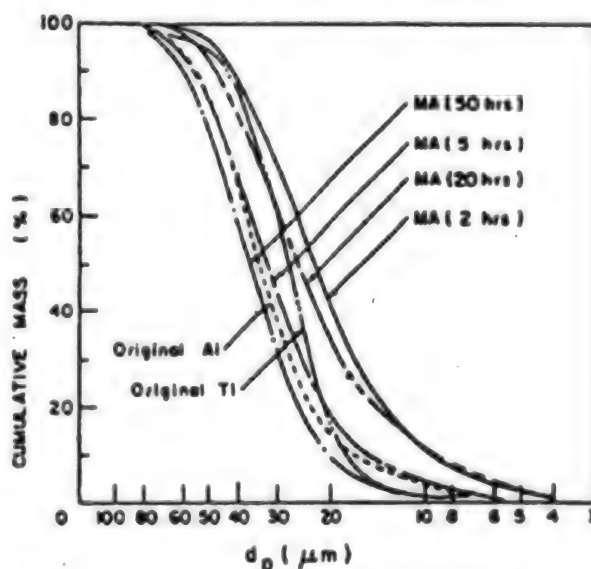


Figure 2. Powder Size Distribution

blung of the agglomerated powder up to a processing time of 20 hours. It also can be seen that a mean diameter of about 25 μm , a diameter suitable for plasma spraying, can be obtained with 20 hours of MA processing. Based on these results, we created an MA powder for plasma spraying by setting the methanol weight percentage at 2 wt%, and MA processing time at 20 hours for Ti-Al-system materials. It was found that the change in the weight of the balls before the start of MA processing and after the processing was finished under above conditions was about ± 0.1 g. This indicates that the introduction of foreign metallic elements into the processed powder is negligible.

To study element diffusion conditions within the MA powder, we performed pressureless sintering using the powder. Figure 3(A) shows the result of X-ray diffraction analysis conducted with another sintered powder. For a comparison,

the result of X-ray diffraction analysis conducted with another sintered powder, composed of a mechanical mixture of Ti and Al powders, is shown in Figure 3(B). According to these analyses, MA powder attains a higher Ti_3Al peak in the diffraction analysis than the mechanically mixed Ti/Al powder when sintering is conducted under the same conditions. This indicates that the MA powder has a higher element diffusion reactivity between the two material powders involved. Based on these results, it can be expected that an intermetallic matrix composite coating can be formed through the progress of diffusion reaction during the plasma spraying process of this MA powder.

3.2 Plasma Spraying of Ti-Al-System MA Powder

Figure 4 shows the sectional structure of a coating film that was created by rf plasma spraying of a Ti-Al-system MA powder. The concave portions between adjoining powder grains in the figure were created by the selective etching of grain boundaries. The density in the coating thus created is not so high. However, it can be seen that the coating film is composed of a uniform phase wherein the lamellar structure that was observed in the MA powder has completely disappeared. After cutting the coating on a plane parallel to the boundary with the substrate, and after polishing the cut surface, an X-ray diffraction analysis was conducted to study the compositional pattern. Figure 5(B) shows the results. For a comparison, an X-ray analysis of an MA powder is also shown in Figure 5(A). These analyses reveal that the MA powder displays peaks for Ti and Al as its starting material powders, while the sprayed coating displays peaks for Ti_3Al only.

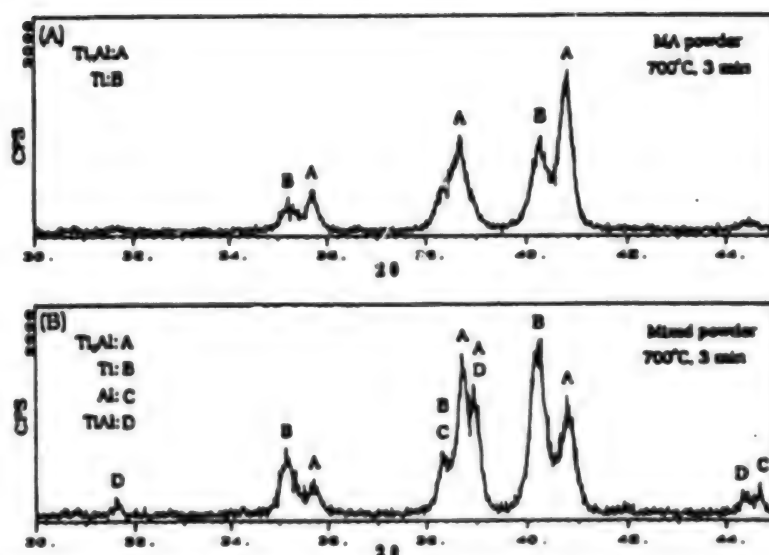


Figure 3. X-Ray Diffraction Patterns of Consolidated Powders

(A) MA powder; (B) Mixed powder

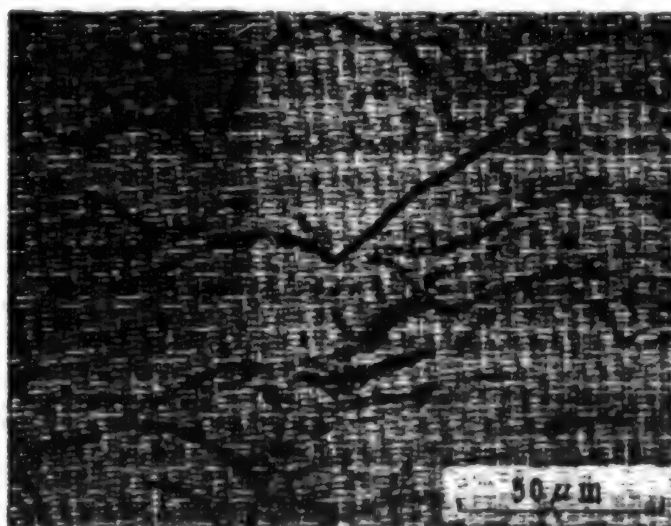


Figure 4. Cross Section of the Coating (Etched, 500 Torr, 50 g/min, 30 cm)

There have been a number of attempts to form intermetallic matrix composite coatings by fusion spraying a mechanically mixed powder or a granulated coating powder. However, no uniform compositional pattern and no satisfactory intermetallic matrix composite structure has been obtained in the coatings created using these powders without giving them an additional treatment. The reasons for this are the lack of diffusion reactions among the different metallic materials

involved, and the poor wettability between them, which cause the materials to separate. In contrast to these powders, the MA powder used in this experiment made it possible to attain a strong bond between the two metallic materials, which formed a neat lamellar-like compositional pattern through cold welding. It is believed that the MA powder condition made it possible for the diffusion reaction to occur satisfactorily during the short fusion spraying time. These results indicate that an MA powder can be suitable for forming intermetallic matrix composite coatings through diffusion reactions between different kinds of metallic materials.

In addition, we conducted pressureless sintering of a Ti-Al-Si₃N₄MA powder, as well as fusion spraying of the powder. The Ti-Al/Si₃N₄ composite MA powder was created under almost the same conditions as those used to produce the Ti-Al-system MA powder. The only difference is that the weight percentage of methanol was increased to 5 wt%, because, in this material system, the powder's adhesion to the balls was considerably higher at 2 wt%. Figure 6 shows the sectional composition of the composite MA powder thus created. From this figure it can be seen that Si₃N₄ powder grains scatter uniformly between Ti-Al lamellar layers, and this indicates that the MA method is effective in producing a powder-grain-scattered composite powder, as described above.

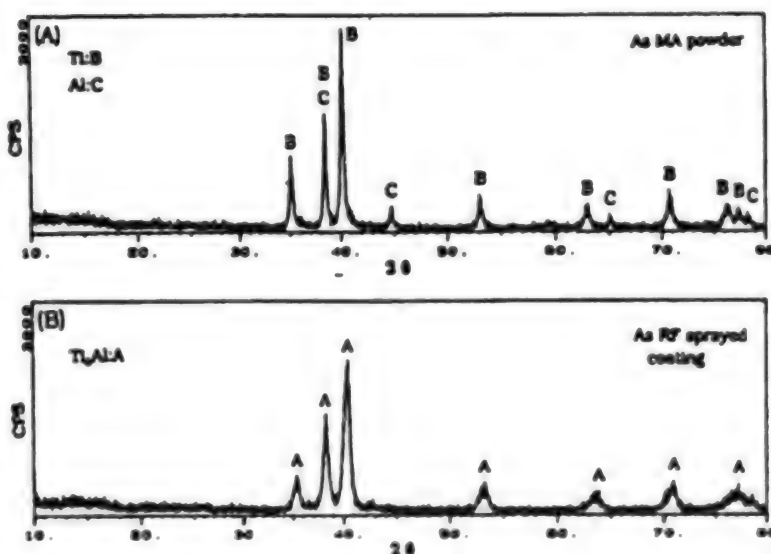


Figure 5. X-Ray Diffraction Patterns
(A) as MA powder; (B) as RF sprayed coating



Figure 6. Cross Section of Ti-Al/Si₃N₄ Precomposite MA Powder (Vf = 10%)

Using the ceramic powder-scattered Ti-Al/Si₃N₄ composite MA powder thus created, rf plasma spraying was conducted under the same conditions as those used with the Ti-Al-system powder. This created a coating with an average hardness of about 1,000.

Figure 7 shows the results of an X-ray diffraction

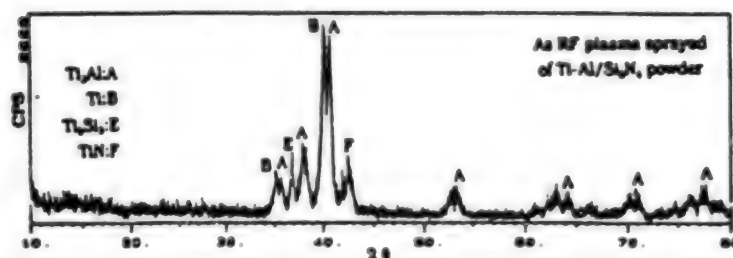


Figure 7. X-Ray Diffraction Pattern of Composite Coating

analysis of this coating structure, which indicates the presence of Ti₃Si₂ and TiN phases, in addition to the Ti₃Al phase, within the coating. This suggests that there was a reaction between the matrix material (Ti-Al) and the scattered material grains (Si₃N₄) during the plasma spray process. The observation of the coating's sectional structure found the presence of comparatively large-diameter Si₃N₄ grains that did not bond well with the matrix material, and boundary peeling was observed in some of these grains. This demonstrates the importance of selecting a scattered material powder that has good reactivity and wettability with the matrix material. Figure 7 indicates the presence of a pure Ti phase within the coating. Further studies must be made to find the mechanism that caused the appearance of such a phase.

For a comparison with an rf plasma sprayed coating, a dc plasma sprayed coating was created using Ti-AlMA powder. Figure 8 is a sectional view of the dense two-phase structure of this coating. An electron probe microanalyzer (EPMA) analysis of this coating found a difference in the Al density of these two phases of the materials (Figure 9). An X-ray diffraction analysis of this coating also found the presence of a pure Ti phase (Figure 10). These results suggest that a dc plasma sprayed coating is formed through the following processes. First, as shown in Figure 8, the coating

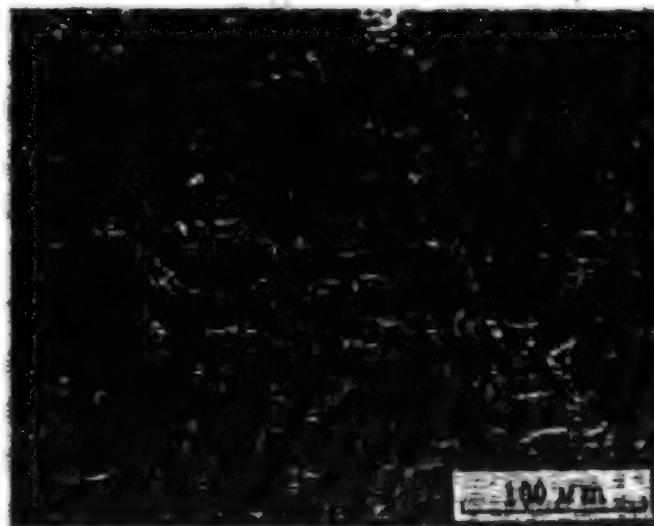


Figure 8. Cross Section of the Coating Obtained by DC Plasma Spray

structure displays a laminar condition pattern that runs parallel to the coating surface, and this structure is clearly different from the lamellar structure observed in the original MA powder. It is believed that this laminar structure was created as a result of a fused powder separating into two phases for some unclear reasons in the process of diffusion and solidification. We have found that separation between ceramics and metallic materials occurs when forming a dc plasma sprayed coating using a ceramic metallic material composite powder because of problems associated with wettability between the two materials, and because of the high plasma acceleration. The possibility

that nonuniformity in element density may occur within the plasma sprayed material grains due to reactions between these grains and the ambient atmosphere has been pointed out in other studies. In our experiment, which also involved dc plasma spraying of the MA powder, there was a possibility of material separation occurring due to this reaction, and because of the high plasma acceleration speed. When this separation occurs, it hinders the diffusion reaction, and the presence of pure Ti remaining in the dc plasma sprayed coating can be traced to this source.

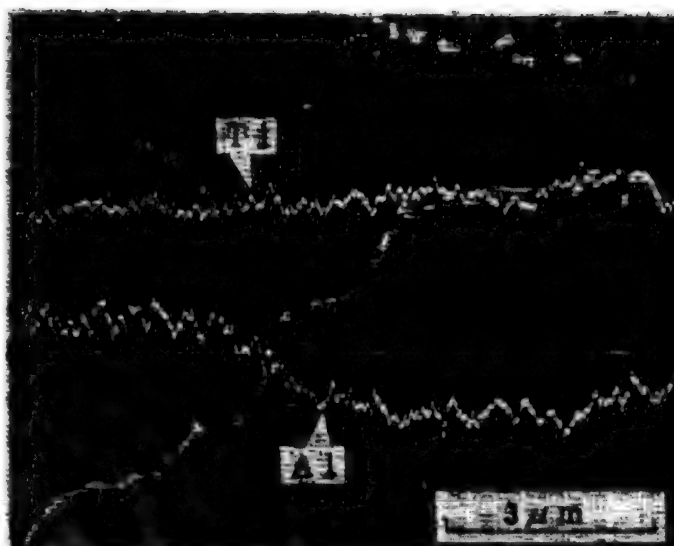


Figure 9. Line Analysis of dc Sprayed Coating

3.3 Pressureless Sintering of Mo-Si-System MA Powder and Plasma Spraying

We also created an Mo-Si-system MA powder, and conducted pressureless sintering and rf plasma spraying using this powder. The MA powder was created under the same

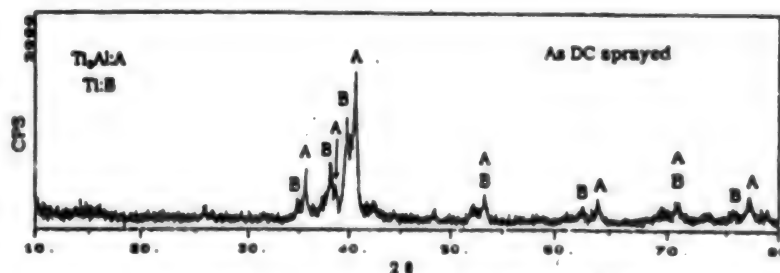


Figure 10. X-Ray Diffraction Pattern of dc Sprayed Coating

conditions as those used to create its Ti-Al counterpart, as listed in Table 2. A blackish Mo-Si-system MA powder was obtained after 20 hours of MA processing. The poor ductility of both Mo and Si caused the resultant MA powder to display a fine particle agglomerated structure—a structure that is different from the lamellar structure of its Ti-Al-system counterpart. Figure 11(A) is a sectional view of the Mo-Si-system MA powder. Almost no adhesion of the powder to the balls and the vial containing the balls was observed, and powder recoverability reached about 97 percent. The decrease in the weight of the balls after the MA processing was finished stood at about 0.6 g. This corresponds to about 0.3 percent of the weight of the recovered powder, which raises the possibility that some of the ball material may have mingled with the MA powder. Pressureless sintering of this powder at a preset temperature produced a low-grade sintered powder composed of highly porous agglomerations of the material powder. Figure 12(A) shows the result of an X-ray diffraction analysis of this powder. The results indicate that the sintered powder is composed mostly of MoSi_2 , with the presence of a smaller amount of $\text{Mo}_{0.5}\text{Si}_{1.3}$. Figure 11(B) is a sectional SEM photo of a coating that was created by rf plasma spraying the Mo-Si-system MA powder under the conditions listed in Table 3. Figure 12(B) shows the results of an X-ray diffraction analysis of the cross section of this coating. The SEM photo reveals the presence of three

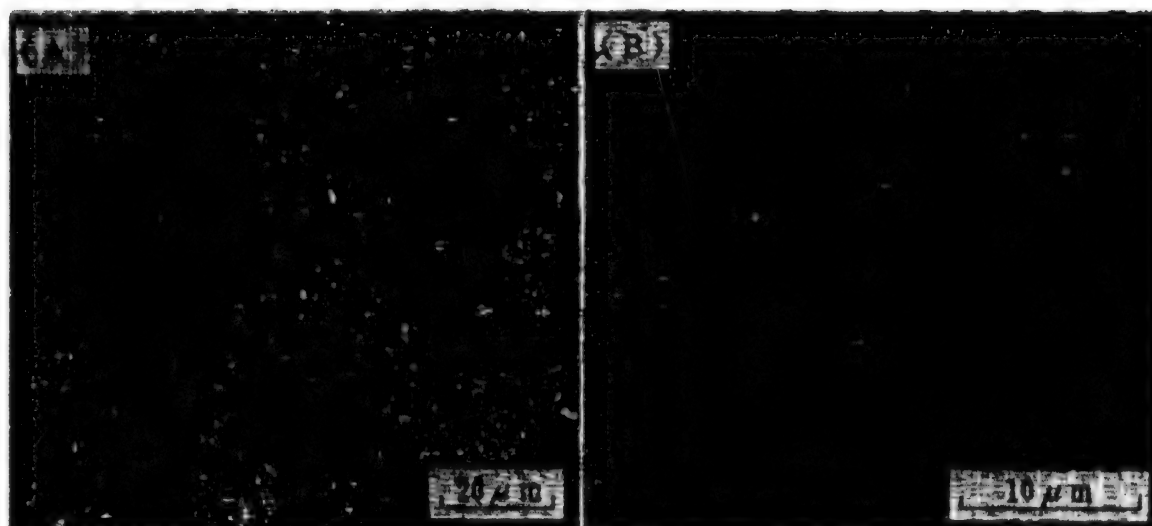


Figure 11. Cross Sections of Mo-Si Material System

phases having different shades, while the X-ray diffraction analysis reveals the presence of Mo_3Si_3 and Mo_3Si phases in addition to the MoSi_2 phase. The relationship between these three SEM phases and the same number of X-ray diffraction analysis phases has yet to be investigated.

Through these experiments and analyses, it has been found that the compositional differences in Mo-Si-system material coatings depends on thermal load conditions. These results demonstrate that in this material system,

it is important to ensure an optimum material powder mixing ratio in MA processing, together with optimum plasma spraying conditions in forming coatings.

4. Conclusion

The research presented in this paper focused on creating intermetallic composite coatings and intermetallic matrix composite coatings by sintering material powders under pressureless conditions; by creating Ti-Al system, Ti-Al/ Si_3N_4 -system, and Mo-Si-system MA powders; and by plasma spraying these powders. The results can be summarized as follows:

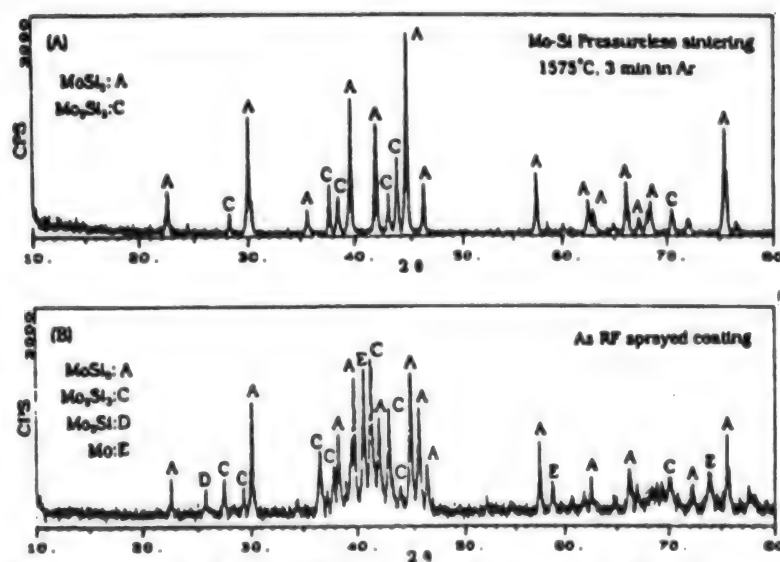


Figure 12. X-Ray Diffraction Pattern of Mo-Si Material

(A) Sintered powder; (B) rf sprayed coating

(1) With regard to the Ti-Al-system powder, the MA processing conditions necessary to realize the powder grain size and powder mixing ratio suitable for creating good plasma sprayed coatings are 2 wt% for the weight percentage of methanol against powder weight, and 20 hours for MA processing time.

(2) A good Ti_3Al single-phase intermetallic composite coating has been created without post-coating heat treatment. This was achieved by rf plasma spraying using an optimized MA powder, and it is possible to create an intermetallic matrix composite coating by plasma spraying a ceramic particle-scattered composite MA powder.

(3) In plasma spraying a composite MA powder, in selecting the scattered material powder it is important to take into account the reactivity and wettability between the matrix material powder and the scattered material powder.

(4) In dc plasma spraying of an MA powder, a coating composed of two different material phases in laminar structure has been obtained. One possible reason for this is the high acceleration speed of the plasma jet.

(5) The Mo-Si system MA powder undergoes a compositional change when it is subjected to repeated heat load processes, such as pressureless sintering and plasma spraying. Because of this, it is important to determine a material powder mixing ratio that takes this change into account when creating Mo-Si-system intermetallic composite materials.

Effect of Microstructure on Properties of Sintered FGMs

926C0014N Tokyo FGM '91 in Japanese 8-9 Oct 91 pp 291-294

[Article by Shunsuke Yamakawa, Akira Kawasaki, and Ryuzou Yatanabe, Faculty of Engineering, Tohoku University]

[Text] **Abstract:** This paper reports an evaluation of the mechanical properties of a metal/ceramic composite in relation to microstructural features. A zirconia/stainless steel mixed composite having definite metal/ceramic ratios was fabricated by a powder metallurgical method. A variation of flexural strength has been found to depend on the composition and microstructure. An acoustic emission (AE) analysis for the fracture behaviors during crack propagation during loading in the indentation fracture test along with microstructural investigation was made. It has been found that fracture behaviors are strongly dependent on the continuity and morphology of the metallic phase; that means that the skeletal to dispersive structural transition and the cluster formation dominate the fracture behaviors.

1. Introduction

In zirconia/stainless steel-system functionally gradient materials (FGMs), partially stabilized ZrO_2 (PSZ) becomes a scattered phase in a stainless steel phase-dominated composition, and, conversely, stainless steel becomes a scattered phase in a zirconia-dominated composition. When an FGM is composed of an equal amount of these material phases, a continuous structure of these materials is formed. These changes in material composition cause changes of mechanical characteristics. It is known that four-point flexural strength in a ceramic-continuing FGM does not conform to the mixture linear rules, and in the ceramic-rich side of the material it displays W-shaped complex flexural strength characteristics (Figure 1).

In our research, the observation of crack propagation in an FGM was made by press-fitting a Vickers indentator into the material. The relationship between material strength and material composition also was studied by combining the indentator test with an acoustic emission (AE) test.

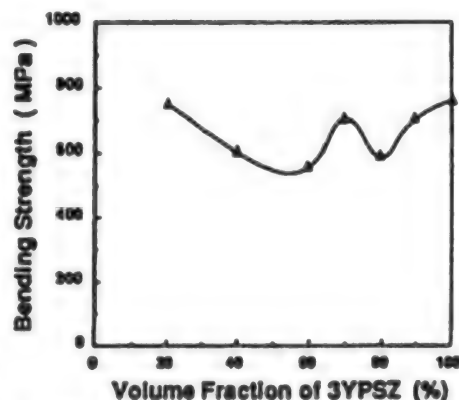


Figure 1. Relationship Between PSZ Composition Ratio and Four-Point Flexural Strength

2. Experiment Method

The powders used in our experiment consisted of $\text{ZrO}_2\text{-3mol\%Y}_2\text{O}_3$, with an average grain diameter of $0.07\text{ }\mu\text{m}$, and of SUS304 stainless steel powder, with an average diameter of $3\text{ }\mu\text{m}$. We used various combinations of these powders to produce powders with mixture ratios of 20, 40, 60, 70, 80, and 90 volume percent PSZ by mixing them in a ball mill. These powders were sintered at normal pressure in an H_2 environment of $1,350^\circ\text{C}$ for 1 hour after metallic and cold isostatic pressing (CIP) moldings. These sintered compacts were mirror finished on the surface, and then a Vickers indentator was press-fitted onto the surface. The AE waves generated by the fitting were measured simultaneously using LOCAN (Physical Acoustics Corp.). The measurement was made by setting preamp amplification at 40 dB, main amp amplification at 40 dB, and the threshold value at 32 dB. The sensed waves were converted into electric signals and sent to an envelope detection device to obtain various parameters on their amplitude, energy, and duration.

3. Results

(1) Effect of Composition on Hardness and Fracture Toughness

The length of the cracks caused by the press-fitting of the indentator decreased when the stainless steel content increased, and at a indentator load of $P = 20\text{ kg}$, cracks were no longer detected at 40 volume percent PSZ. Consequently, fracture toughness data were obtained by studying cracks in these samples having PSZ contents higher than 60 volume percent. It was difficult to confirm whether the generated cracks were of the Palmquist or Median/Radial type. Based on our analysis, we determined that they were of the Palmquist type. Considering that the l/a value was smaller than 2.5 for all of these powder samples, we adopted the Niihara evaluation formula described below:

$$(K_{\text{IC}}\phi/\text{Ha}^{1/2})(\text{H}/\text{E}\phi)^{0.4} = 0.035 (l/a)^{-1/2}$$

where E: Young's modulus,
H: hardness, and
 ϕ : restraining coefficient (43)

Figure 2 shows the fracture toughness measurements. It can be seen that fracture toughness does not change significantly from 100 volume percent PSZ down to around 80 volume percent PSZ. However, it sharply increases at 70 volume percent PSZ.

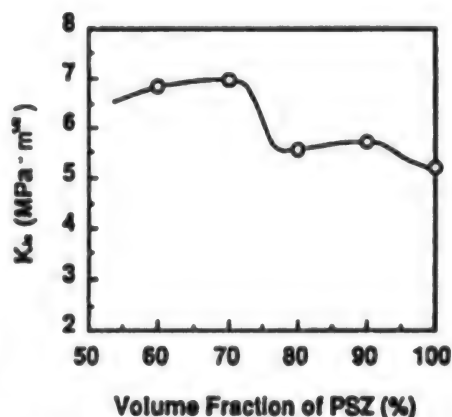


Figure 2. Relationship Between PSZ Composition Ratio and Fracture Toughness

(2) Condition of Generated AE Signal

(a) Condition of AE signal in 3Y-PSZ

Figure 3 shows the changes in the indentator load level over time when the indentator was press-fitted. The load level abruptly shoots up during the very short initial fitting stage, and then it remains at a constant level. Most of the AE signals are generated when the load increases abruptly. Figure 4 shows the relationship between PSZ AE signal amplitude and the cumulative signal value under different load conditions—5, 10, and 20 kg. When the load level is low, small amplitude signals dominate; as the load increases, the ratio of larger amplitudes increases. Figure 5 shows the relationship between the PSZ AE energy level and the cumulative signal value. When the load is small, low energy signals dominate, with the ratio of high energy signals increasing in proportion to an increase of the load.

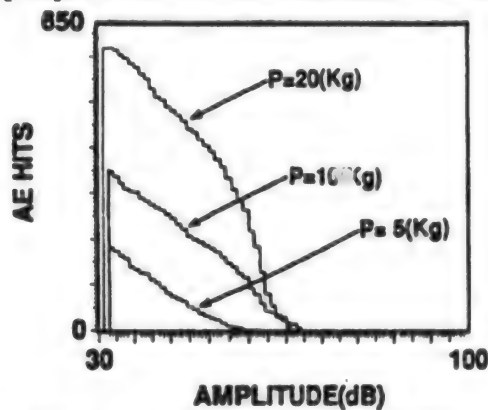


Figure 4. Relationship Between PSZ AE Amplitudes and Cumulative Signal Values

It is believed that in PSZ, AE signals are generated by a stress-induced transformation, and by the appearance of cracks. It also is believed that the low amplitude, low energy signals that are generated under low load conditions, which cause small crack propagation, are generated by the transformation, and that the large amplitude, high energy signals that occur under high load conditions, which cause larger crack propagation, are generated by the appearance of cracks.

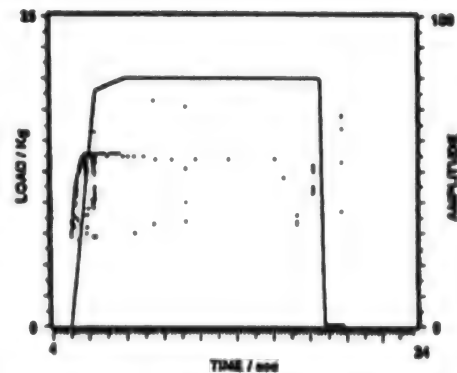
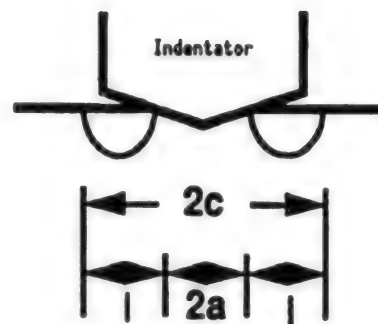


Figure 3. Changes in Load Level Over Time and AE Characteristics of 3Y-PSZ

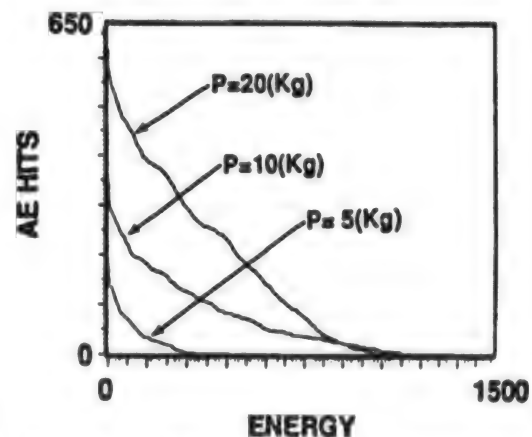


Figure 5. Relationship Between PSZ AE Energy Levels and Cumulative Signal Values

(b) Compositional dependence of AE signals

Figure 6 shows the relationship between the compositional ratio of the cumulative signal value. The cumulative level declines as the stainless steel content increases, and when the PSZ content is less than 40 volume percent, no such signals were detected. Based on these results, we believe that the stainless steel itself is AE inactive, and consequently, that no signals are generated when friction occurs between the indentator and a material sample.

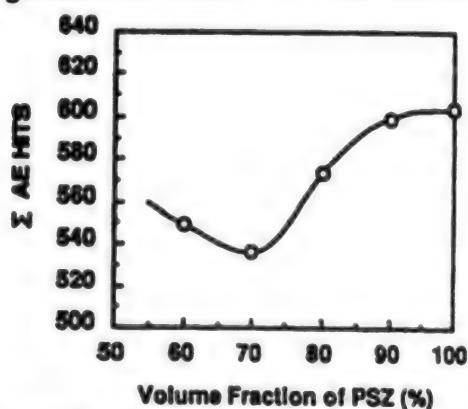


Figure 6. Relationship Between PSZ Compositional Ratio and Total Signal Value

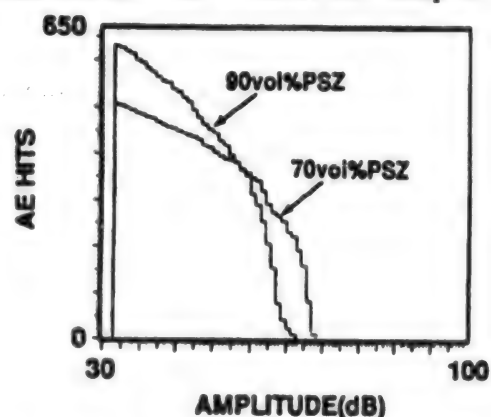


Figure 7. Relationship Between AE Amplitudes of PSZ/SUS Composite Materials and Cumulative Signal Values

Figure 7 shows the relationship between generated signal amplitude and cumulative value distribution. As representative examples, the cases of 70 volume percent PSZ and 90 volume percent PSZ are shown. It can be seen that when the stainless steel content increases, the small amplitude signal ratio declines, while the large amplitude signal ratio gains. The signal energy vs. cumulative signal value distribution curves (Figure 8) indicate that an increase in the stainless steel content causes a decline in the low energy signals, and an increase in the high energy signals.

These results indicate that the signals associated with a stress-induced transformation in PSZ decrease when the stainless steel content increases, and that, instead, large amplitude, high energy signals become increasingly dominant. In a PSZ/SUS composite material containing 90 volume percent PSZ, the stainless steel phase exists as a scattered phase of circular steel grains. In this composite material, a crack runs through a zirconia phase section, and through the boundary between the two material phases. Judging from the fact that no signals were detected when a boundary break occurred, we believe that bonding in the boundary was not strong. This indicates that the scattered phase does not contribute much

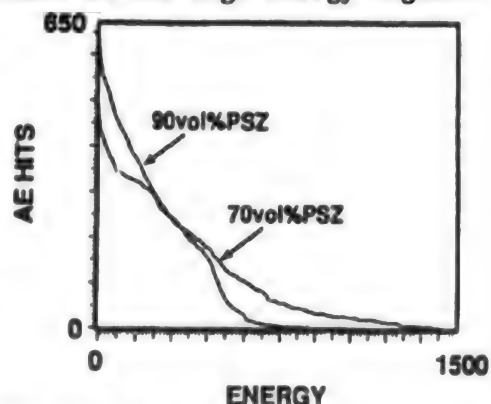


Figure 8. Relationship Between AE Energy Levels of PSZ/SUS Composite Materials and Cumulative Signal Values

to improving fracture toughness or strength. When the PSZ content decreases to 70 volume percent, the shape of the scattered stainless steel phase becomes more complex, and the phase bridges the cracks (arrows in Figure 9). It is believed that this bridging serves to improve flexural strength and fracture toughness. It is common knowledge that signals generated by a boundary break between the mother phase and the scattered phase, by friction between different phases, and by fractures in the scattered phase have a high AE activation level. Consequently, the degree of improvement can be ascertained by measuring the high energy signals that are detected around 70 volume percent PSZ.

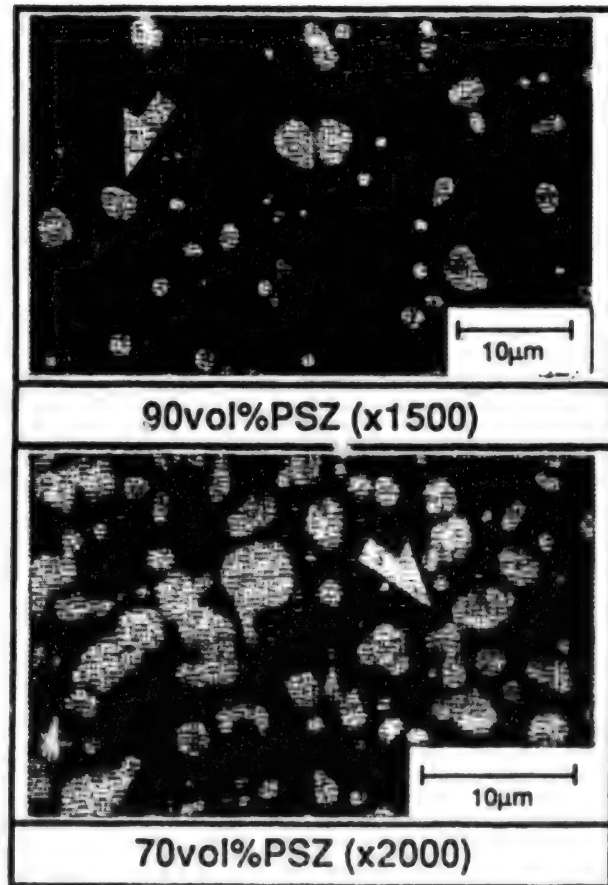


Figure 9. Photos of Cracks in Two Types of PSZ/SUS Composite Material Samples

Joining of Metal, Alloy to Magnesia Using FGM

926C00140 Tokyo FGM '91 in Japanese 8-9 Oct 91 pp 295-297

[Article by Koji Atarashiya, High Temperature Metal Chemistry Laboratory, Metals Research Institute, Faculty of Engineering, Hokkaido University]

[Text] Abstract: In order to obtain joints of nickel and magnesia, a functionally gradient material of Ni-NiO was used for joining fillers. The joints of permalloy and magnesia were also done with the same fillers. The joints of cobalt and magnesia were accomplished using a functionally gradient material of Co-CoO. Furthermore, in order to obtain joints of nickel and magnesia, I tried to use a functionally gradient material of Ni-MgO. Such a joint has no flat joining interfaces which are weak point against fractures. Thus, bending strength of the joints increased more than that of the direct joints of metal or alloy and magnesia. It seems that using the FGM block filler in joinings is useful to reduce residual thermal stress.

The FGM block was made by the process of powder metallurgy. The several layers consisting of metallic powder and the mixed powder of metal and metal oxide, whose composition gradually changed, were compacted in a steel die under pressure. The compacts were sintered at 1,573 K for several hours in air.

1. Introduction

This author has conducted a series of Ni-MgO, Co-MgO, Fe-MgO, and Cr-Al₂O₃ bonding tests using functionally gradient material (FGM) fillers under pressureless, heated conditions in the air. In all of these cases, bonding was achieved when the oxides of the metals formed complete solid solutions with magnesia or alumina. In these bonds, bonding reaction layers were formed by diffusion of the materials involved, and, in this sense, these bonds can be regarded as having been achieved using FGMs as fillers. A study of the interface between a metallic layer and a solid solution layer in these bonded samples revealed discontinuous and flat features, and it is believed that this interface condition causes a degradation of the bonding strength. In order to improve this interface, a bonding experiment has been conducted using FGMs composed of metals and their oxides as fillers. The results showed an improvement of bonding strength through the alleviation of residual stress in the interface.

2. Experiment Method

The experiment involved the use of metal and ceramic powders. These powders were mixed to form a functionally gradient structure, and then the mixture was molded within a cylindrical steel die (inner diameter: 13 mm) at a pressure of 20 MPa. The green compacts thus obtained were sintered in an argon or nitrogen environment at 1,573 K using an electric furnace.

The compositions and structures in the longitudinal as well as the lateral sections of these FGMs were studied by scanning electron microscope (SEM), EDX, and electron probe microanalyzer (EPMA). The bonding of these FGM samples and metallic samples took place within an air or Ar gas flow environment at temperatures ranging from 1,373 to 1,673 K.

3. Results

The bonding of a nickel sample to a magnesia sample formed a continuous structure of Ni/Ni-NiO FGM/NiO-MgO ss/MgO. Figure 1 is a photograph of this bonding-formed structure.

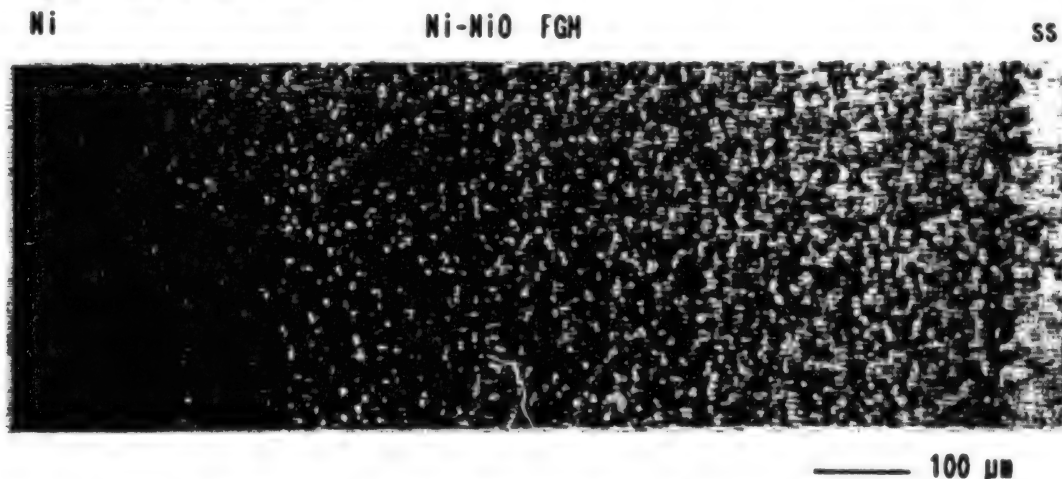


Figure 1. Optical Microscope Photo of Ni/Ni-NiO FGM/NiO-MgO ss Structure

After a bonding process at 1,573 K for 12 hours, a three-point flexural strength of 130 MPa was attained. This compares with a maximum three-point flexural strength of 55 MPa that was achieved in direct bonding between nickel and magnesia samples. The Weibull's coefficient also has approved from 6 for the direct bonding to 11, thereby improving bonding reliability.

A cobalt sample was bonded to a magnesia sample to form a structure of Co/Co-CoO FGM/CoO-MgO ss/MgO (Figure 2). Bonding at 1,373 K for 14 hours resulted in a three-point flexural strength of 35 MPa. This is a substantial improvement from the maximum strength of 20 MPa attained through direct bonding between cobalt and magnesia samples.

The bonding of Permalloy sample to a magnesia sample was attained through a structure of Permalloy/Ni-NiO FGM/NiO-MgO ss/MgO. In the bonding of this

alloy-system material, the presence of iron oxides on the FGM/NiO-MgO ss interface resulted in a poor bonding strength than that obtained in the two cases discussed above. The three-point flexural strength attained after bonding at 1,473 K for six hours stood at 10 MPa.

The use of an Ni-MgO FGM filler for bonding between nickel and magnesia samples attained a high three-point flexural strength of 100 Mpa after bonding was carried out at 1,573 K for 12 hours. This bonding was attained through a structure of Ni/Ni + NiO-MgO ss + MgO/MgO. This interlocked three-dimensional FGM structure is probably the reason for such a high flexural strength value.

4. Conclusion

The experiments described in this article have demonstrated that stress alleviation at the bonded interface between magnesia and metal-alloy materials can be attained effectively by forming a complete solid solution bonding layer or by bonding using FGM fillers. The formation of these bonding layer structures involves a chemical process, and bonding is achieved through solid phase diffusion. The residual stress produced by bonding can be relieved by the moderate presence of pores, by the mixed presence of metal-alloy and metal-alloy oxides, or by the presence of a gradient structure composed of these oxides.

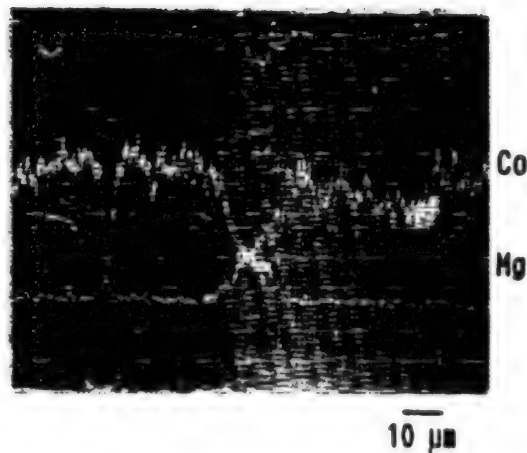


Figure 2. SEM Photo of MgO/Co-CoO FGM Structure and Results of a Linear Analysis of the Structure

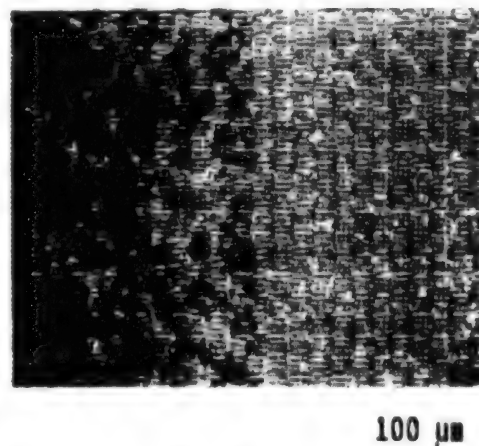


Figure 3. SEM Photo of Ni + NiO-MgO ss + MgO/MgO Structure

Study of Cooling Structure to FGM

926C0014P Tokyo FGM '91 in Japanese 8-9 Oct 91 pp 299-303

[Article by Shinya Akama and Shin-ichi Ohama, Ishikawajima-Harima Heavy Industries, Co., Ltd.]

[Text] Abstract: In the thermal fatigue evaluation test for an FGM at high-temperature difference, the ceramic-rich side of the FGM is heated, and the opposite side is cooled by a coolant passing through the grooves in the cooling structure that is bonded to the metal-rich side of the FGM. In the case of bonding the cooling structure to the FGM, it is necessary to void the deformation of the FGM by a heating process; thus the electroforming process is a suitable method, because it is free from a heating process. The Ni-electroforming process of a small panel for a thermal fatigue test of the FGM was investigated.

1. Introduction

When using FGMs in the walls of the combustion chambers of a scramjet engine for the projected space plane, or in the strut, the FGMs must be provided with a cooling system, and this necessity poses a major problem. To address this problem, the sample to be used in the second research phase of the Science and Technology Agency-subsidized FGM development program will use a small panel shape which combines an FGM plate with the structural cooling panel. The panel will be used to evaluate the characteristics of the FGM in a simulated actual utilization environment. The panel will be subjected to a large temperature difference environment to test the material's thermal fatigue capability. The panel is designed for an evaluation test that involves the cyclical heating of one surface of the panel while cooling the other surface. This report presents the results of a study on fabricating a small FGM panel equipped with a cooling structure to evaluate the FGMs thermal fatigue characteristics using the electroforming method. The report also describes the fabrication of an experimental panel by employing an SUS304 plate as a dummy FGM plate and by the Ni electroforming method.

2. Method for Creating Coolant Channels for FGM Plate Cooling

Figure 1 shows the outline of the thermal fatigue test panel.

The panel is composed of an FGM plate, a cooling structure, and coolant inlet/outlet manifolds with the shape and size shown in the figure. In fabricating the small test panel, it was important to ensure good contact between the FGM plate and the cooling structure. There are a number of methods that can be used to achieve this. These methods include: 1) synthesizing an FGM layer on a cooling structural panel; 2) bonding an FGM plate to a cooling structural panel—a) by brazing, and b) by diffusion bonding; and 3) electroforming (a layer of coolant channels is formed on an FGM plate by raising the height of the plated layer on the plate).

In the first case, the layer of sprayed material grains must be sintered by the hot isostatic pressing (HIP) method. In the second case, there is a possibility that deformations may occur on the FGM plate because of the high temperatures involved in the bonding process, and these deformations adversely affect the ensuring processing steps. In contrast, the third method makes it possible to carry out processing at room temperature.

Based on these considerations, we adopted an electroforming method that causes little heat-associated deformation—and little thermal stress—in the processing.

For electroforming, two methods are available—copper electroforming and Ni electroforming. The advantage of the former is the high thermal conductivity of the copper plate. The latter method, however, makes it possible to form a stronger plate than can be achieved with the copper method. Thus, we adopted the Ni electroforming method for our experiment.

3. Fabrication of Small panel by Electroforming Method

1) Small Testing Panel

Figure 2(a) is a schematic diagram of the small testing panel to be created by the electroforming method.

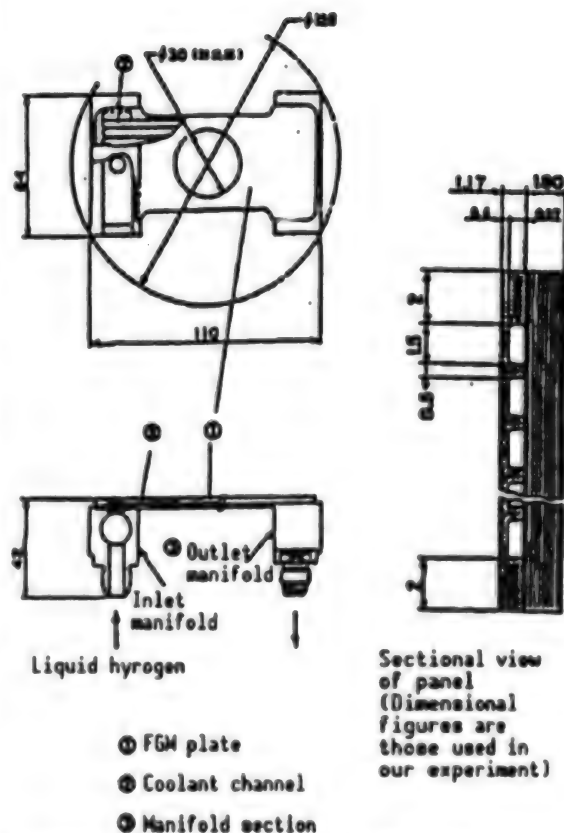
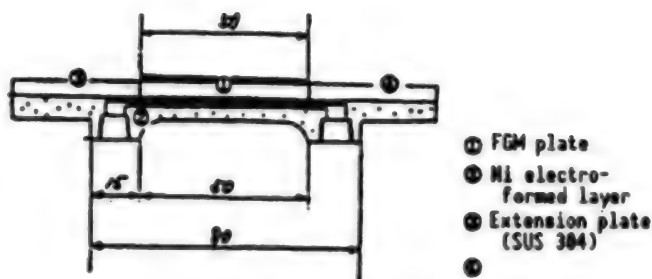


Figure 1. Outline of a Cooling Structure-Equipped FGM Panel for Thermal Fatigue Test Use

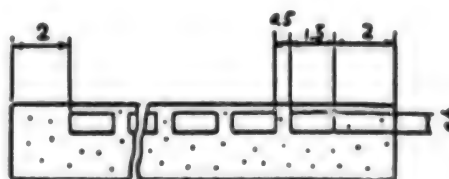
As shown in the figure, the panel consists of 1) an FGM plate; 2) an Ni electroformed layer comprising the coolant channels, manifolds, and coolant inlet/outlet threaded joints; and 3) and 4) extended plates (SUS304). As illustrated in Figure 2(b), the FGM plate consists of a PSZ/SUS-system material that was sintered by the grain sintering method. The plate measures 50 mm wide by 50 mm long, and its thickness ranges from 4-5 mm. Of this thickness, a layer up to about 1 mm deep from the heated-side surface has a gradient composition with the PSZ content decreasing progressively from 100 percent PSZ on the surface to smaller percentages as the depth increases. The layer beyond the depth of about 1 mm has a uniform 100 percent SUS304 composition. The Ni electroforming takes place on the SUS304 plate side of the FGM/SUS304 plate combination. The coolant channels are created by those processes illustrated in Figure 1. The ends of the inlet and outlet channels for the coolant are fitted with electroformed manifolds and threaded joints for connecting the panel to an external cooling unit.



(a) Diagram of a small test panel



(b) Detailed structure of an FGM plate



(c) Detailed structure of the cooling elements

Figure 2. Cooling Structure-Equipped FGM Panel for Thermal Fatigue Test Use

2) Creating Coolant Channels and Manifolds

Creating coolant channels involves the following steps. First, electroforming is performed on the SUS304 surface to a predetermined thickness (first-stage electroforming), and the channels are created on the electroformed layer by electric discharge processing. After applying an insulating treatment, a second-stage electroforming is performed on these channels. Then the manifolds are created, and after applying a third-stage electroforming, the threaded joints are created.

3) Process for Fabricating a Small Panel

Figure 3 illustrates the process for fabricating the small FGM/cooling structure panel. The process involves: 1) First-stage electroforming-creation of coolant channels by electric charge processing-applying an insulating material-electric conduction treatment; 2) second-stage electroforming-creation manifolds by electric discharge processing-applying an insulating material-electric conduction treatment; and 3) third stage electroforming-threaded joint processing-finishing treatment.

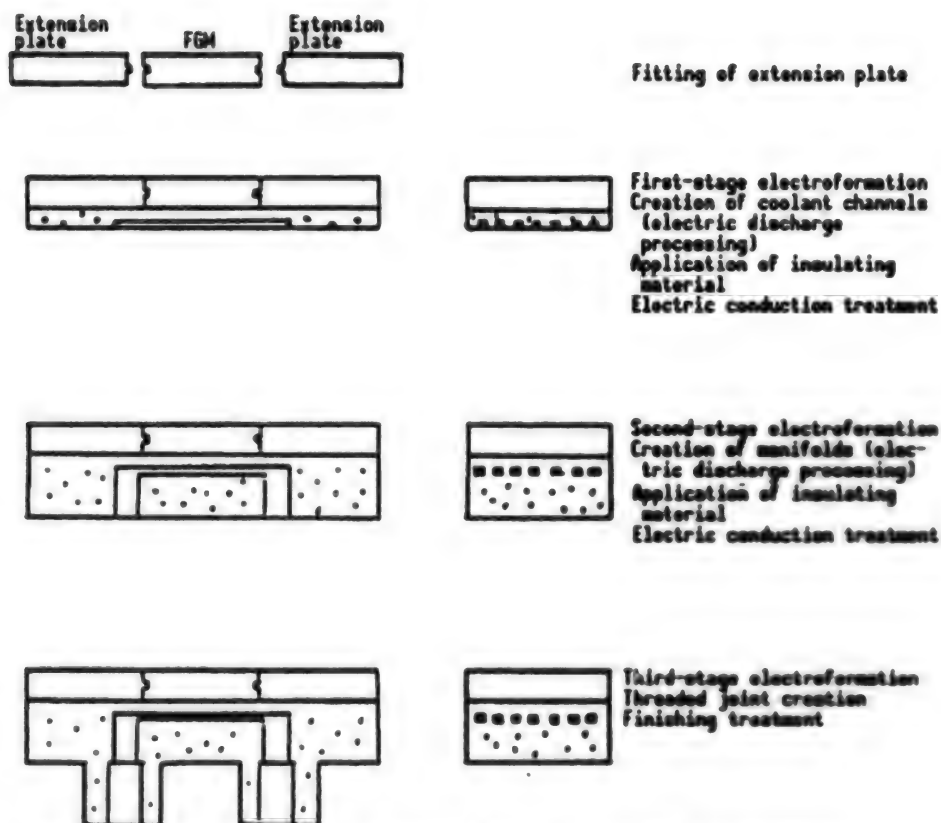


Figure 3. Fabrication Process for a Cooling Structure-Equipped FGM Panel

4. Fabrication of a Prototype Small Panel Using Dummy FGM Plate

As the first step in fabricating a full-fledged small cooling structure—equipped FGM panel, we created a prototype panel using a SUS304 plate as a dummy FGM plate. The fabrication of the prototype involved electroformations, and the creation of coolant channels, manifolds, and threaded joints in the prototype.

To check the channel fabrication condition, the same channel creating processing was given to the electroformed extension plates when coolant channels were created into the section beneath the FGM plate. The study of the channels thus created was conducted by cutting out the extension portion at a fabrication stage prior to giving finishing treatment and by observing the sectional condition. Photo 1 [not reproduced] is a sectional view of these channels.

5. Conclusion

As part of various efforts to equip an FGM plate for use in thermal fatigue testing with a cooling structure, we fabricated a small prototype using a SUS304 plate-based dummy FGM, and by creating electroformed layers on the plate to fabricate an FGM cooling structure on the metal plate.

(1) An electroforming method that is suitable for combining an FGM plate with a cooling structure has been found.

(2) We have studied a method for fabricating a small cooling structure-equipped FGM panel using an electroformation method.

(3) Based on the results of our study, we have fabricated a prototype panel by using a SUS304 plate as a dummy FGM plate, and by creating the cooling structure using the Ni electroforming method.

(4) We succeeded in obtaining the intended processing shape and dimensions for the channels and manifolds.

Our research was conducted as part of a project subsidized by the Science and Technology Agency to develop a basic technology for fabricating thermal stress-alleviating FGMs.

Temperature Response, Thermophysical Properties of FGMs

926C0014Q Tokyo FGM '91 in Japanese 8-9 Oct 91 pp 305-310

[Article by Nobuyuki Araki, Atsushi Makino, and Tatsuo Ishiguro, Department of Energy and Mechanical Engineering, Faculty of Engineering, Shizuoka University]

[Text] **Abstract:** Wide attention has been given to multilayered materials as electronic materials and materials resistant to wear, corrosion, and heat; they are expected to improve the specific nature of the conventional materials with homogeneity in composition, structure, and texture. Among these advanced materials, functionally gradient materials (FGMs), which are composed of different components such as ceramics and metals with continuous profiles in composition, have attracted special interest as advanced heat-shielding structural materials in future space applications.

The objectives and contributions of the present study are the following. First, an analytical solution of the temperature rise in the multilayered material, which is subject to transient heating, is developed. This solution is easily extended to the temperature rise for FGM if the thickness of each layer is put to be infinitesimal. Second, estimation of a profile function of the thermal diffusivity has been made when inside and rear-surface temperature rises are known. Fair agreement is demonstrated between given and estimated profiles of mixture ratio and thermophysical properties. Finally, estimation of the profile function is considered when only the rear-surface temperature rise is known. An equivalent profile function of the thermophysical properties, which gives the same temperature rise, is obtained although it is quite different from the given profile.

1. Introduction

Research is under way to develop multilayered materials for use in electronic fields, and in applications in which materials are required to have good antiwear and heat-resistant capabilities. Functionally gradient materials (FGMs), which have gradient profiles of ceramics and metals as their compositional components, are attracting attention as heat-insulating materials for use in space development applications. In designing heat-resistant materials, including FGMs, it is important to make an accurate evaluation of the materials involved by measuring their thermal conductivity

and other related thermophysical properties. In dealing with single-layer materials, the pulse method commonly is used to measure the thermal diffusion rate, from which their thermal conductivity can be calculated. There have been very few reports that evaluate thermal conductivity in FGMs using unconventional methods. In our current research, we have attempted to obtain an analytical solution for the measurement of the temperature response within multilayered materials and FGMs when they are subjected to nonsteady state heating. We also have studied a method to calculate the thermophysical properties of materials, and the thermophysical property value profile within them using the information on the temperature response of FGMs.

2. Temperature Response in Multilayer Materials

We used an infinitely parallel n layer plane (Figure 1) as a material sample model and tried to analyze temperature response within the plate when the topmost layer surface was heated. To simplify our discussion the following assumptions will be made:

- The sample is a one-dimensional thermal conductor.
- There is no heat loss in each layer.
- No contact thermal resistance exists between the adjoining layers.
- Heat flux is absorbed uniformly on the topmost layer surface.
- Each layer has a uniform material composition
- The property values in each layer are constant within a narrow temperature range.

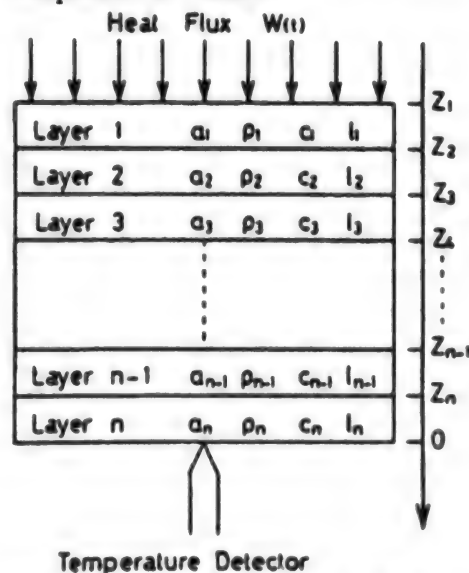


Figure 1. Concept of a Multilayered Test Sample

Under these conditions, the thermal conduction, boundary condition, and the initial conditions can be expressed by the following formulas:

$$\frac{\partial \theta_i(z, t)}{\partial t} = \alpha_i \frac{\partial^2 \theta_i(z, t)}{\partial z^2} \quad (i = 1, 2, \dots, n) \quad (1)$$

$$\theta_i(z, 0) = 0 \quad (i = 1, 2, \dots, n) \quad (2)$$

$$\theta_{i-1}(z_i, t) = \theta_i(z_i, t) \quad (i = 2, \dots, n) \quad (3)$$

$$-\lambda_1 \frac{\partial \theta_1(z_1, t)}{\partial z} = W(t) \quad (4)$$

$$\lambda_{i-1} \frac{\partial \theta_{i-1}(z_i, t)}{\partial z} = \lambda_i \frac{\partial \theta_i(z_i, t)}{\partial z} \quad (i = 2, \dots, n) \quad (5)$$

$$\lambda_n \frac{\partial \theta_n(0, t)}{\partial z} = 0 \quad (6)$$

By solving equation (1) under the initial and the boundary condition after the equation has undergone a Laplace transform, the following equation can be derived:

$$-\left[\frac{W(s)}{B_n \lambda_1 \sqrt{s}}\right] = U(s) = [1 \ 0] E_1 E_2 \cdots E_{n-1} E_n \begin{pmatrix} 0 \\ 1 \end{pmatrix} \quad (7)$$

If Λ denotes the heat penetration coefficient and η is the square root of the thermal diffusion time, then matrix E can be expressed by the following equation:

$$E_i = \begin{bmatrix} \Lambda_{i/i-1} \cosh(\sqrt{s} \eta_{i/i/n}) & -\Lambda_{i/i-1} \sinh(\sqrt{s} \eta_{i/i/n}) \\ -\sinh(\sqrt{s} \eta_{i/i/n}) & \cosh(\sqrt{s} \eta_{i/i/n}) \end{bmatrix}; \quad \Lambda_{1/0} = 1 \quad (8)$$

The temperature response on the i th layer plane, which is located at a distance of z from the back surface plane of the sample, is given by:

$$\Theta_i(z, s) = B_n [1 \ 0] E_i^* E_{i+1} \cdots E_{n-1} E_n \begin{pmatrix} 0 \\ 1 \end{pmatrix} \quad (9)$$

$$E_i^* = \begin{bmatrix} \cosh(\sqrt{s} \eta_{i/i/n}^*) & -\sinh(\sqrt{s} \eta_{i/i/n}^*) \\ -\sinh(\sqrt{s} \eta_{i/i/n}^*) & \cosh(\sqrt{s} \eta_{i/i/n}^*) \end{bmatrix} \quad (10)$$

$$\begin{aligned} \eta_i^* &= (z_{i+1} - z) / \sqrt{s} \lambda_i; \\ \eta_{i/n}^* &= \eta_i^* \eta_n \end{aligned} \quad (11)$$

In performing an inverse Laplace transform using Cauchy's residue theorem, the value of matrix element ($E_{12}^{(n)}$) in the specific equation (7) must be calculated. This can be calculated by the mathematical induction method using the following equations:

$$E_1 E_2 \cdots E_{n-1} E_n = \left(\frac{\Lambda_{n/1}}{2^{n-1}} \right) \begin{bmatrix} E_{11}^{(n)} & E_{12}^{(n)} \\ E_{21}^{(n)} & E_{22}^{(n)} \end{bmatrix} \quad (12)$$

$$E_{12}^{(n)} = - \sum_{j=1}^{2^{n-1}} \chi_j \sinh(\sqrt{s} \eta_n \omega_j) \quad (13)$$

$$\chi_j = \prod_{m=1}^{n-1} (\Lambda_{m/m+1} + \alpha_{j,m} \alpha_{j,m+1}) \quad (14)$$

$$\omega_j = \sum_{m=1}^n \alpha_{j,m} \eta_{m/n} \quad (15)$$

where $\alpha_{j,m}$ under $m \geq 2$ assumes all the combinations equivalent to ± 1 . In this case $\alpha_{j,1} = 1$. The number of combinations is equivalent to $j = 2^{n-1}$. The matrix element ($E_{12}^{(n-1+1)}$) in equation (9) is calculated by:

$$E_1^* E_{1+1} \cdots E_{n-1} E_n = \left(\frac{\Lambda_{n/1}}{2^{n-1}} \right) \begin{bmatrix} E_{11}^{*(n-i+1)} & E_{12}^{*(n-i+1)} \\ E_{21}^{*(n-i+1)} & E_{22}^{*(n-i+1)} \end{bmatrix} \quad (16)$$

$$E_{12}^{(n)} = - \sum_{j=1}^{2^{n-1}} \chi_j \sinh(\sqrt{\sigma \eta_n} \omega_j) \quad (17)$$

$$\chi_j = \prod_{m=1}^{n-1} (\Lambda_{m/m+1} + \alpha_{j,m} \alpha_{j,m+1}) \quad (18)$$

$$\omega_j = \sum_{m=1}^n \alpha_{j,m} \eta_{m/n} \quad (19)$$

In equations (17)~(19), the expression $\alpha_{j,m}^*$, when $m \geq i+1$, assumes all combinations for ± 1 . In this case $\alpha_{j,1}^* = 1$.

The dimensionless temperature response within a multilayered sample when subjected to pulse-mode heating can be expressed by the following equation:

$$V = 1 + 2 \sum_{k=1}^{\infty} \left[\frac{\sum_{j=1}^{2^{n-1}} \chi_j^* \cos(\gamma_k \omega_j^*)}{\sum_{j=1}^{2^{n-1}} \chi_j^*} \right] \left[\frac{\left(\sum_{j=1}^{2^{n-1}} \omega_j \chi_j \right) e^{-(\gamma_k/\eta_n)^2 t}}{\sum_{j=1}^{2^{n-1}} \omega_j \chi_j \cos(\gamma_k \omega_j)} \right]; \quad (20)$$

$$V = \frac{\theta_1(z, t)}{\theta_1(z, \infty)}$$

These mathematical analyses have made it possible to define the dimensionless temperature response in a multilayered material more clearly. In a like manner, the temperature response of a multilayered material when subjected to step-mode heating can also be determined.

3. Temperature Response of FGM

In equation (20), if a material has a smooth property value profile, and if it has an infinite number of layers, the value of $\Lambda_{m/m+1}$ becomes almost equal to 1, and consequently, χ_j , ω_j , χ_j^* , ω_j^* becomes zero, excluding the first term. In this case, the dimensionless temperature response within an FGM can be expressed by the following equation:

$$V = 1 + 2 \sum_{k=1}^{\infty} \left[\frac{\cos(k\pi S(z)/S)}{\cos(k\pi)} \right] e^{-(k\pi/\sigma)^2 t} \quad (21)$$

$$S(z) = \int_z^0 \frac{dz}{\sqrt{\sigma}} = \int_z^0 \eta(z) dz \quad (22)$$

$$S = S(L)$$

where S denotes the total integral value η from 0 to z , and $S(z)/S$ is the rate of the integral value of η . $S(z)/S$ is called an area ratio.

The temperature response within a single-layer material, meanwhile, can be determined by assuming that the thermal diffusion time of equation (22) takes a constant value.

4. Approximation Method

We have studied a method for evaluating the property value profile within an FGM, and for evaluating the properties of an FGM sample when the data on the temperature response within the sample and on its back face are available. The temperature response data contain information on the heat diffusion rate only. So when it is important to determine the thermo-physical property values of an entire sample it becomes necessary to use the mixture rule data for the sample. Here, we will discuss a method for calculating the property value distribution within a two-component FGM, and the property values of an entire FGM sample, from the temperature response of this material. Figure 2 shows the temperature response of a Fe/TiO₂ FGM with a straight line compositional distribution gradient derived by calculation. In this instance, mean rules are used in place of mixture rules. Before using Fe and TiO₂ in an experiment, the mixture rules of Fe and TiO₂ must be investigated.

It is known that materials with the same area ratio exhibit an identical temperature response. So we tried to calculate the temperature response by calculating the temperature ratio $V_{t1/2}$ at the half time of $t_{1/2}$. Figure 3 shows the relationship between the area ratio and $V_{t1/2}$. In FGMs there is a constant relationship between these two factors. Consequently, the area ratio can be calculated from $V_{t1/2}$ values, the distribution of thermal diffusion time can be derived from the area ratio, the approximate distribution function of the mixture ratio can be determined from the mixture rules, and, finally, the property values for the entire sample can be calculated using the appropriate distribution function.

Next, we will consider a case in which a temperature response at a distance ratio vis-a-vis the back face of 0.5 has been obtained.

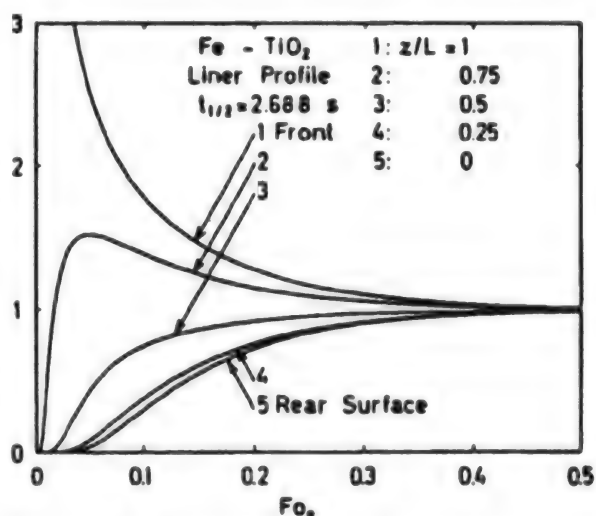


Figure 2. Dimensionless Temperature Response Within an FGM Sample

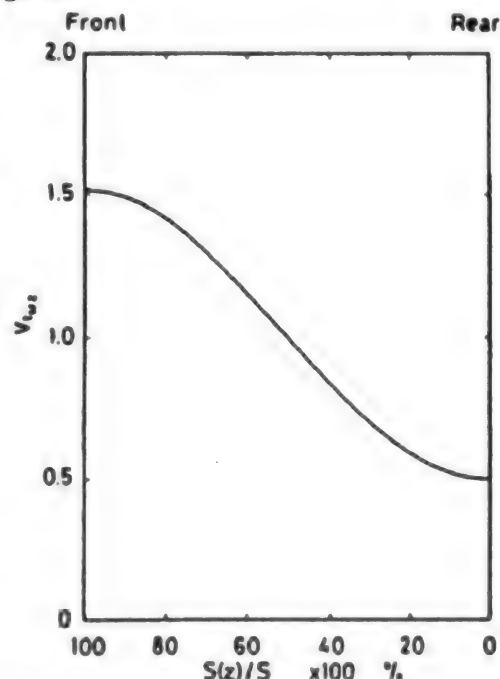


Figure 3. Relationship Between $S(z)/S$ and $V_{t1/2}$

Figure 4 shows the results of conducting calculations by approximation. In the figure, curve 1 represents a given profile, while curve 2 is an approximate profile.

When the internal temperature response is known, the thermophysical property values for the entire sample can be calculated to within 1 percent by calculating a profile function of the mixing ratio through approximation. Even when either the combination of property values or the given profile function is changed, it is possible to calculate the thermophysical property values of the entire sample with a high degree of accuracy.

5. Equivalence Method

Approximation calls for processing a sample in order to calculate its internal property value distribution and the thermophysical property values of the entire sample with a high degree of accuracy. This poses a problem when the sample is going to be used in a practical application, or in a case in which only the property values of the entire sample need to be known. The equivalence method can meet this requirement.

The equivalence method is based on the concept of using an equivalent distribution function of the mixing ratio to calculate the property values for an entire sample from the temperature response on the back face of the sample. Here, we will consider a function that forms a convex shape vis-a-vis the straight line distribution. The deviation of the convex function from the straight line distribution is defined as δ , and the relationship between them is shown in Figure 5.

$$y = \frac{C}{(z/L) - A} + B; \quad (C < 0) \quad (23)$$

$$A, B = \frac{1 \pm \sqrt{1 - 4C}}{2} \quad (24)$$

$$\delta = \pm \sqrt{1 - 4C} - \sqrt{-4C} \quad (25)$$

We calculated the relationship between $t_{1/2}$ and the deviation of profile function δ . Figure 6 shows the results of these calculations. When there is a 1:1 relationship between $t_{1/2}$ and δ , it is possible to calculate the value of δ from the value of $t_{1/2}$, and then to determine the property values for the entire sample from the equivalent profile function.

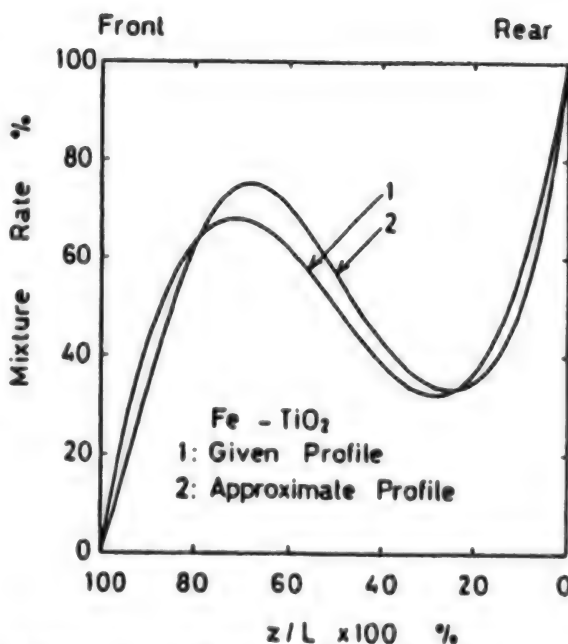


Figure 4. Results of Approximated Calculation

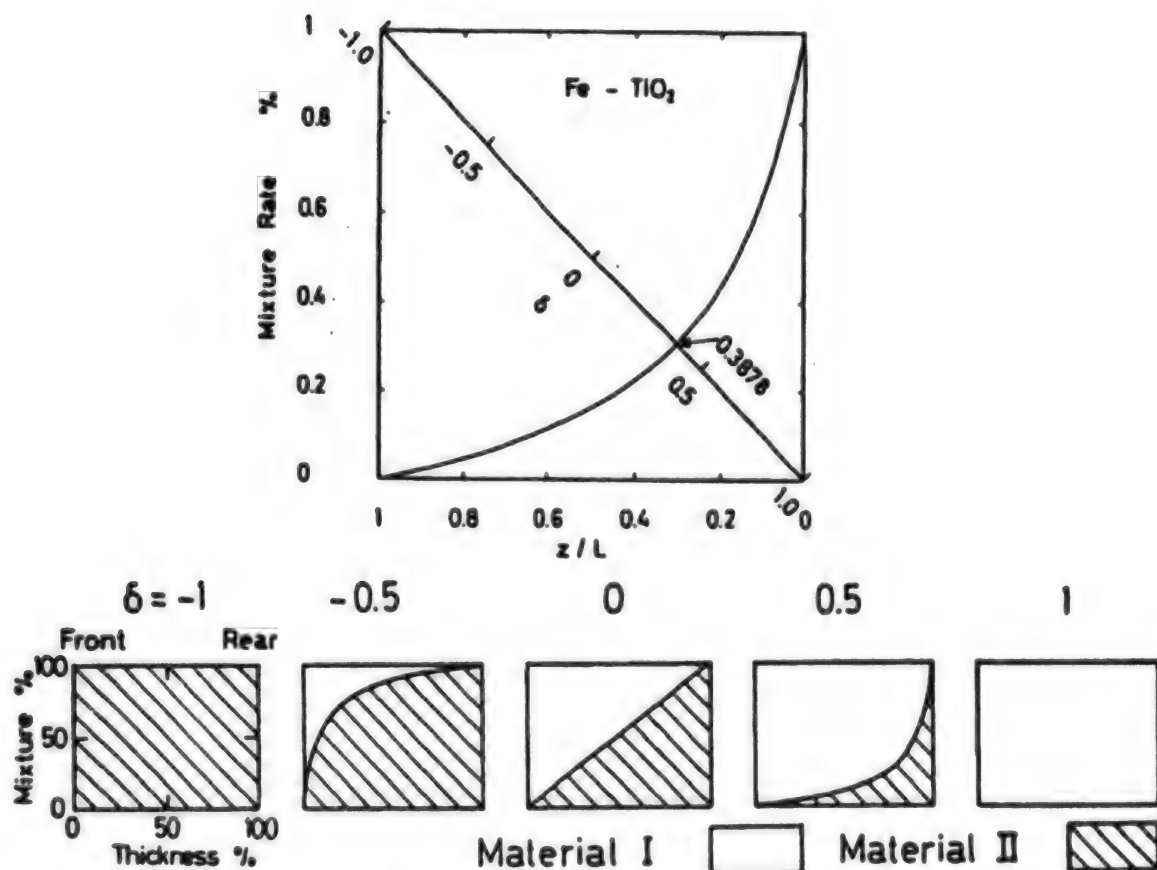


Figure 5. Conceptual Illustrations of Equivalent Profile Function

We calculated the relationship between the mixing ratio and the distance ratio. Figure 7 gives the results of these calculations. In the figure, curve 1 represents the given profile, while curve 2 is the equivalent profile. This equivalent profile does not represent the actual compositional profile within a material. It is the equivalent of the actual profile that is used to calculate the property values of an entire sample. By using this equivalent profile function, the property values for an entire sample can be calculated with an error less than 5 percent. Almost the same error level can be maintained when the property values and the given profile function are changed.

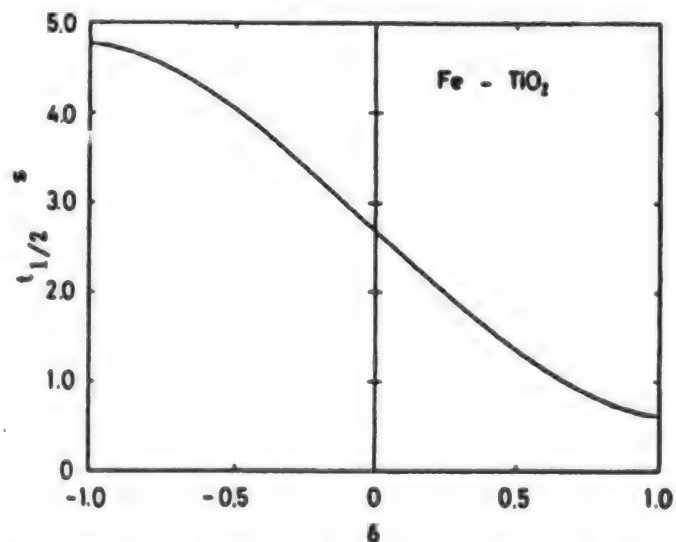


Figure 6. Relationship Between $t_{1/2}$ and δ

5. Conclusion

We have discussed a theoretical method for calculating the temperature response within a multilayered FGM sample when it is subjected to nonsteady state heating. A theoretical method for calculating temperature responses on the front face and back face of an FGM, and within the material also has been discussed. We have demonstrated that the profile function of the compositional mixing ratio can be calculated from the temperature responses on the back face of an FGM and within the material. In addition, it has been demonstrated that the thermophysical properties of an entire FGM can be calculated within an error range of about 1 percent. At the same time, we also described how the thermophysical property values can be calculated by the mixing ratio's equivalent profile function using the information about the temperature response on an FGM's back face within an error range of about 5 percent.

6. Acknowledgements

Our current research was conducted for the National Aerospace Laboratory as part of a project subsidized by the Science and Technology Agency program to develop a basic technology for fabricating thermal stress-alleviating FGMs.

Nomenclature

a	: thermal diffusivity
A	: parameter
B	: parameter
C	: parameter ($C < 0$)
Fo_0	: Fourier number ($= a_0 t / L^2$)
L	: thickness of FGM
n	: number of layers
$S(z)$: integral value of η from 0 to z
S	: total integral value of η from 0 to L
$S(z)/S$: rate of integral value of η
t	: time
$t_{1/2}$: half time (at $V = 0.5$)
V	: temperature ratio
$V_{t_{1/2}}$: temperature ratio at $t_{1/2}$
y	: profile function of mixture rate
z	: length
γ	: positive root of the characteristic eq.
δ	: deviation of the profile function

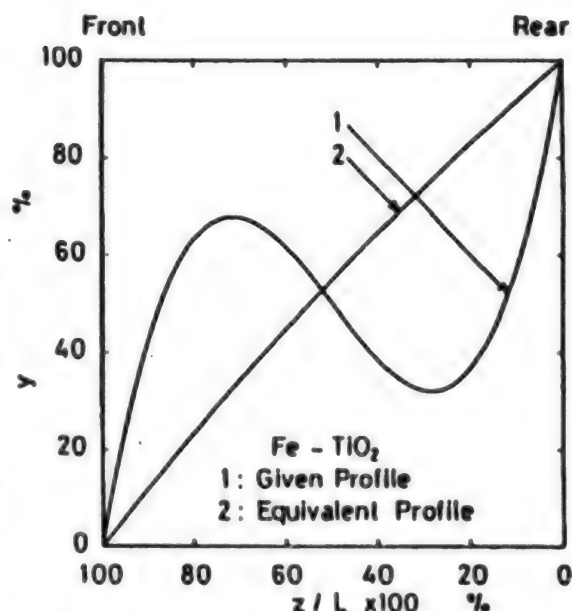


Figure 7. Results of Equivalent Method Calculations

η : square root of thermal diffusion time
 λ : thermal conductivity
 A : heat penetration coefficient ($= \lambda/\sqrt{a}$)
 X : parameter
 ω : parameter

Subscripts

i : the i -the layer
 i/j : (i -the layer)/(j -the layer)
 n : the n -the layer

Superscript

$*$: inside

Evaluating Thermal Barrier Property by Burner Heating Test

926C0014R Tokyo FGM '91 in Japanese 8-9 Oct 91 pp 311-314

[Article by Atsushi Hibino, Akira Kawasaki, and Ryuzo Watanabe, Department of Materials Processing, Faculty of Engineering, Tohoku University]

[Text] Abstract: The burner heating test for thermomechanical evaluation of a functionally gradient material (FGM) on a laboratory scale has been described. A temperature difference was given by heating the ceramic side with a burner flame and cooling the metal side with water flow. The damage at the specimen surface was monitored with a microscope. A vertical crack formation at the ceramic surface was observed during the cooling cycle. The test temperature for the first crack formation was defined as a thermal barrier performance value for the test sample. It has been found that the crack formation temperature is almost constant for the various samples and heating conditions, which indicates a material dependency of the thermal barrier property. The crack formation mechanism is discussed on the basis of a thermal stress analysis using the finite element method.

1. Introduction

Progress in functionally gradient material (FGM) fabrication technology has made it possible to obtain small FGM testpieces measuring about 30 mm in diameter. However, not much is known about the heat-resistant and heat-insulation properties of these FGMs under actual utilization conditions. Thus, there must be an increased effort to clarify fracture mechanisms in order to promote research and development of FGMs. Solving these problems is very important in formulating guidelines for material design and synthesis. With this recognition, we have developed a simple burner heater evaluation system for testing FGMs under simulated actual utilization conditions. In this report, the results of the evaluation of a SUS/PSZ-system FGM, which we have conducted using the burner heating evaluation method, will be introduced.

2. Experiment Method

1) Burner Heating Evaluation System: Figure 1 is a schematic diagram of the evaluation system. We designed an experiment to study the heat-resistant capacity and heat-insulation characteristics of an FGM. This involved silver brazing the FGM sample onto a Cu holder, heating the sample's upper surface

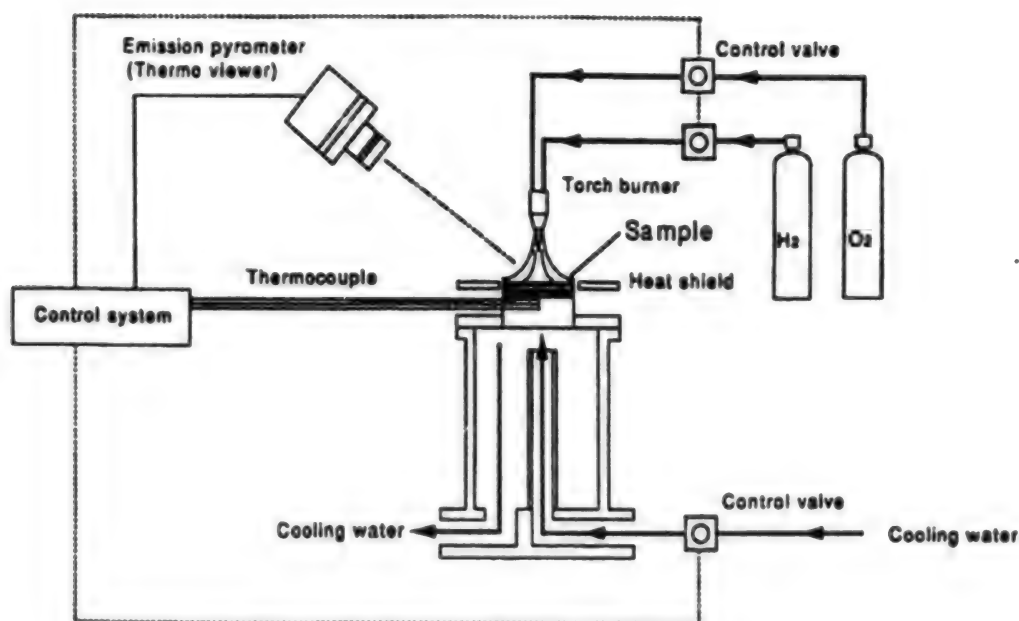


Figure 1. Burner Heating Test System

with an H_2/O_2 burner flame, and cooling the lower surface of the holder by having water run through a jacket fitted to the holder. The quantitative control of heat input and cooling was attained by adjusting the gas flow in the burner by a mass flow controller, and by adjusting the water flow rate within the jacket by a flow controller. The sample's surface temperature during a temperature difference test was monitored by a radiation pyrometer (thermo viewer) installed above the sample, and its bottom surface temperature and the heat flux passing through the sample were measured by several thermocouples inserted into the holder.

2) Burner Heating Test: We conducted a heat-resistance capability test by heating a sample surface for a predetermined time, cooling it to room temperature, and checking the cooled sample for any cracks both by visual observation and by optical microscope (Figure 2). When no cracks were found, the same process was repeated by raising the burner output. Once cracks were found, the sample was studied to determine the morphology of the surface crack and the sectional conditions. The heat-insulation capability was studied by measuring the heat flux level with the thermocouples inserted into the Cu holder.

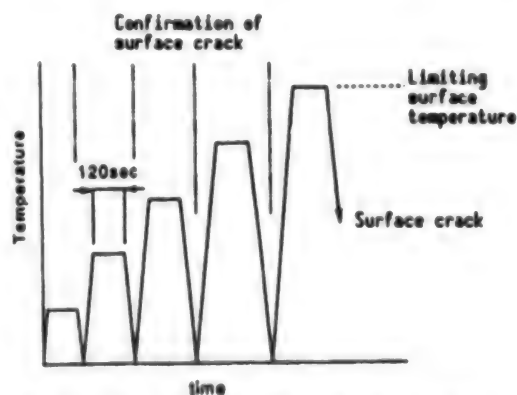


Figure 2. Procedure of Burner Heating Test

3) Fabrication of SUS/PSZ-System FGM Testpieces: Testpieces were created from an SUS304 powder with average grain diameters of 3 and 9 μm , and from a 3Y-PSZ powder with average diameters of 0.07 and 0.18 μm . These powders were mixed in a ball mill. The laminated cast bodies of these mixtures were obtained by putting the mixed powder into a metallic mold to form laminated profiles and

pressing at 150 MPa. These laminated bodies were sintered in an electric furnace at 1,473 K in the Ar-H₂ hot pressing environment, or at 1,523 K in an H₂ environment to obtain FGM samples 4 mm thick and 30 mm in diameter. The samples had different material compositional distributions and different gradient profiles.

3. Results

1) Heat-Insulation Capability of SUS/PSZ-System FGM: Figure 3 shows the relationship between the top-to-bottom surface temperature differences of these SUS/PSZ-system FGM samples when burner output was increased in steps, and the permeated heat flux Q . The plotted points in the figure represent measured values, while the solid lines represent top-to-bottom surface temperature differences that were calculated from the thermal conductivities of the NFGMs. It can be seen that there is a very close correspondence between the measured values and the calculated ones. This indicates that these surface samples have heat-insulation capabilities close to the designed capabilities.

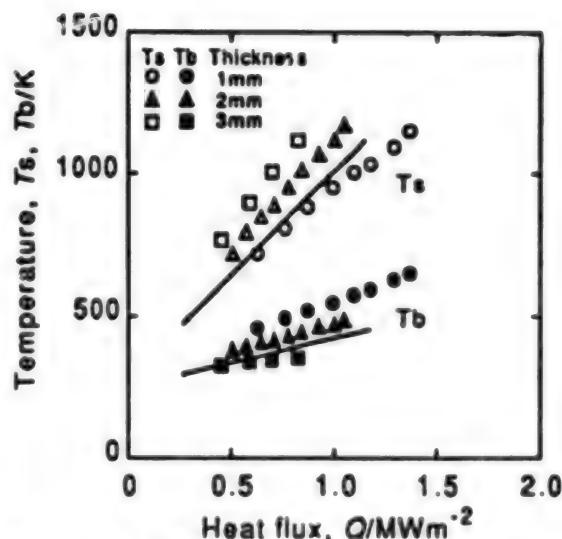


Figure 3. Sample Surface and Bottom Temperatures Vs. Heat Flux for PSZ/Stainless Steel FGM

2) Heat-Resistant Capability of SUS/PSZ-System FGM: Burner output was increased gradually and carefully. Cracks appeared on the surface of the PSZ layer at temperatures ranging from 1,200 to about 1,400 K. These cracks did not develop during heating, but appeared during the cooling process. Also, they developed almost at the same temperature regardless of differences in the samples' material compositional distribution and in the thickness of FGM layers (Figure 4). The figure shows the turtle shell cracks that developed on the PSZ layer surface in an area that was exposed to the burner flame. A study of the sectional structure of this sample found that these cracks run vertically from the PSZ layer down into the FGM layers (Figure 5). Judging from the timing of the appearance of the cracks, their shape, and the presumed thermal stress conditions in the sample when it was subjected to the burner heating test, we believe that the heat-resistant capability of SUS/PSZ-system FGMs depends on the high temperature strength of PSZ surface layer.

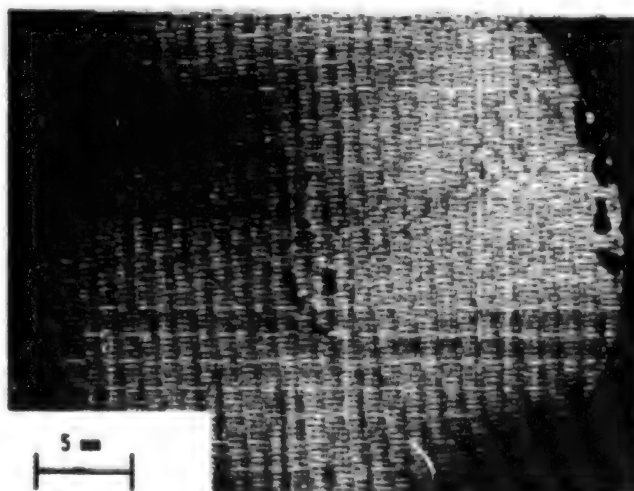


Figure 4. Vertical Crack Formation in Burner Heating Test

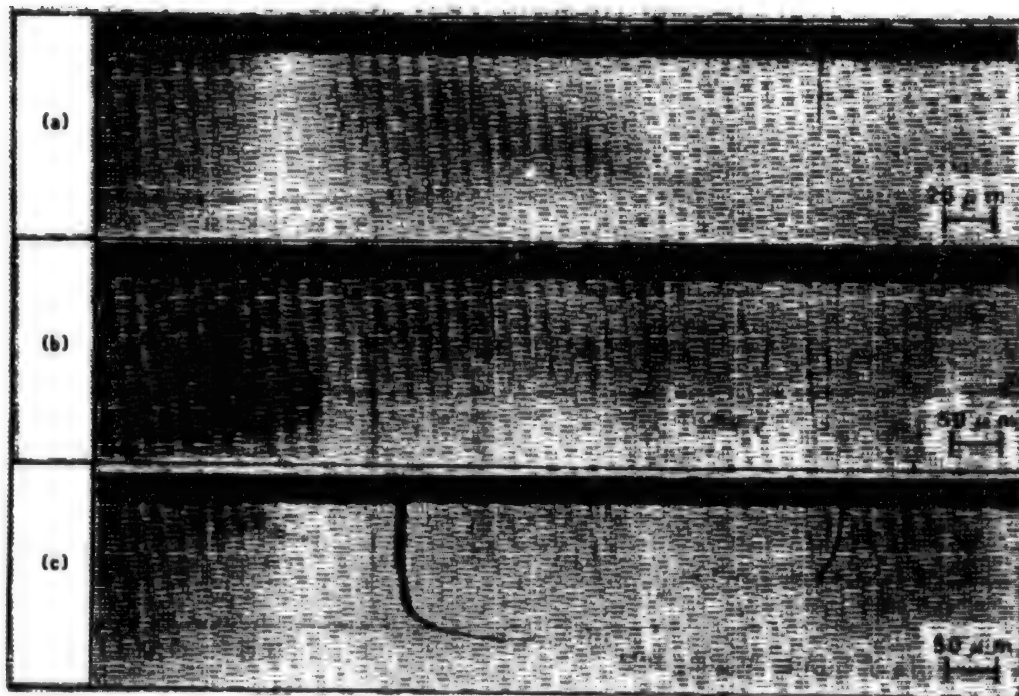


Figure 5. Cross Section of FGM After Burner Heating Test

- (a) 1 mm, linear profile (n-1)
- (b) 2 mm, linear profile (n-1)
- (c) 3 mm, linear profile (n-1)

Evaluation of 8YSZ/NiCrAlY FGM in Arc-Heated Flow

926C0014S Tokyo FGM '91 in Japanese 8-9 Oct 91 pp 315-319

[Article by Yasuo Watanabe, Takashi Matsuzaki, and Yoshio Aoki, National Aerospace Laboratory, Science and Technology Agency; and Masataka Yamamoto, National Space Development Agency]

[Text] Abstract: An evaluation study of 8YSZ/NiCrAlY FGM materials was carried out in arc-heated high-enthalpy flows. A heating rate of 0.25 MW/m^2 was applied to 30 ϕ testpieces, which were placed flat to the flow direction. The surface and cross section of exposed testpieces were observed and analyzed by EPMA.

1. Introduction

There are great expectations that functionally gradient materials (FGMs) will prove to be heat-resistant materials whose excellent heat-insulation capability will make them suitable for use in the projected space plane. We have conducted a simulated actual utilization condition test of FGMs within a 450 kW arc-heated high-enthalpy flow to evaluate their performance at high temperatures. The evaluation test was conducted using 30 ϕ 8YSZ/NiCrAlY FGM/NFGM plates. Using these samples, heating tests were performed in a high-enthalpy gas flow environment. This involved measuring the heating rate and the top surface and bottom surface temperatures, and evaluating the measurement technique to establish the technology for heating tests. The surface and cross sections of the test samples were studied by electron probe microanalyzer (EPMA) after a heat test was completed.

2. Test Method

The heating evaluation test was conducted within an arc-heated chamber (Figure 1) using various samples (Figure 2). These samples were mounted on a water-cooled holder sitting at the tip of a supporting arm so that the heating test would produce a temperature difference. The test samples, each composed of FGM and NFGM layers, and measuring 3 mm thick and 30 mm in diameter, were synthesized on ferromagnetic ferrite-system SUS430 substrates by the plasma spraying method. Their material composition and the thickness of the coated film are given in Table 1. The difficulty in machining these samples, because of their small dimensions and for heat-related reasons, let us employ a contact cooling mechanism to cool the sample's bottom surface.

Table 1. FGM Evaluation Test of 8YSZ/NiCrAlY FGM/WFEM Samples Within Arc-Heated High-Enthalpy Flow Environment:
Test sample specifications and test conditions

NO.	Test sample No.	Test sample specifications NiCrAlY : 8YSZ	Film thickness (mm)	A HWT testing conditions						Sample fixing/measured values				
				RUN NO	q(MW/m ²)	GAS	P ₀ (MPa)	H ₀ (MJ/kg)	T ₀ (K)	Ar-ranger	Sample fixing	TC fixing	Bottom surface temp. T _b	Top surface temp. T _t
1	MA01A	0 : 10	0.51	360	0.758 (1.7)	AIR	1.213	4.687	--	--	I	Pressure contacting: X	X (Over-heating)	0.85
2	MA01B	0 : 10	0.51	363	0.290 (0.65)	AIR	0.819	4.766	--	--	II	Pressure contacting: X	X	0.3
3	MA02A	10 : 0	0.52	360	0.245 (0.55)	AIR	0.928	4.622	--	--	I	Pressure contacting: X	Δ	0.85
4	MA02B	10 : 0	0.52	---	---	---	---	---	--	--	---	---	---	---
5	MA03A	7 : 3	0.41	360	0.236 (0.53)	AIR	0.803	4.612	--	--	II	Pressure contacting: X	X Inadequate bonding	0.7
6	MA03B	7 : 3	0.41	360	0.236 (0.53)	AIR	0.831	4.725	--	--	II	Pressure contacting: X	X Inadequate bonding	0.7
7	MA04A	5 : 5	0.43	361	0.250 (0.56)	AIR	0.821	4.575	--	--	II	Pressure contacting: X	Δ	0.85
8	MA04B	5 : 5	0.43	---	---	---	---	---	--	--	---	---	---	---
9	MA05A	3 : 7	0.63	361	0.250 (0.56)	AIR	0.842	4.578	--	--	II	Pressure contacting: X	Δ	0.85
10	MA05B	3 : 7	0.63	---	---	---	---	---	--	--	---	---	---	---
11	MA06A	FGH	0.79	362	0.263 (0.59)	AIR	0.852	4.986	--	--	II	Pressure contacting: X	Δ	0.3
12	MA06B	FGH	0.79	---	---	---	---	---	--	--	---	---	---	---

3. Results of Heating Test

The heating test caused discoloration on the surface of these test samples. On the surface of a sample containing NiCrAlY, nonuniform peeling of the surface layer was observed. Visual observation detected no cracks on the surface of these samples. It was confirmed that the surface of these samples was heated almost uniformly. Figure 4 shows the temperature measurements for the top and bottom surfaces of a test sample having a compositional ratio of 5:5. In measuring surface temperature, an emissivity of 0.85 was employed. The bottom temperature was measured by press-contacted thermocouples. This raised the possibility that there may have been an incomplete contact between the bottom surface of the sample and the thermocouples when measurement was taken, thereby reducing the reliability of the measured temperature.

4. EPMA Analysis

We studied the condition of these heat-tested samples by an electron probe microanalyzer (EPMA). This analysis is designed to study changes in surface conditions, boundary conditions, and composition after heating test. This is done by observing secondary electron (SE) images of the surface and a cross section of the samples, and through qualitative analysis. Figure 5 shows SE images of the surface, sectional, and boundary conditions for these FGM samples.

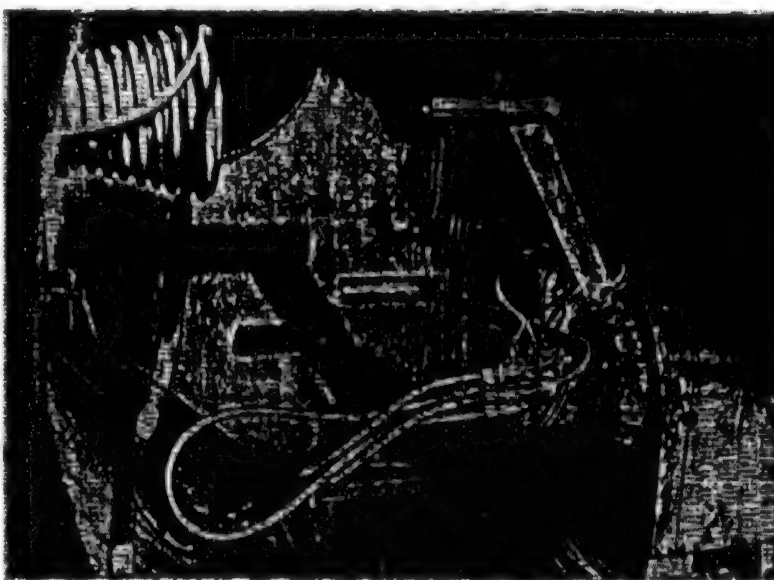


Figure 3. Sample Cooling Setup and Test Sample Supporting Arm in FGM Heat Testing System

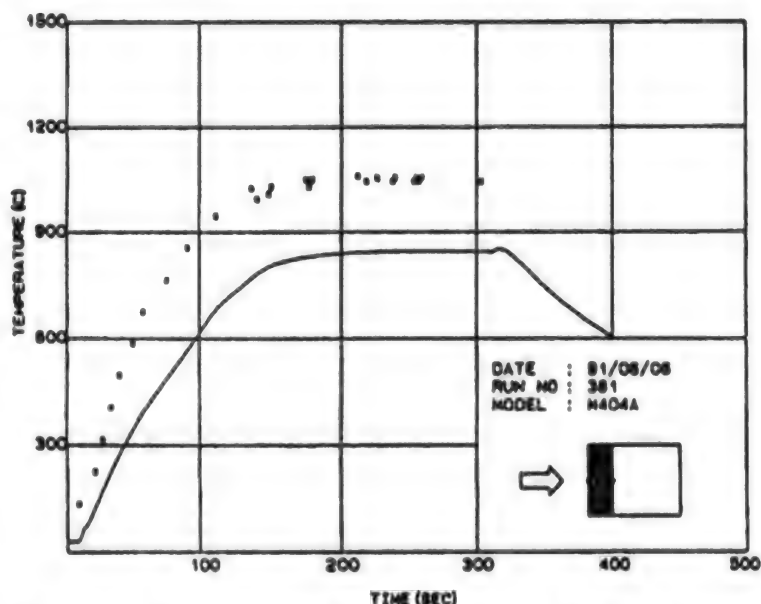
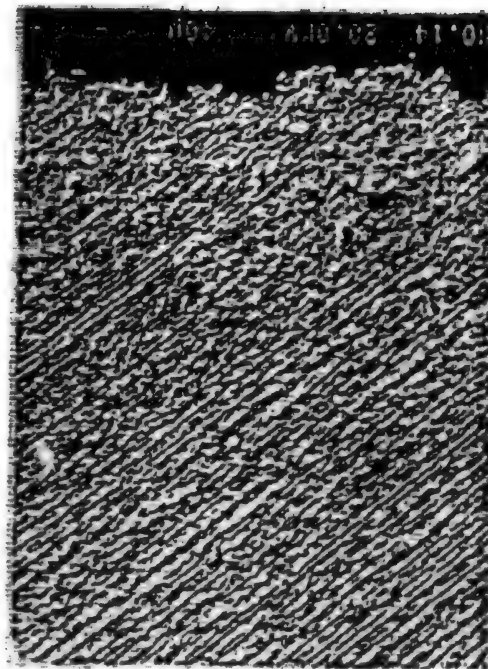


Figure 4. Temperature Hysteresis on Top and Bottom Surfaces (NiCrAlY:YSZ = 5:5)



Surface SEM image (x 2,000)



Sur-
face

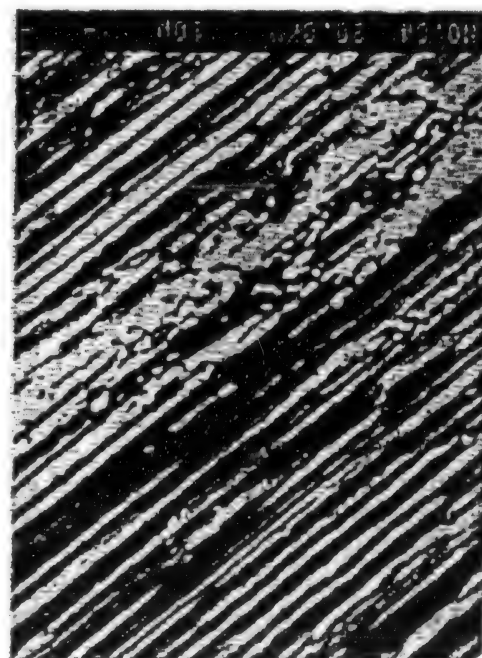
Sectional BSE image (x 500)



Substrate
boundary

Substrate

Ni image



Sectional BSE image

Sectional substrate boundary image (x 2,000)

Figure 5. EPMA Analysis Photos of FGM Test Samples

5. Discussion

Table 1 lists the test conditions of these samples in our arc-heated high-enthalpy flow test. The use of a contact-type water cooling structure failed to produce the intended results in terms of creating a large temperature difference. It may be possible to solve this problem by equipping the test sample substrates with a water-cooling structure. The same can be said of the thermocouples pressure-contacted to the sample's bottom surface. The measurement of a sample's surface temperature by an infrared thermometer is affected by the surface emissivity and the wavelength sensitivity of the thermometer. There are no readily available data on the surface temperature of FGMs, and, because of this, efforts must be made to measure the temperature. If this temperature and the heating rate were measured with a high degree of accuracy, it will become possible to infer the high-temperature property values of FGMs from the results of thermal conduction analysis.

We conducted an EPMA analysis of those test samples that underwent a heating test. Through an analysis of the surface as well as sectional conditions of these samples, we sought to grasp the changes in crystal structure, material composition, boundary conditions between the metallic phase and ceramic phase, and the interface between the FGM layer and the substrate. The scanning electron microscope (SEM) image in Figure 5 shows the presence of fine cracks on the surface of the sample. The sectional BSE image reveals the history of the formation process of the FGM layers. The sectional BSE image shows the boundary conditions between the FGM layer and the substrate, and the Ni component image shows a condition in which the substrate and the NiCrAlY layer are bonded by a compositionally gradient layer consisting of an alloy inserted between the substrate and the NiCrAlY layer. Similar studies and analysis are being conducted with other types of test samples.

6. Conclusion

The evaluation of 30 ϕ 8YSZ/NiCrAlY FGM/NFGM samples within an arc-heated high-enthalpy flow environment has revealed a number of problems that must be solved to improve measurement techniques in material evaluation experiments. The EPMA analysis of heating-tested samples has produced a number of useful results. Feeding these results back to material design and production processes will contribute to improving the characteristics of FGMs.

Evaluation of FGM for Simulated High-Temperature Rotors

926C0014T Tokyo FGM '91 in Japanese 8-9 Oct 91 pp 321-324

[Article by Masanobu Taki, Yoshiaki Fujusawa, and Toyoaki Yoshida, Thermofluid Dynamics Division, and Yasushi Sufue, Aeroengine Division, both divisions of the National Aerospace Laboratory, Science and Technology Agency]

[Text] Abstract: The fundamental evaluation method of functionally gradient materials (FGMs) applied to the combined condition of thermal and mechanical load has been developed, which condition is commonly observed in rotating members, e.g., gas turbine rotors. The pipe-shaped FGM testpieces were heated from their outer side by an image furnace and simultaneously cooled from their inner side. Under this condition, they were subjected to one-dimensional mechanical loads by a tension test apparatus. Their thermal barrier effect and mechanical damage have been investigated to evaluate the practical property of FGMs. With the combination of 8Y-PSZ and NiCoCrAlY as the two component materials of the FGM, at some hundred kW/m² level heat flux, it has been shown that the FGMs have an equally good bonding property compared with the conventional thermal barrier coating (two-layered TBC) having the same material combination. A fundamental evaluation method under the combined condition has been established.

1. Introduction

The introduction of functionally gradient materials (FGMs) for use in the high-temperature sections of gas turbines could improve the performance of these turbines significantly. To promote the utilization of FGMs, it is necessary to evaluate their performance under high-temperature load conditions. However, research on this topic has been hampered by many problems related to the techniques used to clarify the characteristics of those candidate materials for use in fabricating FGMs. In our current research, we have evaluated the heat insulation capability and mechanical strength of an FGM to promote its use in rotating machinery members. In this article, we will discuss the prospects for using FGMs in heat insulation coatings.

2. Test Sample

There is a comparatively large degree of freedom in designing an FGM because of the fact that the material's property values change depending on various

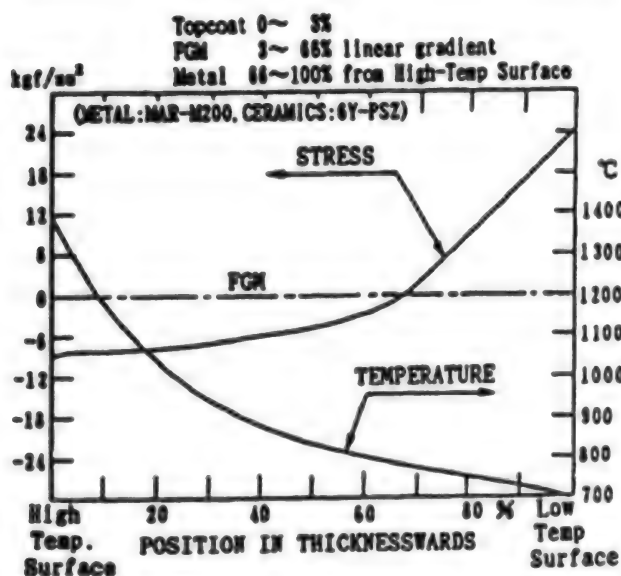
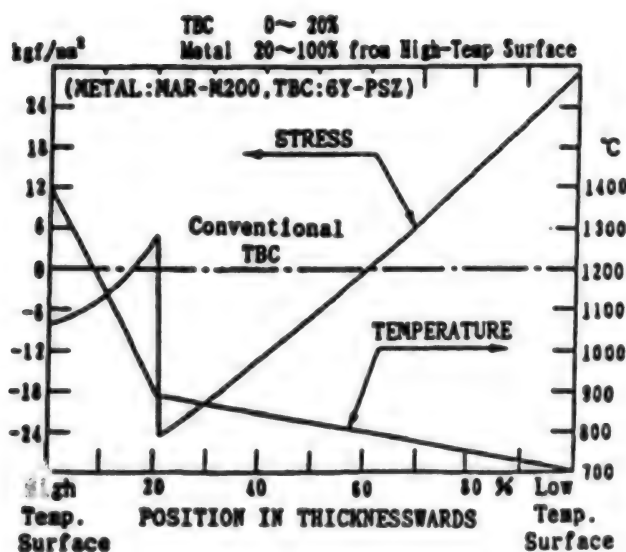


Figure 1. Thermal Stress Alleviation by Introducing a Gradient Profile Heat-Insulation Layer

factors. This makes it very difficult to determine these property values by experimentation, and this is the reason for the scarcity of relevant data. Under these circumstances, we have simulated the alleviation of thermal stress using material property values that have been obtained using an improved numerical analytical code based on Kerner's method. Figure 1 shows that the straight-line gradient in the boundary thermal stress change in a conventional TBC sample can be alleviated substantially by using FGMs.

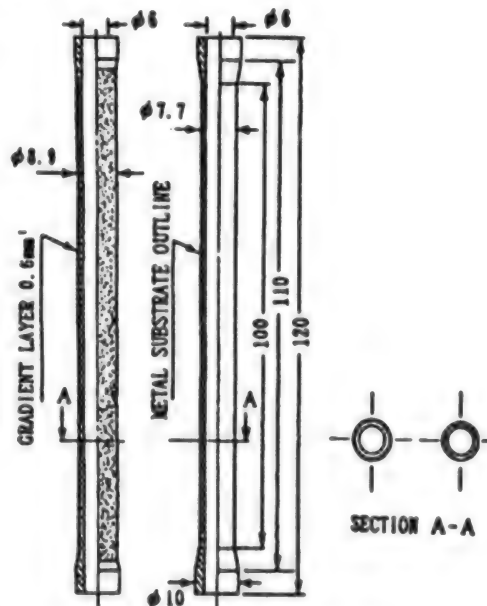


Figure 2. Sample Shape and Structure

PSZ is commonly used as a TBC material. Thus, we conducted a high-temperature difference tensile test using a TBC composed of NiCoCrAlY and ZrO_2 (8wt% Y_2O_3), and FGM samples in which the composition of these materials was changed in a number of ways. (SUS304 was used for FGM substrates (Figure 2)). The ratio between the ceramic layer as a conventional TBC and the bonding layer was determined using the analytical code so that it would be at the same level as the FGM's heat transmission coefficient. The test samples had a tubular shape. In order to improve their heat-insulation capability, a coating was applied on the circumferential surface of the substrate by the one-gun plasma spray method at atmospheric pressure. In applying coatings to FGM samples, the supply volume and feed rate of the ceramic and metallic components were varied for each scan, and a total of nine scans was made. In our present research,

the TBC thickness was set at a comparatively thick 600 μm because the minimum coating thickness synthesized by the single pass of a plasma gun was restricted by the limitations associated with plasma gun adjustment. This compares with the conventional TBC thickness of 300 μm . Another reason for adopting a thickness of 600 μm is to ensure matching with the FGM. The coated surface was polished.

3. Test Apparatus and Test Method

The required temperature difference was attained by setting a six-lamp infrared image furnace on a universal test unit, and by heating the external surface of the tubular FGM samples while cooling the inner surface by forced circulation water. In our experiment, the maximum temperature difference was set at about 550°C. the combined effect of heat and load was simulated by applying a tensile load in the axial direction using a universal tester. In the case of a rotating member, this load simulates the axial direction load generated by centrifugal force. In order to evaluate the amount of heat insulation, we measured the surface temperature of the sample, the temperature of the water both before it entered the sample and after it passed through, and the water flow rate. The surface temperature was measured by a thin-film-type thermocouple sensor, while the water's temperature was measured by a sheath-type K thermocouple inserted into the sample. The flow rate was measured using a turbine-type flow meter. Test samples were put under acoustic emission (AE) monitoring to detect damage. An AE sensor is vulnerable to heat, so it was cooled by a forced air current.

Prior to conducting this experiment, we carried out a high-temperature tensile strength test of a conventional TBC to grasp the coating's fracture characteristics at high temperatures. In this test we used a large, tubular test sample that was cooled by an air current running through it. This test was conducted at a temperature difference of about 100°C. When the surface temperature of the sample went up over 900°C, the AE frequency increased sharply. This probably indicates that thermal stress-induced damage is in progress within the ceramic layer. However, no significant rise in the temperature of the cooling water was detected, and it is believed that the crack is a minor one that is developing perpendicular to the sample's surface. The development of cracks relieves the thermal stress within the sample, and this causes a decline in AE frequency over time. The application of a tensile load produced AE signals that were detected near the maximum apparent stress point (tensile load: about 9 kN [kiloneutons], apparent stress 150~160 MPa. A color contrast penetrant examination of the sample conducted immediately after heat test was completed revealed turtle shell pattern-like cracks caused by thermal stress on the sample's surface. Another observation near the breakdown point of the coating showed numerous cracks running toward the sample's circumference.

5. Results and Discussion

Figure 3 shows the results of this water-cooled temperature difference evaluation test. Some conventional TBC samples suffered heat stress-induced damage during heating (temperature difference: 200~300°C) before a tensile load was applied. This damage took the form of peeling of the surface TBC layer, with the long axis of the peeling running in the axial direction.

No FGM samples suffered similar damage caused by thermal stress only. In these samples, damage developed only after a tensile load (6-7 kN, apparent stress 160-190 MPa) was applied. The damage consisted of cracks running toward the sample's circumference. As for the surface coating peeling caused by thermal stress, a burst of AE signals was detected shortly before the peeling occurred during heating. The signal generation point almost coincided with the damage area that was found in post-heating test observation. The tensile load-induced fracture generates almost no AE signals, and the fracture occurs suddenly during heating. In general, in high-temperature conditions, AE frequency decreases. This is believed to be caused by the softening of the ZrO_2 at high temperatures. Some of the environment TBC samples suffered damage at very small temperature differences. One of the reasons

for this is the comparatively large thickness of the coatings necessary to make TBC thickness match that of the FGM samples. We believe that the damage in these TBC samples is caused by the progress of heat stress-induced crack propagation. Initially, this takes the form of buckling while heating continues, and, after the temperature sensor on the sample surface was broken, the sample broke due to the impact generated by the sudden discontinuation of heating when the safety mechanism shut down the furnace.

The thermal load values in the figure were calculated from the increase in the temperature of the cooling water. Calculations using Dittus-Boelter's empirical formula showed a temperature on the inner wall of the test sample of about 40°C. For both conventional TBC and FGM samples, heating and/or applying a load led to a slight improvement of their heat insulation capability. We believed that this was caused by the occurrence of very slight peeling in

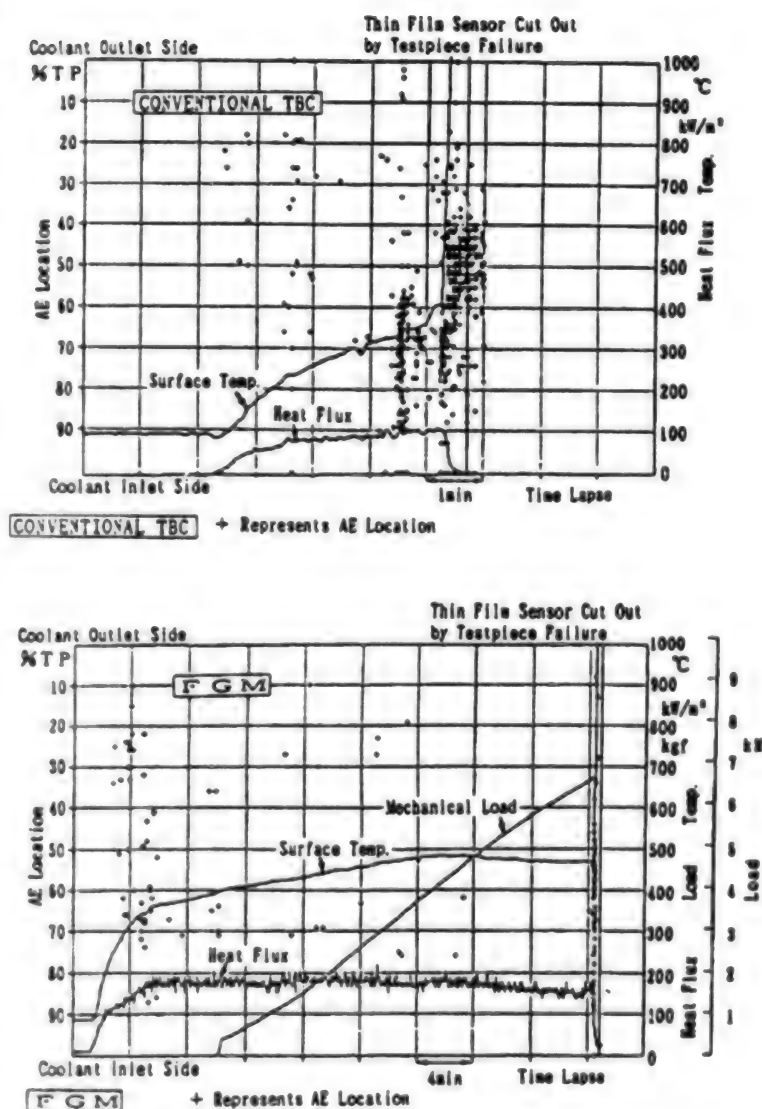


Figure 3. Tensile Strength Profiles Obtained by Temperature Difference Environment Testing

their plasma sprayed layers. In these FGM samples, the heat-insulation capability varied from sample to sample. As far as the data in the figure are concerned, the surface temperature of the samples for which the data are shown in the figure went up to no higher than about 500°C because of limitations in the furnace's output. However, there were some samples whose surface temperature went above 700°C. The destructive inspection of these samples after they underwent a heating test found that the FGM layers were peeling away from their substrates. The fluctuation in the heat-insulation capability of these samples probably is caused by the introduction of a defective layer that ultimately is responsible for such fluctuations in the samples during their production process.

Figure 4 shows the relationship between the thermal load testing environment and the damage load level in conventional TBC and FGM samples. As for load withstanding capability, there is little difference between FGMs and conventional TBC. We believe that this close similarity of load withstanding capability results from a deterioration of the mechanical strength in these FGM samples, which in turn is the result of the generation of residual thermal stress within the ceramic phase of these samples. During the fabrication of these samples, a metallic phase invades the ceramic phase area, and this generates thermal stress due to the difference in thermal expansion coefficients between these phases when they are cooled after a coating was finished. These FGM samples have been fabricated by the same method used to create conventional TBC. However, if this method is to be used in fabricating FGMs, it must be improved. The color contrast penetrant examination detected turtle shell pattern-like cracks on the surface of some FGM and conventional TBC samples even before they were subjected to the heat evaluation test. When TBC thickness remains comparatively small, it is believed that the coated layer contributes to relieving thermal stress. However, in the case of FGMs that require the formation of relatively thick layers, the introduction of a crack-arresting measure would be necessary.

6. Conclusion

Our basic experiments and analyses have shown that FGM coating is better than conventional TBC in terms of temperature difference withstanding capability. and it is believed that FGM coatings can be used in various applications, such as on the inner walls of a furnace, where the coating's strength is not required to be very high. The maximum level of stress generated by the

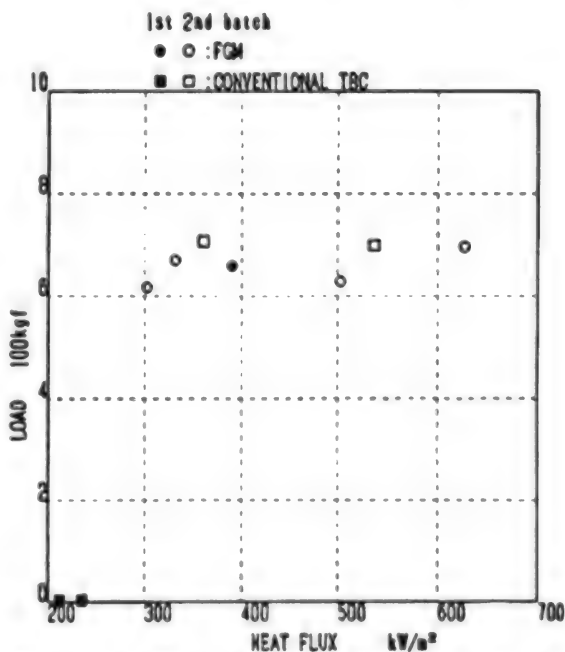


Figure 4. Relationship Between Heat Flux Level and Load Withstanding Capability

centrifugal force in small high-performance turbines is expected to reach a hundred and a few tens of MPa. It would not be very difficult to produce an FGM coating with sufficient strength to withstand such a stress in the laboratory. The FGM coatings that have been created to date have a comparatively large thickness, and the strength changes from sample to sample. However, with further improvement in coating formation techniques, FGM coatings will begin to replace conventional TBC as heat-insulation layers in applications that involve a heat stress level that is more than TBC can handle safely.

Evaluation of Cylindrical High-Pressure Thrust

926C0014U Tokyo FGM '91 in Japanese 8-9 Oct 91 pp 325-334

[Article by Akinaga Kumakawa, Hiroshi Sakamoto, Kazuo Sato, Fumiei Ono, and Nobiyuki Yatsuyanagi, Kakuda Research Center, National Aerospace Laboratory, Science and Technology Agency; and Hiroshi Takigawa, Plant and Machinery Division, Nippon Steel Corp.]

[Text] Abstract: Three cylindrical rocket thrust chambers with conventional ceramic-coated layers as thermal barriers were tested using liquid oxygen and gaseous methane propellants at chamber pressures of 3.5-5.0 MPa and heat fluxes of 3.5-6 MW/m². Two of them were damaged at only one thermal cycle, probably due to severe thermal stress. The other one apparently remained adhered throughout 14 firing tests. In the post-test observation, two spalling modes were inspected. It was thought that nonuniformity of plasma-spray coated layers and severe thermal stress due to the mismatch of top and bond layers caused the spallings.

1. Introduction

As the performance of rocket engines has improved in recent years, the thrust pressure produced by these engines has increased. The thrust pressure in the first stage of the domestically developed next-generation H-II rocket is about 13.5 MPa, while that of the main engine for the projected space shuttle (SSME) reaches about 21 MPa. These thrust pressures increases mean a proportionally higher increase in the thermal load exerted on the walls of the rocket engine combustion chambers, with the maximum load value reaching about 100 MW/m² at the nozzle throat. Currently, copper and copper alloys, which have excellent thermal conductivity, are the only combustion chamber materials used in engine parts that must be capable of withstanding high thermal loads. However, these copper-based materials have relatively low melting points. This, coupled with the considerations about rigorous thermal load conditions, makes it necessary for the combustion chamber to have a wall thickness between 0.6 and 0.8 mm, and to be able to withstand a maximum surface temperature of 800 K. This wall thickness is near the limit, judging on the basis of currently available processing technology, and the same can be said of the surface temperature, because at higher temperatures the effects of low cycle thermal fatigue become conspicuous. Under these circumstances, it is essential to introduce a heat-insulation layer to meet the higher engine thrust pressure by relieving the

thermal load on the inner walls of the engine's combustion chambers. Like the engines in the SSME, the propulsion system that will be used in the space vehicles of the future will have to be reusable. The introduction of a heat-insulation layer on the inner walls of the combustion chamber will alleviate the thermal load, and this, in turn, will lead to a longer service life of the engines by lowering the temperature in the chamber wall parent material. In the United States, research to promote the utilization of heat-insulation materials in space vehicle engines was launched in the latter half of the 1970s, and efforts to accumulate data have continued. In Japan, meanwhile, full-fledged systematic research has yet to begin. There have been only a few instances of attempts to develop experimental models of ceramic layer-coated small rocket combustors.

In this article we will discuss the result of combustion experiments conducted using a cylindrical rocket combustor model equipped with a conventional NFGM ceramic heat-insulation layer. The discussion will refer, among other topics, to the method used to evaluate the layer's heat-insulation capability and its durability, and the problems that must be solved to create such an insulation layer.

2. Experiment Method

2.1 Experiment Samples

In our experiment, we produced a heat-insulation coating using partially stabilized zirconia (PSZ), a material that is popularly used in the United States, and nickel-20% chromium (Ni-20Cr). These materials were applied on the inner wall of the combustion chamber by the low-pressure plasma spray (LPPS) method. For a comparative evaluation a PSZ film having a 2.5 time thickness of $170\text{ }\mu$ was also created. The Ni-20Cr layer had a thickness of about $60\text{ }\mu$. The combustor lined with the layers of these materials was cooled by water to make it easy to measure the loaded heat flux level.

The sample layer was created by the electroformed pickup (EP) method, which made it possible to produce comparatively good results in similar experiments conducted in the United States. The advantage of this method is that it makes it possible to create experiment samples irrespective of their dimensions under almost the same conditions. Another advantage of the method is that it can create a coating with a low residual stress, and it can reduce layer surface roughness, a factor affecting heat transfer within the layer. Following is a description of how our experimental model was fabricated. First, a PSZ layer was formed by spraying the material on the surface of an aluminum ring by the LPPS method, followed by the spraying of an Ni-20Cr layer. Then an electroformed layer of copper was created in the external surface of these layers. Coolant channels running in the circumferential direction were created on this copper layer. Then a stainless steel lid was welded around this ring by an electron beam. Cooling water inlet and outlet pipes, and a water pressure gauge were attached to the ring. In addition, a 0.5ϕ CRC thermocouple was buried into the steel lid to a depth of 1 mm from the surface. A total of three test samples—two samples with a PSZ layer thickness of about $65\text{ }\mu$ (C-1, C-2) and one sample with the thickness of $170\text{ }\mu$ (C-3)—were created (Table 1).

Table 1. Dimensional Information for Test Samples

Sample type		C-1	C-2	C-3
Inner diameter	mm	66.0	+	+
Length	mm	50.0	+	+
PSZ layer thickness	μm	65	+	170
Ni-20Cr layer thickness	μm	55	+	60
Electroformed copper layer thickness (minimum)	mm	5.0	+	+

2.2 Combustion Test

Liquid oxygen and methane gas were used as the propellant. The samples were inserted into the combustion chamber by cutting the combustor into two parts near the fuel inlet (Figure 1). The fuel was injected into the combustion chamber through 18-element coaxial jet nozzles. The experiment was started by conducting a 30-second steady state test to obtain heat flux data under steady state conditions. A heat cycle test was begun when no external abnormalities were detected in the steady state test. This time, the experiment was conducted

with a thermal load lower than 10 MW/m^2 or less than 5 MPa in combustion chamber pressure, in view of the fact that this is the first time we had conducted such a test. The heat flux level changes almost in proportion to combustion chamber pressure, and, because of this, the heat flux level was adjusted by changing combustion chamber pressure. That is, in the experiment using C-1 and C-2 samples, both having a heat-insulation layer thickness of about 65μ , combustion chamber pressures of 5 MPa and 3.4 MPa were used to effect different thermal flux conditions. In contrast, in the case of a C-3 sample having a layer thickness of 170μ , the experiment was conducted at 3.4 MPa.

The experiment was conducted with a thermal load lower than 10 MW/m^2 or less than 5 MPa in combustion chamber pressure, in view of the fact that this is the first time we had conducted such a test. The heat flux level changes almost in proportion to combustion chamber pressure, and, because of this, the heat flux level was adjusted by changing combustion chamber pressure. That is, in the experiment using C-1 and C-2 samples, both having a heat-insulation layer thickness of about 65μ , combustion chamber pressures of 5 MPa and 3.4 MPa were used to effect different thermal flux conditions. In contrast, in the case of a C-3 sample having a layer thickness of 170μ , the experiment was conducted at 3.4 MPa.

3. Results

Table 2 gives the results of these combustion tests. We will elaborate on the results of these tests for each of the samples.

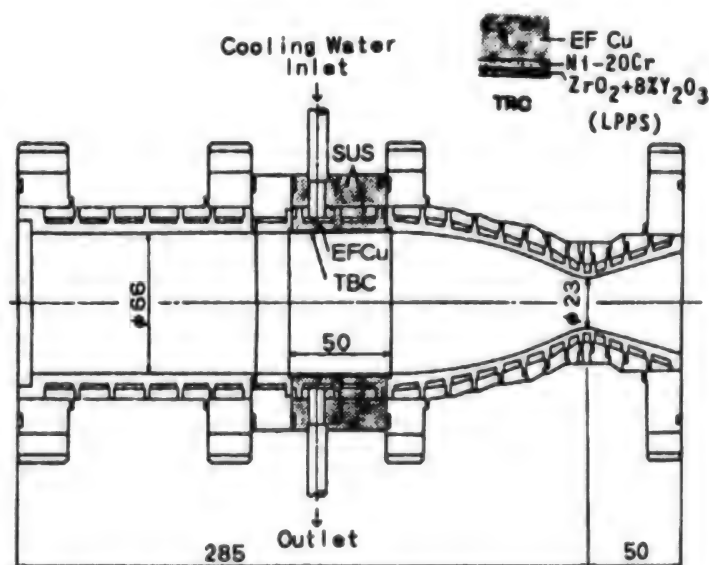


Figure 1. Water-Cooled Rocket Combustor Having a Test Sample Fixed in Place Within the Combustion Chamber

Table 2. Combustion Test Results

Sample type		C-1	C-2	C-3
Combustion chamber pressure	MPa	5.0	3.4	3.4
Mixing ratio		2.8	2.5	2.9
C* efficiency	%	92.3	93.0	93.1
Combustion gas temperature	K	2,900	2,800	2,900
Number of tests conducted		2	14	1
Cumulative length of combustion time	(sec)	50	145	30
Average heat flux level	MW/m ²	6.0	4.0	3.8

3.1 Sample C-1

Using a C-1 sample, we conducted the experiment twice, both times at a combustion chamber pressure of 5 MPa. In the first experiment, peeling and a subsequent blowing out of the coated layer occurred shortly after the combustion test started. A study of the internal conditions conducted after the combustion test was finished found that the coated layer was missing, in a striped pattern, at three places, each of which had a width of some 6 mm with the stripes running in the circumferential direction. Another test conducted using the same sample and under the same combustion conditions caused two of these adjoining stripes to merge into a single one. The area of this merged stripe accounted for about 5 percent of the total coated area. Figure 2 is a photo of the inner wall of sample C-1 after these tests were completed. The arrows indicate the two areas where the coated layer is missing. Figure 3 is an illustrative sketch of the peeled sections and their dimensions. In addition, on the coated surface of the sample, discolored black and white areas were observed. Each area was placed alternately at almost equal intervals (Figure 2). Heat-insulation capability is affected significantly by the condition of pores present within the ceramic coating. The porosity in the layer sections that were little affected by the combustion tests ranged between 1.0 and 3.9 percent with an average of 2.6 percent.

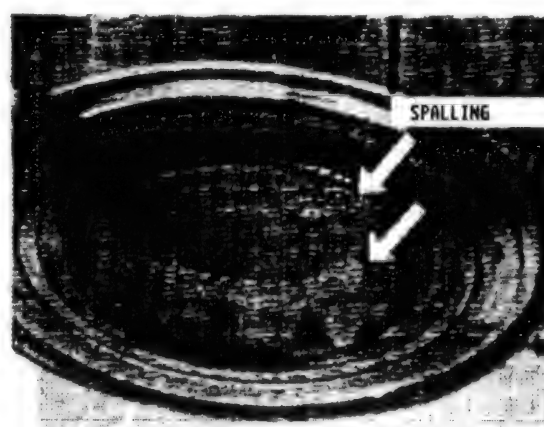


Figure 2. External Appearance of the Surface Condition of C-1 Sample After a Combustion Test

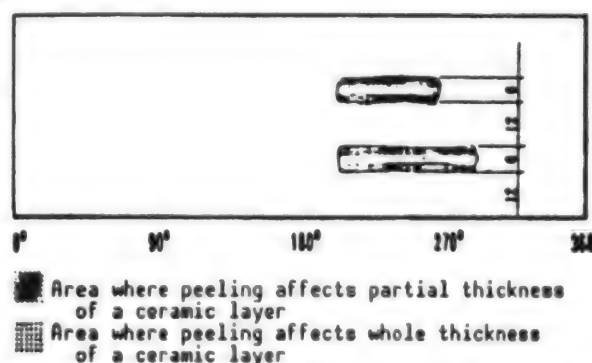


Figure 3. Coating Peeling Areas in C-1 Sample Observed After a Combustion Test

Porosity was obtained by measuring the total pore area ratio on the polished sectional face of the coated layers using a LUZE500 image analyzer.

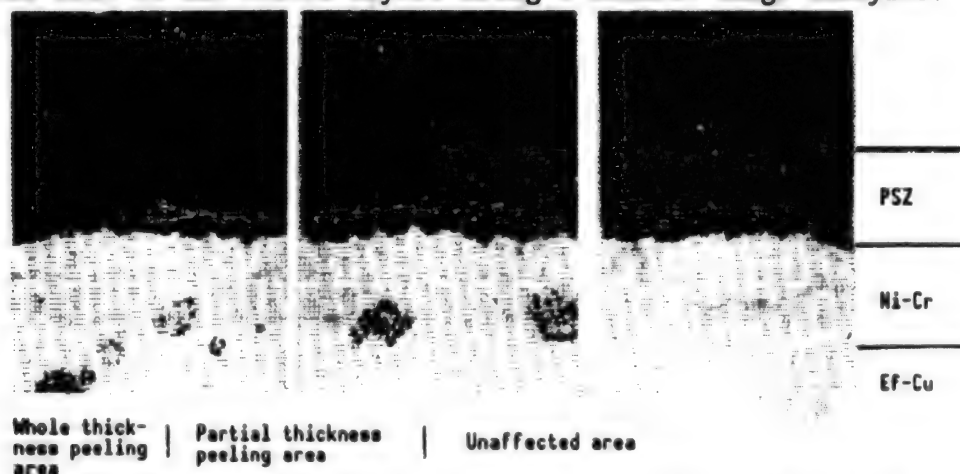


Figure 4. Cross Sectional Photos of C-1 Sample Taken After a Combustion Test

Next, a sectional observation of the tested sample was performed, centering on the areas where the coating was missing (Figure 4). As can be seen in Figures 2 and 3, the stripes where the coating is totally missing occurred at almost equal intervals with each of these stripes sandwiched by partially missing PSZ layer stripes, and no peeling stripes further out. These results suggest insufficient bonding strength in the coating interface due to nonuniformity in the plasma sprayed ceramic layer (Figure 5). Considering the fact that the

thickness of the heat-insulation layer is so thin, about $65\ \mu$, and that the aluminum surface was scanned with the spray gun no more than twice, the bonding strength was not very high.

The black discolored areas were found in areas where the oxygen density was particularly high, with the blackened areas located at places corresponding to the arrangement pattern of the oxygen injecting elements. Meanwhile, a compositional analysis of the white parts revealed that the white areas were caused by a lack of oxygen near the PSZ layer surface. This lack of oxygen is

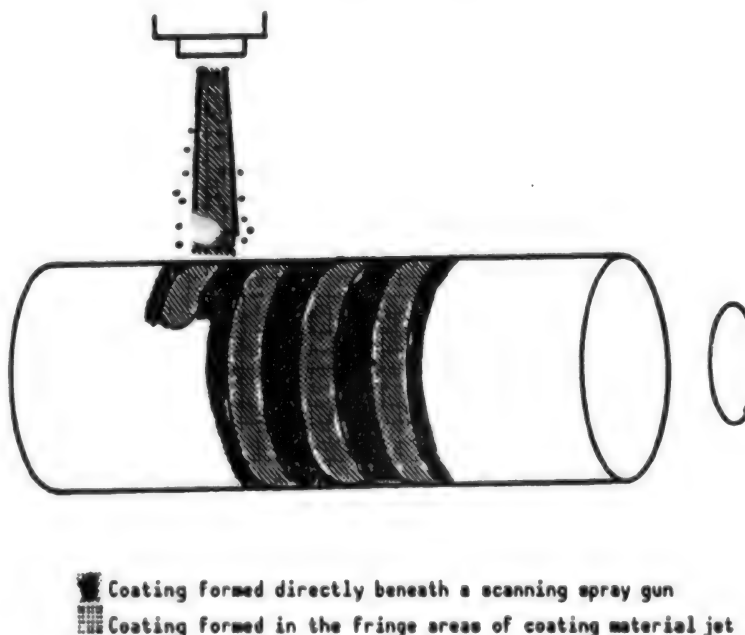


Figure 5. Formation of a Test Sample Coating by Plasma Spraying

believed to have been caused by the presence of a strong reducing atmosphere in regions where the density of fuel methane and hydrogen as an intermediate product is high. In the meantime, the heat flux level in sample C-1 was measured at about 6 MW/m^2 . This was about 25 percent lower than the 8 MW/m^2 for a noncoated copper sample, indicating the effectiveness of the heat-insulation layer even though part of the coating was blown out during the combustion test.

3.2 C-2 Sample

The C-2 sample test was conducted at a combustion chamber pressure of 3.4 MPa, a thermal load level lower than that employed in the C-1 sample test. No abnormalities were noted in the C-2 sample after it went through two steady state tests. Thus the sample was subjected to an 11-cycle combustion test in which each combustion lasted for five seconds followed by three seconds of cooling. After this cyclic test was finished, the sample underwent a 30-second steady state combustion test. During these tests, no abnormalities were detected in the sample. However, an alternate black and white striped pattern identical to the one observed in the C-1 sample was found during observations made after these tests were completed. The measurement of porosity of a portion where the sample maintained good post-test conditions found that porosity ranged from about 3.0-11.9 percent with an average of 5.2 percent.

Figure 6 is a sectional view of the C-2 sample. When the sample was cut, a small piece of the coating came off. This piece showed evidence of peeling, with the peeling running in the circumferential direction, as was observed in the C-1 sample. The peeled area represented less than 1 percent of the sample's total surface area, and thus was negligible. Microscopic observation revealed the absence of a PSZ layer, while localized boundary peeling between the middle layer and the electroformed copper layer in parts of the sample were observed. However, in general, the sample remained in good condition. Because the C-2 sample test was conducted at a thermal load of about 4 MW/m^2 —a thermal load that is two-thirds the level applied to the C-1 sample—a smaller thermal stress generated. It is believed that this prevented the effect of the nonuniform coating bonding strength from appearing. A compositional analysis of the blackened and white areas produced the same results as that for the C-1 sample.

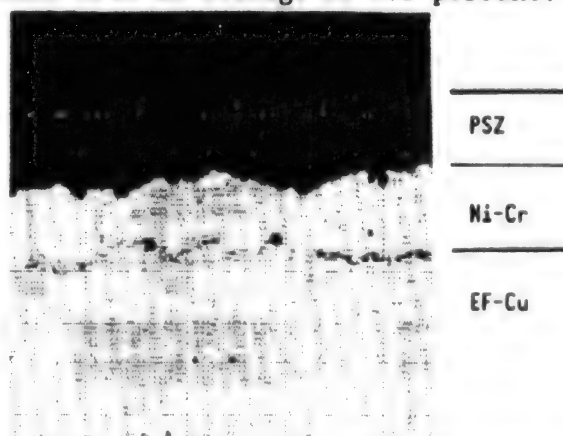


Figure 6. Photo of a Cross Section of the Sample Taken After a Combustion Test

The heat flux level of about 4 MW/m^2 applied to the C-2 sample was about 20 percent lower than the 5 MW/m^2 applied to a noncoated copper sample. The fact that the C-2 sample demonstrated less heat-insulation capability than the C-1 sample, even though their heat-insulation layers are of equal thickness, can be attributed to a factor related to the heat transfer coefficient of the

coated layer on the combustion gas current side. That is, if the heat transfer coefficient on the gas current side is high, the temperature difference between the current-side face and the back face of the heat-insulation layer increases. This pushes up the temperature on the gas current side surface, which in turn reduces the temperature potential difference between the combustion gas temperature and the surface temperature. This produces an easing of the thermal load, and, consequently, an improved heat-insulation capability. On the other hand, if the heat transfer coefficient on the gas current side is low, the temperature potential difference is not reduced significantly. This makes it necessary to increase the thickness of the heat-insulation layer to attain a desired level of heat insulation, which in turn causes the surface temperature to rise even further. To confirm this hypothesis, we conducted an experiment using the C-3 sample, which had a thicker heat-insulation layer than the C-2 sample, at a combustion chamber pressure of 3.4 MPa, a pressure equal to the one used in the C-2 sample test.

3.3 C-3 Sample

During the combustion test of the C-3 sample, it was observed that part of the coated layer peeled, and that the peeled sections were blown out by the combustion gas current shortly after the combustion test started. An examination of the inner surface of the C-3 sample after the combustion test found a stripe 7-8 mm wide where the coating was missing. The stripe ran in the axial direction (arrow in Figure 7). In addition, numerous pits were found around this stripe. (The area where the coating was missing accounted for about 7 percent of the total coated area.)



Figure 7. External Appearance of the Sample After a Combustion Test

Alternate blackened and white areas having almost the same width also were observed on the sample surface. The coating generally was missing on the white areas. As described above, the white areas correspond to those areas that had a high fuel gas density and a strong reducing atmosphere, and the blackened areas correspond to areas with a high oxygen density. The heat flux values in these areas varied, with the highest value registering in the white area where peeling occurred. Judging from these results, we believe that the peeling was caused by the difference between thermal expansion coefficients. A measurement of the porosity in the area where the coating surface remained found it to range between about 0.6 and 2.3 percent with an average of 1.5 percent.

Next, we studied a cross section of the sample, focusing on the area where the coating was missing. Figure 8 is a photo of a cross section of the sample. Figure 8(a) shows the portion where the PSZ coating is missing. It can be seen that cracks developed within the PSZ layer around the areas where the coating was missing, near the PSZ/Ni-20Cr boundary, and along the boundary. Figure 8(b) represents the white surface area where cracks were observed.

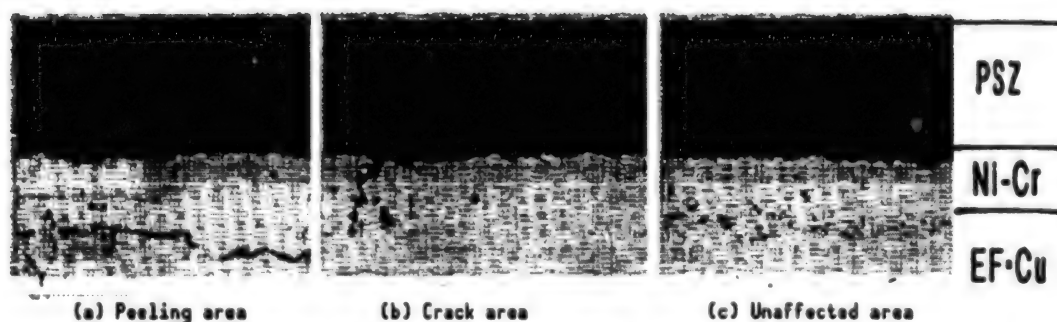


Figure 8. Photos of Cross Sections of the C-3 Sample After a Combustion Test

It can be seen that the PSZ layer has an oblique crack, while the Ni-20Cr layer has a vertical one. These cracks probably are caused by the difference in thermal expansion rates between the two layers. The combustion heat generates a strong compression force in the PSZ layer and a tensile force in the Ni-20Cr layer. It is likely that similar forces are exerted on the area where the coating is missing (Figure 8(a)), and that the peeling and dropping of the coating occurred after the portion was exposed to a localized high-level heat flux. This conjecture is backed by the fact that part of the coating peeled and was blown out shortly after the combustion test started. Except for this minor peeling and dropping, the C-3 sample generally remained in good condition throughout the test. For the C-3 sample, there was no peeling or dropping of the coating as occurred in the C-1 sample. It is believed that the almost uniform layer conditions, and the high material density with the porosity ranging between 0.7 and 2.3 percent, as seen in Figure 8(c), contributed to this generally good condition. Seven passes of the spray gun to form a PSZ coating $170\ \mu$ thick also probably helped to create a uniform film quality and to realize a high bonding strength.

The heat flux of about $3.8\ \text{MW/m}^2$ that was applied to the C-3 sample was about 25 percent lower than the heat flux level of about $5\ \text{MW/m}^2$ that was applied to a noncoated copper sample. This percentage compares to a figure of about 20 percent for the C-2 sample, proving that the C-3 sample, which has a PSZ layer thickness of about 2.6 times that of the C-1 and C-2 samples, has a greater heat-insulation capability.

3.4 Evaluation of Heat-Insulation Properties

Combustion tests of these three types of samples demonstrated the effectiveness of the ceramic coating as a heat-insulation layer, even though part of the layer in these samples was blown out and cracks developed within them. The extent of heat insulation provided by the insulation layer is dictated mainly by the layer's thickness and by its effective thermal conductivity. And it is known that the effective thermal conductivity is affected greatly by the condition of pores present within the layer. As can be seen in Figures 6 and 8(c), different pore conditions result even if a heat insulation was made using the same material and same spray method. So it is possible that the effective thermal conductivity also differs. Although the number of samples tested is small, and although the effect of peeling in some of these test

samples was not analyzed fully, we tried to calculate the effective thermal conductivity of each sample using the data obtained through our experiments.

The results of these calculations are shown in Figure 9 along with the data obtained from a sample created by the conventional atmospheric pressure spray method. The effective thermal conductivities obtained through our experiments were larger than about 0.6 W/mK, an effective thermal conductivity obtained from a conventional sample with a comparatively large porosity (about 10-20 percent). Also, the conductivity varied from sample to sample. The LPPS method used in our experiment to create the samples is capable of forming a coating with a comparatively high material density. Using this method made it possible to create samples having about 10 percent less porosity than those created using the conventional atmospheric pressure spray method. This made it possible for us to create test samples with larger effective thermal conductivity values. It is believed that differences in porosity are the cause of this variation in effective thermal conductivity among these samples.

We also studied the relationship between porosity and effective thermal conductivity. Figure 10 shows the relationship between the porosity of these samples and the mean values of their effective thermal conductivity. The figure clearly shows that there is a strong relationship between porosity and thermal conductivity, and that the effective thermal conductivity decreases steeply when porosity increases. Although they have the same coating thickness, the effective thermal conductivity in the PSZ layer of the C-1 sample stood at about 1 W/mK, as compared to about 0.8 W/mK for the C-2 sample. This lower value for the effective thermal conductivity probably was caused by

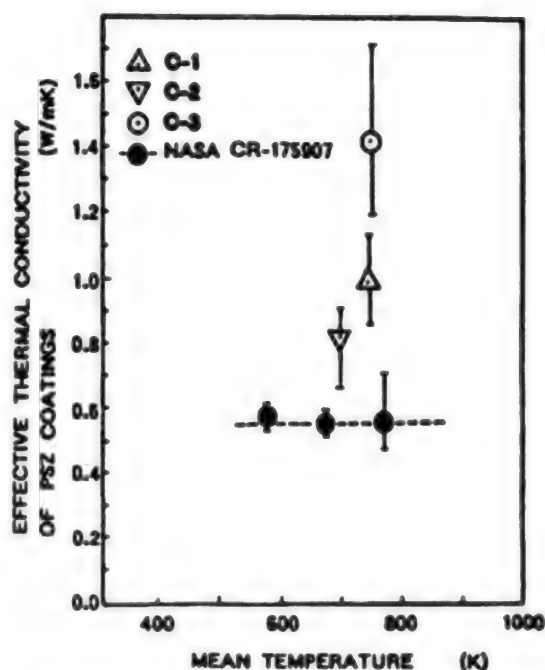


Figure 9. Comparison of Effective Thermal Conductivity Among Different PSZ Coating Samples

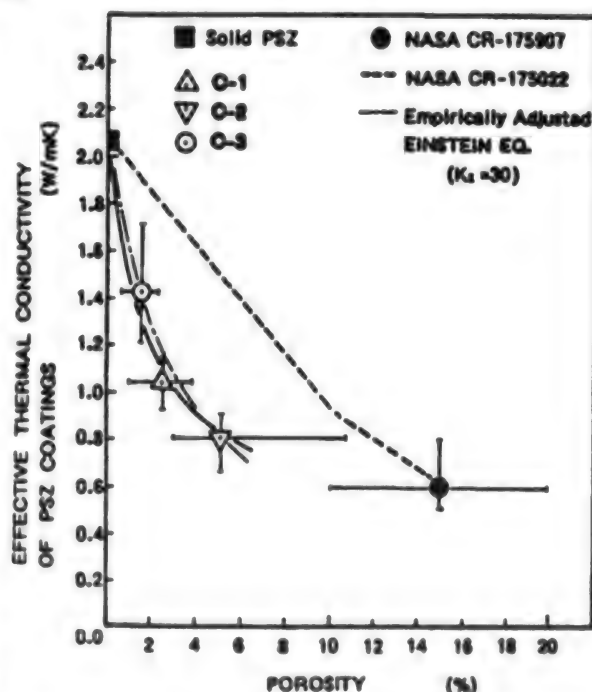


Figure 10. Relationship Between Porosity and Effective Thermal Conductivity

the increased porosity of the C-2 sample due to the progress of microscopic cracks that were caused by repeated thermal stress cycles. Although the C-2 sample was subjected to a lower heat flux level—two thirds that of the flux level applied to the C-1 sample—it underwent as many as 14 heat cycles. The C-3 sample was measured to have an effective thermal conductivity of about 1.4 M/mK, a value larger than those of two other thinner PSZ coating samples. As described above, this is because the C-3 sample is less porous than the other two samples. Figure 10 also shows the experimentally obtained porosity vs. effective thermal conductivity (shown as a dotted line curve) that was cited in a reference paper. This paper points out that when there is a change in porosity, the effective thermal conductivity of a plasma-coated sample is smaller than the value inferred by the mixture rules. As is clear from Figure 10, our test result indicates still smaller values than those cited in the reference paper. This paper uses a simplified Einstein formula as a formula to calculate the effective thermal conductivity of a sample containing pores.

$$k_c/k_s = 1/(1 + K_E \cdot p)$$

Here, K_c denotes the effective thermal conductivity of a heat-insulation layer, k_s is the thermal conductivity of a solid body containing no pores, K_E is a coefficient, and p represents porosity. For the K_E value, the paper adopted a value of 14. Our experiment produced a good coincidence at a K_E value of 30, as shown by the alternate long and short dash line in the figure. The reason for this K_E value difference, possibly can be attributed to the effect of thermal hysteresis. That is to say, conventional evaluations of effective thermal conductivity were conducted using samples that were not subjected to heat load processes. In contrast, the data in our experiment were obtained from steady state samples that underwent at least one period of nonsteady state heating by being subjected to a combustion test. In those samples in which blowing out of part of the coating was observed, there is a good possibility that numerous microscopic cracks developed within the heat-insulation layer because of the large thermal stress generated by the nonsteady state heating. It is believed that in our experiment this caused the values for effective thermal conductivity to be substantially smaller than conventional experiments conducted at the same level of porosity.

This represents a very important finding in view of current efforts to develop a better heat-insulation layer. In practical utilization, combustors experience nonsteady state heating for a while after combustion begins until a steady state heating condition is reached. If many microscopic cracks develop within the heat-insulation layer, even when no abnormalities appear on the surface, the effective thermal conductivity decreases. This causes the surface temperature of the heat-insulation layer to rise higher than the designed temperature ceiling, and this, in the worst case, causes the insulation layer to melt.

As described above, the effective thermal conductivity of a heat-insulation layer is affected by porosity and by heat load conditions. Because of this, it is important to accumulate data on the relationship between porosity and effective thermal conductivity to promote adequate designs of heat-insulation layers and FGMs. It also is important to establish porosity control

technology, and to promote relevant research by emphasizing the evaluation of relationship between porosity and effective thermal conductivity in utilization conditions.

4. Conclusion

We have conducted combustion tests of water-cooled samples protected by ceramic coatings formed by the LPPS method. As the combustion fuel, liquid oxygen and methane gas were used. In some of these samples, peeling of the coating running in either the circumferential direction or axial direction was observed after the combustion test was finished. The axial direction peeling occurred in a sample having a comparatively thick heat-insulation coating. This peeling is believed to have been caused by a localized high thermal load generated by the nonuniformity of combustion gas intensity on the coating surface, and by the large compressive thermal stress caused by the thermal load. Circumferential peeling occurred in samples having a relatively thin heat-insulation layer. This peeling is believed to have been caused by the nonuniformity of intralayer bonding strength because of an insufficient number of surface scannings by the spray gun. This leads to selective peeling of the coating under thermal stress where the bonding strength is low. When the coating is thin, it is believed that nonuniform film quality is unavoidable to a certain degree. Under these circumstances, it is important to promote the utilization of FGMs to alleviate thermal stress, and to seek structural control to improve film quality. It also should be noted that the heat flux levels measured in each of these samples were about 20-25 percent lower than the corresponding values for a copper sample having no heat-insulation coatings. Although minor peeling of the coating was observed in some of these samples, the effectiveness of the heat insulating layer was ascertained. When samples having a porosity lower than about 10 percent are involved, our experiment demonstrated that the effective thermal conductivity of the samples is lower than the conductivity value inferred by the mixture rules, and also is lower than that of samples created by the conventional atmospheric pressure spray method. The reason for this probably is related to the appearance of many microscopic cracks within the heat-insulation layer that were caused by the large thermal stress that is generated immediately after the start of a combustion test.

Structure, Function of FGM Database Network

926C0014V Tokyo FGM '91 in Japanese 8-9 Oct 91 pp 335-337

[Article by Takayasu Sudo, Katsuto Kisara, Akio Moro, and Masayuki Niino, Kakuda Research Center, National Aerospace Laboratory, Science and Technology Agency]

[Text] Abstract: Functionally gradient materials (FGMs) are promised for the space plane. This report mentions the operation and structure of the functionally gradient materials database.

1. Introduction

Research is under way to develop functionally gradient materials (FGMs) that will be used as heat-insulation materials in the projected space plane and in rocket engines. Many research organizations have been involved in the FGM development program, conducting research on different subjects and problems. To make it possible for these research efforts to be conducted efficiently, it is important to ensure the smooth flow of information among these organizations, and to promote close cooperation among them.

In this article, we will discuss the database network system and knowledge base that have been developed to promote the effective sharing of research data.

2. Database Structure

The FGM database has 23 subject tables that are grouped into five categories corresponding to the same number of data sheets for inputting data. Figure 1 shows the relationship between these tables and the data sheets. Each table is linked with the other tables by access numbers.

The "common" data table is linked to the four other group items, and it enables researchers to obtain information on the registered materials.

The tables of "thermophysical properties," "microstructure," and "structural control method" store data on the properties of evaluated materials, measurement methods, and other related subjects. In these tables, property value data

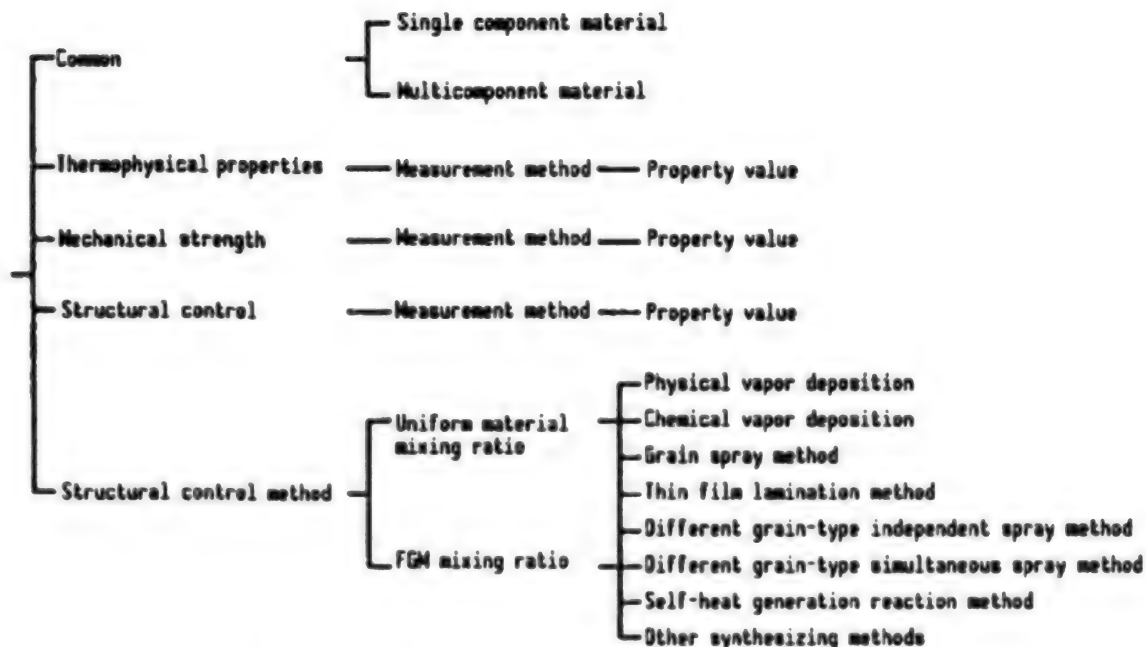


Figure 1. Relationship Among Table Items

can be registered in variable lengths. This is because these data, which include information about mixing ratios and temperature dependence, assume a two-dimensional or three-dimensional form. The "thermophysical property" table accommodates data on density, linear expansion coefficients, thermal conductivity, thermal diffusivity, and specific heat. The "mechanical strength" data table contains data on Young's modulus, Poisson ratio, flexural strength, tensile strength, compression strength, SP energy, SP strength, stress, and distortions. The "structural control method" data table houses data on pore rate and contraction rate.

In the "structural control method" table, the compositional mixing ratio and material synthesizing conditions are registered according to the production method.

3. Database System

The large number of data items involved makes it difficult to access a specific data item directly. To make such access easier, we have developed a database manipulation program that guides users to the data item by offering frames of menus that allow users to select suitable listed items easily. This database can be accessed by these organizations any time via the network communication line.

The program also makes it possible to use an identically structured separate database on off-line personal computers. The time-consuming inputting of data and editing of the data thus entered are carried out on off-line computers, and the newly entered data are then transferred to the database on the network using the communication line or a floppy disk. The program also makes it

possible to call up data lists on a display screen for data checking or data search.

As of 6 September 1991, there were 413 material system data items (Table 1) registered in this database.

Table 1. Registered Material Systems

MoS ₁₂	-	TiAl	-	SiC
PSZ	-	Ni		
PSZ	-	NiCr		
PSZ	-	NiCoCrAlY		
PSZ	-	NiCrAlY		
PSZ	-	SUS		
PTFE	-	Ag		
PTFE	-	C		
SiC	-	C		
SiC	-	TiC		
TiB ₂	-	Cu		
TiB ₂	-	Ti		
TiC	-	Ti		

4. Network System

We have developed a network management system that makes it possible for these research organizations to access the database directly and easily from their workstations. The network (Figure 2) uses public telephone lines to connect these workstations to the database. And to facilitate communication, we also

we also developed an exclusive software program that supports FGM data communications. The development of this software has made it possible for these research organizations not only to use the database and the FGM design support system, but also to use electronic bulletin board, electronic conference, and electronic mail. This program also

makes it possible to transfer word processed document files, programs, and image data in the form of electronic files in both directions.

5. Image Database

As a step toward building the image database—which will include figures, tables, and photographs of such things as microstructures—we have sought to develop an image database prototype. Our image data included report documents, graphs, and photographs. Figure 3 [not reproduced] shows an example of a CRT screen display for the database prototype.

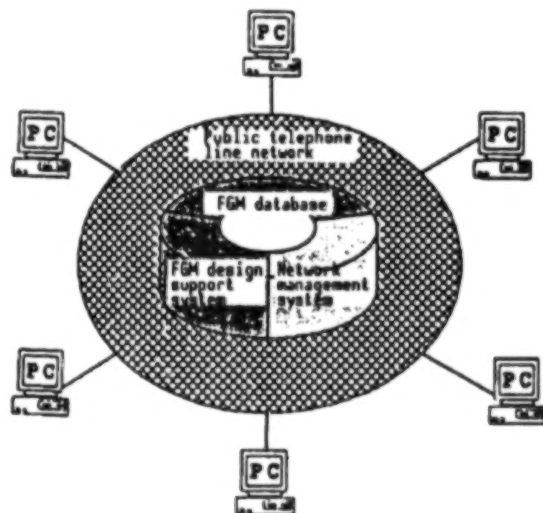


Figure 2. Network System

There are a number of problems that must be solved to build the image database, including hardware capability, matching with image processing hardware, the method of preserving image data files, the huge, time-consuming workload involved in data building, and the usage of network communication lines. Efforts to solve these problems are under way.

6. Building the Knowledge Base

In preparation for the construction of the FGM knowledge base that will be used as the core of the projected FGM design support system, we have selected and arranged the reports on FGM research results publicized to date. The documents include various reports and symposium papers. The selection was made by confining the subject to ZrO_2 -system and SiC-system materials. In selecting the data, we emphasized process parameters and microstructure, microstructure and properties, composition and properties, and evaluation test results. These selected reports were rearranged into a decision table format, and then they were converted into a simple tree-structured frame-type knowledge base using the table designing tool included within "ESHELL," an expert system development support program (language used: LISP).

7. Conclusion

FGMs are regarded as very promising heat-insulation materials that can be used in the projected space plane. The study for formulating FGM design standards to promote the utilization of these materials in the plane started this year. We hope that efforts to expand the database will continue to promote FGM development.

- END -

END OF

FICHE

DATE FILMED

30 Nov 1992

